THE BRAIN'S VALIUM: INSIGHTS INTO DIAZEPAM BINDING INHIBITOR EFFECTS ON GABA-MEDIATED INHIBITION

By

Jennifer S. Borchardt

A dissertation submitted in partial fulfillment

of the requirements for the degree of

Doctor of Philosophy
(Cellular and Molecular Biology)

at the

UNIVERSITY OF WISCONSIN – MADISON

2021

Date of final oral examination: 7/14/2021

This dissertation is approved by the following members of the Final Oral Committee:

Cynthia Czajkowski, Professor, Neuroscience

Mathew Jones, Associate Professor, Neuroscience

Robert Pearce, Professor, Anesthesiology

Luigi Puglielli, Professor, Medicine

Gail Robertson, Professor, Neuroscience

Avtar Roopra, Associate Professor, Neuroscience

TABLE OF CONTENTS

FIGURES

TABLES

ABBREVIATIONS

5-HT_3R	serotonin receptor
A1	agonist binding site 1
A2	agonist binding site 2
ABC	ATP binding cassette
ACBP	acyl-coA binding protein
ACN	acetonitrile
ALP	alprazolam
ANOVA	analysis of variation
BZD	benzodiazepine
cryoEM	cryogenic electron microscopy
D	benzodiazepine binding site
DBI	diazepam binding inhibitor
df	fast desensitization gate
DMCM	methyl-6,7-dimethoxy-4-ethyl-beta-carboline-3-carboxylate
ds	slow desensitization gate
DZP	diazepam
EC	effective concentration
ECD	extracellular domain
EPR	electron paramagnetic resonance
ER	endoplasmic reticulum
ETO	etomidate
F1	intermediate F element 1
F2	intermediate F element 2
FC	fluorocitrate
FEP	fluorinated ethylene propylene
FLZ	flumazenil
FTICR	Fourier-transform ion cyclotron resonance

FZM	flurazepam
GABAR	gamma-aminobutyric acid type A receptor
GARLH	GABAR regulatory Lhfp1
GLIC	*Gleobacter violaceus*
GlyR	glycine receptors
GPCR	G-protein coupled receptors
HNR	HEPES normal Ringer's
HSQC	heteronuclear single quantum correlation
ICD	intracellular domain
ID	inner diameter
IDA	imidazole
iPSC	induced pluripotent stem cell
IPSC	inhibitory postsynaptic current
IPSP	inhibitory postsynaptic potential
Kan	kanamycin
LB	luria broth
LGIC	ligand-gated ion channels
lnRNA	long noncoding RNA
m	main channel gate
MALDI	matrix-assisted lasor desorption/ionization
MEA	multielectrode array
mIPSC	miniature inhibitory postsynaptic potential
MWC	Monod, Wyman and Changeux model
nAChR	nicotinic acetylcholine receptor
NAM	negative allosteric modulator
NiNTA	nickel nitrilotriacetic acid
NMR	nuclear magnetic resonance
nRT	thalamic reticular nucleus

NX	normalized expression
OD	outer diameter
ODN	octadecaneuropeptide
OP	octapeptide
P4S	piperidine-4-sulphonic acid
PAM	positive allosteric modulator
PB	pentobarbital
PE	1-palmitoyl-2-oleoyl-sn-glycero-3-phosphoethanolamine
PG	1-palmitoyl-2-oleoyl-sn-glycero-3- phospho- (1'-rac-glycerol)
PKC	protein kinase C
pLGIC	pentameric ligand-gated ion channels
PPF	propofol
PS	pregnenolone sulfate
PTFE	polytetrafluoroethylene
PTX	picrotoxin
RAD	resting-active-desensitized model
SDSL	site-directed spin labelling
sIPSC	spontaneous inhibitory postsynaptic potential
TFA	trifluoroacetic acid
THDOC	Tetrahydro-deoxycorticosterone
THIP	4,5,6,7-tetrahydroisoxazolo[5,4-c]pyridin-3-ol
TMD	transmembrane domain
TSPO	translocator protein
TTN	triakontetraneuropeptide
TV	transcript variants
wt	wild-type
τ_w	weighted tau

PUBLICATIONS

Manuscripts:

1. Tiwari, V., **Borchardt, J.S.**., Schuh, A., Klug, C., and Czajkowski, C. (2020). Ligand-induced motions in pentameric ligand-gated ion channels revealed by EPR spectroscopy. bioRxiv. (In review at eLife).

2. **Borchardt, J.S.,** Blecker, L., Tung, A., Satyshur, K., and Czajkowski, C. (2021). The diazepam binding inhibitor's modulation of the GABA-A receptor is subunit-dependent. bioRxiv. (In review at PLoS ONE).

3. **Borchardt, J.S.,** Pearce, R.A., Czajkowski, C. (2021). The diazepam binding inhibitor positively modulates αβ GABA receptors. *Manuscript in preparation.*

Abstracts:

1. **Borchardt, J.S.**, Mangan, K., Czajkowski, C. (2017). The Brain's Valium: Investigating the role of DBI in regulating GABA-mediated inhibition. Abstract for poster presentation, Society for Neuroscience, Washington D.C.

2. **Borchardt, J.S.**, Giezendanner, N., Pearce, R.A., Czajkowski, C. (2019). Effects of the diazepam binding inhibitor on GABA-mediated currents. Abstract for poster presentation, Society for Neuroscience, Chicago

ACKNOWLEDGMENTS

Firstly, I would like to thank my advisor, Dr. Cynthia Czajkowski, for all of her hard work as my advisor and mentor. I could never have performed these experiments or written this thesis without her guidance and support. In my time in Cindy's lab, I learned crucial lessons about how to design thoughtful, well-controlled experiments, how to troubleshoot seemingly insurmountable problems, and how to use data to tell a meaningful story. I am so grateful for the opportunities and guidance I received as a member of Cindy's lab, and for how she showed me what it meant to be a true scientist.

I must also thank the members of my thesis committee, Drs. Mathew Jones, Robert Pearce, Luigi Puglielli, Gail Robertson, and Avtar Roopra for all of their help and guidance over the years. Their thoughtful questions and advice have been essential to my development as a student and scientist. I am particularly grateful to Dr. Robert Pearce, who taught me patch clamp recording, showed me how to build ultra-rapid application pipettes, and provided countless hours of both technical and experimental advice. Much of this thesis would have been impossible without his input.

I am also grateful to the members of the Czajkowski lab, both past and present. Starting in this lab and getting to work with Varun Tiwari, Teja Karimikonda, Vicki Tsao, Namrta Purwar, and Cassie Theusch was such a delight. I learned so much from each of them and miss all of the fun we shared both in and out of the lab. It has been wonderful getting to know the newer members of this lab as well. I so appreciate Luke Blecker and Anton Tung for all of the enthusiasm, energy, fun, and riddles they have brought to the lab, and am so privileged to have gotten to work alongside Nathalie Dinguirard for these last two years. Nathalie's help, advice, and sense of humor was truly essential in helping my cling to my remaining sanity as I finished my thesis work.

I would like to thank my family and friends for their continual love and support. In particular, I am so grateful to my parents, Ron and Sara, for all of their guidance, support and inspiration throughout my life, and to my sister, Kate, whose love of frequent video calls kept me feeling close to home and connected to family during these long years in grad school.

There is no way I could write an acknowledgments section for any document without thanking my wife, Jocelyn. Seven years ago, you agreed to move 2000 miles away from where we lived in sunny California to come to grad school with me in snowy Wisconsin, and I am so grateful that you did. There is absolutely no way I could have done this without you. Thank you for proofreading this thesis even if I didn't include most of your parenthetical jokes. Thank you for cutting just about every vacation short so that I could come back in time to take care of my cells. Thank you for the countless hours you spent waiting after I needed to run into lab but promised it would "just take twenty minutes." Most of all, thanks to you and to the entire menagerie (Troll, Potato, and Bartleby), for always making me laugh and for being a constant, daily source of support.

ABSTRACT

THE BRAIN'S VALIUM: INSIGHTS INTO DIAZEPAM BINDING INHIBITOR EFFECTS ON GABA-MEDIATED INHIBITION

Jennifer S. Borchardt

Cellular and Molecular Biology PhD Program, University of Wisconsin-Madison

Benzodiazepines (BZDs) were discovered in the mid-1950s and have been widely prescribed since their synthesis. BZDs are used to treat a wide variety of conditions based on their antiepileptic, anxiolytic, and sleep-inducing properties, and act by binding gamma-aminobutyric acid type A receptors (GABARs). GABARs are found in synapses between neurons and mediate the majority of fast inhibition in the brain. Disruptions in GABA-mediated inhibition has been linked to Alzheimer's, anxiety, epilepsy, autism, and other diseases. In order to exert their clinical effects, BZDs bind to a specific pocket in the extracellular domain between two subunits of the GABAR. Generally, the binding of a BZD increases the amount of GABA-elicited current, thus increasing inhibition.

Scientists have long theorized that there is an endogenous ligand for the BZD binding site. In 1983, a candidate protein was identified based on its ability to displace a radiolabeled BZD from GABARs. This protein, the diazepam binding inhibitor (DBI), is proposed as an endogenous benzodiazepine or endozepine, but evidence for its direct effects on GABA-mediated inhibition are limited.

In my thesis, I take a reductionist approach to understand how DBI interacts with and affects GABAR activity. After purifying DBI, I used multiple electrophysiology techniques to study how the effects of DBI vary with alternate GABAR subunit composition. I found that α3-containing GABARs are weakly negatively modulated by DBI, while α5-containing receptors are

positively modulated. I also found that GABARs without γ subunits are strongly positively modulated by DBI and used kinetic modeling to explore how this potentiation might be achieved. The ability of DBI to modulate αβ GABARs provides the first evidence that DBI does not need a BZD binding site to modulate GABARs.

Taken together, my results provide novel insights into DBI's role in GABA-mediated inhibition. I found that not only do the effects of DBI vary by GABAR subunit composition, but that DBI can modulate GABARs without binding to the BZD site. My findings dispute the role of DBI as an endogenous version of a classical benzodiazepine, and shed new light on how this peptide is able to modulate GABA-mediated inhibition.

CHAPTER I:

Introduction

Chemical Signaling in the Brain

The brain is one of the most important organs in the body. It regulates the functions of other organs, monitors sensory input, and processes information into learning, memory and feeling. Much of this function is performed by communication between neurons, where chemical signals are passed from one cell to another and are transformed into electrical signals known as action potentials. This electrochemical communication occurs at the synapse (Figure 1.1) where bioactive chemicals called neurotransmitters are released from one neuron to the next. The presynaptic neuron has vesicles packed with neurotransmitters which fuse to the cell membrane and release their contents into the synaptic cleft. These neurotransmitters then diffuse across the synapse and bind to receptors embedded in the membrane of the post-synaptic neuron, which transduce binding of the neurotransmitter into downstream signals.

These receptors fall into two general classes – G-protein coupled receptors (GPCRs) and ligand-gated ion channels (LGICs). In response to neurotransmitter binding, GPCRs initiate an internal signal cascade which can lead to changes in gene expression and protein production. Faster communication, on the order of microseconds to milliseconds rather than milliseconds to minutes, occurs when neurotransmitters bind to LGICs, which causes these proteins to open an integral ion-conducting pore. As the pore opens, charged ions will flow into or out of the postsynaptic neuron depending on the LGIC type and the ion's electrochemical gradient. This flow of ions will alter the membrane voltage of the neuron.

Neurons have a threshold membrane voltage which, when reached via excitatory signaling, will trigger an action potential. An action potential is a signal which propagates along the axon of the neuron to the nerve terminal. Depolarization in the nerve terminal causes the influx of calcium from voltage-gated channels. The calcium triggers the fusion of

neurotransmitter-packed vesicles to the cell membrane. Releasing these neurotransmitters into the synaptic cleft initiates communication with downstream neurons. Inhibitory signaling makes it harder for the neuron to reach the threshold voltage, and thus less likely to fire an action potential. This thesis focuses on one specific LGIC, the gamma-aminobutyric acid type A receptor (GABAR).

pLGIC Family

GABARs are part of the pentameric ligand-gated ion channel (pLGIC) superfamily. These are proteins comprised of five homologous subunits arranged around a central, ion-conducting pore (Figure 1.2). The binding sites for specific neurotransmitters are found at subunit interfaces in the extracellular domain (ECD), and the channel is lined by the second transmembrane domain (TMD) spanning alpha helix, M2, from each of the five subunits. Members of the pLGIC superfamily bind distinct neurotransmitters and are either cation-selective (K^+, Na^+) or anion-selective (Cl^-). Excitatory cationic-conducting pLGICs include serotonin type 3 receptors (5-HT_3Rs) and nicotinic acetylcholine receptors (nAChRs), while inhibitory anionic-selective pLGICs include glycine receptors (GlyRs) and GABARs. Recent cryogenic electron microscopy (cryoEM) studies of members of the pLGIC superfamily including the GABAR (Laverty et al., 2019; Masiulis et al., 2019; Phulera et al., 2018), the nAChR (Walsh et al., 2018), and 5-HT_3R (Basak et al., 2018a; Basak et al., 2018b), have generated high-resolution structures of these receptors. In brief, each of the five subunits have large N-terminal extracellular domains (ECDs) primarily composed of beta-strands, four transmembrane-spanning alpha-helices, and additional intracellular structure (daCosta and Baenziger, 2013). While prokaryotic pLGICs like GLIC and ELIC are made up of five identical subunits, the majority of eukaryotic channels are hetero-oligomeric.

GABA Receptors

The GABAR is made up of five heterologous subunits (Figure 1.3). There are nineteen different subunits, including six α subunits, three β, and three γ subunits. The majority of

GABAR receptors are comprised of $\alpha_1\beta_2\gamma_{2L}$ subunits arranged in a clockwise pattern of α-β-α-β-γ around a central, chloride-conducting (Olsen and Sieghart, 2008). The γ subunit can also be replaced with a δ, ε, π, θ or one of three ρ subunits, or an additional α or β subunit. The receptor has two binding sites for GABA, located in the ECD at the interfaces between α and β subunits. Binding GABA makes the receptor more likely to shift from its closed, non-conducting state into an open, chloride-conducting state. In the continued presence of GABA, the channel transitions to a non-conducting, desensitized state.

GABAR Function

GABARs are the primary inhibitory neurotransmitter receptors in the brain and are responsible for the majority of the fast inhibition. This fast inhibition is also known as phasic inhibition. When synaptic GABARs are exposed to short, sub-millisecond exposures (Mozrzymas et al., 2003) of high, millimolar concentrations of GABA (Mody et al., 1994), they open the chloride-conducting channel. Given a mature neuron has a resting voltage of approximately -65mV and the equilibrium potential for chloride is roughly -75mV (Ben-Ari, 2002), chloride will flow in a net inward direction and cause an inhibitory postsynaptic potential (IPSP) which makes the cell less likely to fire an action potential (Farrant and Nusser, 2005). These inhibitory, GABAergic synapses have an important role in regulating neuronal firing and signal propagation. For example, phasic inhibition regulates rhythmic thalamocortical oscillations which are important for cognition and sleep-wake cycles (Llinás et al., 2005), as well as hippocampal network oscillations which are needed for navigation and memory (Mann and Paulsen, 2007).

GABARs also function as regulators of tonic inhibition. Tonic inhibition occurs when GABARs expressed extrasynaptically bind ambient, micromolar levels of GABA found in the brain and reduce the excitability of the neuron (Farrant and Nusser, 2005; Mody and Pearce, 2004; Semyanov et al., 2003). For example, the dentate gyrus, which regulates hippocampal excitability, contains granule cells that exhibit more polarized membrane potentials and lower

firing rates than other neurons. These differences are attributed to tonic inhibition from extrasynaptic receptors, and are important for regulating the excitability of the hippocampus (Lee and Maguire, 2014). This tonic inhibition is mediated primarily by δ and α6 subunit-containing receptors (Stell et al., 2003), though other combinations are also observed. αβ GABARs are also located extrasynaptically and believed to play a role in regulating tonic inhibition (Mortensen and Smart, 2006).

The GABAR's role in regulating inhibition in the brain through both phasic and tonic inhibition makes it important for a variety of normal brain functions including sleep, learning, and memory. Disruption or deficits in GABAR function are associated with a variety of diseases and disorders including: anxiety (Engin et al., 2018), Alzheimer's (Calvo-Flores Guzmán et al., 2018; Govindpani et al., 2017), epilepsy (Palma et al., 2017), insomnia (Wisden et al., 2019), autism (Vien et al., 2015), Fragile X (Van der Aa and Kooy, 2020), and schizophrenia (de Jonge et al., 2017).

Subunit Composition and Location

Multiple subtypes of GABAR pentamers are possible, based on assembling nineteen different subunit isoforms. There are six possible α subunits, three β, and three γ subunits, and the γ subunit can be replaced with a δ,ε,π, or one of three ρ subunits, or an additional α or β subunit. Receptor subunit composition varies based on developmental stage (Barnard et al., 1998) and also by brain region (Sequeira et al., 2019).

Immunocytochemistry and immunogold electron microscopy experiments have shown that the majority of GABARs in the brain are made up of α, β and γ subunits (Bohlhalter et al., 1996; Fritschy et al., 1992; Nusser et al., 1995; Somogyi et al., 1996), and the most abundant combination across the brain is $\alpha_1\beta_2\gamma_2$. However, regional expression of alternate subunit combinations has been observed. For example, analysis of mRNA and protein expression using *in situ* hybridization and immunohistochemistry in mouse brains reveals high expression of α3 in the thalamic reticular nucleus, while α5 and β3 are highly expressed in the hippocampus

(Hörtnagl et al., 2013). GABARs can also be found extrasynaptically as well, where they bind low levels of GABA and regulate tonic inhibition of neurons. These extrasynaptic receptors are generally $\alpha_5\beta\gamma_2$ in hippocampal and neocortical pyramidal cells; $\alpha_4\beta\delta$ in thalamic relay neurons, neocortical pyramidal cells, and hippocampal dentate granule cells; $\alpha_6\beta\delta$ in cerebellar granule cells; and $\alpha_1\beta\delta$ in hippocampal and neocortical interneurons (Brickley and Mody, 2012). Using immunogold electron microscopy in cerebellar granule cells, the Somogyi group was able to detect high level of the δ subunit in extrasynaptic regions, but did not reveal any synaptic expression of δ subunits (Nusser et al., 1998).

In 2008, Olsen and Sieghart generated a list of known, native combinations of GABAR subunits based on the criteria of being functionally expressed in heterologous systems with unique properties; being seen to colocalize in native tissue as observed via *in situ* hybridization, single-cell RT-PCR, light and electron microscopy; coimmunoprecipitation; and evidence of function in a native environment. Their list (Olsen and Sieghart, 2008) is comprised of three categories with minor adjustments in Smart and Stephenson's 2019 review (Smart and Stephenson, 2019):

- Identified –
  - $\alpha_1\beta_2\gamma_2$
  - $\alpha_2\beta\gamma_2$
  - $\alpha_3\beta\gamma_2$
  - $\alpha_4\beta\gamma_2$
  - $\alpha_4\beta_2\delta$
  - $\alpha_4\beta_3\delta$
  - $\alpha_5\beta_2\gamma_2$
  - $\alpha_6\beta_2\gamma_2$
  - $\alpha_6\beta_2\delta$
  - $\alpha_6\beta_3\delta$
  - ρ1-3

- Existence with High Probability –
  - $\alpha_1\beta_3\gamma_2$
  - $\alpha_1\beta\delta$
  - $\alpha_5\beta_3\gamma_2$
  - $\alpha\beta_1\gamma/\alpha\beta_1\delta$
  - $\alpha\beta$
  - $\alpha_1\alpha_6\beta\gamma/\alpha_1\alpha_6\beta\delta$

- Tentative –
  - $\alpha\beta\gamma_1$
  - $\alpha\beta\gamma_3$
  - $\alpha\beta\theta$
  - $\alpha\beta\epsilon$
  - $\alpha\beta\pi$
  - $\alpha_x\alpha_y\beta\gamma_2$ where α_x and α_y represent two different α subunits

Due to advances in RNASeq, scientists are able to evaluate levels of GABAR subunit gene expression across the brain in a higher throughput manner. In 2019, the Limon group used microarray and RNA-Seq datasets from the Allen Institute to evaluate transcription of GABAR subunits across 111 substructures in the human brain (Figure 1.4). For example, high levels of α5, β3 and γ2 can be seen in the hippocampal region, while notable levels of α3, β3 and γ2 can be observed in the hypothalamus. Their study demonstrates the frequent co-expression of some GABAR subunit genes and the similarities across tissues with common embryonic structural origin (Sequeira et al., 2019), and illustrates how large-scale databases can be used to evaluate expression of GABARs across the brain.

The subunit composition of the GABAR affects the function and pharmacology of the receptor. GABA potency and efficacy is affected by different subunit combinations, with shifted GABA EC_{50} values and changes in maximum evoked currents for expressed receptors (Mortensen et al., 2012). Subunit composition can also alter the effects of different GABAR-modulating drugs (Knoflach et al., 1996).

Accessory/Auxiliary Subunits

GABARs also are associated with proteins that function as auxiliary subunits which stabilize their position and function at the synapse. One such protein family, the GABAR regulatory Lhfp1 (GARLH), are associated with the gamma subunit of the GABAR and neuroligin-2. Yamasaki et al. use mass spectrometry to show that GARLH3 and GARLH4 stabilize synaptic expression of gamma subunit containing GABARs at the synapse (Cho, 2017;

Yamasaki et al., 2017). Shisa7 has also been shown to co-localize with GABARs and the trafficking protein, gephyrin. Shisa7 also co-precipitates with some GABAR subunits and may potentiate BZD effects for some subunit combinations (Han et al., 2019). Proteins like gephyrin, GABARAP and radixin have also been shown to affect trafficking of GABARs to the cell surface (Lorenz-Guertin et al., 2018).

GABAR Ligands

Orthosteric Agonists

GABA is the endogenous neurotransmitter ligand for the orthosteric binding site of the GABAR. GABA interacts with residues located in regions A, B and C in the ECD of the β subunit and regions D, E and F of the α subunit (Ernst et al., 2003; García-Nafría and Tate, 2020; Smith and Olsen, 1995). GABA binding at both β-α interfaces is required to open the channel with high probability. Additional, exogenous compounds are able to bind to the orthosteric site including muscimol; partial agonists such as 4,5,6,7-tetrahydroisoxazolo[5,4-c]pyridin-3-ol (THIP) or piperidine-4-sulphonic acid (P4S), which bind in the orthosteric site but elicit smaller currents than GABA or muscimol even at saturating concentrations (Mortensen et al., 2004); and competitive antagonists like gabazine (SR95531) and bicuculline that bind in the orthosteric site but do not open the channel.

Allosteric Modulation

In addition to binding ligands at the orthosteric site, the GABAR also binds ligands which can modulate GABA-elicited current. By binding at alternate sites in the receptor, they act as either positive allosteric modulators (PAMs), which increase the amount of current elicited by GABA; negative allosteric modulators (NAMs), which decrease the amplitude of GABA-elicited current; or zero modulators, which bind the modulatory site but do not affect the GABA-gated current (Figure 1.5). These allosteric modulators do not promote high probability opening or closing of the channel on their own, rather they amplify or inhibit the GABA-elicited currents.

See Figure 1.6 for a summary of GABAR drug binding sites from the 2020 Garcia-Nafria and Tate review of crystal and cryoEM structures.

Benzodiazepines

Benzodiazepines (BZDs) are one of the most common classes of drugs that target the GABAR. They have been widely prescribed since their 1955 discovery and have been included on the World Health Organization's list of essential drugs since the list was first compiled in 1977 (Organization, 1977). BZDs are prescribed for a wide variety of therapeutic effects including anxiogenic, sleep aid and antiepileptic properties.

BZD effects are mediated by binding to an intersubunit pocket in the ECD between α and γ subunits (Figure 1.6). Experiments using mutagenesis and cysteine modification have identified key regions and residues for BZD-binding and efficacy in regions A-F, much like the GABA-binding site (Morlock and Czajkowski, 2011; Olsen and Sieghart, 2009). Recent high resolution cryoEM structures of the GABAR in the presence of BZDs have confirmed this extracellular BZD site location (Masiulis et al., 2019; Zhu et al., 2018). A second BZD site in the TMD was also observed for diazepam (valium) but not for alprazolam (Xanax). A histidine residue, H101 in α_1 subunits, is present in the extracellular BZD binding site and is conserved in α subunits 1, 2, 3, and 5, and is critical for high-affinity binding of classical BZDs (Rudolph et al., 1999). α4 and α6 have an arginine instead of the histidine residue at this locus; this substitution renders them insensitive to classical BZDs (Kelly et al., 2002).

BZDs comprise a wide variety of clinical drugs. Some BZDs, like flurazepam (FZM), have a classical BZD structure, with two benzene rings and a cycloheptane, while others like Ro15-4513 have a more novel imidazobenzodiazepine structure (Figure 1.5A). When PAMs like FZM bind the BZD site, they increase the current elicited by a sub-saturating concentration of GABA. This increase in current results in a left-shifted GABA dose-response curve. In the presence of saturating concentrations of GABA, BZD binding prolongs the deactivation phase of macroscopic currents, which slows the channels' transition from a conducting to a non-

conducting state (Bianchi, 2010). Conversely, the binding of NAMs like the beta carboline methyl-6,7-dimethoxy-4-ethyl-beta-carboline-3-carboxylate (DMCM) act as inverse agonists and decrease the current elicited by a given amount of GABA, which shifts the GABA dose response curve to the right (Figure 1.5B, C). Drugs like flumazenil (FLZ, Ro15-1788) act as zero modulators or BZD antagonists in that they elicit no change in current and prevent the binding of other drugs to the BZD site that may potentiate or inhibit GABA-induced currents. Zero-modulators do not shift the GABA dose-response curve. Whether a BZD is a PAM, NAM or a zero modulator can be influenced by subunit composition of the GABAR. For example, while Ro15-4513 acts as a NAM for $\alpha_1\beta_2\gamma_2$, it is a PAM for $\alpha_4\beta_2\gamma_2$ and $\alpha_6\beta_2\gamma_2$ (Knoflach et al., 1996). The structural and kinetic effects of BZDs will be described later in this chapter.

Neurosteroids

When progesterone and deoxycorticosterone are metabolized, they can create neurosteroids which bind and positively modulate the GABAR (Belelli and Lambert, 2005). These endogenous compounds can affect stress, anxiety, and seizure-susceptibility by binding the GABAR and are released in the brain in response to stress or pathophysiological conditions (Carver and Reddy, 2013; Reddy, 2010). Tetrahydro-deoxycorticosterone (THDOC) is one of the most potent GABAR ligands and acts as a PAM. There are also neurosteroids such as pregnenolone sulfate (PS) which act as NAMs (Laverty et al., 2017).

Mutagenic studies and crystallography experiments indicate that neurosteroid binding sites are found within the TMD. Site-directed mutagenesis suggests that the cytoplasmic end of the M1 helix in the α_1 subunit is required for neurosteroid effects (Bracamontes et al., 2012), while recent crystal structures of chimeric GABARs indicate that THDOC binds at the cytoplasmic side of the β-α interface in the TMD, while the PS binds between the M3 and M4 helices of a single subunit (Laverty et al., 2017; Miller et al., 2017).

Other GABAR Ligands

In addition to BZDs and neurosteroids, GABARs also bind intravenous anesthetics including etomidate (ETO), ketamine, propofol (PPF) and barbiturates like pentobarbital (PB), as well as volatile anesthetics like isoflurane, nitrous oxide, and halothane. These compounds all enhance the effects of the GABAR and cause analgesia, amnesia, hypnosis or muscle relaxation (Garcia et al., 2010). Photolabeling studies indicate PB binds in the TMD between the M1 and M3 helices of α-β and γ-β interfaces (Chiara et al., 2013), while ETO and PPF bind at both β-α M1-M3 TMD interfaces (Chiara et al., 2012; Yip et al., 2013). The results of these experiments were validated by recent cryoEM studies (Masiulis et al., 2019). Both ETO and PB act as PAMs at low concentrations, but directly gate the channel open at higher concentrations, greater than 3μM and 50-500μM, respectively (Jackson et al., 1982; Rüsch et al., 2004). When used in concentrations greater than 1mM, PB will block the channel (Muroi et al., 2009).

GABAR currents can also be blocked by compounds like picrotoxin (PTX). PTX is a non-competitive antagonist which blocks the effects of GABA without binding to the orthosteric site. This compound is derived from plants in the moonseed family and can inhibit GABA-mediated signaling (Olsen, 2006). Recent cryoEM of the picrotoxin-bound GABAR suggest that PTX binds in the channel pore between M2 2' and 9' rings and stabilizes a closed channel (Masiulis et al., 2019).

GABAR Structure

In an effort to visualize GABARs and other pLGICs and to examine how structure is linked to function, scientists have purified these proteins in both unliganded and liganded states, including in the presence of different allosteric modulators, and used x-ray crystallography and cryoEM to evaluate their structure. While x-ray crystallography can yield high-resolution structures, the sample needs to form a crystal which can be challenging for membrane-bound proteins like pLGICs. CryoEM structures do not require crystallization, but they tend to be slightly lower resolution. In addition, each image from a cryoEM experiment must be correctly oriented in order to assign subunit position in the final structure. Because these samples do not

need to be crystallized, it is easier to study the protein in a native lipid environment. Many pLGIC structures have been resolved including prokaryotic channels GLIC and ELIC (Bertozzi et al., 2016; Gonzalez-Gutierrez et al., 2013; Kumar et al., 2020), $5HT_3R$ (Basak et al., 2018a), GluCl (Althoff et al., 2014), nAChR (Morales-Perez et al., 2016), and GlyR (Huang et al., 2017a; Huang et al., 2017b). β3-homopentameric GABARs have also been crystalized in a desensitized, GABA-bound state (Miller and Aricescu, 2014). Recent cryoEM studies of hetero-oligomeric GABARs have shed additional light on the structure, stoichiometry, and pharmacology of these receptors (Laverty et al., 2019; Masiulis et al., 2019; Phulera et al., 2018; Zhu et al., 2018).

While the Hibbs, Gouaux, and Aricescu groups used GABARs comprised of different subunits – $\alpha_1\beta_2\gamma_{2L}$, $\alpha_1\beta_1\gamma_{2S,}$ and $\alpha_1\beta_3\gamma_{2L,}$ respectively, each of the structures was expressed in a lipid environment, and shared a common stoichiometry of 2 alpha, 2 beta and 1 gamma subunit arranged in a clockwise α-β-α-β-γ pattern. The receptors form a cylinder that is approximately 110 Å high and 80 Å wide, and confirm previously established principles of GABAR structure: the ECD is composed of beta sheets, ECD subunit interfaces make up the agonist binding sites, and the TMD is composed of four alpha helices where the second M2 helix from each subunit lines the ion-conducting pore (Scott and Aricescu, 2019). Each structure also revealed N-linked glycosylation of residues in the alpha subunits in the ECD vestibule, which may play a steric role in determining the stoichiometry of the receptors by blocking the incorporation of more than two alpha subunits in a single pentamer. The Hibbs structure includes a gamma subunit which has collapsed into the transmembrane pore. This likely represents a non-physiologically relevant conformation and makes the TMD region of this structure less interpretable (Zhu et al., 2018).

The Hibbs sample was prepared in the presence of GABA and flumazenil (Zhu et al., 2018), the Gouaux in the presence of GABA (Phulera et al., 2018), and the Aricescu samples were prepared in the presence of a PAM megabody, as well as multiple drug combinations: PTX, PTX and GABA, bicuculline, alprazolam and GABA, and diazepam and GABA (Laverty et

al., 2019; Masiulis et al., 2019). These ligand-bound structures confirm the orthosteric and BZD binding sites and suggest ways that drug binding may alter receptor structure (Figure 1.7). Based on comparing structures in the presence of different ligands, gating motions have been postulated. GABA-bound structures have a more closed loop C region, which is hypothesized to cause a rotation of the five ECDs. When the ECDs rotate, the TMD helices move to open the channel gate. BZD binding also stabilizes a closed loop c at the α/γ interface, which helps to facilitate the lock and pull motion and suggests that the binding of a PAM at this site may stabilize a pre-open conformation.

GABAR Kinetics

In an effort to understand mechanisms underlying GABAR activity, scientists examine the kinetics of ligand binding and channel gating. When GABA binds the receptor, it increases the probability that the channel will open and current will flow. The initial current rise is called the activation phase. In the continuous presence of GABA, current decays and some of the receptors will transition into a desensitized state where they are still bound to GABA but the channel does not conduct chloride. As GABA is washed off or removed from the synapse, the current decays faster as GABA unbinds and the GABAR returns to an unbound, resting closed channel state (Figure 1.8). Kinetic models describing this behavior have grown more complicated as they seek to account for allosteric drug modulation and current desensitization.

One of the earliest models was the Monod, Wyman and Changeux (MWC) model, which was an initial attempt to model transitions in multi-oligomeric proteins (Monod et al., 1965) (Figure 1.8B). The MWC shows how a protein with multiple ligand-binding sites can move from a resting to active state based on the higher affinity of the open state versus lower affinity of the resting state for the ligand, unliganded gating, and the number of binding sites.

However, earlier MWC models did not account for desensitization. Jones and Westbrook proposed a linear kinetic model that includes desensitized states in addition to multiple open states, and microscopic rate constants to govern agonist binding and unbinding, channel

opening and closing, and desensitization and recovery from desensitization (Jones and Westbrook, 1995) (Figure 1.8C).

Recently, the Akk group has expanded the MWC model to include the role of desensitization in steady-state kinetics (Akk et al., 2020; Germann et al., 2019). They call their three-state model the resting-active-desensitized (RAD) model, which incorporates a GABA high affinity, non-conducting, desensitized receptor state (Figure 1.8D). They suggest that PAMs and NAMs can increase GABA binding by binding to and stabilizing a high- or low-affinity state of the receptor for GABA (Akk et al., 2020).

While key GABAR residues for BZD binding have been identified (Morlock and Czajkowski, 2011; Olsen, 2018), exactly how BZDs affect GABA binding and channel gating is still under study. Perrais and Ropert used outside-out patch clamp electrophysiology to evaluate the effect of the PAM zolpidem on miniature IPSCs and concluded that the modulator effects are not due to increased channel conductance or increasing the channel's maximal open probability, but instead are due to increasing the receptor's affinity for GABA (Perrais and Ropert, 1999). However, Li et al. later used single-channel patch clamp to demonstrate that the application of PAM diazepam increases channel open-time, and decreases the rate of channel closing, suggesting that BZD modulation is mediated by increased gating activity (Li et al., 2013).

In an alternate model, Goldschen-Ohm et al. used patch-clamp electrophysiology and kinetic modeling to suggest that BZD binding modulates an intermediate element between ligand binding and channel gating (Goldschen-Ohm et al., 2014). The binding of this intermediate element stabilizes the receptor's transition from agonist binding to opening the main channel gate (Figure 1.8E). The Smart group also offers an model of BZD effects where BZD binding stabilizes an intermediate preactivated receptor state which enhances the transition between agonist binding and channel gating (Gielen et al., 2012).

Diazepam Binding Inhibitor

Discovery

Scientists have long theorized that the brain may modulate GABARs with its own endogenous BZD, or “endozepine”. Much of the evidence for the endozepine comes from the use of flumazenil (FLZ, Ro15-1788), a BZD binding site antagonist. Studies in the hippocampus (King et al., 1985), dentate gyrus (Leroy et al., 2004), neocortical pyramidal neurons (Ali and Thomson, 2008) and the thalamic reticular nucleus (Christian et al., 2013) all showed a reduction in amplitude or duration of GABA-evoked IPSCs in the presence of FLZ, a zero-modulator. This raises the possibility that there is an endogenous chemical in the brain that is a positive modulator of the GABAR which is blocked by binding of the BZD-site antagonist, FLZ. However, it is not known whether in some brain regions of the brain FLZ may act as a negative modulator due, for example, to the presence of various GABAR accessory subunits.

In 1983, a candidate polypeptide that displaced [^{3}H]diazepam (a classic BZD ligand) in a radioligand binding assay was initially isolated from brain homogenates, and called the ‘diazepam binding inhibitor’ (DBI, Figure 1.9) (Guidotti et al., 1983). This 87 aa, 10kD peptide is considerable larger than the BZDs that competitively bind the same site.

DBI Transcription, Expression and Structure

The single human DBI gene encodes eleven mRNA transcription variants, which are translated into seven protein isoforms (Figure 1.10). Isoform 3 is the 87aa protein sequence most scientists refer to as DBI, while the other isoforms are not well characterized. Nitz et al. used real-time qPCR and 5’-RACE and showed that DBI transcript variants can be synthesized through the use of alternate promoters (Nitz et al., 2011). The variants are completely homologous on the 3’ end but have different 5’ UTRs and alternate starts to their protein-coding regions. The other ten variants have also been detected in human tissue, though at significantly lower levels (Nitz et al., 2005; Nitz et al., 2011).

DBI is expressed across many tissue types, with high expression in liver, breast, blood, and the brain (Thul et al., 2017; Uhlén et al., 2015). mRNA expression patterns for DBI obtained

from the Protein Atlas are shown in Figure 1.11. In the brain, some of the highest levels of mRNA expression are found in the hypothalamus, hippocampus, and striatum (Tonon et al., 2020). Additionally, DBI-like immunoreactivity using antibodies for human DBI is detected in the cerebellum, brain stem, amygdala, and sacral spinal cord (Ball et al., 1989; Ferrarese et al., 1989), and is generally highest in glial cells (Alho et al., 1990).

DBI has a number of biologically active cleavage products including octadecaneuropeptide (ODN), octapeptide (OP), and triakontetraneuropeptide (TTN). Taskinen *et al.* solved high-resolution crystal structures of unliganded human DBI (PDB 2FJ9) (Taskinen et al., 2007). DBI is comprised of four alpha helices connected by short loops. Figure 1.12 shows the complete structure of the most abundant human DBI isoform, with common cleavage products highlighted. DBI and ODN (residues 33-50) both displaced radiolabeled BZD or beta-carboline binding from brain membrane homogenates (Ferrarese et al., 1987; Ferrero et al., 1984; Ferrero et al., 1986; Guidotti et al., 1983), while DBI and TTN (residues 17-50) bind the mitochondrial translocator protein (TSPO) and contribute to neurosteroidogenesis by increasing cholesterol transport through the TSPO. The physiological effects of the third known cleavage product, OP (residues 43-50) (Farzampour et al., 2015), have not been well-documented.

Evidence for DBI's role in GABAR signaling in the brain

Using DBI RNAi knock-down experiments in the subventricular zone of the lateral ventricles, it was demonstrated that DBI and one of its peptide fragments, ODN, inhibit GABA-induced currents and promote neurogenesis (Alfonso et al., 2012), indicating that DBI and ODN work as NAMs of GABARs *in vivo*. Further experiments in hippocampal stem cells provide additional evidence for DBI's role in neurogenesis as a NAM of GABA-mediated activity. In addition to detecting DBI in the neural stem cells of all postnatal neurogenic niches, they found that knocking-out DBI in the hippocampal subgranular zone reduced the number of stem cells and favored a neuronal fate, whereas DBI overexpression increases the progenitor pool (Dumitru et al., 2017). These effects may be mediated via GABAR signaling given GABA is a

well-known regulator of adult neurogenesis (Aimone et al., 2014). Patch clamp recordings from stem cells in the subgranular zone of hippocampal slices showed that exogenously applied ODN acted as a NAM for GABAergic currents, while puffs of GABA in slices from mice with a BZD-insensitive mutation (F77I in the γ subunit) were significantly less affected by ODN (Figure2.13A) (Dumitru et al., 2017). Similarly, DBI overexpression had significantly less effect on proliferation in F77I mice (Dumitru et al., 2017). Both papers studying the effects of DBI on neurogenesis indicate that DBI is a NAM of GABA-induced currents in these neurogenic niches.

However, in the thalamic reticular nucleus (nRT), knock-down and over-expression studies provide evidence that DBI may work *in vivo* as a PAM where it suppresses epileptic activity (Christian et al., 2013). When the Huguenard group compared spontaneous IPSCs (sIPSCs) from the thalamic reticular nuclei of wild-type and BZD-insensitive mice (using an H126R mutation in the α3 subunit), they found the BZD-insensitive mice had a shorter IPSC duration. They also found that the zero-modulator FLZ reduced duration of sIPSCs for wildtype but not α3-H126R mice. They saw this same reduction in sIPSC duration when they compared wild-type mice to those with a chromosomal deletion of DBI and several proximal genes (Figure 1.13B). Taken together, their results indicate that wild-type mice have an endogenous positive modulator of the GABAR and that its effect is blocked by rendering the BZD site insensitive to modulation, blocking the BZD site with a zero-modulator, or removing the DBI gene (Christian et al., 2013). This group also went on to show that DBI is expressed in both neurons and astrocytes in the nRT, and that use of the gliotoxin fluorocitrate (FC) also shortens sIPSC duration. No effect of FC is observed in either α3-H126R mice or those lacking the DBI gene, suggesting that astrocytic function is necessary for the PAM effects of DBI (Christian and Huguenard, 2013).

Experiments from the Christian lab used a DBI knockout mouse to study the effects of DBI on hippocampal learning and memory, and found that DBI knockout mice showed a disruption in spatial learning and memory (Ujjainwala et al., 2019) and social behavior

(Ujjainwala et al., 2018). The GABAR plays a large role in these hippocampal-dependent forms of learning and memory, usually mediated via α5-containing receptors (Collinson et al., 2006; Crestani et al., 2002; Joksimović et al., 2013; Timić et al., 2013). The disruption in these GABAR-dependent forms of learning and memory by the loss of DBI provides additional indirect evidence that DBI may alter GABA-mediated signaling. The Christian lab also recorded somatic IPSCs from the hippocampal CA1 and dentate gyrus regions. They found that a loss of DBI altered miniature IPSCs (mIPSCs) in both regions – CA1 knockout mIPSCs were more frequent with larger amplitudes, while in the dentate gyrus the mIPSCs had smaller amplitudes but longer decay times (Courtney and Christian, 2018). However, these fast IPSCs recorded from the soma of pyramidal neurons are unlikely to capture the effects of DBI on α5-containing receptors which are expressed primarily in the distal dendritic regions and responsible for much of hippocampal learning and memory (Groen et al., 2014; Rodgers et al., 2015).

Taken together, these results provide strong evidence that DBI has a functional effect *in vivo* and may work as an endogenous modulator of GABARs. However, they raise the question of how a single peptide can generate contrasting effects. **The underlying hypothesis of my thesis is that the effects of DBI are GABAR subunit dependent.** GABAR subunit composition varies between regions of the brain and the effects of some BZDs such as Ro15-4513 differ depending on GABAR subunit expression. I hypothesize that the role of DBI as a PAM or NAM is dependent on regional variation of GABAR subunits in the brain.

Intracellular actions of DBI

Our understanding of DBI's role in regulating GABAR-mediated inhibition is complicated by the fact that sequencing the human genome revealed that DBI is also acyl-CoA binding protein (ACBP) (Knudsen, 1991). ACBP is expressed in many tissues, most abundantly in the liver and adipose tissue and plays a role in lipid metabolism (Færgeman et al., 2007). Recombinant, purified human DBI/ACBP binds the long-chain fatty acid palmitoyl-CoA which promotes DBI to form a dimer around the ligand (Augoff et al., 2010). In astrocytes, DBI/ACBP

regulates long-chain fatty acid metabolism by binding long-chain acyl-CoA esters (Bouyakdan et al., 2015) and delivering them to the TSPO.

The TSPO protein has important intracellular roles and binds some ligands that also interact with the GABAR. This protein is primarily located in mitochondria, where it is part of a complex for importing cholesterol. Cholesterol is a key metabolite in neurosteroidogenesis (Slobodyansky et al., 1989). As described above, neurosteroids can modulate GABARs, suggesting an alternate, indirect pathway through which DBI may be able to alter GABA-mediated signaling. BZDs like diazepam and Ro5-4864 have been shown to bind the TSPO. Radiolabeled diazepam has been shown to bind TSPO and even led to its original name, the peripheral benzodiazepine receptor (Squires and Braestrup, 1977). The TSPO binding site for radiolabeled Ro5-4864 has been identified via site-directed mutagenesis (Farges et al., 1994). DBI has also been shown to interact with the TSPO in experiments where purified DBI and its proteolytic peptides were added to multiple cell-lines and increased neurosteroid production in a dose-dependent manner. This increase was blocked by the use of flunitrazepam, a BZD which has been shown to bind the TSPO (Papadopoulos et al., 1991; Regan et al., 1981; Rupprecht et al., 2010). Additionally, the DBI cleavage product TTN displaces radiolabeled Ro 5-4864, a BZD-derived compound which selectively binds the TSPO rather than GABARs (Slobodyansky et al., 1989).

In addition to their interactions with TSPO, DBI and its proteolytic peptides have been suggested to interact with other important cellular components. DBI, ODN and TTN have been suggested to interact with GPCRs and initiate signaling cascades. Experiments using cultured rat astrocytes demonstrated that ODN increases inositol triphosphate and decreases phosphatidylinositol diphosphate. These effects are blocked by pertussis toxin and unaffected by the use of FLZ or PK 11195, a TSPO ligand (Patte et al., 1995), suggesting that ODN interacts with a pertussis toxin-sensitive GPCR. Experiments using human polymorphonuclear leukocytes showed that TTN increased intracellular calcium via a protein kinase C (PKC)-

dependent pathway (Marino et al., 2004). TTN also increased intracellular calcium via a PKC-dependent pathway in cultured rat astrocytes (Gandolfo et al., 1997) and cerebellar granule neurons (Kaddour et al., 2013). A putative GPCR-mediated DBI/TTN signaling pathway is shown in Figure 1.14, though scientists have not identified a specific GPCR which binds DBI or TTN (Tonon et al., 2020).

Disease phenotypes

DBI knockout mice have greasy fur, orangey skin (Neess et al., 2011), disrupted social behavior (Ujjainwala et al., 2018), and reductions in hippocampal-dependent learning and memory (Ujjainwala et al., 2019). No mutations in the *DBI* gene have been directly associated with human pathology. However, changes in DBI expression and activity have been implicated in multiple diseases.

Beta-amyloid protein, which forms plaques in the brains of Alzheimer's patients, increases the expression and secretion of ODN from astrocytes as measured using antibodies for ODN intracellularly and in cell serum (Tokay et al., 2008). Additionally, an RNA-Seq experiment performed by Mills et al. comparing healthy parietal zones to those of Alzheimer's patients showed altered transcript variant expression patterns for DBI mRNA in Alzheimer's brains (Mills et al., 2013). Moreover, DBI/ODN is elevated in the cerebral spinal fluid of patients with Alzheimer's and Parkinson's disease (Barbaccia et al., 1986; Ferrarese et al., 1990).

DBI and its cleavage products are also highly expressed in brain tumors, including medulloblastomas, glioblastomas, and astrocytomas (Alho et al., 1995; Miettinen et al., 1995), perhaps due to their effects on cell proliferation. Additionally, a multi-omic study from Pichitpunpong et al. found DBI protein expression in patient-derived lymphoblastoid cell lines to be significantly reduced in autism spectrum disorder (Pichitpunpong et al., 2019). Changes in DBI protein expression has also been associated with both obesity (Siejka et al., 2015) and anorexia (Conti et al., 2013).

Release of DBI

In the brain, DBI is generally thought to be released from astrocytes, and this release is regulated by extracellular factors (Farzampour et al., 2015). GABA and somatostatin, a peptide hormone secreted by neuroendocrine neurons in the hypothalamus, both reduce the amount of DBI secreted by cultured astrocytes (Masmoudi et al., 2005; Patte et al., 1999), while beta-amyloid protein increases DBI secretion from cultured astrocytes (Tokay et al., 2008).

The mechanisms underlying the release of DBI are currently unknown. Experiments in yeast, social amoeba, and astrocytes found that disrupting Golgi-mediated protein release prevents the release of DBI, suggesting that the protein is released via an autophagic process (Duran et al., 2010; Loomis et al., 2010). However, experiments in cultured rat astrocytes suggest an ATP binding cassette (ABC) transporter mediates the process. Astrocytic DBI release was blocked by somatostatin, a PKA inhibitor, a phospholipase C inhibitor, a PKC inhibitor, and an ABC transport blocker, all of which are associated with release from an ABC transporter (Tokay et al., 2008). This potential DBI release pathway is depicted by cartoon in Figure 1.15.

Overview and Significance of this Dissertation

The goal of my thesis work is to understand the role that DBI plays in modulating inhibition in the brain. I sought to understand how DBI's modulatory effects vary based on alternate GABAR subunit composition, and to explore the mechanism via which DBI exerts its positive or negative effects.

In Chapter II, I describe the process for purifying the DBI protein, which was required for the experiments performed in this thesis. I also describe the steps I took to ensure the protein was pure and folded correctly. Because this purified DBI was needed for all of my experiments, purification of sufficient quantities and the quality of the purification were essential.

In Chapter III, I discuss the experiments I performed using two-electrode voltage clamping of GABARs heterologously expressed in *Xenopus laevis* oocytes. I hypothesized that the effects of DBI on GABA-elicited currents would vary based on the subunit composition of the

receptor. To test this theory, I compared the effects of a known PAM and NAM (FZM and DMCM, respectively), as well as DBI on GABA-elicited currents of $\alpha_3\beta_3\gamma_{2L}$ and $\alpha_5\beta_3\gamma_{2L}$ receptors. I also used *in silico* protein-protein docking to suggest ways that DBI may positively modulate one receptor combination, but negatively modulate another.

In Chapter IV, I used outside-out patch-clamp electrophysiology to study the effects of DBI on the macroscopic currents of $\alpha_5\beta_3\gamma_{2L}$ receptors. I theorized that if DBI is an endogenous benzodiazepine, it would affect GABAR macroscopic kinetics similarly to a BZD. To test this hypothesis, I compare the effects of DBI and FZM on the amplitude, activation rate, and deactivation phases of GABA-elicited currents to determine whether these drugs modulate the receptor using similar kinetic mechanisms.

In Chapter V, I use outside-out patch-clamp electrophysiology to compare the effects of DBI on $\alpha_5\beta_3\gamma_{2L}$ and $\alpha_5\beta_3$ receptors. I hypothesized that if DBI mediates its effects by binding to the BZD site on GABARs, only $\alpha_5\beta_3\gamma_{2L}$ receptors should be modulated by this peptide. I compare the effects of DBI on amplitude, activation, and deactivation on GABARs with and without the γ subunit to evaluate the importance of the BZD site in mediating the effects of DBI.

In Chapter VI, I describe experiments to evaluate the release of DBI from neurons and astrocytes. I used neurons derived from induced pluripotent stem cells (iPSCs) to evaluate how an endogenous, BZD-site modulator may alter electrical communication between neurons. I used a variety of mass spectrometry techniques to evaluate whether ODN was being released by iPSC-derived neurons and astrocytes.

In the first appendix to this thesis, I discuss experiments I performed to study the macroscopic effects of the BZD negative modulator DMCM, and used the elements kinetic model (Goldschen-Ohm et al., 2014) to determine effects of DMCM on GABA binding rates. In the second appendix, I describe experiments I performed to test the function of mutant GLIC protein reconstituted in liposomes and injected into *Xenopus* oocytes. These mutations were

designed and used by Dr. Varun Tiwari to monitor extracellular motions of GLIC in response to agonist binding.

Chapter VII summarizes and discusses the overall findings of my thesis and their impact. I discuss the results of my experiments and their implications for DBI's role in regulating neuronal inhibition. My experiments represent some of the first approaches to understanding how purified DBI interacts with specific populations of GABARs. My data and findings advance our understanding of the role that DBI plays in regulating GABA-mediated inhibition in the brain.

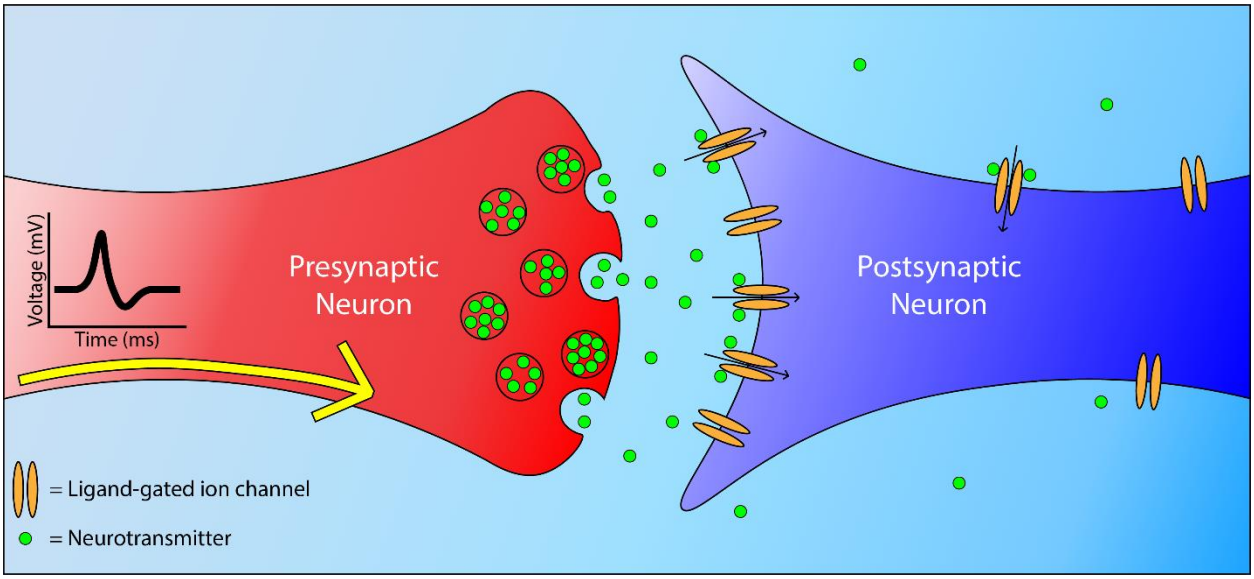

Figure 1.1 – Synaptic cartoon. Cartoon depicting a synapse between a presynaptic and postsynaptic neuron. Vesicles in the presynaptic neuron (shown in red) contain neurotransmitters (green circles). These neurotransmitters are released into the synapse when the vesicles fuse with the neuronal membrane in response to an action potential. Neurotransmitters diffuse across the cleft and bind to ligand-gated ion channels (orange ovals) on the postsynaptic neuron (shown in blue). These ligand-gated ion channels open after neurotransmitter binding and conduct ions in and out of the neuron.

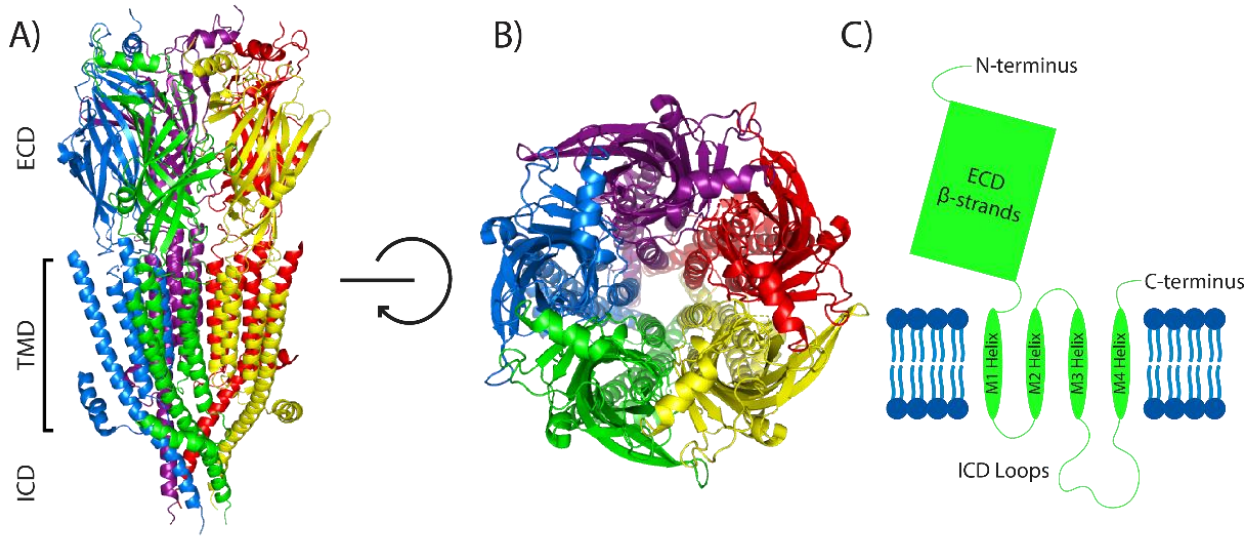

Figure 1.2 – Structure of pLGICs. A) Crystal structure of the pLGIC 5-HT_{3A}R (PDB 4PIR) in side-view with the extracellular domain (ECD), transmembrane domain (TMD), and intracellular domain (ICD) labelled. The ECD of each subunit is comprised mainly of beta sheets and TMD is made up of four alpha helices. Colors pertain to individual subunits B) Top-down view of pLGIC showing arrangement of subunits around a central pore. C) Cartoon showing structure of a single pLGIC subunit. The N-terminus is in the ECD which is comprised primarily of beta-strands. This region connects to four transmembrane alpha-helices (M1-M4). The ICD is made up of loops between these helices.

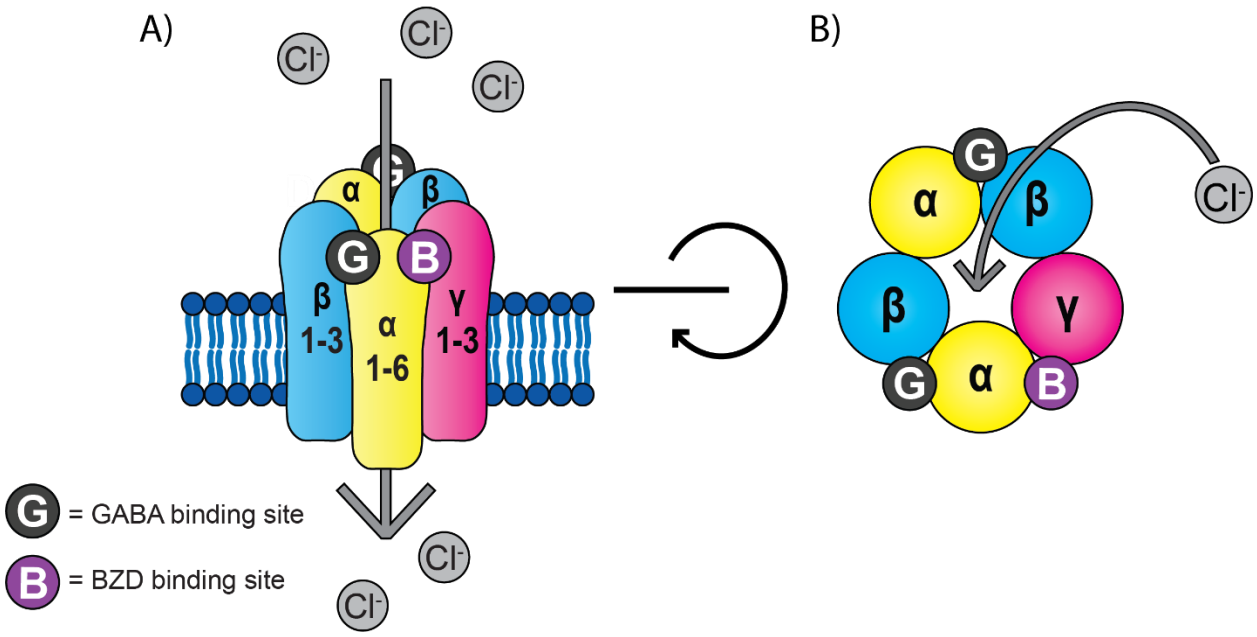

Figure 1.3 – Cartoon showing GABAR subunit stoichiometry and arrangement. A) Side view of a GABA containing five subunits (2α in yellow, 2β in blue, 1γ in pink) surrounding a channel with a central, chloride-conducting pore in a lipid membrane, shown in dark blue. GABAR contains two neurotransmitter ligand binding sites (G) in the extracellular domain (ECD) and one BZD binding site (B). B) Top-down view of pLGIC cartoon showing arrangement of the five subunits.

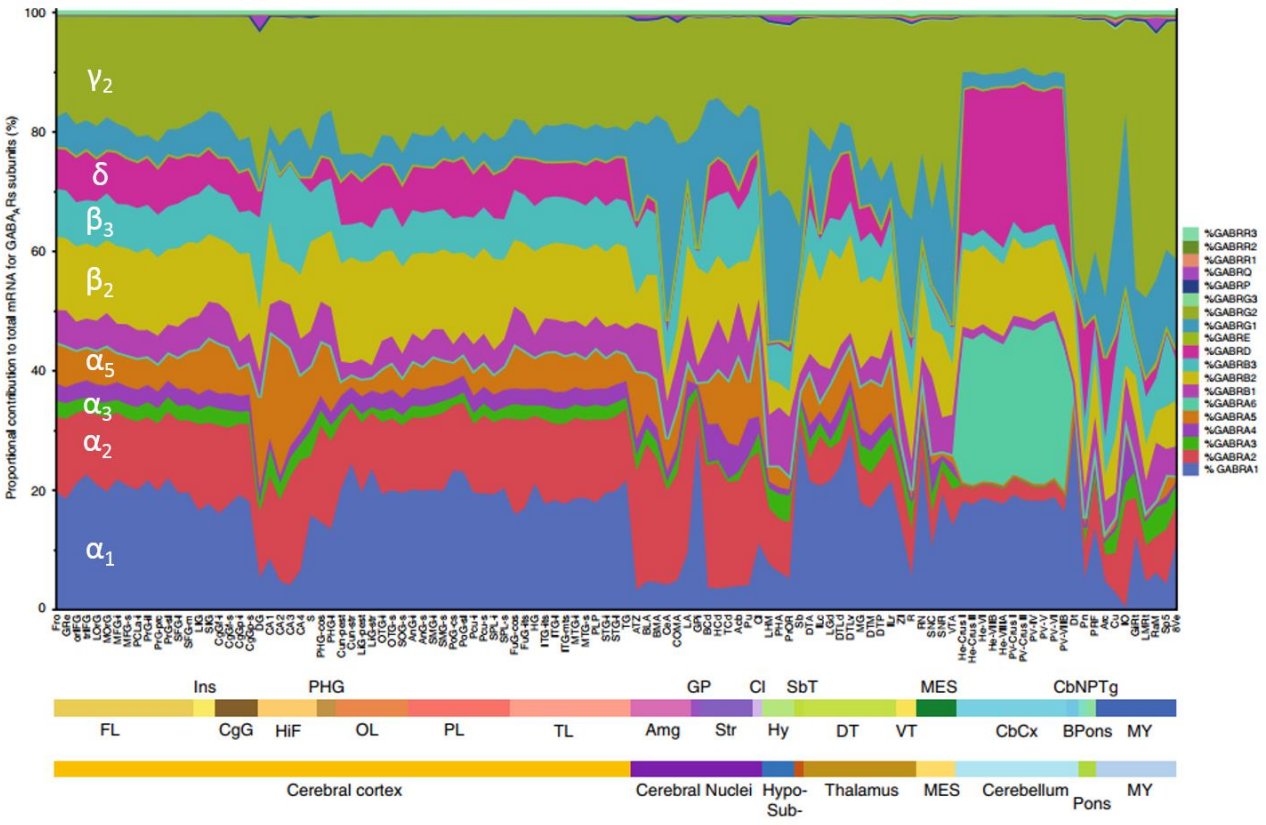

Figure 1.4 – Regional expression of GABAR subunit mRNA. Figure adapted from Sequeira *et al*. 2019. Subunit labels show the expression of each GABAR subunit using data from the Allen Brain Institute. Colored bands show the percentage of total GABAR expression for each region displayed along x-axis. The first bar below the graph indicates specific brain regions with second bar showing more general brain regions. Key GABAR genes are highlighted on graph for clarity. Abbrevations: “FL frontal lobe, Ins insula, CgG cingulate gyrus, HiF hippocampal formation, PHG parahippocampal gyrus, OL occipital lobe, PL parietal lobe, TL temporal lobe, Amg amygdala, GP globus pallidus, Str striatum, Cl claustrum, Hy hypothalamus, SbT subthalamus, DT dorsal thalamus, VT ventral thalamus, MES mesencephalon, CbCx cerebellar cortex, CbN cerebellar nuclei, Bpons basal part of the pons, PTg pontine tegmentum, MY myelencephalon” (Sequeira et al., 2019).

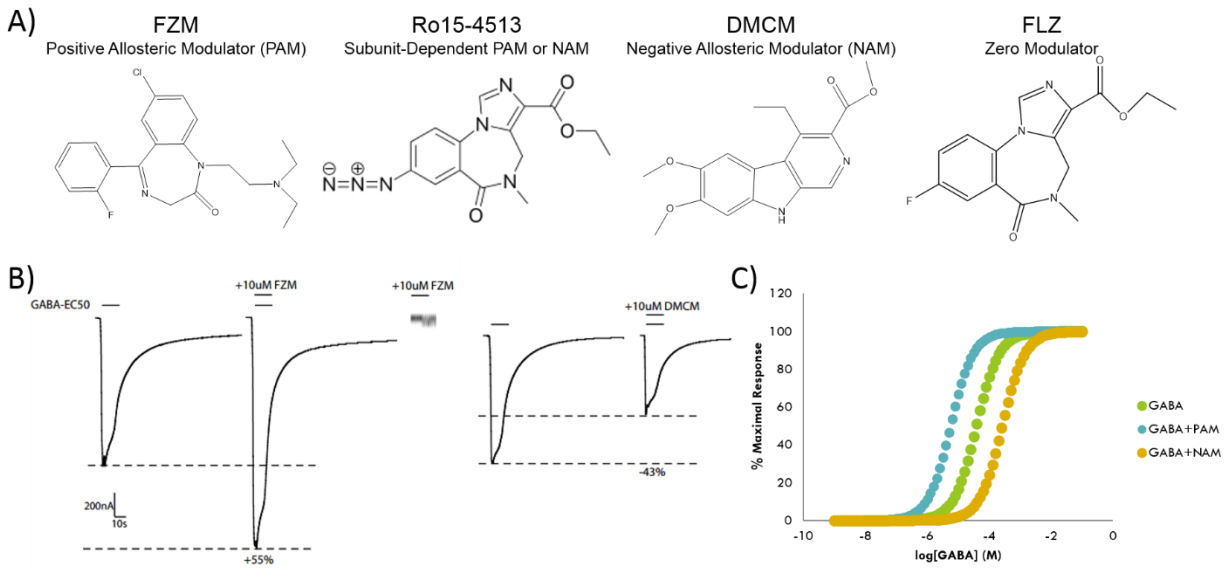

Figure 1.5 – Benzodiazepine structures and effects A) Examples of BZD chemical structures: flurazepam (FZM), a classical PAM; Ro15-4513, a non-classical, subunit-dependent PAM or NAM; methyl-6,7-dimethoxyl-4-ethyl- β-carboline-3-carboxylate (DMCM), a beta carboline NAM; and flumazenil (FLZ, Ro15-1788), a zero-modulator. B) Sample GABA-mediated current traces from oocytes expressing WT GABARs showing the effects of FZM and DMCM on GABA-elicited currents. C) Theoretical GABA dose-response curves showing EC50 shifts resulting from PAM (blue) or NAM (orange).

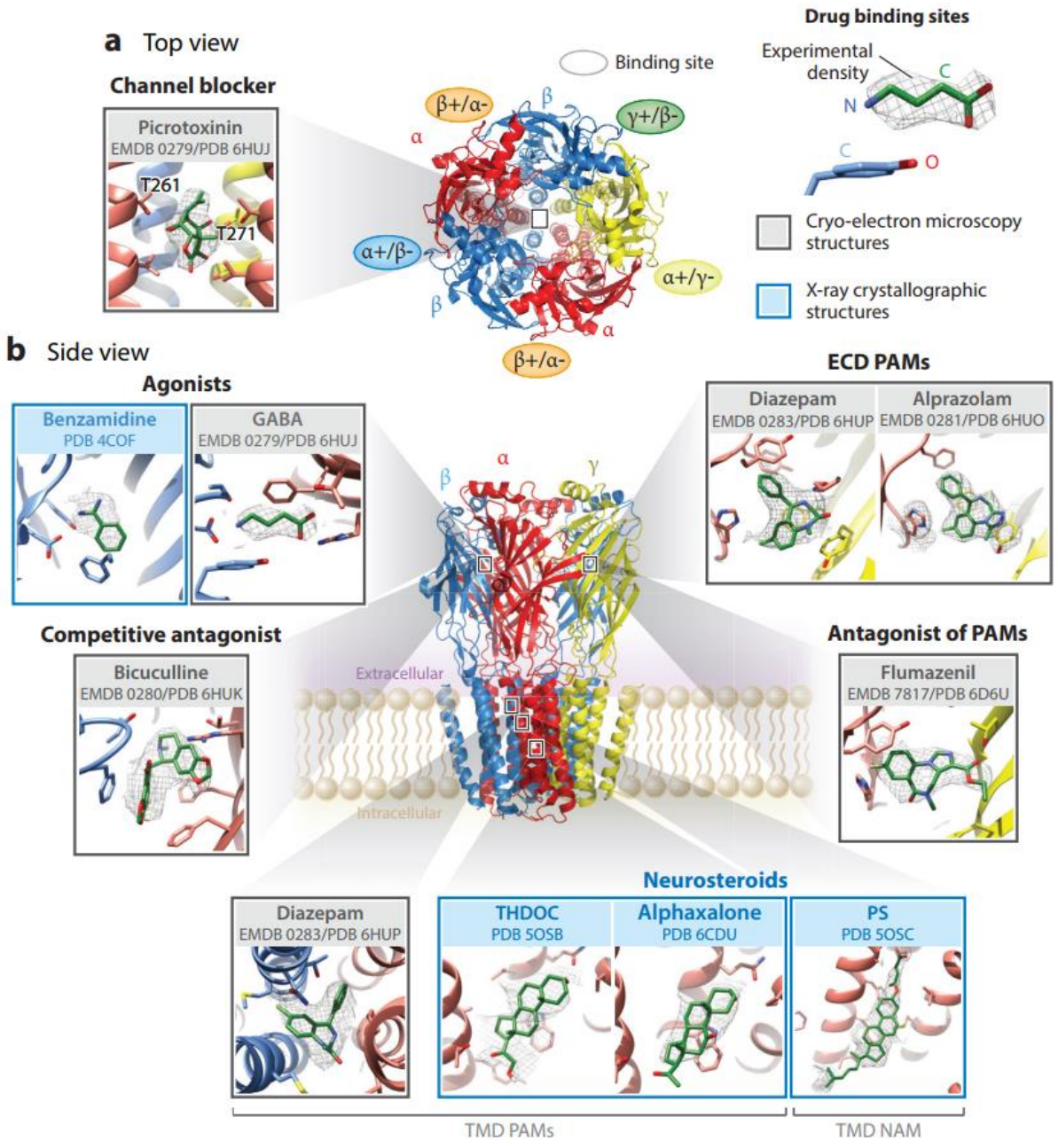

Figure 1.6 – Drug binding sites observed in GABAR structures. Figure from Garcia-Nafria and Tate showing GABAR structure from the top (A) and side views (B). Insets show binding sites for agonists, benzamidine and GABA; orthosteric antagonist, bicuculline; PAMs, diazepam and alprazolam; PAM antagonist, flumazenil; and neurosteroids, THDOC, alphaxalone and PS from various crystal and cryoEM structures. α subunits shown in red, β in blue, and γ in yellow (García-Nafría and Tate, 2020).

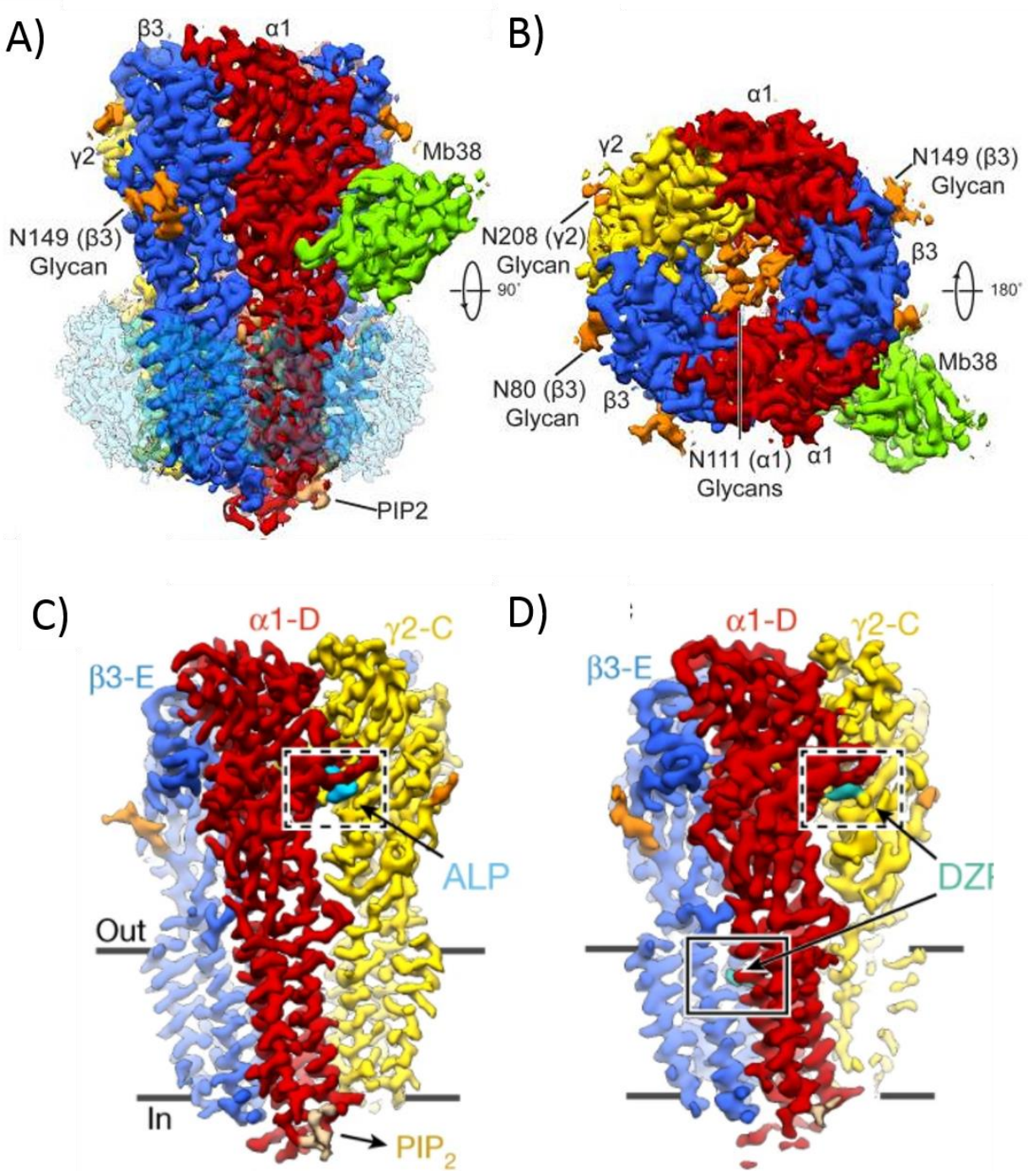

Figure 1.7 – CryoEM structures of GABAR. Figures adapted from Aricescu publications (Laverty et al., 2019; Masiulis et al., 2019). A) Side view of $\alpha_1\beta_3\gamma_{2L}$ GABAR in the presence of megabody expressed in lipid nanodiscs, Mb38, for cryoEM orientation. B) Top view of receptor showing N-linked glycans from alpha subunits in the central pore. C) and D) show cryoEM

structures of GABARs in the presence of alprazolam (ALP) and diazepam (DZP). ALP and DZP bind in ECD between alpha and gamma subunits (shown in red and yellow), and DZP also binds in the transmembrane domain. PDB 6I53, 6HUO, 6HUP

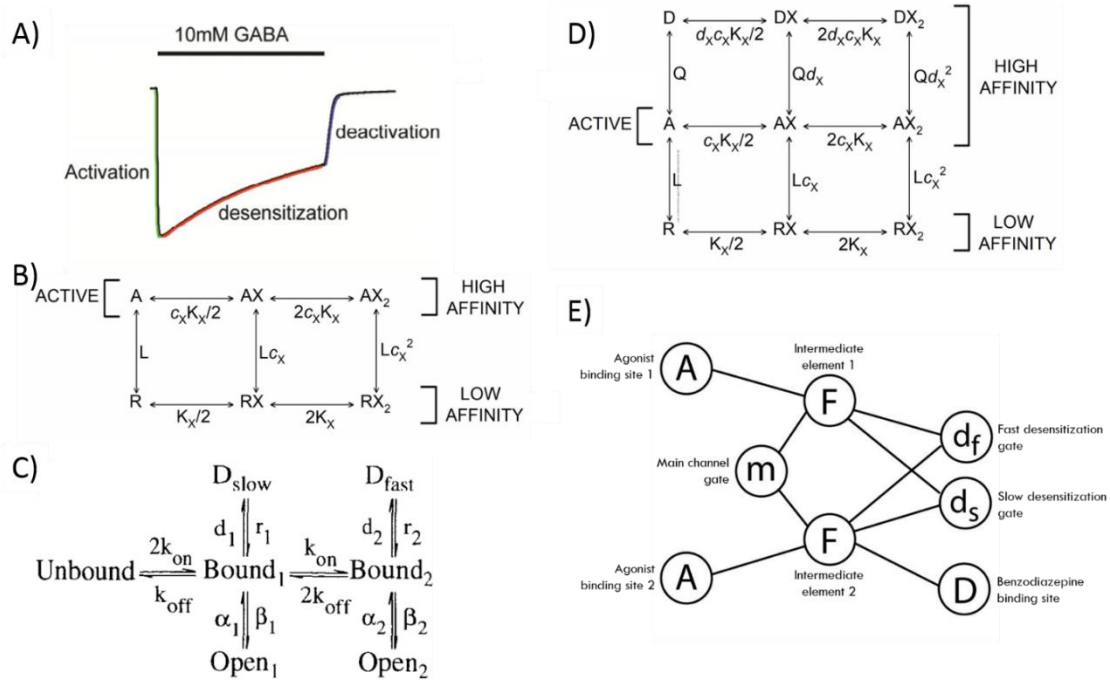

Figure 1.8 – GABAR Kinetic Models. Suggested models for receptor gating and ligand binding A) Sample GABA-elicited current trace showing rising current phase (activation), desensitization of channels in the presence of GABA, and deactivation as channels transition from desensitized to open to closed, unliganded states as GABA washes off. B) MWC model of GABAR function taken from Akk et al., 2020 showing the active, high affinity state A binding agonist X with two sites and resting, low affinity state R, with equilibrium rates L between A and R states and Kx as equilibrium dissociate constants for X binding. C) Jones-Westbrook model taken from Jones and Westbrook, 1995 showing binding of two agonists and transitions to open or desensitized states. Desensitized states represent fast (D_{fast}) and slow (D_{slow}) desensitization. Forward and reverse rate constants are indicated alongside each arrow. D) Updated three-state kinetic model taken from Akk et al., 2020 showing the addition of a desensitized state to the MWC model, with additional rate constants Q. E) Elements model taken from Goldshen-Ohm et al, 2014, with two agonist binding sites (A), a main channel gate (m), two intermediate elements (F), fast and slow desensitization gates (d_f and d_s), and a BZD-binding site (D).

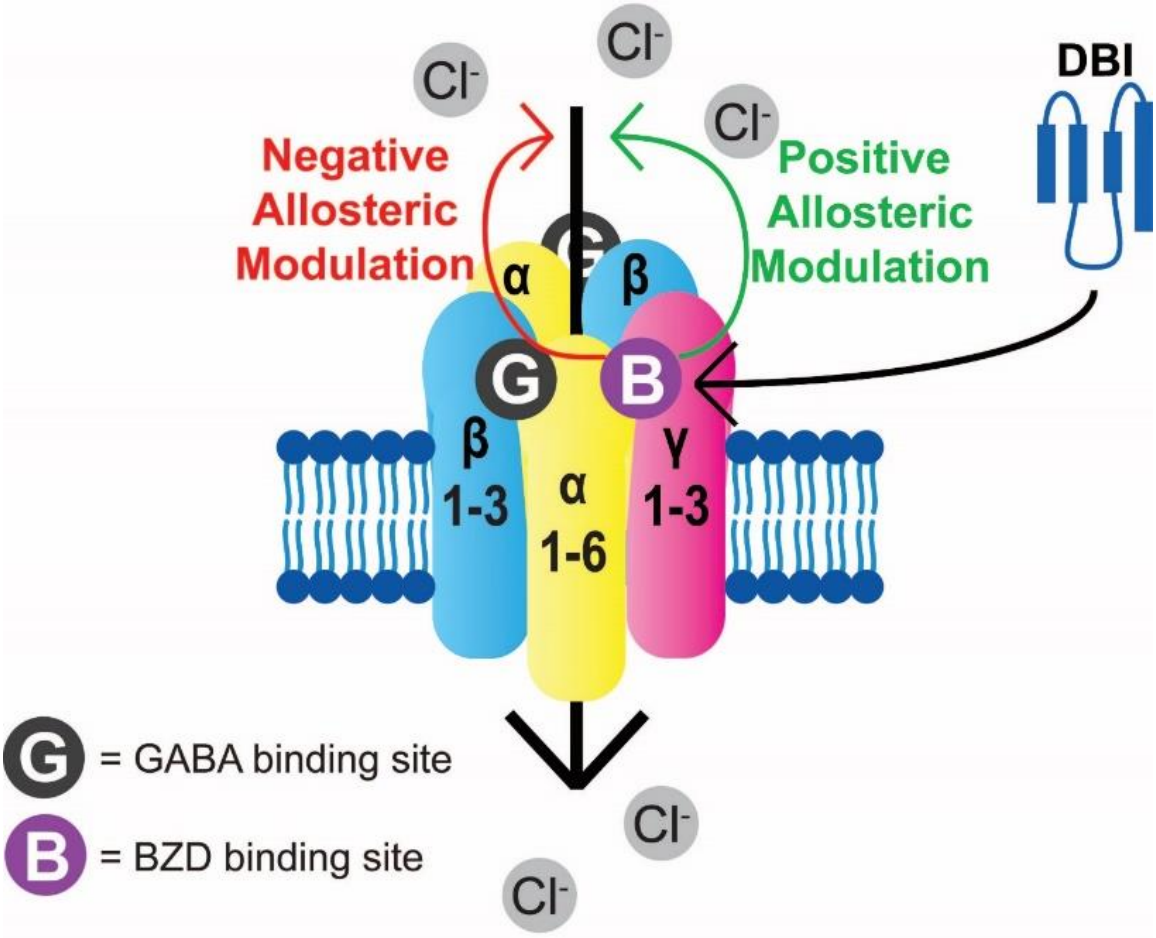

Figure 1.9 – Cartoon of DBI interacting with GABAR. GABAR cartoon with subunits in yellow (α), light blue (β), and pink (γ) shown in a transmembrane. GABA (G) and BZD (B) binding sites are shown in the extracellular domain. DBI binding at the BZD site causes either positive or negative modulation, which alters the amount of chloride ions that flow through the channel upon GABA binding.

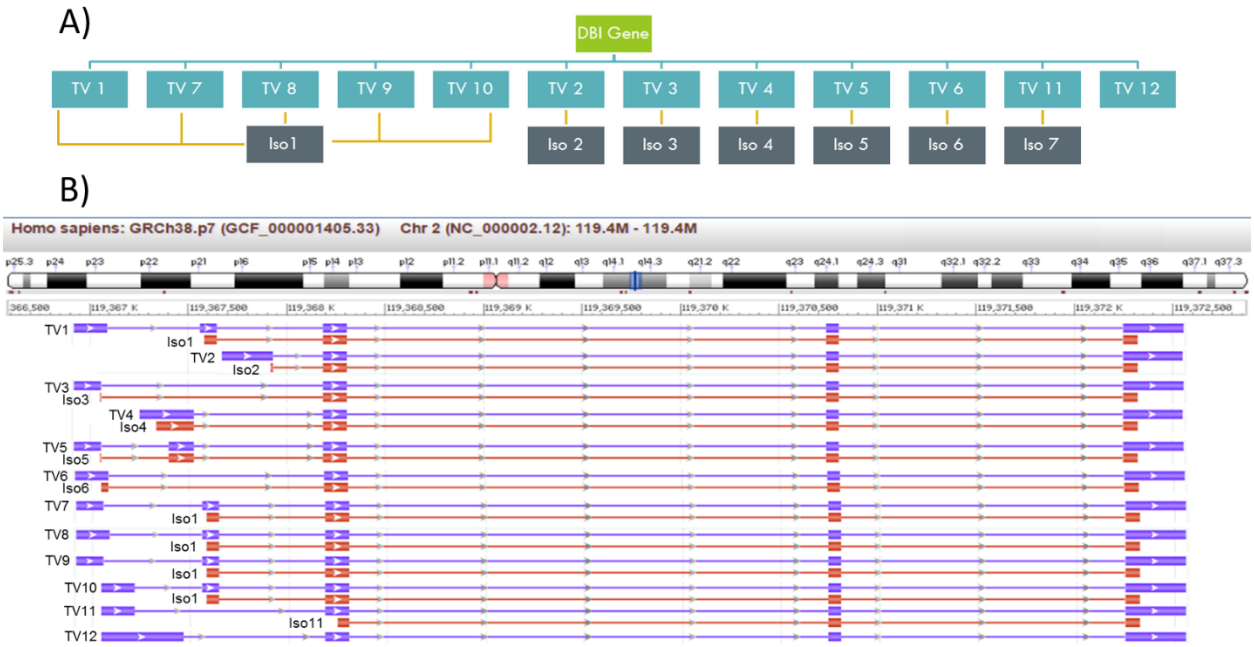

Figure 1.10 – DBI transcript variants and isoforms. A) The single human DBI gene shown in green encodes twelve different RNA transcript variants (TVs) shown in light blue. Those TVs can be translated in seven different protein isoforms, with TVs 1, 7, 8, 9 and 10 encoding the same isoform. TV12 is long noncoding RNA (lnRNA) and is thus untranslated, while TV3 is translated into the most abundant isoform, Iso3. B) Data is taken from the NCBI database and shows the region of human chromosome 2 which encode DBI. Purple boxes represent exons for each RNA TV and purple lines represent introns. Red boxes represent translated regions and red lines are untranslated regions of each isoform.

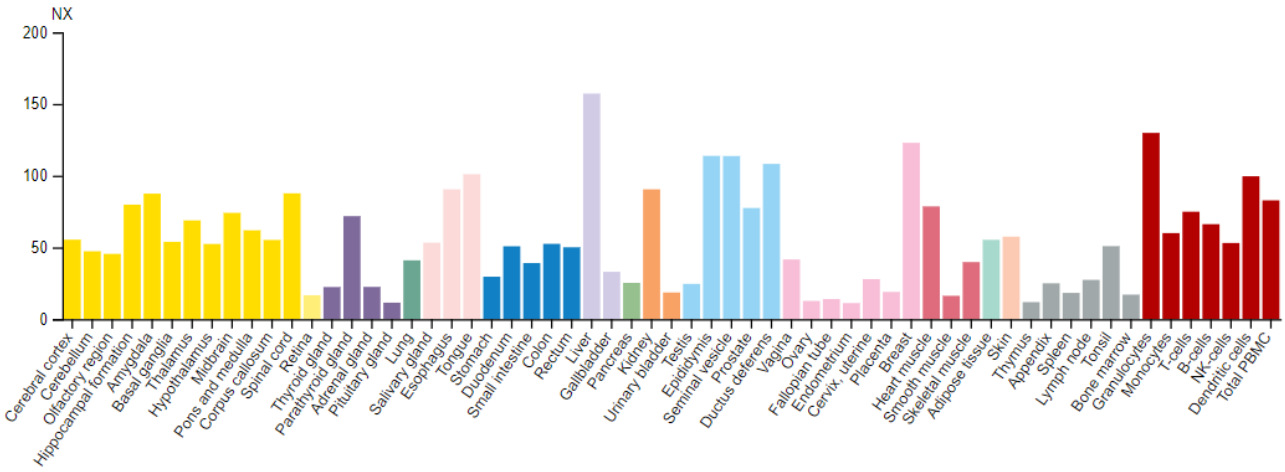

Figure 1.11 – DBI mRNA expression levels across human tissue. Figure taken from proteinatlas.org representing a consensus of mRNA expression in human tissue of DBI from the HPA, GTEx and FANTOM5 databases (Thul et al., 2017; Uhlén et al., 2015). Normalized expression (NX) is shown for 55 tissues and 6 blood cell types using the normalization pipeline from proteinatlas.org. Tissue groups are indicated by color with tissue types labelled below.

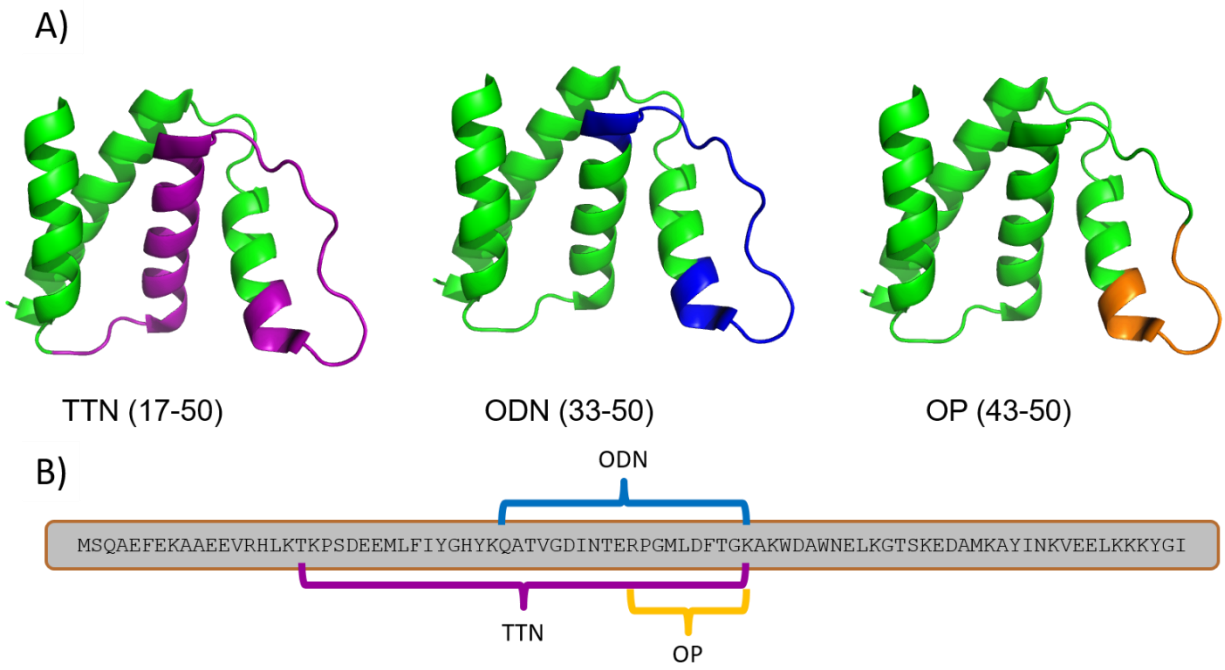

Figure 1.12 – Structure of DBI with cleavage products highlighted. DBI crystal structure (PDB 2FJ9) shown in green with biologically active cleavage products highlighted: triakontatetraneuropeptide (TTN, residues 17-50) in purple, octadecaneuropeptide (ODN, residues 33-50) in blue, and octapeptide (OP, residues 43-50) in orange. Full DBI amino acid sequence is shown below with cleavage product residues indicated via brackets.

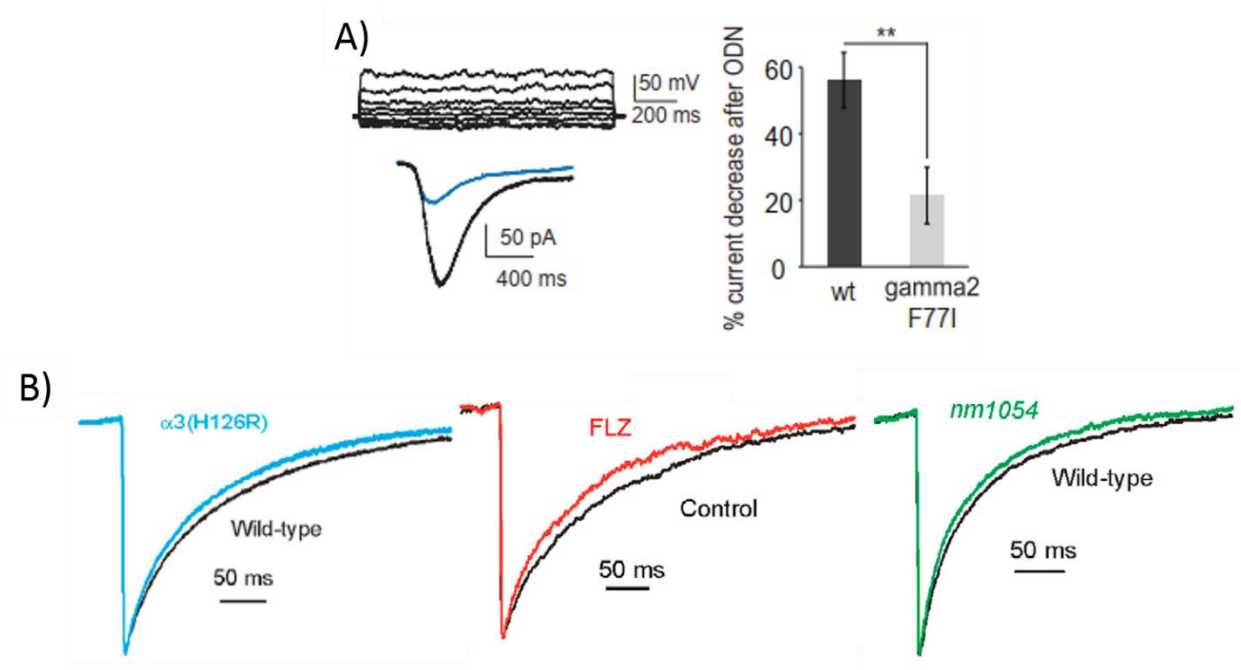

Figure 1.13 – Effects of DBI on inhibition in the brain. A) Adapted from Dumitru et al., 2017. Sample traces evoked by a puff of GABA onto patch pulled from a wild-type hippocampal subgranule zone stem cell in black with GABA+ODN overlayed in blue. Summary bar graph shown on right with the percent current decrease from ODN for wild-type and BZD-insensitive γ2-F77I mutant. Mutant mice are less affected by ODN. ODN negatively modulates GABA-elicited currents. B) Adapted from Christian et al., 2013, showing spontaneous inhibitory post-synaptic currents (sIPSCs) recorded from neurons in the thalamic reticular nucleus. Disrupting the BZD site via α3-H126R mutation (blue), blocking BZD site using zero-modulator FLZ (red), and deleting the DBI gene using the *nm1054* partial chromosomal deletion mutant (green) all reduce the duration of the sIPSC compared to traces from wild-type mice (black). These results suggest that in the thalamic reticular nucleus that DBI is acting as an endogenous PAM of inhibitory currents.

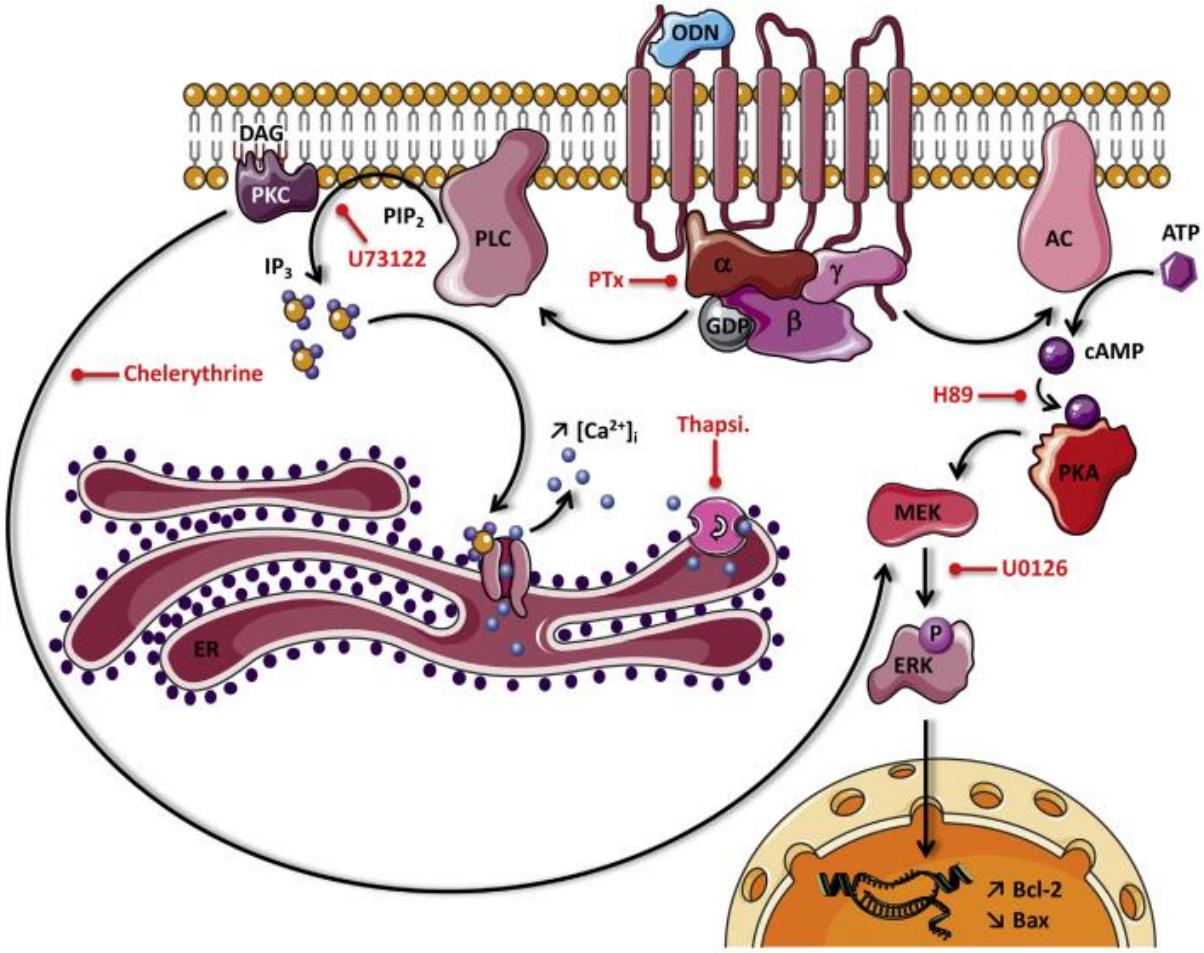

Figure 1.14 – ODN-triggered GPCR signaling cascade. Figure from Tonon *et al.,* 2020, showing the hypothesized GPCR signal cascade triggered by ODN binding. ODN-binding of the transmembrane GPCR triggers a PLC/PKC-dependent cascade which can lead to release of intracellular calcium from the endoplasmic reticulum (ER) and MEK-mediated changes in transcription.

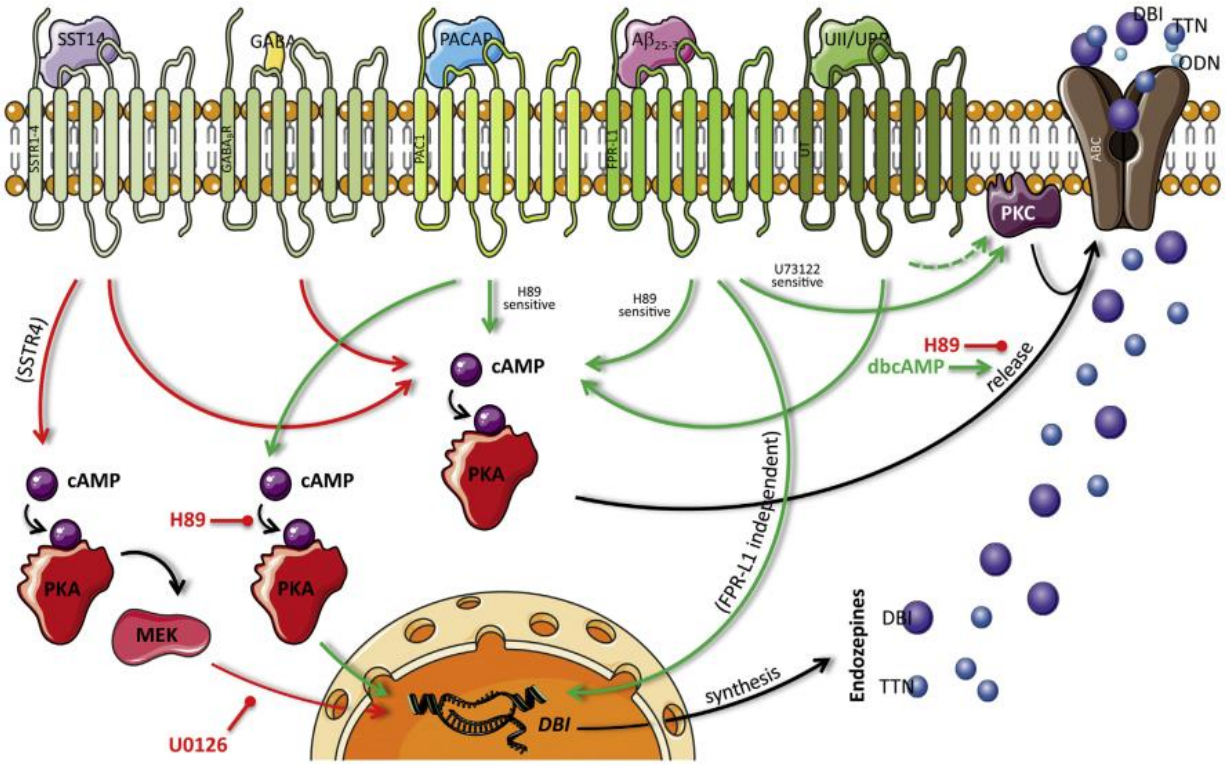

Figure 1.15 – Putative DBI release. Figure from Tonon *et al.*, 2020, showing a potential method of release for DBI and its cleavage products. Signaling from GPCRs triggers cAMP-mediated increases in transcription of the DBI gene. Products are released via an ATP binding cassette (ABC) transporter protein into extracellular space. Activation of PKC promotes release of DBI.

Chapter II:

DBI purification and verification of folding

Introduction

In order to study the effects of DBI on the GABAR, I needed to purify DBI on order of tens to hundreds of milligrams, as a single electrophysiology experiment uses approximately 2mg of protein. DBI is a soluble, cytosolic 11kD protein (Farzampour et al., 2015) that can easily be over-expressed in *E. coli* cells and purified. Although a bacterial expression system will not provide any post-translational modifications, it will allow the synthesis of hundreds of milligrams of protein necessary for my purposes (Rosano and Ceccarelli, 2014). I utilized a histidine-tagged human DBI construct inserted into a pET28a vector, which has been optimized for inducible expression of protein in bacterial cells (Shilling et al., 2020). This plasmid was transformed into BL21 DE3 cells, which are competent *E. coli* cells designed for high-efficiency protein expression. I then utilized a nickel nitrilotriacetic acid (NiNTA) column to purify the histidine-tagged protein. Finally, I used SDS-PAGE and NMR to confirm the purity and identity of DBI.

As DBI's function may be regulated by post-translational modifications and phosphorylation, acetylation, and methylation modification sites have been predicted based on DBI's amino acid sequence (Wang et al., 2020), we also examined if mammalian cells (HEK 293T cells) could be used to express DBI. My short experiment revealed that our current HEK culturing and over-expression protocol would not express enough DBI for our electrophysiology needs.

Methods and Results

A summary of the DBI purification process is shown below in Figure 2.1.

Expression

In order to express DBI, we used cloned cDNA for human DBI isoform3 (GeneBank ID CAG33237.1) containing a C-terminal histidine tag in a pET28a vector (generously provided by Dr. William Zagotta). The plasmid was chemically transformed into BL21 DE3 competent cells (ThermoFisher Scientific, Waltham, MA) following recommended protocol. Transformation reaction was plated on on luria broth (LB) LB containing Kanamycin (Kan, 30µg/mL) agar plates, and grown overnight at 37°C. A single colony was picked and grown overnight in a 5mL culture of LB supplemented with Kan (30µg/mL) while shaking at 37°C. The resulting cell culture was used to inoculate a 500mL of LB containing Kan. Culture was grown until OD_{600} of 0.6-0.8. Protein expression was then induced with IPTG (500µM) for 4 hours at 37°C under constant agitation (250rpm). After induction, cells were pelleted by centrifugation at 10,000xg for 10min at 4°C. Pellet was frozen at -80°C until purification steps.

NiNTA Column preparation

A 2mL NiNTA flowthrough column was packed using NiNTA agarose beads (Qiagen, Hilden, Germany) which uses Ni^{2+} ions to bind the electron donor groups from the imidazole rings of the histidine tag (Bornhorst and Falke, 2000). Column was pre-equilibrated with 40 mL of Buffer A supplemented with 10mM IDA at room temperature to prevent non-specific protein binding to the column. The Qiagen NiNTA beads have a binding capacity up to 50mg/mL.

Purification

Cell pellet was thawed and resuspended in 50mL Buffer A (50mM sodium phosphate, 300mM NaCl, pH 7.4) supplemented with 25mM imidazole (IDA) and a protease inhibitor cocktail (pepstatin, aprotinin, leupeptin). An Emulsiflex (ATA Scientific, Taren Point, NSW Australia), kept on ice, was used to break open the cells and homogenize the solution, which was then spun at 16,800xg for 20min at 4°C. Supernatant containing soluble DBI was then

loaded to the pre-packed 2 mL NiNTA column. Column was then washed with 10mL of Buffer A supplemented with 20mM IDA, followed by 6 mL of Buffer A supplemented with 30mM IDA. DBI was eluted using 5mL Buffer A containing 250mM IDA. Increasing the concentration of IDA outcompetes the IDA-rings in the histidine tag for the Ni^{2+} ions in the column, causing the histidine-tagged sample to be washed out of the column as the IDA concentration increases (Bornhorst and Falke, 2000). IDA was removed from the protein sample by using a desalting gravity column pre-packed with Sephadex G-25 resin (PD10 column, Sigma-Aldrich, St Louis, MO). Sephadex uses size-exclusion chromatography to remove low molecular weight substances from proteins greater than 5kDa, which also separates out small molecules and salts such as IDA (GE-Healthcare, 2007). Two PD10 columns with a maximum loading capacity of 2.5mL were equilibrated with 25mL Buffer A. Purified DBI was then added to each column and eluted using 3.5mL Buffer A.

Purity and Yield

Protein samples from each step of the purification process (supernatant, flow-through, washes and elution from NiNTA column, and flow-through and final elution from the desalting column) were separated on a 15% SDS-PAGE and stained with Coomassie Blue to assess eluted protein size and purity and efficiency of purification (Figure 2.2). Histidine-tagged DBI has an expected molecular weight of 10.87kDa, which corresponds to the overexpressed and purified protein observed on the SDS-PAGE (Figure 2.2). DBI concentration was measured using a Nanodrop 2000 (Thermo Fisher Scientific, Waltham, MA) using an extinction coefficient of 1.68, which reflects how the protein absorption at 280 nm is affected by the number of aromatic residues in the protein and is calculated using ExPasy's ProtParam tool (Duvaud et al., 2021). Protein yield was calculated by dividing the mass of protein from the final PD10 elution (53mg) and the total mass of protein in the supernatant (192mg), resulting in an approximate

30% purification yield and a final quantity of more than 50mg of protein, which is sufficient for over twenty electrophysiology experiments.

NMR Purification and Spectrum

^{1}H-^{15}N heteronuclear single quantum coherence (HSQC) spectroscopy elicits a two-dimensional spectrum, with one for ^{1}H and the other ^{15}N. When a protein sample is translated in a ^{15}N-rich environment, the amino acid backbone nitrogen atoms will be isotopically labelled. HSQC measures the corresponding chemical shifts of the nitrogen and amide proton of the peptide bond for each residue excluding proline when the sample is held in a strong, constant magnetic field and perturbed by a weaker, oscillating magnetic field. Local molecular environment, chemical links between atoms and freedom of movement all effect the resulting NMR spectra. Residues with NH groups in the sidechain will yield additional HSQC peaks. Based on the noise and number of peaks predicted from the protein sequence, a HSQC spectrum can be used to estimate sample purity and folding. Distinct, well-dispersed peaks indicate a correctly folded protein, whereas an excess of peaks would indicate additional protein in the sample and large overlapping peaks indicate unstructured regions in the protein (Dyson and Wright, 2004; Marion, 2013).

In order to evaluate DBI's purity and folding, DBI-containing plasmid was transformed into BL21DE3 cells and grown in ^{15}N-labelled M9 media. DBI was purified as described above and sent to the Henzler-Wildman lab to collect a ^{1}H-^{15}N HSQC spectrum (Figure 2.3) with a Bruker Avance III 600 MHz spectrotometer, with 5-10% D_2O added to the DBI sample. The data was collected at 25°C and analyzed using NMRPipe (Delaglio et al., 1995). The spectrum showed low noise, appropriate spectral dispersion, and close to the expected number of peaks (93 expected, 96 detected). This number of peaks indicates that the sample is pure, unaggregated and uniformly folded.

DBI Expression in HEK Cells

HEK 293T cells were cultured in Minimum Essential Media with Earle's salts with L-glutamine (Corning, Corning, NY), supplemented with 10% fetal bovine serum (Atalanta Biologics, Atlanta, GA), penicillin-streptomycin (Sigma-Aldrich, St Louis, MO) and Plasmocin™ (Invivogen, San Diego, CA) and grown in a 37°C incubator with 5% CO_2. Cells were plated on twenty 10cm dishes and transfected at approximately 70% cell confluency, with 18µg pUNIV-DBI per plate, using standard calcium phosphate transfection protocol (Graham and Van Der Eb, 1973). Cells were washed 6 hours after transfection with Dulbecco's Phosphate-Buffered Saline (Corning, Corning, NY) to remove residual calcium phosphate precipitant. 48 hours after transfection, cells were scraped and pelleted at 1000xg for 8min at 4°C. The pellet was homogenized in HEPES Glucose buffer (124mM NaCl, 2.9mM KCl, 1.3 mM MgSO4, 1.2mM KH2PO4, 25mM HEPES, and 5.2mM D-glucose; pH 7.4) using a Polytron homogenizer (Brinkman Instruments, Westbury, NY) and spun at 36,000xg for 25min at 4°C. Samples containing the putative soluble DBI protein and specific *E.coli* purified-DBI concentrations (1.2, 0.6, 0.2, 0.12, 0.06 and 0.02µg) were analyzed on a Coomassie Blue stained 15% SDS-PAGE (Figure 2.4). Although *E. coli*-produced DBI was observed at concentrations as low as 3.3ug/mL, no HEK-produced DBI was detected using a Coomassie stained gel, suggesting that HEK cells did not produced enough DBI protein in quantity needed for detection nor for electrophysiology experiments.

Discussion

The quality and quantity analysis of DBI revealed that a single batch of *E. coli* over-expression and column-based purification systems yield approximately 50mg of pure, unaggregated and uniformly folded DBI, while the HEK/ mammalian-based over-expression system did not yield enough soluble DBI for our experiments.

It is possible that the use of a vector optimized for mammalian expression could have increased transfection efficiency and resulting protein expression yield. Similarly, using a non-adherent cell culturing system could also benefit protein yield. As we produced and purified enough soluble, uniformly folded pure DBI using *E. coli*, all remaining experiments were performed using unmodified DBI expressed in *E. coli* BL21 cells.

Figures

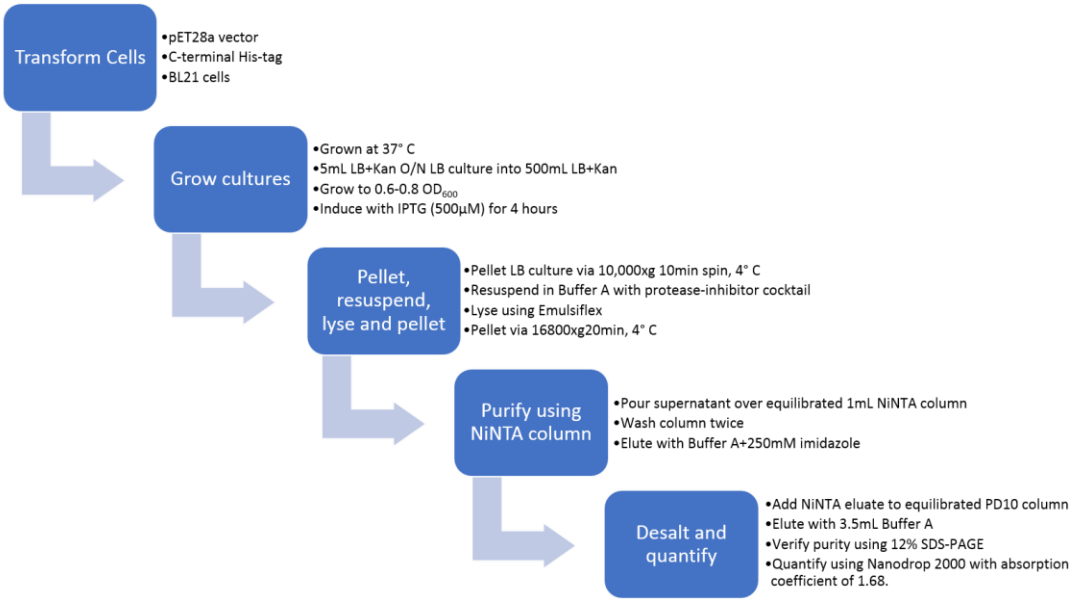

Figure 2.1 – Flow chart of DBI purification process. BL21 *E. coli* cells were transformed with a His-tagged DBI in a pET28a vector. 500mL cultures were grown to 0.6-0.8 OD_{600} and induced with IPTG for 4 hours. Cells were pelleted, resuspended in Buffer A and protease-inhibitor cocktail, and lysed using the Emulsiflex prior to a high-speed spin. Supernatant was poured through an equilibrated NiNTA column, then washed twice and eluted with 250mM imidazole (IDA). A desalting PD10 column was used to remove IDA from the soluble DBI protein sample. Protein purity and concentration was determined using 15% SDS-PAGE and a Nanodrop 2000.

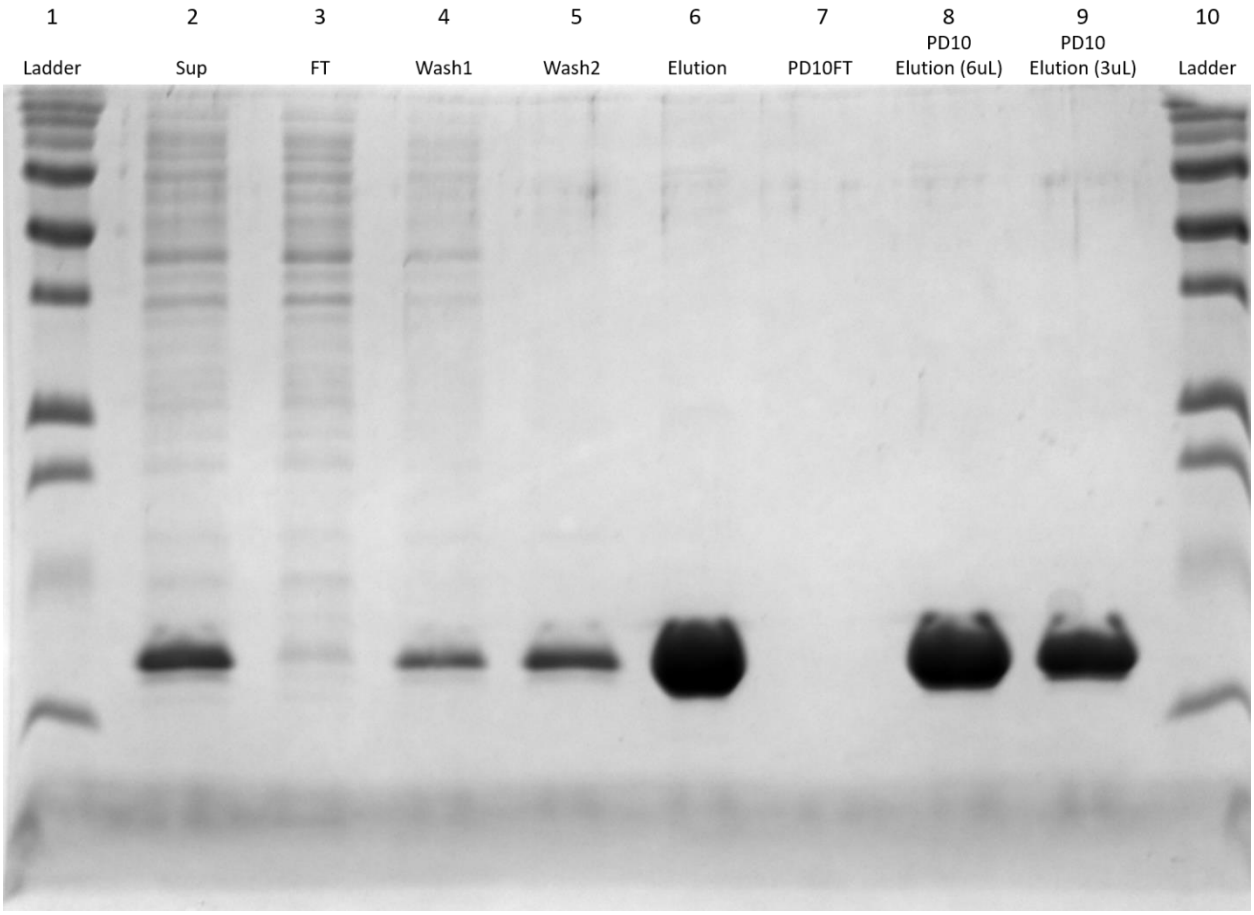

Figure 2.2 – 15% SDS-PAGE showing isolation of pure DBI. Lanes 1 and 10 show Biorad's Precision Protein Plus All Blue protein standards ranging from 10 kD to 75 kD. Lane 2 shows protein content of the supernatant after emulsion and final high-speed spin. Proteins contained in flow-through, first and second washes are observed in lanes 3, 4 and 5, respectively. Sample was then eluted from the NiNTA column with a single band observed at the expected size of 11kD (lane 6). Lane 7 is the flow-through when the sample is loaded onto the PD10 desalting column. Lanes 8 and 9 are 12 and 6µL of the PD10 elution, which represents the final, purified and desalted DBI. Overall, we observed the purification of a single ~11 kDa protein, which is the expected size of His-hDBI.

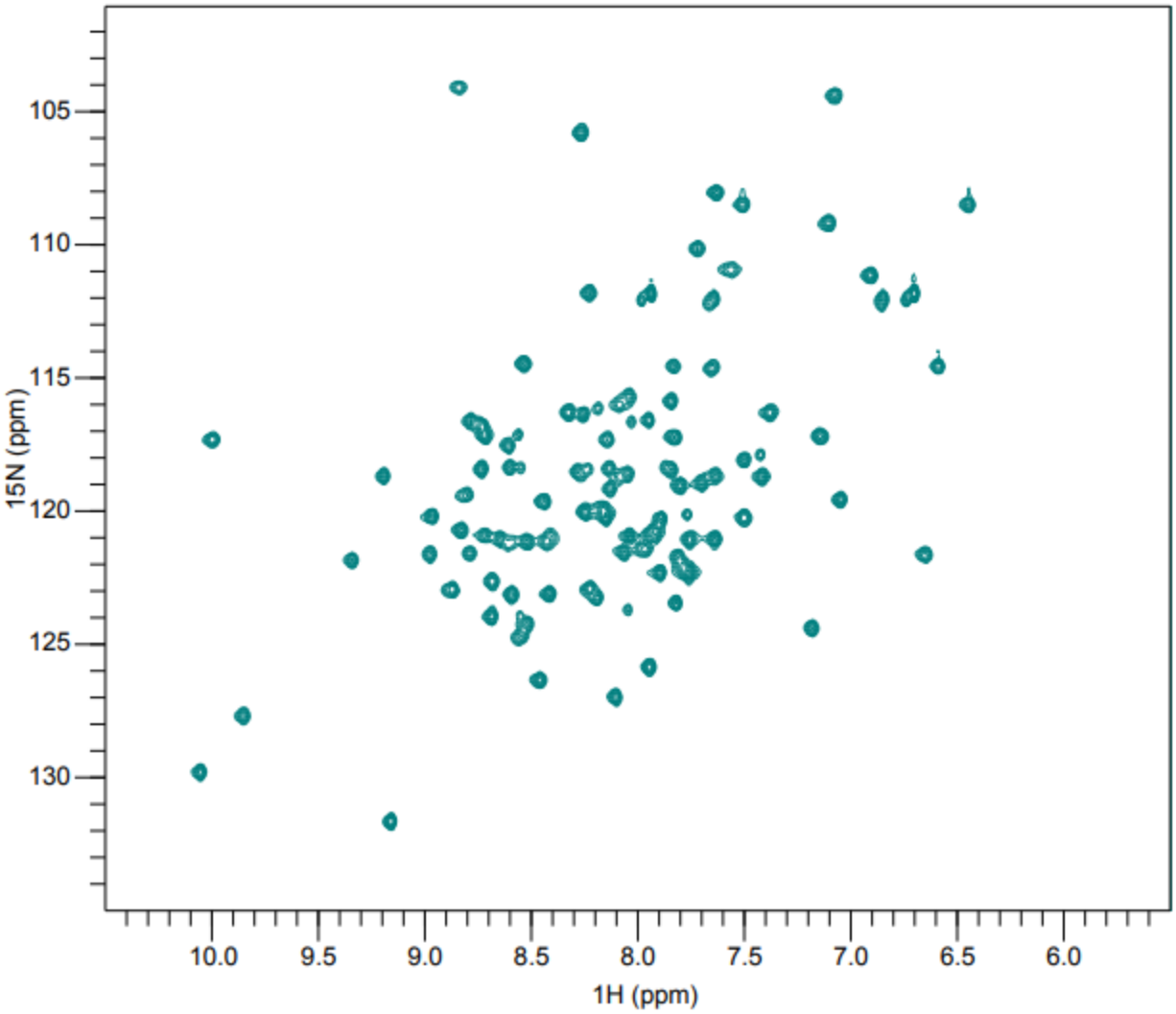

Figure 2.3 – ^{1}H-^{15}N spectrum shows DBI is folded and non-aggregated. DBI grown in ^{15}N M9 media was analyzed using Bruker Avance III 600 MHz spectrometer to create a ^{1}H-^{15}N HSQC spectrum. The spectrum shows close to the expected number of peaks (93 expected, 96 detected) as well as appropriate spectral dispersion and low noise, which indicates the protein sample is pure, folded and non-aggregated. NMR was performed by the lab of Dr. Henzler-Wildman.

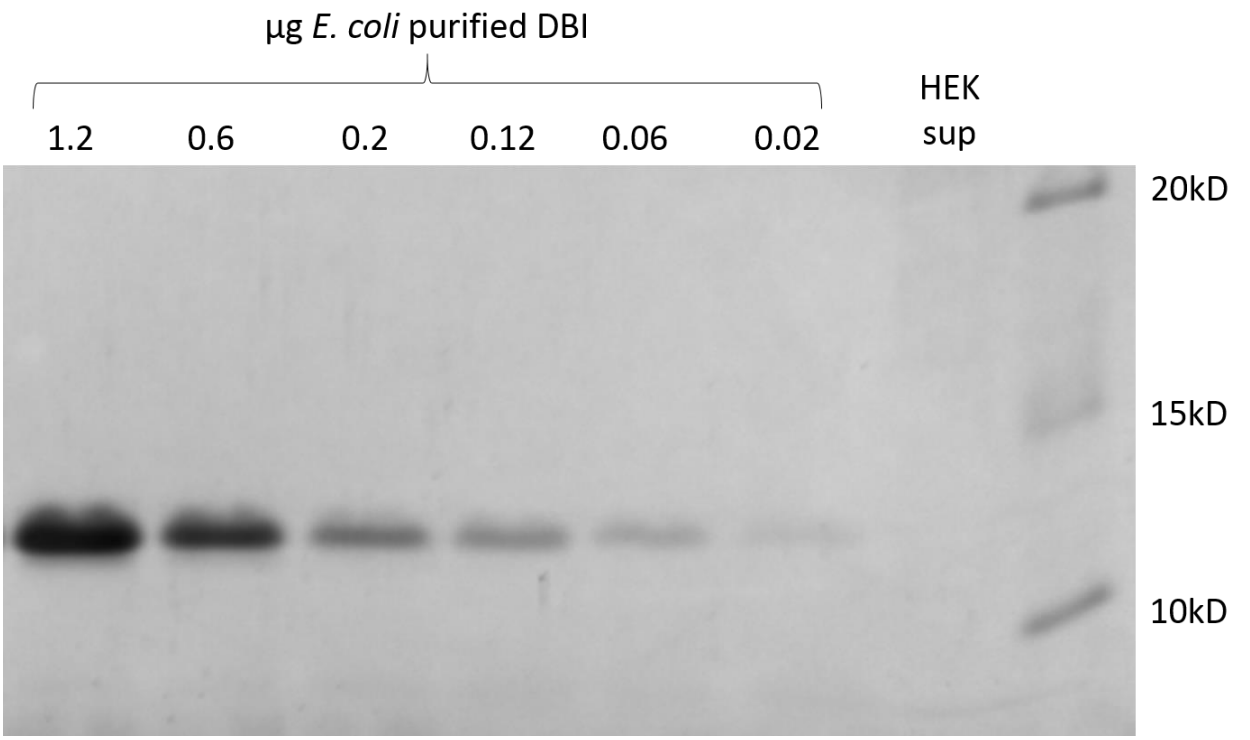

Figure 2.4 – 15% SDS-PAGE showing HEK 293T cells do not express high levels of transiently-transfected DBI. HEK cells were transfected with pUNIV-DBI. DBI-transfected HEK 293T cell-homogenate supernatant sample was collected and analyzed on a 15% SDS-PAGE with known masses of *E. coli* purified ranging from 1.2-0.02µg. Coomassie Blue staining allowed detection up to 0.02µg of DBI, but no bands were observed in the HEK supernatant lane, indicating that our current HEK transfection conditions are unable to express sufficiently high concentrations of DBI necessary for electrophysiology experiments.

CHAPTER III:

The diazepam binding inhibitor's modulation of the GABA-A receptor is subunit-dependent

Introduction

Since their discovery over fifty-five years ago, benzodiazepines (BZDs) have been some of the most widely prescribed drugs in the world and have remained on the World Health Organization's list of essential drugs since the list's inception in 1977 (Organization, 1977). BZDs are used to treat a variety of conditions ranging from epilepsy to insomnia to anxiety (Engin et al., 2018; Palma et al., 2017; Wisden et al., 2019), and mediate their effects by binding to the main inhibitory neurotransmitter receptor in the brain, the gamma-aminobutyric acid-A receptor (GABAR) (Mohler, 2011). BZDs modulate GABAR activity, and thus alter neuronal signaling.

GABARs are heteropentamers comprised from nineteen possible subunits (α1-6, β1-3, γ1-3, δ, ε, θ, π and ρ1-3) that are expressed in distinct brain regions, with distinct pharmacological properties. There are two GABA binding sites in the extracellular interfaces between β and α subunits, while BZDs bind in an extracellular pocket at the α/γ subunit interface. BZDs, such as diazepam or flurazepam (FZM), can act as positive allosteric modulators (PAMs), which increase GABA-mediated currents, or negative allosteric modulators (NAMs) like methyl-6,7-dimethoxy-4-ethyl-beta-carboline-3-carboxylate (DMCM) which decrease GABA-elicited currents. Zero-modulators, such as flumazenil (FLZ, Ro15-1788), occupy the BZD site but do not alter GABA-elicited currents. The effects of some BZDs like Ro15-4513 are subunit dependent. Ro15-4513 acts as PAM when interacting with $\alpha_4\beta_2\gamma_2$ and $\alpha_6\beta_2\gamma_2$ GABARs, but is a NAM when bound to $\alpha_1\beta_2\gamma_2$ receptors (Knoflach *et al.*, 1996)**.**

The presence a binding site on the GABAR for synthetically manufactured BZDs has long suggested the existence of an endogenous synthesized molecule that binds to the same site. In 1983, a candidate peptide was isolated from rat brain homogenates, which displaced

tritiated diazepam in a radioligand binding assay (Guidotti et al., 1983). This 10kD, 87 amino-acid protein was named the diazepam binding inhibitor (DBI). Recent DBI knock-down and over-expression studies in the thalamic reticular nucleus (nRT) demonstrate that DBI works in vivo as a PAM where it potentiates GABA-mediated currents and suppresses epileptic activity(Christian et al., 2013). In contrast, DBI knock-down in the subventricular zone of the lateral ventricles and in the hippocampal subgranular zone demonstrate that DBI and one of its peptide fragments, ODN, inhibit GABA-induced currents (Alfonso et al., 2012; Dumitru et al., 2017)**,** indicating that in these brain regions DBI and ODN work as NAMs of GABARs. We hypothesize that the differences in DBI's modulatory effects are due to regional differences in GABAR subunit expression and GABAR subunit composition.

Here, we used two-electrode voltage clamping and measured DBI effects on GABA-activated currents from GABARs expressed in *Xenopus laevis* oocytes. Given DBI is highly expressed in the hippocampus and thalamus (Costa and Guidotti, 1991; Liu et al., 2005), we focused on $\alpha_5\beta_3\gamma_{2L}$ and $\alpha_3\beta_3\gamma_{2L}$ GABAR subtypes which are enriched in these regions (Mortensen et al., 2012). We found that DBI positively modulates $\alpha_5\beta_3\gamma_{2L}$ receptors, whereas DBI is a weak negative modulator of $\alpha_3\beta_3\gamma_{2L}$ GABARs. We used *in silico* protein-protein docking to visualize DBI-GABAR interactions and highlight some differences that may explain DBI's distinct effects on these two GABAR subtypes.

Methods

DBI expression and purification for functional testing

We used cDNA for human DBI isoform3 (GeneBank ID CAG33237.1) with a C-terminal histidine tag in a pET28a vector. The plasmid was chemically transformed into BL21 DE3 competent cells, plated on LB-Kanamycin (Kan) agar plates, and grown overnight at 37°C. A single colony was picked and grown overnight in a 5mL culture of LB with 250µg Kan while shaking at 37°C. This culture was used to inoculate 500mL LB + Kan and the culture was grown until OD_{600} reached 0.6-0.8. Protein expression was induced with IPTG (500µM) for 4 hours at

37°C. After induction, cells were pelleted by spinning at 10,000xg for 10min at 4°C. The bacterial cell pellet was frozen at -80°C. Cell pellet was thawed and resuspended in 50mL Buffer A (sodium phosphate, 50mM, pH 7.4; NaCl, 300mM) and 25mM imidazole (IDA) with a protease inhibitor cocktail (pepstatin, aprotinin, leupeptin). After lysis using an Emulsiflex (ATA Scientific, Taren Point, NSW Australia), samples were spun at 16800xg for 20min, 4°C. The supernatant was bound to an Ni-NTA column which was pre-equilibrated in column buffer (Buffer A and 10mM imidazole, pH 7.4). His-tagged DBI was eluted using elution buffer (Buffer A and 250mM imidazole). A PD10 desalting column was used to remove imidazole, DBI was eluted in Buffer A. DBI molecular weight was verified via 15% SDS-PAGE stained with Coomasie blue and protein level quantified using a Nanodrop 2000 (Thermo Fisher Scientific, Waltham, MA), using an absorption coefficient of 1.68. DBI with the histidine tag attached has a mass of 10.87kDa.

DBI purification for NMR

DBI was transformed into BL21 DE3 cells, grown in ^{15}N-labeled M9 media, and purified as described above. A ^{1}H-^{15}N HSQC spectrum was obtained using a Bruker Avance III 600 MHz spectrometer, with 5-10% D_2O added to the protein sample. The spectrum was collected at 25°C. Data were processed using NMRPipe (Delaglio et al., 1995) and analyzed using CcpNmr analysis (Vranken et al., 2005).

DBI Vector Mutagenesis and Purification

In order test the function of DBI without the histidine tag attached, a histidine tag and TEV cleavage site was introduced at the N-terminus of the protein, and a stop-codon was inserted before the original C-terminal histidine tag. This mutagenesis was performed using QuikChange site-directed mutagenesis with *PfuUltra* II Fusion HS DNA polymerase (Agilent, Santa Clara, CA) using a large ultramer primer (Integrated DNA Technologies, Coralville, IA) for 5' insertions and single primer for 3' insertions. Reaction products were digested with *Dpn*I (Thermo Fisher Scientific, Waltham, MA) and transformed into Top10F' *E. coli* cells. Clones

were selected and successful mutagenesis was confirmed via sequencing. DBI was purified as described above, and incubated overnight with TEV protease at 4°C.

Palmitoyl-CoA Incubation

To assess whether DBI function may change in the presence of the long-chain fatty acid ligand palmitoyl-CoA, purified DBI was pre-incubated with palmitoyl-CoA. Palmitoyl-CoA was suspended at 1mM in Buffer A and combined with DBI in final concentrations of 50μM DBI and 100μM palmitoyl-CoA. Samples were incubated for 30min or 3 hours at 4°C or room temperature.

Expression in Xenopus laevis oocytes

Rat cDNA encoding the GABAR α3, α5, β3 and γ2L subunits subcloned into the pUNIV vector (Venkatachalan et al., 2007) were used. cRNA was transcribed from *NotI* digested cDNA using the mMessage T7 kit (Ambion, Austin, TX). *Xenopus laevis* oocytes were harvested and prepared as described previously (Boileau et al., 1998). Oocytes were injected with 27-54nL of GABAR subunit cRNA at 10ng/μL α, 10ng/μL β and 100ng/μL γ2L following previously described methods (Boileau et al., 2002), stored at 16°C in ND96 buffer (96mM NaCl, 2mM KCl, 1mM MgCl2, 1.8mM CaCl2, and 5mM HEPES, pH 7.2) supplemented with 100μg/ml bovine serum albumin and gentamycin and recorded from 2-7 days after injection.

Two Electrode Voltage Clamp

Electrophysiological recordings were performed as described previously (Hanson and Czajkowski, 2008). Oocytes expressing GABARs were held at -40 to -80 mV under a two-electrode voltage clamp and continuously perfused with ND96 at 5mL/min in a 200 μL volume chamber. Borosilicate glass electrodes (0.4-1.0mΩ, Warner Instruments, Hamden, CT) were filled with 3M KCl. Data were collected at room temperature using two different voltage clamps. One was a GeneClamp 500 (Molecular Devices, Sunnyvale, CA) interfaced to a computer via a Digidata 1200 device (Molecular Devices) with data recorded using Whole Cell Program, version 3.6.7 (J. Dempster, University of Strathclyde, Glasgow, UK). The other was an Oocyte

Clamp OC-725A (Warner Instruments, Hamden, CT) with a Digidata 1440A (Molecular Devices, Sunnyvale, CA) with data recorded using AxoScope, pCLAMP 10 (Molecular Devices, Sunnyvale, CA). Data and results obtained from the clamps were indistinguishable.

A stock solution of 1 M GABA (Sigma-Aldrich, St Louis, MO) was made in water, stored at -20 C and thawed before use. GABA dilutions for experiments were prepared fresh daily in ND96. A stock solution of 10 mM FZM (Sigma/RBI, Natick, MA) in water was diluted in ND96 for working concentrations daily. A stock solution of 10mM DMCM (Sigma/RBI, Natick, MA) was prepared in dimethyl sulfoxide and diluted daily in ND96 for working concentrations in which the final concentration of dimethyl sulfoxide (≤0.1%) did not affect GABAR function.

Concentration-response analysis

GABA concentration-response curves were determined as described previously (Hanson and Czajkowski, 2008). Seven concentrations of GABA (1μM, 3μM, 10μM, 30μM, 100μM, 1mM and 10mM) were used to fit concentration response curves and determine GABA EC50 values. Concentration-response data were fit using Prism version 8.4 (GraphPad Software Inc., San Diego, CA) to the equation: $I = Imax/[1 + (EC50/[A]nH)]$, in which I is the peak current response to a given GABA concentration, Imax is the maximal amplitude of GABA activated current, EC50 is the GABA concentration that produces the half-maximal response, [A] is the GABA concentration, and nH is the Hill coefficient.

Drug modulation

Drug modulation was measured at GABA EC_{20} and evaluated as $I_{GABA+Drug}/I_{GABA}$, where $I_{GABA+Drug}$ is the GABA-mediated current in the presence of drug and I_{GABA} is the GABA-mediated current in the absence of drug. To measure drug modulation, a 5 sec pulse of GABA EC_{20} was applied and followed immediately by a 5 sec pulse of GABA EC_{20}+Drug. When multiple drugs were applied to a single oocyte, GABA EC_{20} was applied following drug treatment until current amplitudes returned to initial GABA EC_{20} level to ensure complete washout of drugs between different drug treatments.

Statistical analysis

All data were from at least three different oocytes from at least two different frogs. Data are represented as mean ± SD. Significant differences in drug modulation between subunit compositions were calculated via Kruskal-Wallis test with a Dunn's multiple comparisons (Prism v9.1, GraphPad Software Inc, San Diego, CA). This test was selected due to the non-normal distribution of data, as evaluated using a D'Agostino and Pearson test which evaluates skewness and kurtosis and generates a P value based on how much these values differ from a Gaussian distribution (D'Agostino et al., 1990). Normalized values are used to compare the effects of drug or DBI between $\alpha_3\beta_3\gamma_{2L}$ and $\alpha_5\beta_3\gamma_{2L}$ GABARs. Normalized values were also compared to a hypothetical null value of 1 using a one-sample t-test in Prism.

Statistical differences in GABA+drug versus GABA alone current amplitidues elicited from the same oocyte were calculated using a ratio paired t-test of raw, non-normalized values using Prism software rather than a standard paired t-test. For our data, differences between control and treatment is not a consistent measure of effect. The differences are larger when the control current amplitudes are larger. Thus, the ratio (treated/control) is a more consistent way to quantify the effect of the treatment (GraphPad, 2021).

The effects of DBI on $\alpha_5\beta_3\gamma_{2L}$ GABA-elicited currents were more variable than effects observed with FZM, a BZD (coefficient of variation for FZM $\alpha_5\beta_3\gamma_{2L}$ is 17.2%, DBI is 36.0%). The variation was not correlated with DBI purification batch nor oocyte/frog. We hypothesize that flexibility and conformation dynamics of DBI (11kDa) may contribute to the increased variability of its effects as compared to a small BZD drug.

Protein-protein docking

We made $\alpha_3\beta_3\gamma_{2L}$ and $\alpha_5\beta_3\gamma_{2L}$ GABAR homology models based on the cryoEM structure of the $\alpha_1\beta_3\gamma_{2L}$ GABAR obtained in the presence of the BZD alprazolam (PDB 6HUO) (Masiulis et al., 2019). The homology models were built on Sybil, Tripos Inc. The GABAR α3 or α5

sequences were manually threaded on to the cryoEM model of the $\alpha_1\beta_3\gamma_{2L}$ GABAR based on their sequence alignment with the a1 subunit using the graphical interface of the Sybil program. After resolving steric clashes, the resulting structures were subject to energy minimization using the Tripos force field. The $GABA_AR$ model images were developed using PyMOL (Schrödinger, LLC, New York).

Protein-protein interactions between the $\alpha_3\beta_3\gamma_{2L}$ and $\alpha_5\beta_3\gamma_{2L}$ GABAR models and the unliganded human DBI crystal structure (PDB 2FJ9) (Taskinen et al., 2006) were identified using ClusPro a web-based program for computational docking of proteins (Kozakov et al., 2013; Kozakov et al., 2017; Vajda et al., 2017). ClusPro analyzes 70,000 rotations of the ligand and generates up to 30 highly populated clusters of ligand structures docked in similar locations on the receptor with low energy scores. Clusters are ranked by population size rather than an energy score. Docking clusters selected for analysis were based on their proximity to the BZD binding site. We analyzed the hydrogen bonding between the alpha subunit and DBI (Figure 4B-C) and the gamma subunit and DBI (Figure 4D-E) using Pymol's hydrogen bonding feature.

Results

In order to study the effects of DBI on the GABAR receptor, we needed to efficiently purify milligram quantities of pure, non-aggregated and correctly folded DBI. We used a histidine-tagged human DBI construct (His-DBI) inserted into a pET28A vector, which is optimized for inducible expression of protein in bacterial cells (Shilling et al., 2020). We expressed the His-DBI in BL21 *E. coli* cells and purified the protein as described in Methods. DBI purity and size was evaluated using 15% SDS-PAGE (Figure 3.1A). Following purification, a single Coomassie stained band was observed with a molecular weight of 11kDa. DBI with the histidine tag attached has a mass of 10.87kDa. Heteronuclear single quantum correlation (HSQC) nuclear magnetic resonance (NMR) of ^{15}N-labeled DBI demonstrated that our DBI purification methods produced pure, non-aggregated and correctly folded protein, as number of

peaks was very close to the total number of residues in the His-tagged DBI, spectral dispersion was good, and the linewidths were relatively uniform (Figure 3.1B).

We expressed $\alpha_3\beta_3\gamma_{2L}$ and $\alpha_5\beta_3\gamma_{2L}$ GABARs in *Xenopus laevis* oocytes and used two-electrode voltage-clamping and measured the effects of a BZD PAM (FZM), a BZD NAM (DMCM) and DBI on GABA-elicited currents. Initially, we measured GABA concentration responses from oocytes expressing $\alpha_3\beta_3\gamma_{2L}$ and $\alpha_5\beta_3\gamma_{2L}$ GABARs. GABA EC_{50} values were 47±11.8 μM, n=5 for $\alpha_3\beta_3\gamma_{2L}$ GABARs (Figure 3.2A) and 34±8.6 μM, n=3 for $\alpha_5\beta_3\gamma_{2L}$ GABARs (Figure 3.2B), which are consistent with previously published results (Karim et al., 2013; Nimmich et al., 2009).

To evaluate and compare the effects of the positive BZD modulator, FZM, the negative BZD modulator, DMCM and DBI, we applied a low GABA EC20 concentration and then co-applied FZM (10μM), DMCM (10μM) or DBI (50μM) with GABA EC20 (Figure 3.3A). FZM (10μM) significantly increased GABA currents from oocytes expressing $\alpha_3\beta_3\gamma_{2L}$ and $\alpha_5\beta_3\gamma_{2L}$ GABARs: $I_{GABA+FZM}/I_{GABA}$ was 2.73±0.72 and 2.04±0.38, respectively (Figure 3.3; ratio paired t-test $p<0.0001$ for both GABAR subtypes). The effects of FZM on α3-containing receptors compared to α5-containing receptors were not significantly different (Figure 3.3B, Dunn's multiple comparisons $p>0.999$). DMCM (10μM) significantly inhibited GABA currents from both $\alpha_3\beta_3\gamma_{2L}$ and $\alpha_5\beta_3\gamma_{2L}$ GABARs: $I_{GABA+DMCM}/I_{GABA}$ was 0.75±0.13 and 0.60±0.15, respectively (Figure 3.3, ratio paired t-test $p<0.0001$ for both GABAR subtypes) and the effects of DMCM on α3-containing versus α5-containing GABARs were not significantly different (Figure 3.3B, Dunn's multiple comparisons $p>0.999$).

We used the same methods to evaluate the effects of purified DBI (50μM) on GABA EC20 currents from $\alpha_3\beta_3\gamma_{2L}$ and $\alpha_5\beta_3\gamma_{2L}$ GABARs. DBI weakly inhibited GABA currents from $\alpha_3\beta_3\gamma_{2L}$ GABARs (Figure 3.3A). $\alpha_3\beta_3\gamma_{2L}$ GABAR current amplitudes in the presence of DBI were significantly different from currents elicited by GABA alone: $I_{GABA+DBI}/I_{GABA}$ was 0.93±0.10 (Figure 3.3C, ratio paired t-test $p=0.001$). In contrast, DBI significantly potentiated $\alpha_5\beta_3\gamma_{2L}$ GABA

currents, where $I_{GABA+DBI}/I_{GABA}$ was 1.34±0.48 (Figure 3.3, ratio paired t-test $p<0.0001$). The data indicate that DBI acts as a very weak NAM for α3-containing receptors and a modest PAM for α5-containing receptors (Figure 3.3). DBI's effects were not changed by pre-incubating DBI with palmitoyl-CoA (a long-chain fatty acid known to bind DBI), or by cleaving the histidine tag (Supplemental Figure S3.1)

Data for the effects of DBI on $\alpha_5\beta_3\gamma_{2L}$ GABA-elicited currents were more variable than a BZD (coefficient of variation for FZM $\alpha_5\beta_3\gamma_{2L}$ data is 17.2%, DBI $\alpha_5\beta_3\gamma_{2L}$ effects 36.0%). This may be due to either the fact that the structure of the DBI protein is more flexible than the BZD chemical. Alternatively, DBI may bind a more flexible region of the GABAR than the BZD binding site. Increased motility of either DBI or the GABAR could cause more variability in the effects of the DBI/GABAR interaction.

α3 and α5 are homologous GABAR subunit isoforms with many conserved residues (73% identity) (Duvaud et al., 2021). To explore potential mechanisms underlying DBI's different actions on α3-containing versus α5-containing GABARs, we constructed $\alpha_3\beta_3\gamma_{2L}$ and $\alpha_5\beta_3\gamma_{2L}$ GABAR homology models and examined protein-protein interactions with DBI using ClusPro, a web-based program for computational docking of proteins (Kozakov et al., 2013; Kozakov et al., 2017; Vajda et al., 2017). This program generates clusters which represent populations of structures where the ligand has docked with low energy at similar locations on the protein. Clusters are ranked based on population size.

For both $\alpha_3\beta_3\gamma_{2L}$ and $\alpha_5\beta_3\gamma_{2L}$ GABARs, ClusPro generated many highly populated clusters with the ODN loop of DBI penetrating the BZD-binding pocket of the GABAR between the α and γ subunits in the extracellular domain. ODN is a DBI cleavage product that has been shown to displace ^{3}H-BZD binding from primary cultures of rat cerebellar granule cells (Ferrero et al., 1986) and is made up of residues found in the loop between the second and third alpha helices in DBI. We selected two clusters (those that showed the closest ODN-BZD site interactions) for further analysis. Figure 3.4A shows DBI docked at GABAR α3/γ2 and α5/γ2

subunit interfaces. Figure 3.4B highlights differences in residues in the α3 and α5 GABAR subunits that are located at the BZD binding site interface that are within H-bonding distance to DBI while Figure 3.4C highlights differences in DBI residues that interact with the α3 and α5 GABAR subunits. Residues in the GABAR γ subunit interacting with DBI and residues in DBI interacting with the γ subunit are displayed in Figure 3.4D and E.

When comparing DBI docking results to α3 and α5-containing receptors, we identified subtle differences in DBI-GABAR interactions. Non-homologous residues in the α subunits interact differently with DBI. For example, the α3 histidine at position 142 in Loop7 is not predicted to H-bond with DBI but the aligned α5 glutamine does. In Loop C, the α3 Ile202 does not interact but the aligned α5 asparagine does. The GABAR γ subunit residues that interact with DBI were the same for both GABAR subtypes. The GABAR α5 subunit had more residues that H-bonded with DBI than the α3 subunit. In addition, DBI had more H-bond interactions with the γ subunit of α5-containing GABARs. Future studies should examine how mutating these residues in both GABAR subunits and DBI alter DBI effects. While the docking results did not clearly illuminate why DBI is a NAM at α3-containing and a PAM at α5-containing receptors, they provide evidence to support the idea that DBI can bind at the BZD binding site interface of GABARs ad establish potential interactions that may underlie specific response differences in the two receptor subtypes.

Discussion

While DBI was identified as a putative endozepine in the mid-1980s (Guidotti et al., 1983), much of DBI's mechanism of action is still unknown. Due to DBI's intracellular roles in long-chain fatty acid metabolism, and its multiple biologically active cleavage products (Bouyakdan et al., 2015; Knudsen, 1991; Slobodyansky et al., 1989; Tonon et al., 2020), direct effects of DBI on GABAR function have not been extensively studied. The use of FLZ (a BZD antagonist) provides indirect evidence for the existence of an endogenous GABAR modulator. Application of this zero-modulator increased the decay of GABA-evoked inhibitory postsynaptic

currents in neurons in the hippocampus (King et al., 1985), dentate gyrus (Leroy et al., 2004), neocortex (Ali and Thomson, 2008) and the nRT (Christian et al., 2013), suggesting that FLZ is displacing an endogenous GABAR modulator. Recording from cells in the nRT suggested that DBI positively modulates GABARs (Christian et al., 2013) while studies in the subventricular zone and hippocampal subgranular cells suggest DBI is a NAM (Alfonso et al., 2012; Dumitru et al., 2017). Some benzodiazepines like Ro15-4513 have different actions depending on GABAR subunit composition (Knoflach et al., 1996). We hypothesized that the modulatory effects of DBI on GABAR activity are regulated by receptor subunit composition, which varies by brain location. In this study, we found that DBI is a PAM for α5-containing GABARs and a weak NAM for α3-containing receptors.

Recordings from cells in the hippocampal subgranular zone suggest that DBI or its peptide cleavage product, ODN, act as a NAM (Dumitru et al., 2017). Given α5 subunits are highly expressed in the hippocampus (Sequeira et al., 2019), these published experiments predict that heterologously expressed α5-containing receptors would be negatively modulated by DBI versus positively modulated, which we observed (Figure 3). Similarly, patch clamp recordings from the nRT where α3 is highly expressed (Hörtnagl et al., 2013) suggested that these receptors are positively modulated by DBI (Christian et al., 2013), while our experiments with heterologously expressed $\alpha_3\beta_3\gamma_{2L}$ GABARs demonstrated that DBI acts as weak NAM (Figure 3).

There are several possible explanations for differences between our data and previously published results. In our experiments, DBI was expressed in *E. coli* and purified, and GABARs of a single subtype were expressed in *Xenopus laevis* oocytes. The Monyer (Alfonso et al., 2012; Dumitru et al., 2017) and Huguenard (Christian et al., 2013) experiments relied primarily on up- or down-regulating endogenous DBI expression. DBI has several biologically active cleavage products, multiple predicted sites for post-translational modifications, and can bind long-chain fatty acids. The effects of full-length DBI purified from *E. coli* without eukaryotic

modifications may be different than a cleavage product such as ODN, or DBI with post-translational modifications. Moreover, GABARs in neurons are likely associated with accessory subunits like GARLH or Shisa7 (Han et al., 2019; Yamasaki et al., 2017). The absence of these accessory subunits in *Xenopus* oocytes may alter DBI actions. Furthermore, α3 and α 5 are not the only α subunits expressed in nRT and hippocampus, respectively. In neurons, the presence of GABARs which contain other α subunits that might be modulated by DBI make it difficult to assign DBI's effects to one specific GABAR subtype. Here, using a reductionist approach, we demonstrate that DBI is a PAM of $\alpha_5\beta_3\gamma_{2L}$ GABARs and a weak NAM of $\alpha_3\beta_3\gamma_{2L}$ GABARs.

$\alpha_5\beta_3\gamma_{2L}$ GABARs are highly expressed in the hippocampus and can be found both synaptically and extrasynaptically (Mortensen et al., 2012). α5-containing GABARs play a large role in hippocampal-dependent forms of learning and memory (Collinson et al., 2006; Crestani et al., 2002; Joksimović et al., 2013; Timić et al., 2013). Our data demonstrating that DBI acts as a PAM for α_5-containing receptors suggests that DBI may have effects on learning and memory. Consistent with this idea, previous experiments with DBI-knockout mice showed a disruption in spatial learning and memory (Ujjainwala et al., 2019) and social behavior (Ujjainwala et al., 2018). While somatic IPSC recordings from hippocampal CA1 and dentate gyrus regions found that DBI knockout DBI knockout did not change the effects of FLZ on mIPSCs (Courtney and Christian, 2018), these fast IPSCs recorded from the soma of pyramidal neurons are unlikely to capture the effects of DBI on α5-containing receptors which are expressed primarily in the distal dendritic regions and responsible for much of hippocampal learning and memory (Groen et al., 2014; Rodgers et al., 2015).

$\alpha_3\beta_3\gamma_{2L}$ GABARs are highly expressed in the cortex, hypothalamus and nRT (Crestani and Rudolph, 2015; Engin *et al.*, 2018; Fischer et al., 2011; Rudolph and Knoflach, 2011). While they are generally expressed synaptically, it has been suggested that α_3-containing GABARs can be expressed extrasynaptically and mediate tonic inhibition in the nRT (Devor et al., 2001; Pangratz-Fuehrer et al., 2016). Disruptions in the development of the nRT have been tied to

absence seizures (Pangratz-Fuehrer *et al.*, 2016). Additionally, work using mice with BZD-insensitive α_3 subunits has shown that these receptors mediate some of the myorelaxant effect of benzodiazepines (Crestani et al., 2001). Some have suggested that α_3-containing GABARs can also mediate anxiolytic effects of BZDs (Fischer et al., 2011; Morris et al., 2006; Rowlett et al., 2005), though these findings are somewhat controversial (Crestani and Rudolph, 2015; Koester et al., 2013; Löw et al., 2000). Our data showing DBI acts as a weak NAM for $\alpha_3\beta_3\gamma_{2L}$ GABARs suggests that DBI could alter the effects of α_3-containing GABARs in maintaining tonic inhibition in the nRT and in regulating muscle control and anxiety.

Dysregulation of GABA-mediated signaling is implicated in a wide variety of neurological diseases and disorders, including Alzheimer's (Calvo-Flores Guzmán et al., 2018; Govindpani et al., 2017), anxiety (Engin et al., 2018), Parkinson's (Brickley and Mody, 2012) and epilepsy (Palma et al., 2017). Our findings showing that DBI's effects are dependent on GABAR subunit composition lay an important foundation for understanding how inhibition in the brain is regulated.

See bioRxiv paper "The diazepam binding inhibitor's modulation of the GABA-A receptor is subunit-dependent" (Borchardt et al., 2021) for additional analysis and control experiments.

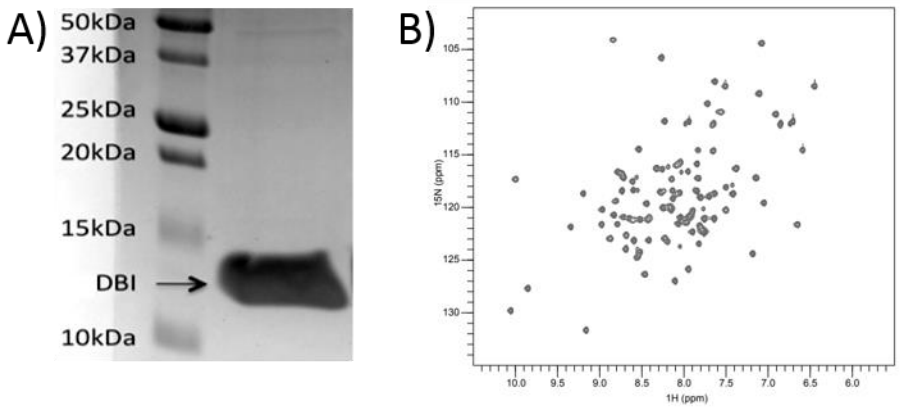

Figure 3.1 - Purified DBI is fully folded. 15% SDS-PAGE (A) showing a marker lane with 50, 37, 25, 20, 15 and 10kDa bands, and histidine-tagged DBI running at the correct weight (11kD). The single band for DBI indicates the protein is pure and unaggregated. 1H-15N HSQC spectrum (B) from DBI grown in ^{15}N M9 media shows close to the expected number of peaks (93 expected, 96 detected), appropriate spectral dispersion and low noise, indicating the protein sample is folded and non-aggregated. NMR was performed by the lab of Dr. Henzler-Wildman.

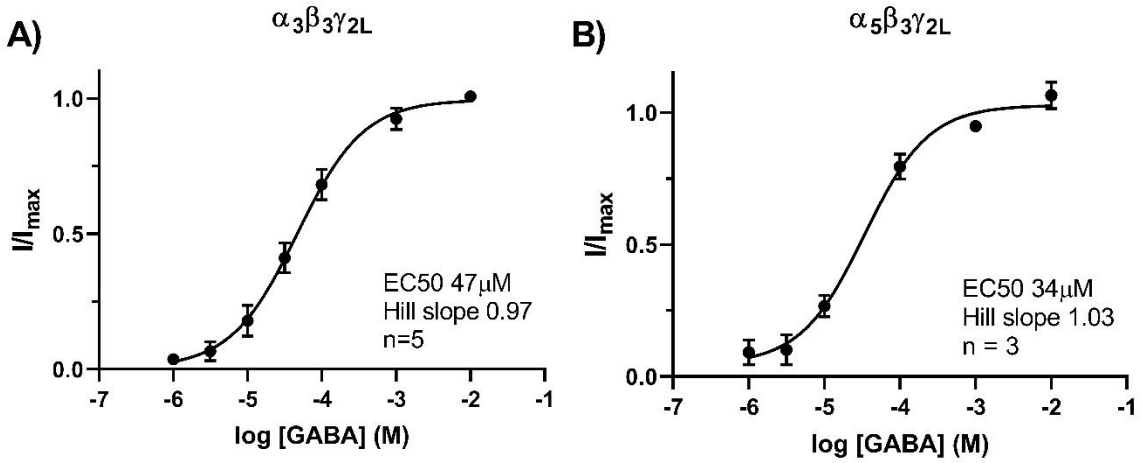

Figure 3.2 – GABA dose response curves for $\alpha_3\beta_3\gamma_{2L}$ and $\alpha_5\beta_3\gamma_{2L}$. Using two-electrode voltage clamping of *Xenopus* oocytes injected with $\alpha_3\beta_3\gamma_{2L}$ (A) and $\alpha_5\beta_3\gamma_{2L}$ (B) cRNA, increasing concentrations of GABA (1μM-10mM) were applied. Data were fit using a non-linear transformation. Data are normalized to calculated top and averaged from three to five different oocytes, with error bars showing SD. Calculated EC_{50} values and Hill slopes were 47μM and 0.97 for $\alpha_3\beta_3\gamma_{2L,}$ and 34μM and 1.03, and are within normal ranges. Data for GABA dose response curves were collected by Luke Blecker.

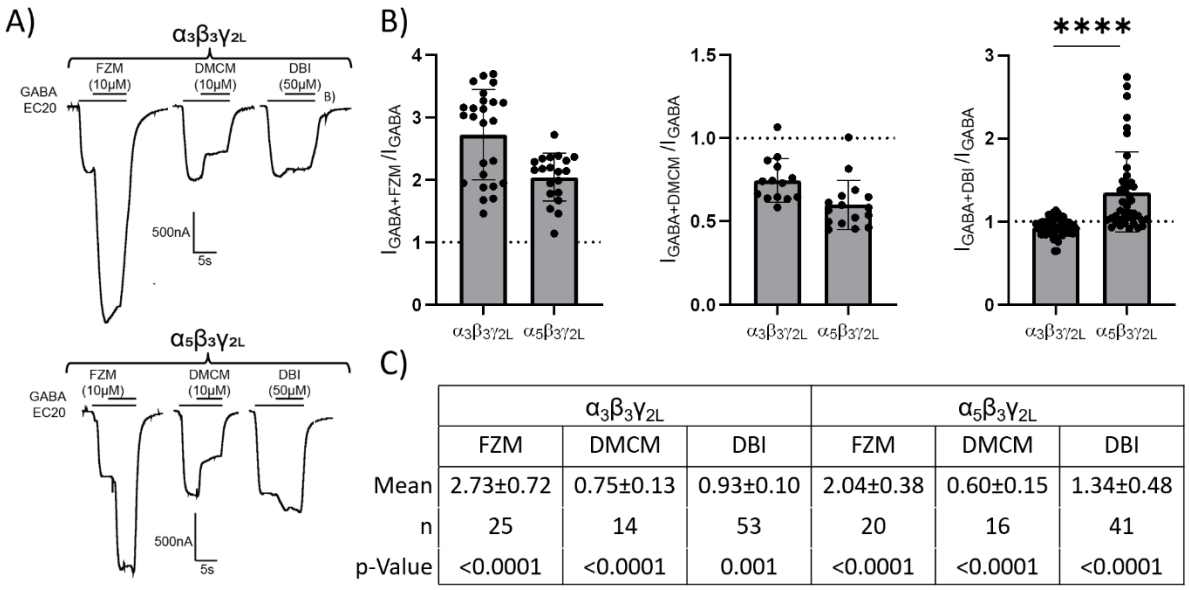

	$\alpha_3\beta_3\gamma_{2L}$			$\alpha_5\beta_3\gamma_{2L}$		
	FZM	DMCM	DBI	FZM	DMCM	DBI
Mean	2.73±0.72	0.75±0.13	0.93±0.10	2.04±0.38	0.60±0.15	1.34±0.48
n	25	14	53	20	16	41
p-Value	<0.0001	<0.0001	0.001	<0.0001	<0.0001	<0.0001

Figure 3.3 – DBI modulates $\alpha_3\beta_3\gamma_{2L}$ differently than $\alpha_5\beta_3\gamma_{2L}$. Sample two-electrode voltage clamp current traces (A) from oocytes injected with $\alpha_3\beta_3\gamma_{2L}$ (top) and $\alpha_5\beta_3\gamma_{2L}$ (bottom) show that co-application of FZM with GABA EC20 increases current as a PAM and co-application of DMCM decreases current as a NAM, while co-application of DBI weakly negatively modulates $\alpha_3\beta_3\gamma_{2L}$ and moderately positively modulates $\alpha_5\beta_3\gamma_{2L}$. The effects of FZM, DMCM and DBI are plotted in B, showing $I_{Drug+GABA}$ normalized to paired I_{GABA}. Data are shown as individual points over bar graphs of mean with SD error bars. A Kruskal-Wallis test with Dunn's multiple comparisons comparing the effects of each drug between $\alpha_3\beta_3\gamma_{2L}$ and $\alpha_5\beta_3\gamma_{2L}$ shows the effect of DBI is significantly different between subunit types, while the effects of FZM and DMCM were not. Panel C is a table of mean normalized current effects for FZM, DMCM and DBI for both receptor combinations and lists total n for each condition and the p-value of paired t-tests comparing I_{Drug} to I_{GABA}, demonstrating co-application of each drug has a significantly different effect than GABA alone.

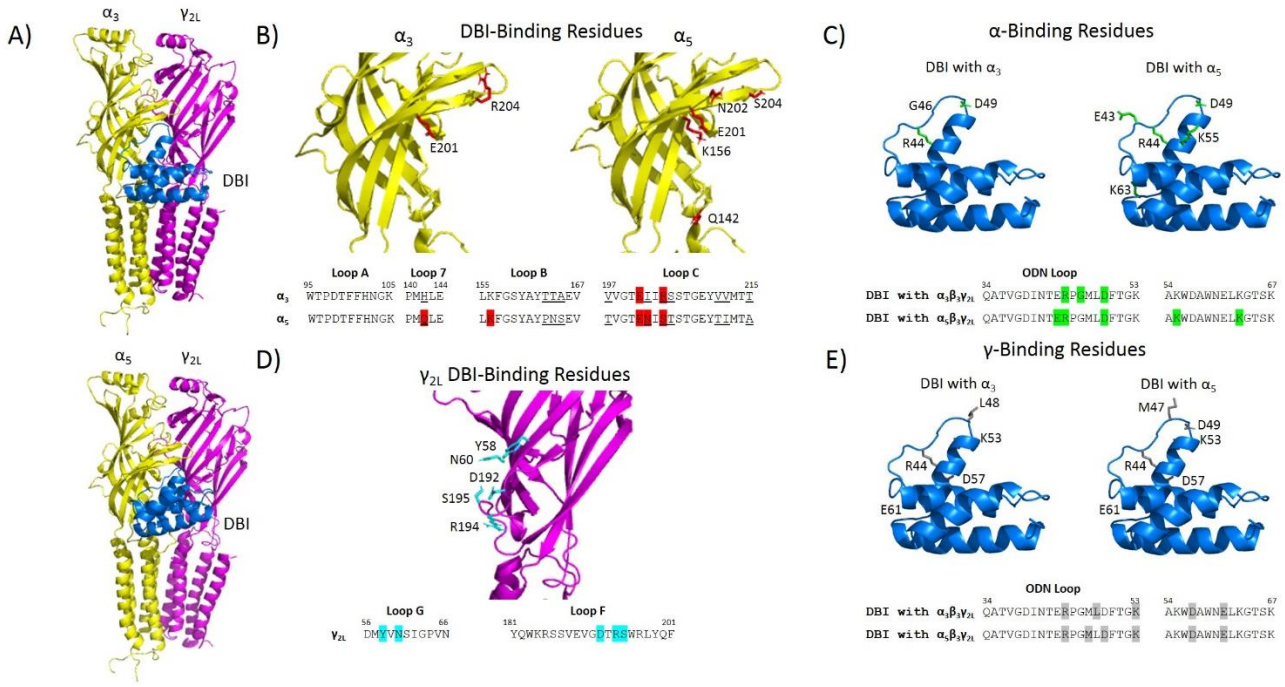

Figure 3.4 – Protein-protein docking of DBI with $\alpha_3\beta_3\gamma_{2L}$ and $\alpha_5\beta_3\gamma_{2L}$ GABARs. $\alpha_3\beta_3\gamma_{2L}$ and $\alpha_5\beta_3\gamma_{2L}$ homology models based on the alprazolam-bound $\alpha_1\beta_3\gamma_{2L}$ cryoEM (6HUO) with alprazolam removed. These structures were docked with the DBI crystal structure (2FJ9) using the ClusPro web server. Clusters where the ODN-loop of DBI interacts with the BZD-binding site of each receptor were compared, with relevant structures shown. A) Full side-view crystal structures of $\alpha_3\beta_3\gamma_{2L}$ (top) and $\alpha_5\beta_3\gamma_{2L}$ (bottom) with sample DBI docking. B) Alpha subunit ECDs with DBI-hydrogen bonding residues highlighted in red. Sequence alignments shown below, with hydrogen-bonding residues highlighted in red and nonhomologous residues underlined. The α5 subunits form more hydrogen bonds. C) DBI structure with alpha-subunit hydrogen bonding residues highlighted in green. Sequence shown below. D) Gamma subunit ECD and sequence with DBI-binding residues shown in blue. The gamma subunit residues which interacted with DBI were the same for both subunit combinations. E) DBI structures and sequences with gamma hydrogen-bonding residues highlighted in grey. DBI has more hydrogen bonds with the gamma subunit of α5-containging GABARs. Homology modeling and protein-protein docking performed by Dr. Ken Satyshur.

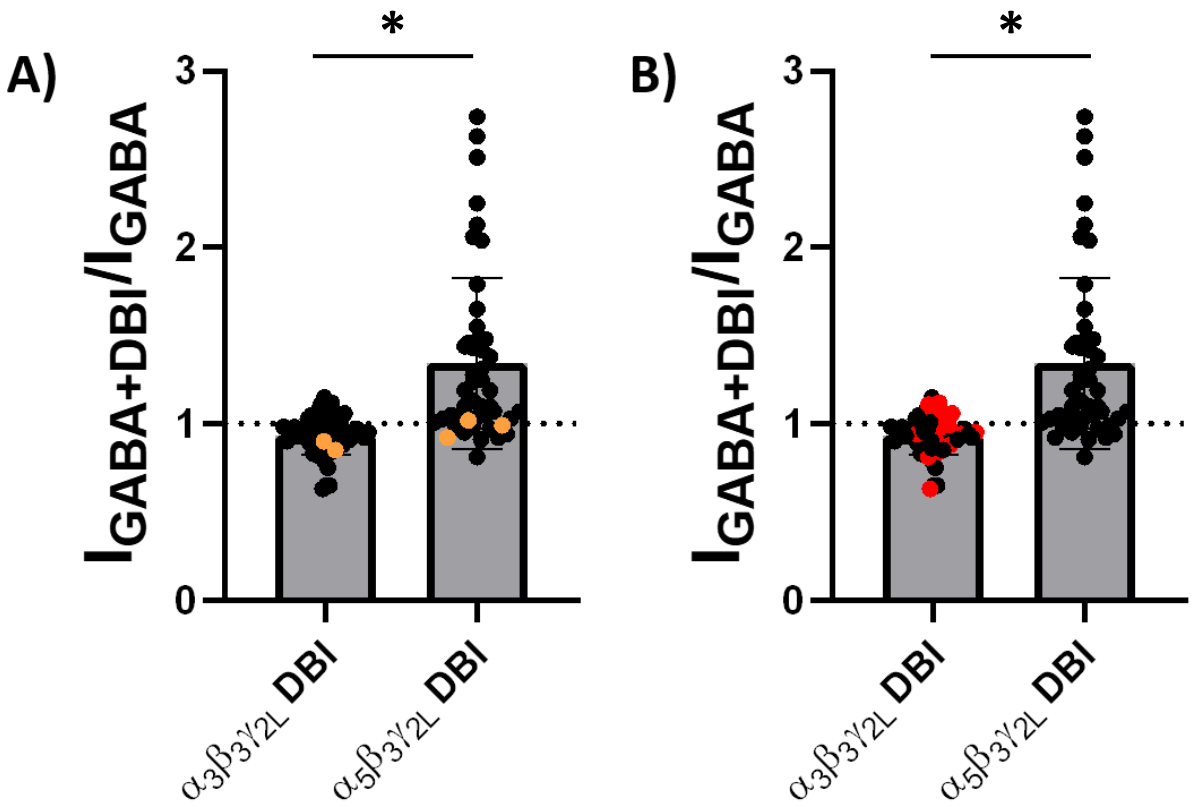

Supplemental Figure 3.1 – Neither the removal of histidine tag nor incubation with palmitoyl-coA affects DBI modulation. The effects of DBI are plotted for $\alpha_3\beta_3\gamma_{2L}$ and $\alpha_5\beta_3\gamma_{2L}$, showing $I_{Drug+GABA}$ normalized to paired I_{GABA}. Data are shown as individual points over bar graphs of mean with SD error bars. A Kruskal-Wallis test comparing the effects of each drug between $\alpha_3\beta_3\gamma_{2L}$ and $\alpha_5\beta_3\gamma_{2L}$ shows the effect of DBI is significantly different between subunit types. Data from DBI with a cleaved histidine tag are highlighted in orange in panel A. Data from DBI incubated with palmitoyl-CoA are highlighted in red in panel B. Highlighted data were compared to the rest of the data using a student's t-test. His-tag cleavage and co-incubation with palmitoyl-CoA did not significantly alter the effects of DBI (α3 His-tag cleavage p=0.45 n=2, α5 His-tag cleavage p=0.18 n=3, α3 palmitoyl-CoA p=0.24, n=18).

Chapter IV:

DBI effects on $\alpha_5\beta_3\gamma_{2L}$ GABAR currents do not mimic BZD actions

Introduction

Benzodiazepines (BZDs) are widely prescribed drugs that target the GABA-A receptor (GABAR). These drugs have a variety of therapeutic effects including antiepileptic, somnogenic, and anxiogenic actions (Sigel and Ernst, 2018). BZDs exert these actions by binding to the GABAR, the main inhibitory receptor in the brain. GABARs are pentameric ligand-gated channels. The majority of GABARs are comprised of two α subunits, two β subunits and one γ subunit. BZDs bind in a pocket located in the GABAR extracellular domain at the interface of α and γ subunits. BZD binding modulates GABA-mediated channel gating.

BZDs that are positive allosteric modulators (PAMs, e.g. diazepam or flurazepam (FZM)) increase the amount of current elicited by a non-saturating concentration of GABA, while negative allosteric modulators (NAMs) like methyl-6,7-dimethoxy-4-ethyl-beta-carboline-3-carboxylate (DMCM) decrease the amount of current elicited by GABA. BZD PAMs increase peak current responses for low concentrations of GABA and slow the rate of current deactivation, with little effect on the rate of current activation (Goldschen-Ohm et al., 2014).

The diazepam binding inhibitor (DBI) was identified in 1983 based on its ability to displace [^{3}H]-diazepam from binding GABARs (Guidotti et al., 1983). While this 11kD protein is significantly larger than a BZD, based on its ability to displace BZDs and research showing that mutating the BZD site or using flumazenil (FLZ), a BZD-site antagonist (Christian et al., 2013) alters DBI's effects on the GABAR, it is widely assumed that DBI binds to the BZD binding site on the GABAR. In Chapter III of this thesis, I used GABAR expression in *Xenopus laevis* oocytes and two-electrode voltage clamping and demonstrated that DBI acts as a PAM for α5-

containing receptors and a weak NAM for GABARs containing α3 subunits. Since DBI is believed to bind to the BZD site, I hypothesized that DBI's effects on GABAR macroscopic current responses would be similar to BZD effects.

In this thesis chapter, I expressed $\alpha_5\beta_3\gamma_{2L}$ receptors in HEK-293T cells and pulled outside-out patches to compare the effects of FZM and purified DBI on GABA-mediated current activation, deactivation, and GABA peak current amplitude. I used rapid application flow pipettes (<1ms solution exchange times) and evaluated if DBI modulates the kinetics of GABAR macroscopic currents in the same manner as a BZD PAM. FZM, as expected, significantly slowed the rate of current deactivation, and did not alter 10-90% rise time (activation) or peak current amplitude in response to a high concentration of GABA (EC_{80}). Surprisingly, at high GABA concentrations, application of DBI did not have a significant effect on any of these macroscopic current properties. These data demonstrate that DBI is not functioning like a BZD positive modulator under these experimental conditions (i.e. GABAR expression in HEK293 cells, outside-outside patch clamp recording, high GABA concentration, lower DBI concentration). At first glance, my data in HEK293 cells are not consistent with data in Chapter III where I showed that DBI potentiated $\alpha_5\beta_3\gamma_{2L}$ GABAR currents elicited by a low concentration of GABA. Using a kinetic model, I identified a potential mechanism that may explain why my patch-clamp data in this chapter and the two-electrode voltage clamp data from Chapter III differ.

Methods

HEK cell culture and DNA transfection

Human embryonic kidney (HEK 293T-17) cells were cultured in Eagle's minimum essential medium with Earle's salt (Mediatech, Manassas, VA). Media was supplemented with 10% fetal bovine serum (Atlanta Biologics, Flowery Branch, GA), penicillin-streptomyacin-glutamine (100U/mL penicillin, 100μg/mL streptomycin, Sigma-Aldrich, St. Louis, MO), and

plasmocin 50µg/mL (InvivoGen, San Diego, CA). Cells were grown at 37°C with 5% CO_2, and plated on 12mm circular glass coverslips in 60mM dishes 48-72 hour before transfection.

Cells were transfected using lipofectamine 2000 (Invitrogen, Carlsbad, CA) at 85-90% confluency. 0.5-2µg of pUNIV GABAR DNA was used, with a 1:1:3-5 ratio of α5:β3:γ2L subunits, and 2-10ng of pUNIV GFP DNA. Cells were used for recording 24-60 hours post transfection.

DBI Purification

DBI was grown and purified as described in Chapter II of this thesis. In brief, BL21 DE3 chemically competent *E. coli* cells were transformed with histidine-tagged DBI cDNA in a pET28a vector. Single colonies were grown in 500mL LB-Kan media at 37°C until OD_{600}=0.6-0.8. Cells were spun at 10,000xg for 10min at 4°C. Pellet was resuspended in Buffer A (sodium phosphate, 50mM, pH 7.4; NaCl, 300mM) with 25mM imidazole (IDA) and protease inhibitors pepstatin, aprotinin and leupeptin. Cells were lysed using an EmuIsiflex (ATA Scientific, Taren Point, NSW Australia) and homogenate was spun at 16,800xg for 20min at 4°C. DBI was bound to a Ni-NTA flowthrough column (Qiagen, Hilden, Germany), washed, and eluted using Buffer A and 250mM IDA. PD10 columns (Sigma-Aldrich, St. Louis, MO) were used to remove IDA, and eluted DBI in Buffer A. Purity and yield were evaluated via SDS-PAGE and Nanodrop (Thermo Fisher Scientific, Waltham, MA).

Patch-clamp solutions and drugs

Recording pipettes were pulled from borosilicate glass using a Flaming-Brown P-1000 mulitstage micropipette puller (Sutter Instruments, Novato, CA). Pipette tips were fire-polished with a Narishige MF-83 microforge (Narishige, Tokyo, Japan) until open tip resistance was between 2-9 MΩ. Electrodes were filled with intracellular solution (140mM KCl, 10mM EGTA, 2mM MgATP, 10mM phosphocreatine, 10mM HEPES, pH 7.3-7.4).

HEPES normal Ringer (HNR) perfusion solution contained 145mM NaCl, 2.5mM KCl, 1mM $MgCl_2$, 1mM $CaCl_2$, and 10mM HEPES, pH 7.3-7.4, 300-310 mOsm. 1M stocks of GABA

and 10mM stocks of flurazepam (FZM) were prepared in water and frozen at -20°C. Fresh drug solutions were prepared daily in HNR and diluted to 10-50µM GABA in the presence and absence of 10µM FZM and 10-50µM DBI. 1mM, 100, 30, 10, 7, 3 and 1 µM GABA solutions were prepared for dose-response curves. Equivalent volumes of Buffer A were added to FZM and GABA solutions to ensure isosmolarity. Recordings were performed at room temperature.

Application Pipette Assembly and Function

Theta-barreled glass (thin walled, filamented glass capillary, outer-diameter (OD) 1.5mm, inner diameter (ID) 1.2mm) was pulled until tip openings were approximately 100µm between the centers of both channels. Glass was cut to 2-3 cm in length and the larger end was fire-polished. 10cm lengths of polyimide tubing (0.24mm OD, 0.2mm ID, Cole-Parmer, Vernon Hills, IL) were inserted into both channels of the theta barrel and pushed up to the tip. The free ends of polyimide tubing were threaded into 30cm lengths of 28-gauge polytetrafluoroethylene (PTFE) tubing. PTFE tubing was pushed flush to the end of the theta-barreled glass. 2-3cm lengths of fused silica tubing (170µm OD, 110µm ID, Trajan Scientific, Victoria, Australia) were inserted into theta barrels to sit 0.5cm behind the openings of polyimide tubing to serve as drains for dead space within glass barrels and to increase liquid exchange time. Glass and tubing were sealed together at interface with PTFE/fluorinated ethylene propylene (FEP) dual shrink tubing (Cole-Parmer, Vernon Hills, IL), and tested for leaking at the end of glass or between channels of glass. Gripper fittings were attached to the ends of PTFE tubing.

Glass slides were prepared with Sylgard 184 (Dow Corning, Midland, MI) material as a border to create approximately 5mL wells. The assembled application pipette was glued to a glass slide with the theta perpendicular to the bottom of the plate. Pipette was secured with quick drying epoxy and left to cure overnight.

The theta application pipette was installed on a piezoelectric biomorph (Physik Instrumente, Costa Mesa, CA) and connected to 6-way Rheodyne low pressure valves (IDEX Health and Science, Rohnert Park, CA). Valves were connected to tubes containing HNR and

drug solution via 26-gauge PTFE tubing. The biomorph is moved to position the application barrel in front of the cell by WinPos (ITK Dr. Kassen GmbH, Hahnau, Germany), with <1msec 10-90% solution exchange times, measured via liquid junction potential tests of open recording pipette tips after experiments. Valve switches took <30sec to fully exchange from low to high concentration and 1min to exchange from high to low concentrations (100% HNR to 10% HNR).

4-barrel application pipettes were also constructed using 4-Square Bore borosilicate glass (VitroCom, Mountain Lakes, NJ), approximately 1mm internal square width, 6mm outer width of all four squares. Glass was heated, pulled, and cut so that tip openings were approximately 200µm from the center of one opening to the next, and cut to be 2-3cm in length. Polyimide tubing threaded into 28-gauge PTFE was inserted into all four barrels, with polyimide extended further into the barrels than PTFE tubing. The barrel/tubing interface was sealed using Norland Optical Adhesive 73 (Norland Products, Cranbury, NJ). Glue was cured using >20min exposure to UV light. After testing seals between each barrel, the 4-barrel application pipette was glued to a glass slide. Borders for glass slides were cut from polycarbonate and adhered to the slide using silicone grease. The fully assembled 4-barrel application pipette was installed in piezoelectric biomorph and connected directly to tubes containing HNR and drug solutions, omitting the need for valves.

Outside-out patch clamp recording

Recording pipettes were sealed onto the membrane of GFP-positive HEK cells to obtain a giga-seal with -5 to -10mmHg pressure. Once a high resistance seal was formed, increased negative pressure was used to break into the cell. The pipette was then immediately withdrawn from the cell, enabling the patch to reseal in an outside-out conformation with the extracellular side of the membrane facing out. Patches were held at -40mV. Currents were low-pass-filtered at 2 kHz with an eight-pole Bessel filter. Data was collected at 20kHz via an Axopatch 200B amplifier (Axon Instruments, Sunnyvale, CA) interfaced to a computer using a Digidata 1440A (Axon Instruments, Sunnyvale, CA). Amplifier function was controlled by Clampex (version

10.4.1.10; Molecular Devices, Sunnyvale, CA) and analyzed using Clampfit (version 10.4.1.10; Molecular Devices, Sunnyvale, CA). Patches were exposed to 100ms pulses of 10-50µM GABA with and without 10µM FZM and 10-50µM DBI, with 10-20sec of HNR wash between pulses to minimize accumulation of desensitization.

Data Analysis

Averaged traces using 3-15 sweeps were generated in Clampfit and used to measure 10-90% rise time of activation and calculate the rate of deactivation via a weighted tau (τ_w). τ_w was calculated by fitting the current decline after GABA removal until a return to baseline with a bi-exponential equation ($I = A_1*e^{-t/\tau1} + A_2*e^{-t/\tau2}$), where I is current, t is time, A_1 and A_2 are the relative amplitudes for the fast and slow components respectively, and τ_1 and τ_2 are the time constants for the fast and slow components. See Figure 4.4 for sample curve fits. These values are used to calculate τ_w where $\tau_w = (A_1\tau_1+A_2\tau_2)/(A_1+A_2)$. Normalized τ_w values were calculated as $\tau_{w(GABA+Drug)}/\tau_{w(GABA)}$. Normalized 10-90% rise times were calculated as $RiseTime_{(GABA+Drug)}/RiseTime_{(GABA)}$. Significance was evaluated using a paired-test for GABA and GABA+drug values within the same patch, and using a one-sample t-test of normalized data comparing to a hypothetical null value of 1. Data were analyzed and displayed using GraphPad Prism (version 9.1.2, GraphPad Software Inc, San Diego, CA).

Peak current responses from outside-out patches often decreased over the course of the experiment (Amico et al., 1998; Gyenes et al., 1994). In order to accurately assess drug-induced changes in amplitude, run-down was taken into account. Peak amplitude for every sweep of GABA was plotted over time and fit with a one-phase exponential decay, where $PeakCurrent = (PeakCurrent_0-Plateau)*e^{-Kt}$. $PeakCurrent_0$ is the current at t=0, Plateau is PeakCurrent at t=∞, K = rate constant of decay (s^{-1}), and t is time. Current amplitudes of GABA and GABA+Drug traces were divided by the decay-predicted amplitude to generate current values corrected for run-down, described as fold increase in amplitude. These values were

averaged for all initial GABA and all GABA+Drug sweeps in a single patch. Data were analyzed as paired data and compared to a hypothetical null value of 1.

GABA concentration-response traces were fit using Prism software to the equation, $I = Imax/[1 + (EC50/[A]^{nH})]$, in which I is the peak response to a given drug concentration, Imax is the maximal amplitude of current, EC50 is the drug concentration that produces the half-maximal response, [A] is drug concentration, and nH is the Hill coefficient.

Kinetic Modeling

GABA-elicited currents from $\alpha_5\beta_3\gamma_{2L}$ GABARs were simulated in Kinetic Model Builder 2.0 (Goldschen-Ohm et al., 2014) in Monte Carlo mode. Currents were simulated for 500ms pulses of 1mM, 100μM, 30μM, 10μM, 3μM, and 1μM GABA, and adjusted to simulate to the experimental dose-response GABA by altering binary element rate constants and interactions between elements. 2s pulses of 5μM and 50μM GABA were also simulated in the presence and absence of 10μM DBI. This model describes the two agonist bindings sites (A1 and A2), two intermediate elements (F1 and F2), fast and slow desensitization gates (Df and Ds, respectively), a benzodiazepine binding site (D), and the channel gate (m) as binary elements. These binary elements can transition between two metastable configurations, like open or closed for the channel gate, or bound or unbound for a drug binding site. The transitions between these states are governed by intrinsic rate constants for the forward and reverse reactions. Interactions between elements can contribute energy towards the transition to an alternate energy state. For this model, rate constants for each element were α_A = [GABA]*1.2*10^{-6} $M^{-1}s^{-1}$, β_A = 500 $M^{-1}s^{-1}$, α_F = 5.5 $M^{-1}s^{-1}$, β_F = 1124 $M^{-1}s^{-1}$, α_{df} = 0.25 $M^{-1}s^{-1}$, β_{df} = 31 $M^{-1}s^{-1}$, α_{ds} = 0.0033 $M^{-1}s^{-1}$, β_{ds} = 0.19 $M^{-1}s^{-1}$, α_D = [BZD]*10^8 $M^{-1}s^{-1}$, β_D = 0.3 $M^{-1}s^{-1}$, is α_m = 380*(-0.5e) s^{-1}, β_m = 380 s^{-1}. Interactions between elements (kcal/mol at 298K) are ΔG_{AF} = -5, ΔG_{Fm} = -3.8, ΔG_{Fdf} = -0.8, ΔG_{Fds} = -1.7, and ΔG_{DA2} = -0.3.

Results

I expressed $\alpha_5\beta_3\gamma_{2L}$ GABARs in HEK cells and used outside-out patch clamping and ultra-fast solution exchange to compare the effects of DBI and FZM on GABA-elicited currents. I examined the effects of FZM and DBI on GABA-mediated current activation, deactivation, and current amplitude. Initially, I measured peak current responses to 1mM, 100, 30, 10, 7, 3 and 1 µM GABA (Figure 4.1) and fit the data as described in Methods to determine the GABA EC50 for $\alpha_5\beta_3\gamma_{2L}$ GABARs. The GABA EC_{50} value was13µM which is similar to published values (Burkat et al., 2014; Neelands and Macdonald, 1999).

To evaluate and compare the effects of the positive BZD modulator, FZM, and DBI, I applied 3-10 applications (150ms) of 50µM GABA (approximately EC80) and then applied 3-10 applications of wash or 50µM GABA solutions containing 10µM FZM or 10-50µM DBI. When recording from outside-out patches, it is common for the currents to rundown over time (Amico et al., 1998; Gyenes et al., 1994) and one observes smaller current responses to the same GABA concentration. In order to accurately assess the effects of FZM and DBI on GABA-elicited current amplitudes, I corrected the amplitudes to account for rundown as described in Methods. (Figure 4.2). Neither FZM nor DBI had any significant effects on GABA peak current amplitudes. DBI data, however, had a larger variability than FZM (Figure 4.2C, D). Recorded peak currents and rundown adjusted current amplitudes for every patch are included in Supplemental Figure 4.1 for DBI and Supplemental Figure 4.2 for FZM. The data were analyzed using a paired t-test between mean GABA and GABA+Drug corrected amplitudes (Figure 4.2C), as well as comparing the mean GABA+Drug corrected amplitudes to a hypothetical null value of 1 (Figure 4.2D).

Data for the effects of DBI on $\alpha_5\beta_3\gamma_{2L}$ GABA-elicited peak currents were more variable than a BZD (coefficient of variation for FZM 6.8%, DBI $\alpha_5\beta_3\gamma_{2L}$ effects 33.1%). This may be due to either the fact that the structure of the DBI protein is more flexible than the BZD chemical. Alternatively, DBI may bind a more flexible region of the GABAR than the BZD binding site.

Increased motility of either DBI or the GABAR could cause more variability in the effects of the DBI/GABAR interaction.

To compare activation rates, I measured the 10-90% rise time of currents elicited by 50μM GABA and compared them to currents elicited by 50μM GABA+Drug. Sample normalized current traces are shown in Figure 4.4A&B. Neither DBI nor FZM altered 10-90% GABA current rise times (Figures 4.3C, D).

The strongest effect of FZM on currents elicited by 50μM GABA, which is approximately EC_{80}, was on the rate of deactivation. I calculated weighted taus (τ_w) to assess current deactivation. FZM significantly slowed deactivation ($\tau_{w(GABA+FZM)}/\tau_{w(GABA)}$=1.50±0.37, p=0.005, n=8), but DBI had no effect (p=0.57, n=14) (Figure 4.4). When comparing normalized τ_w values for DBI and FZM to a hypothetical null value of 1 (Figure 4.4D), the effects of FZM also showed a significant increase in τ_w (one sample t-test p=0.007, n=8), while DBI had no effect (p=0.65, n=14).

Table 4.1 contains mean values (±SD) for DBI and FZM's effects on GABA current peak amplitudes, current rise times, and current deactivation rates. A summary table of the fold increase in amplitude, normalized deactivation, activation, starting amplitude and percent noise/amplitude can be found in Supplemental Table 4.1 which shows that none of the results were dependent on channel expression, signal to noise ratio, or application pipette type.

With the help of Dr. Robert Pearce, I used an elements-based kinetic model to simulate $\alpha_5\beta_3\gamma_{2L}$ current responses and to model the effects of DBI on different interactions within the model. We adjusted the binary element rate constants and the energetics of each interaction to simulate experimental current responses to 500ms pulses of 1mM, 100μM, 30μM, 10μM, 3μM, and 1μM GABA which I recorded using outside-out patches from $\alpha_5\beta_3\gamma_{2L}$ receptors (Figure 4.5). Using this model, I then introduced a DBI-binding element with a weak (ΔG=-0.3) interaction with one of the GABA binding sites, and simulated current responses to 5μM GABA

(approximately EC20) and 50μM GABA (approximately EC80) in the presence and absence of 10μM DBI. I used a longer simulated GABA exposure time of 2s to reflect the longer application times used in two-electrode voltage clamping. This energetically stabilizing ΔG=-0.3 interaction between the DBI and GABA bound states elicited simulated traces with a small increase in amplitude at EC20 GABA ($I_{GABA+DBI}/I_{GABA}$=1.34±0.48), but no change in amplitude or deactivation rates at EC80 GABA (Figure 4.6). I also assessed the effects of DBI interacting with each of the other elements: the F-element (Supplemental Figure 4.3), main gate (Supplemental Figure 4.4), and the fast and slow desensitization gates (Supplemental Figures 4.5 and 4.6, respectively). None of these interactions accurately simulated my experimental data.

Discussion

The effects of BZD PAMs on macroscopic GABAR kinetics have been well-documented. At high concentrations of GABA, BZDs have been shown to slow the rate of GABA-induced current deactivation (Goldschen-Ohm et al., 2014; Jones and Westbrook, 1995; Tsao, 2018). Other groups have suggested that PAM BZDs stabilize a pre-activated, intermediate flip state (Gielen et al., 2012), while others have used single-channel patch clamp electrophysiology to show that BZDs increases channel open-time, and decreases the rate of channel closing (Li et al., 2013). In this chapter, as expected, I showed that FZM slowed rate of GABA current activation elicited 50μM GABA, which is approximately EC_{80} for $\alpha_5\beta_3\gamma_{2L}$ receptors and had no effect on GABA current peak amplitude or GABA current application as measured from 10-90% rise times.

Unexpectedly, DBI did not alter any of the macroscopic kinetic metrics that I evaluated. Previous research has shown that DBI can alter GABA-mediated currents in the brain, though most of these experiments either rely on up- and down-regulating endogenous DBI, or apply synthesized ODN, a DBI cleavage product (Alfonso et al., 2012; Christian et al., 2013; Dumitru

et al., 2017). My data suggest that mechanism underlying DBI effects in the brain are not similar to how BZD PAMs work since DBI had no effect on GABA current deactivation.

Supplemental Figure 4.7 breaks down the outside-out patch data by the type of application pipette used. DBI's effects on current deactivation were not significant when analyzing data obtained using the 4-barrel application pipette or when combining all the data. However, DBI significantly slowed deactivation when data collected using a theta application pipette were analyzed ($p=0.02$, $n=5$). No other parameter for DBI was altered when the data were separated based on application pipette type, which argues that all the data should be combined for analysis. It is not apparent why effects of DBI on deactivation would be different depending on the application pipet. In addition, due to the small number of patches using the theta application pipette ($n=5$) one must be careful not to over-interpret the statistical significance, especially given FZM did not have a statistically significant effect on deactivation when analyzing so few samples ($p=0.051$, $n=5$).

It was somewhat surprising to see no significant effects of DBI using outside-out patch ultra-rapid GABA application experiments when, in Chapter III of this thesis, I showed that DBI acted as a modest positive modulator of GABA-elicited amplitude for $\alpha_5\beta_3\gamma_{2L}$ GABARs expressed in *Xenopus* oocytes using two-electrode voltage clamping (TEVC). Using TEVC, I measured I_{Drug}/I_{GABA} to be 1.3±0.48 ($n=47$) for 50μM DBI and 2.10±0.36 ($n=25$) for 10μM FZM. Additionally, the TEVC data were collected using a low GABA EC_{20} concentration, versus the high EC_{80} GABA concentration that was used in my outside-out patch experiments. I used an elements-based kinetic model (Goldschen-Ohm et al., 2014) to test if changing various interactions in the model, I could model moderate increases in amplitude at low GABA concentrations in the presence of DBI, but no effect on amplitude or deactivation rates at higher GABA concentrations. I found that introducing a weakly stabilizing interaction between DBI and GABA binding was able to increase GABA-elicited amplitude at low concentrations of GABA,

but not at high concentrations, and did not alter the rate of deactivation, similar to what I found experimentally.

If DBI exerts its effects on $\alpha_5\beta_3\gamma_{2L}$ receptors by weakly stabilizing a GABA-bound state, it is unlikely to have much effect on synaptic GABARs. At the synapse, GABA is released from vesicles at high, millimolar concentrations (Mody et al., 1994). However, $\alpha_5\beta_3\gamma_{2L}$ receptors can also be found extrasynaptically (Brickley and Mody, 2012), where they are exposed to only micromolar ambient levels of GABA (Farrant and Nusser, 2005). This proposed mild stabilizing effect of DBI on GABA binding may have a greater effect on extrasynaptic GABARs.

If DBI is weakly stabilizing a GABA-bound state, this phenotype would be very difficult to detect using the high concentration of GABA that was used in my outside-out patch experiments. Moreover, due to the run-down commonly associated with outside-out patch recording, it makes it challenging to reliably record smaller currents elicited by lower concentrations of GABA. In order to use patch clamp to test the effects of DBI on lower concentrations of GABA, whole-cell recordings which have both larger currents and lower noise to amplitude ratios should be used in the future.

It should also be noted that the TEVC experiments were performed using 50μM DBI, while the outside-out patch experiments were performed using 10-50μM DBI. Initial statistical tests showed no functional difference between the effects of 10 and 50μM DBI (data not shown, n=7). However, DBI dose-response experiments should be performed to evaluate whether the effects of DBI vary between 10 and 50μM.

Even though DBI and FZM both potentiate GABA-elicited currents when using low concentrations of GABA, my patch-clamp experiments demonstrate that DBI and FZM do not modulate GABAR function via the same mechanism. FZM, a BZD PAM, slows the rate of GABA-elicited deactivation, while DBI does not. Uncovering the mechanism by which DBI elicits

its effects on GABARs may open new clinical avenues for novel pharmaceutical modulation of GABARs.

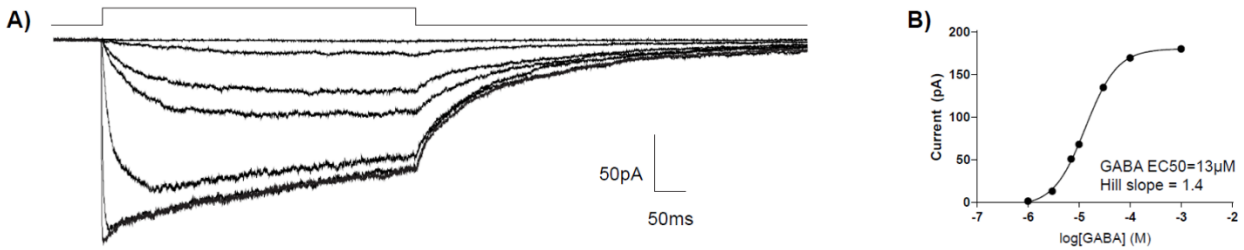

Figure 4.1 – Sample GABA dose-response traces and dose response curve for $\alpha_5\beta_3\gamma_{2L}$ receptors from outside-out patches. A) Overlayed outside-out current responses of $\alpha_5\beta_3\gamma_{2L}$ receptors to 500ms applications of 1mM, 100, 30, 10, 7, 3 and 1 μM GABA. Bar above traces indicates duration of GABA application. B) Concentration-response curve fitted with I = Imax/[1 + (EC50/[A]^{nH})]. I = current, Imax = current elicited by saturating GABA, EC50 = GABA concentration eliciting half of the maximal response, [A] = GABA concentration, and nH = hill slope.

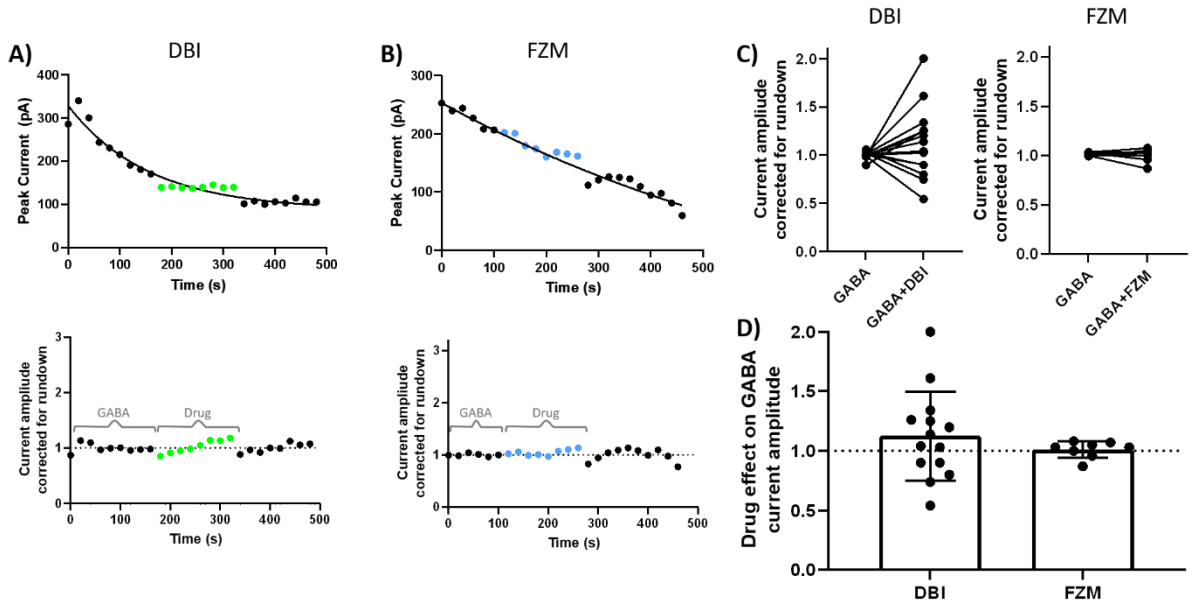

Figure 4.2 – DBI and FZM do not alter GABA-elicited amplitudes for $\alpha_5\beta_3\gamma_{2L}$ receptors. Top graphs showing sample peak current responses over time for GABA (black), GABA+DBI (A, green), and GABA+FZM (B, blue). GABA peak current responses are fit with a one-phase decay equation to monitor run-down of current where PeakCurrent = ($PeakCurrent_0$-Plateau)* e^{-Kt}. $PeakCurrent_0$ is the current at t=0, Plateau is PeakCurrent at t=∞, K = rate constant of decay (s^{-1}), and t is time. Bottom graphs plot fold increase in amplitude (raw amplitude/one-phase decay predicted amplitude) over time. Brackets indicate data averaged to a single data point for plots in C and D. C) Paired data averaging all initial GABA and all GABA+Drug fold increases in amplitude from the same patch. Paired t-tests show no significant effect of DBI (p=0.25, n=14) or FZM (p=0.86, n=8). D) Mean fold increase in amplitude for DBI and FZM was compared to a null hypothesis of one using a one sample t-test. Neither drug had a significant effect on amplitude (DBI p=0.23, FZM p=0.66). Error bars represent SD.

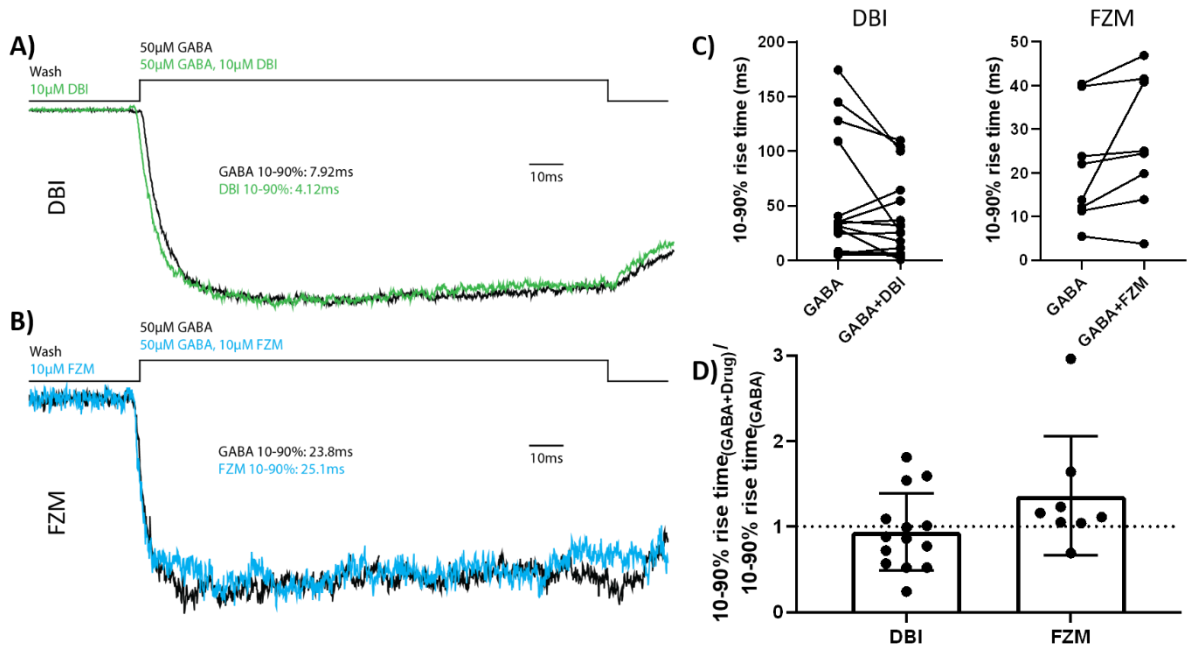

Figure 4.3 – DBI and FZM do not affect the 10-90% rise time of activation. Overlayed, averaged traces for GABA (black) and GABA + DBI (A, green), or FZM (B, blue). Bars above indicate duration of 150ms GABA application. Traces are normalized to peak amplitude. C) Paired 10-90% rise times for GABA and GABA+Drug. Neither drug significantly affected 10-90% rise time (paired t-test DBI p=0.09, n=14, FZM p=0.10, n=8). D) Normalized 10-90% rise times for DBI and FZM show that neither drug significantly affects activation when compared to a hypothetical null value of n=1 (DBI p=0.61, FZM p=0.19). Error bars represent SD.

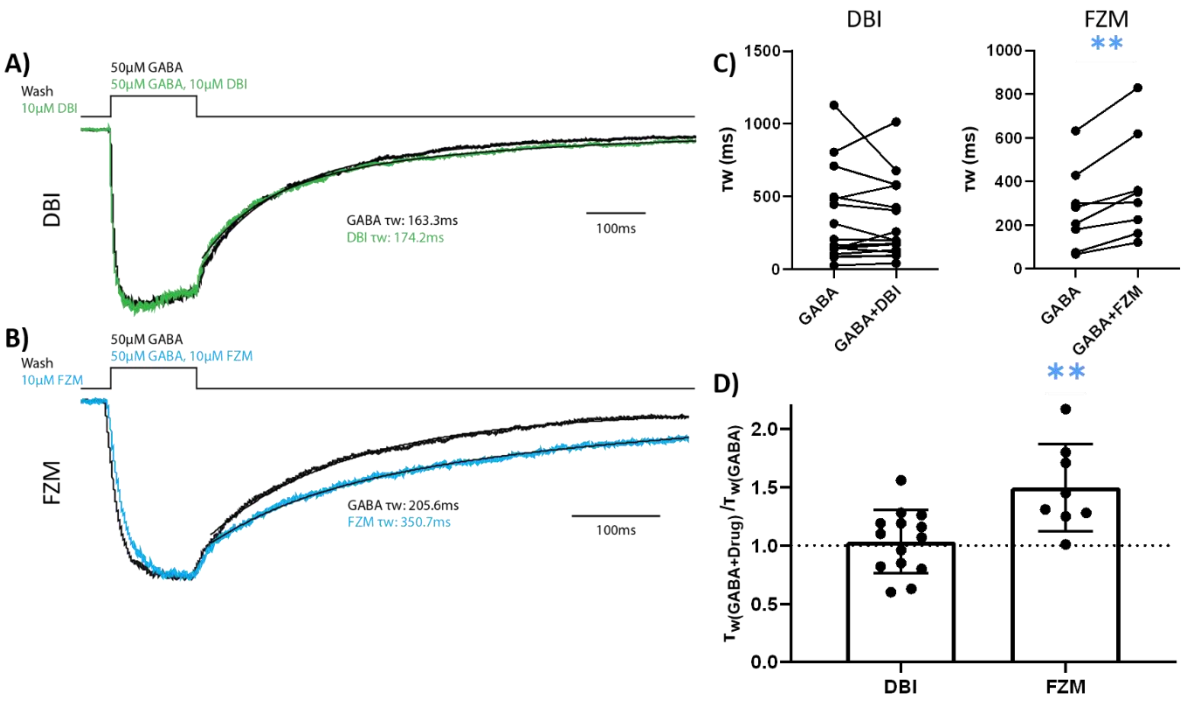

Figure 4.4 – FZM slows the rate of deactivation and increases τ_w, but DBI does not. Overlayed, averaged traces for GABA (black) and GABA + DBI (A, green), or FZM (B, blue). Bars above indicate duration of 150ms GABA application. Traces are normalized to peak amplitude. C) Paired τ_w values for GABA and GABA+Drug calculated by fitting the curve immediately after GABA is removed with the equation $I = A_1*e^{-t/\tau 1} + A_2*e^{-t/\tau 2}$, where I is current, t is time, A_1 and A_2 are the relative amplitudes for the fast and slow components respectively, and τ_1 and τ_2 are the time constants for the fast and slow components. $\tau_w = (A_1\tau_1+A_2\tau_2)/(A_1+A_2)$. FZM significantly slowed the rate of deactivation (paired t-test p=0.005, n=8) but DBI did not (p=0.57, n=14). D) Normalized τ_w values for DBI and FZM. FZM significantly increases the normalized τ_w (p=0.007), but DBI does not (p=0.65). Error bars represent SD.

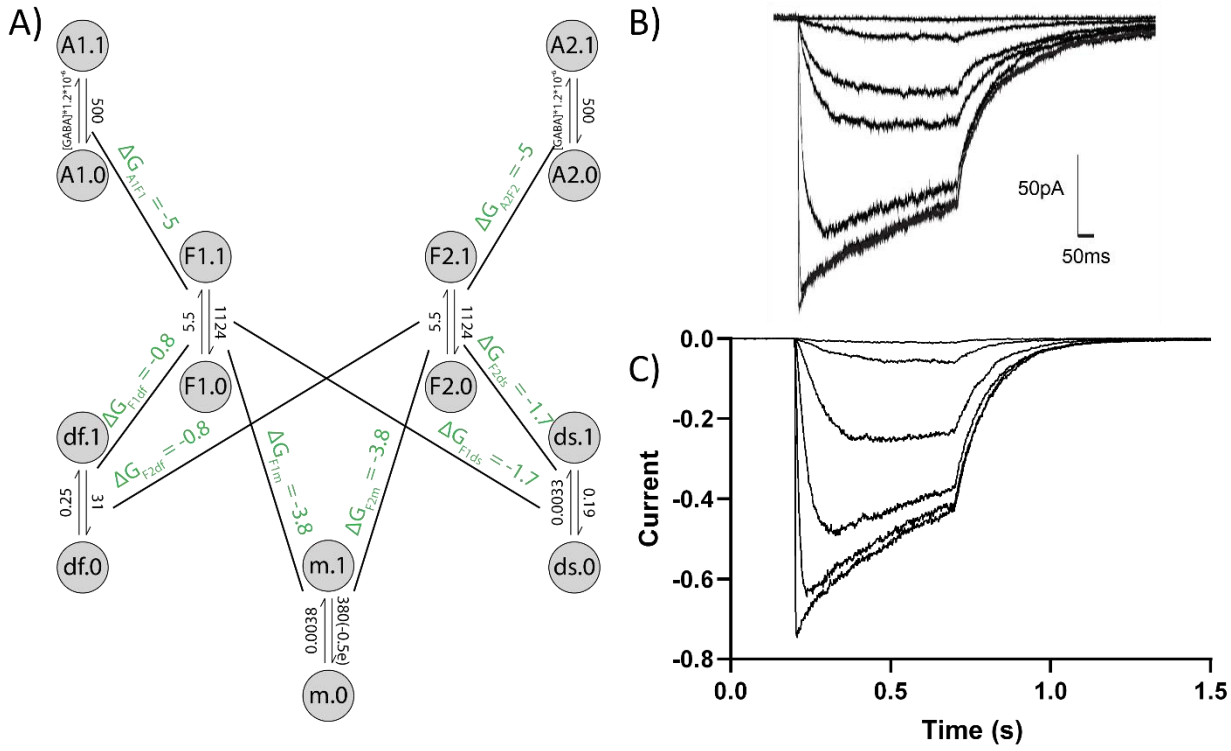

Figure 4.5 – Elements-based kinetic model of $\alpha_5\beta_3\gamma_{2L}$ receptor macroscopic kinetics. An elements model adapted for $\alpha_5\beta_3\gamma_{2L}$ receptors (A) was created to simulate GABA-elicited currents. ΔG values (kcal/mol at 298K) for interactions between elements are shown in green, and element rate constants ($M^{-1}s^{-1}$ for all but channel gate, m, s^{-1} for m) are shown between element states. A1 and A2 represent agonist binding sites, F1 and F2 are intermediate F elements, df is the fast desensitization gate, ds is the slow desensitization gate, and m is the main channel gate. Experimental electrophysiology data from Figure 4.1 (B) and simulated responses to 500ms pulses of 1mM, 100μM, 30μM, 10μM, 3μM, and 1μM GABA (C). Initial elements model was based on $\alpha_1\beta_2\gamma_{2L}$ receptors (Goldschen-Ohm et al., 2014) and adapted to $\alpha_5\beta_3\gamma_{2L}$ with the help of Dr. Robert Pearce.

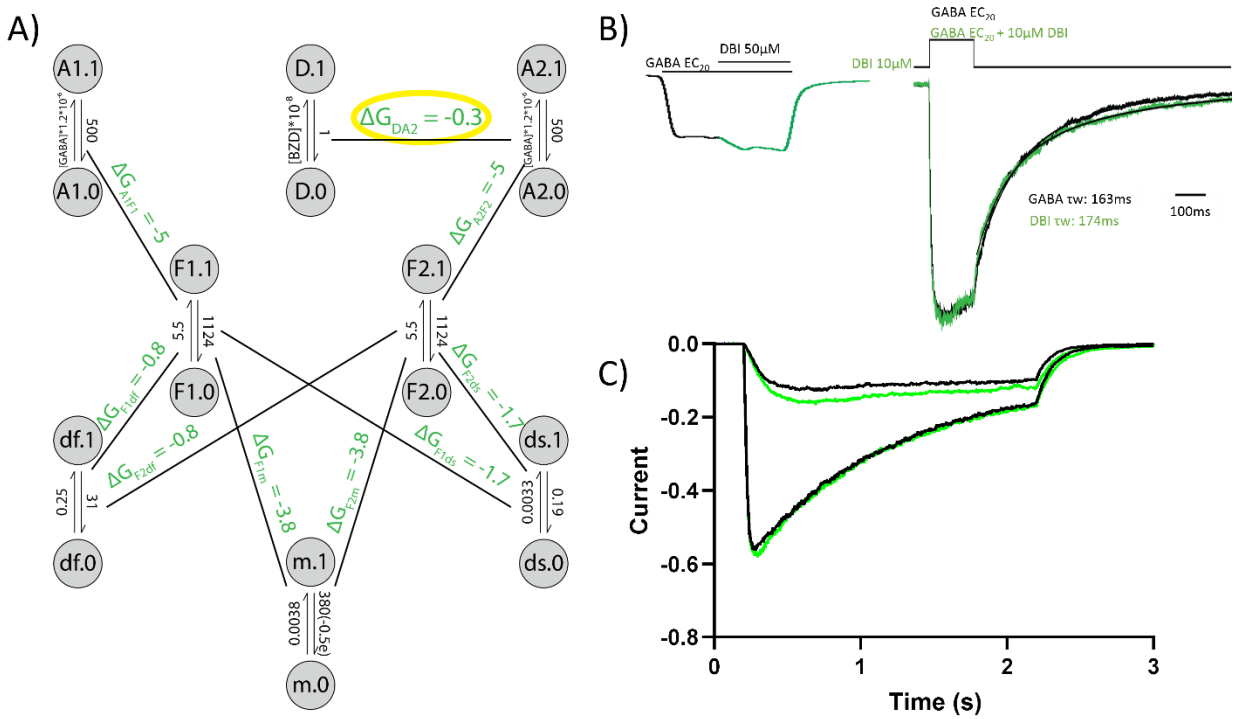

Figure 4.6 – DBI may weakly stabilize the GABA-bound site to increase peak currents at low concentrations of GABA. A) A DBI element (D) is added to the elements-based model described in Figure 4.5, with a direct interaction with the GABA binding site A2 where ΔG_{DA2} = -0.3. B) Sample two-electrode voltage clamping currents showing subsequent application of 50μM DBI (green) slightly increases amplitude elicited by EC20 GABA (left). Sample averaged outside-out patch clamping currents showing applications that co-application of DBI (green) does not increase the rate of deactivation for EC80 GABA. Traces were normalized at amplitude immediately before deactivation, though peak current amplitude was unaffected by DBI data not shown). C) Simulated currents from 2s pulses of 5μM (EC20) and 50μM (EC80) GABA in the presence (green) and absence (black) of 10μM DBI. Simulated traces show that DBI binding causes a small increase in amplitude at EC20 GABA, but no change in amplitude or deactivation rates at EC80 GABA.

	Effect on GABA current amplitude		$\frac{\text{10-90\% Rise Time}_{(GABA+Drug)}}{\text{10-90\% Rise Time}_{(GABA)}}$		$\frac{\tau_{W(GABA+Drug)}}{\tau_{W(GABA)}}$		n
	Mean±SD	p-value	Mean±SD	p-value	Mean±SD	p-value	
DBI	1.13±0.37	0.23	0.94±0.45	0.61	1.03±0.27	0.65	14
FZM	1.01±0.07	0.66	1.36±0.07	0.19	1.50±0.37	0.007	8

Table 4.1 – Summary of drug effects on amplitude, deactivation, and activation for DBI and FZM. Table showing mean±SD and p-values from one sample t-tests for rundown corrected amplitude, 10-90% rise time$_{(GABA+Drug)}$/10-90% rise $_{time(GABA)}$, and $\tau_{w(GABA+Drug)}/\tau_{w(GABA)}$, as well as n of total patches for DBI and FZM.

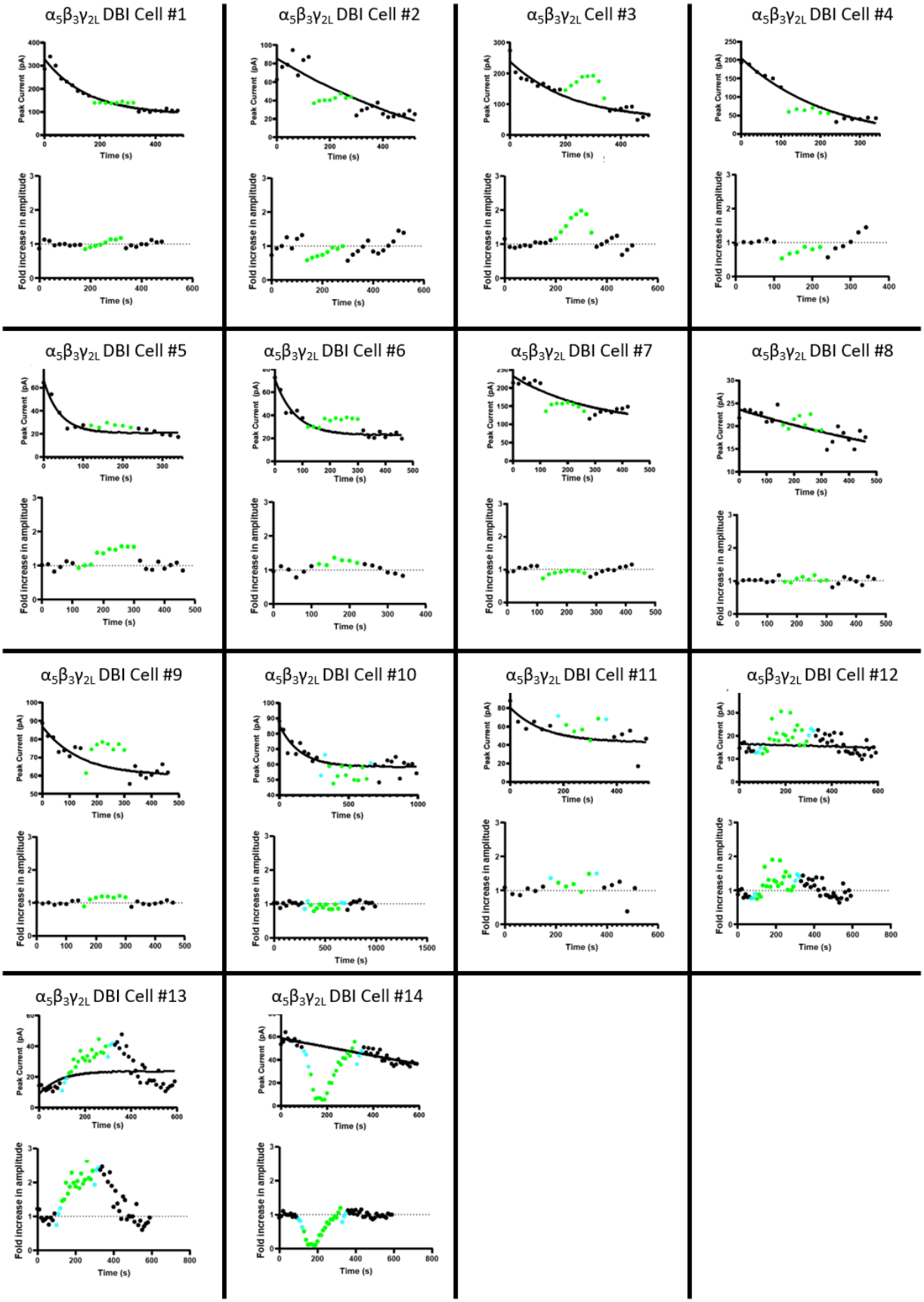
α5β3γ2L DBI Cell #1
α5β3γ2L DBI Cell #2
α5β3γ2L Cell #3
α5β3γ2L DBI Cell #4
α5β3γ2L DBI Cell #5
α5β3γ2L DBI Cell #6
α5β3γ2L DBI Cell #7
α5β3γ2L DBI Cell #8
α5β3γ2L DBI Cell #9
α5β3γ2L DBI Cell #10
α5β3γ2L DBI Cell #11
α5β3γ2L DBI Cell #12
α5β3γ2L DBI Cell #13
α5β3γ2L DBI Cell #14
Peak Current (pA)
Time (s)
Fold increase in amplitude

Supplemental Figure 4.1 – Plots of peak current and fold increase in amplitude for each patch of $\alpha_5\beta_3\gamma_{2L}$ receptors in the presence of GABA and DBI. Top graphs showing peak current responses over time for GABA (black) and GABA+DBI (green). GABA peak current responses are fit with a one-phase decay equation where PeakCurrent = $(PeakCurrent_0 - Plateau)*e^{-Kt}$. $PeakCurrent_0$ is the current at t=0, Plateau is PeakCurrent at t=∞, K = rate constant of decay (s^{-1}), and t is time. Bottom graphs plot fold increase in amplitude (raw amplitude/one-phase decay predicted amplitude) over time.

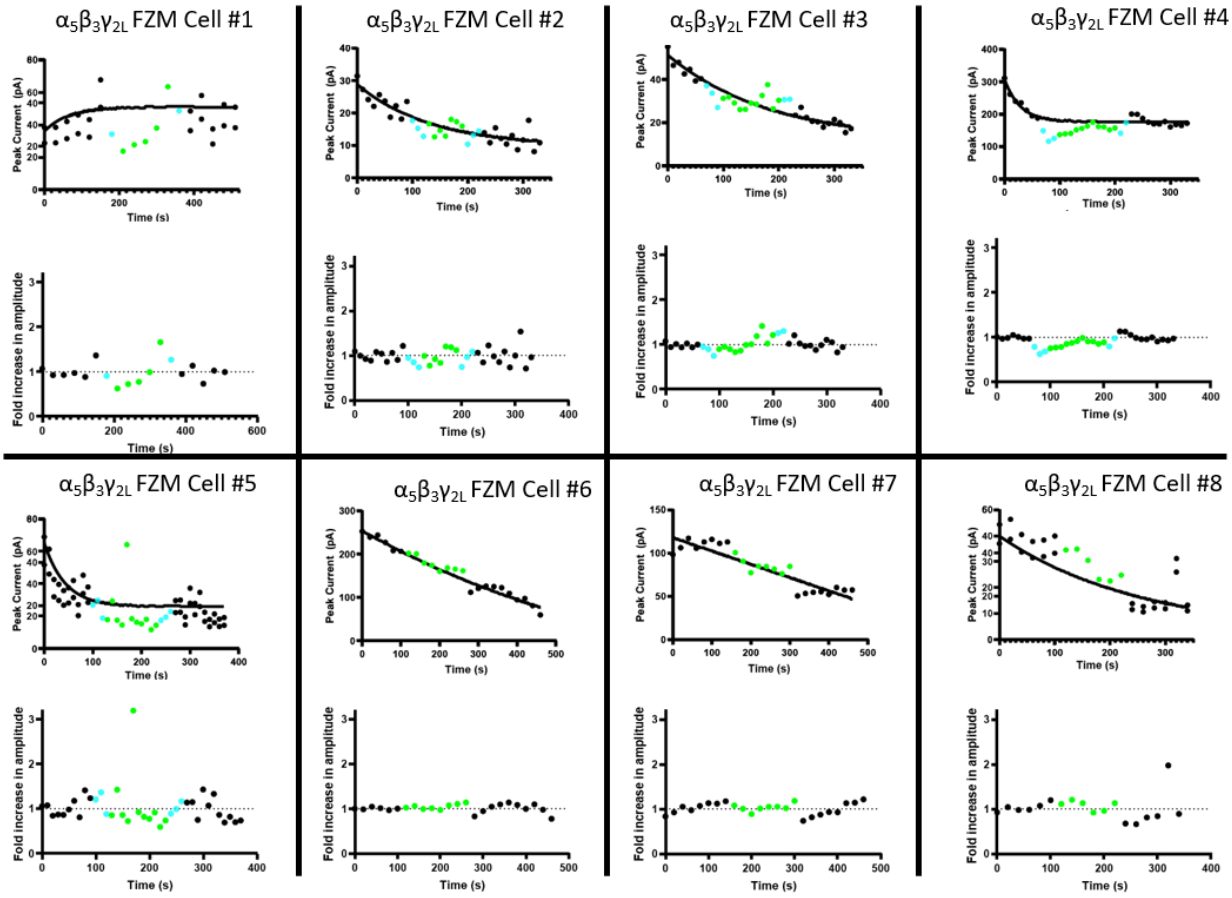

Supplemental Figure 4.2 – Plots of peak current and fold increase in amplitude for each patch of $\alpha_5\beta_3\gamma_{2L}$ receptors in the presence of GABA and FZM. Top graphs showing peak current responses over time for GABA (black) and GABA+FZM (green). GABA peak current responses are fit with a one-phase decay equation where PeakCurrent = $(PeakCurrent_0 - Plateau)*e^{-Kt}$. $PeakCurrent_0$ is the current at t=0, Plateau is PeakCurrent at t=∞, K = rate constant of decay (s^{-1}), and t is time. Bottom graphs plot fold increase in amplitude (raw amplitude/one-phase decay predicted amplitude) over time.

		Effect on GABA current amplitude	Normalized deactivation	Normalized activation	Starting Amp	Noise/ Amp %
α5β3γ2L DBI	Cell #13	2.00	1.56	1.01	13.07	7.65
	Cell #12	1.26	1.28	1.09	14.69	3.40
	Cell #5	1.25	1.26	0.72	32.1	6.23
	Cell #10	0.90	1.19	0.86	71.52	2.10
	Cell #11	1.20	1.19	0.57	65.69	5.33
	Cell #14	0.54	1.16	1.59	56.21	2.67
	Cell #7	0.90	1.07	0.52	204.8	0.24
	Cell #8	1.04	0.96	0.88	17.2	2.91
	Cell #1	1.03	0.91	1.81	191.55	1.04
	Cell #6	1.34	0.85	0.52	96	2.08
	Cell #3	1.61	0.82	0.77	159.3	0.31
	Cell #4	0.74	0.80	1.54	153.7	1.30
	Cell #2	0.80	0.63	0.24	68.2	0.73
	Cell #9	1.14	0.60	0.99	75	0.67
α5β3γ2L FZM	Cell #8	1.08	2.17	2.96	35.7	4.20
	Cell #4	0.87	1.80	1.16	220.25	1.14
	Cell #5	1.07	1.71	1.05	21.29	9.39
	Cell #7	1.03	1.45	1.64	107.9	0.93
	Cell #6	1.05	1.31	1.23	225.60	0.44
	Cell #2	1.00	1.28	1.11	19.14	5.22
	Cell #3	1.03	1.25	1.04	32.88	3.04
	Cell #1	0.96	1.01	0.69	96.33	2.08

Supplemental Table 4.1 – Fold increase in amplitude, normalized deactivation, normalized activation, noise to amplitude ratio and starting amplitude for each patch in the presence of DBI and FZM. Table showing rundown-corrected amplitude, normalized deactivation and activation, noise to amplitude ratios and the starting amplitude for DBI (on top) and FZM (on bottom) for every patch. Columns are colored from white to darkest shade to

indicate lowest to highest value. Rows have been sorted by highest normalized deactivation value. Cells highlighted in grey were obtained using the theta application pipette, non-highlighted cells are from the 4-barrel application pipette.

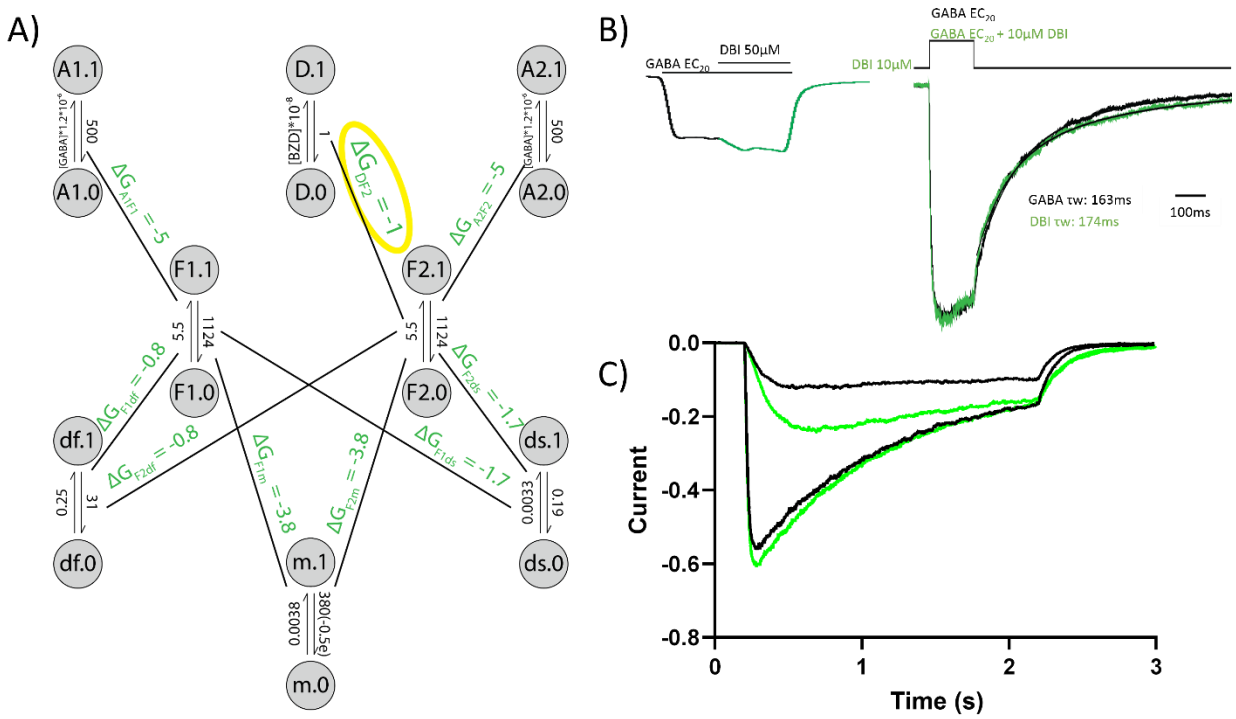

Supplemental Figure 4.3 – A stabilizing interaction between DBI and the F-element does not accurately simulate experimental data. A DBI element (D) is added to the elements-based model described in Figure 4.5, with a direct interaction with the F-element F2 where $\Delta G_{DF2} = -1$. B) Sample two-electrode voltage clamping currents (left) showing subsequent application of 50μM DBI (green) slightly increases amplitude elicited by EC20 GABA. Sample averaged outside-out patch clamping currents (right) showing applications that co-application of DBI (green) does not increase the rate of deactivation for EC80 GABA. Traces were normalized at amplitude immediately before deactivation, though peak current amplitude was unaffected by DBI (data not shown). C) Simulated currents from 2s pulses of 5μM (EC20) and 50μM (EC80) GABA in the presence (green) and absence (black) of 10μM DBI. Simulated traces show that DBI binding causes an increase in amplitude at EC20 GABA, a small increase in amplitude at EC80, and a slowing in the rate of deactivation which does not match experimental data.

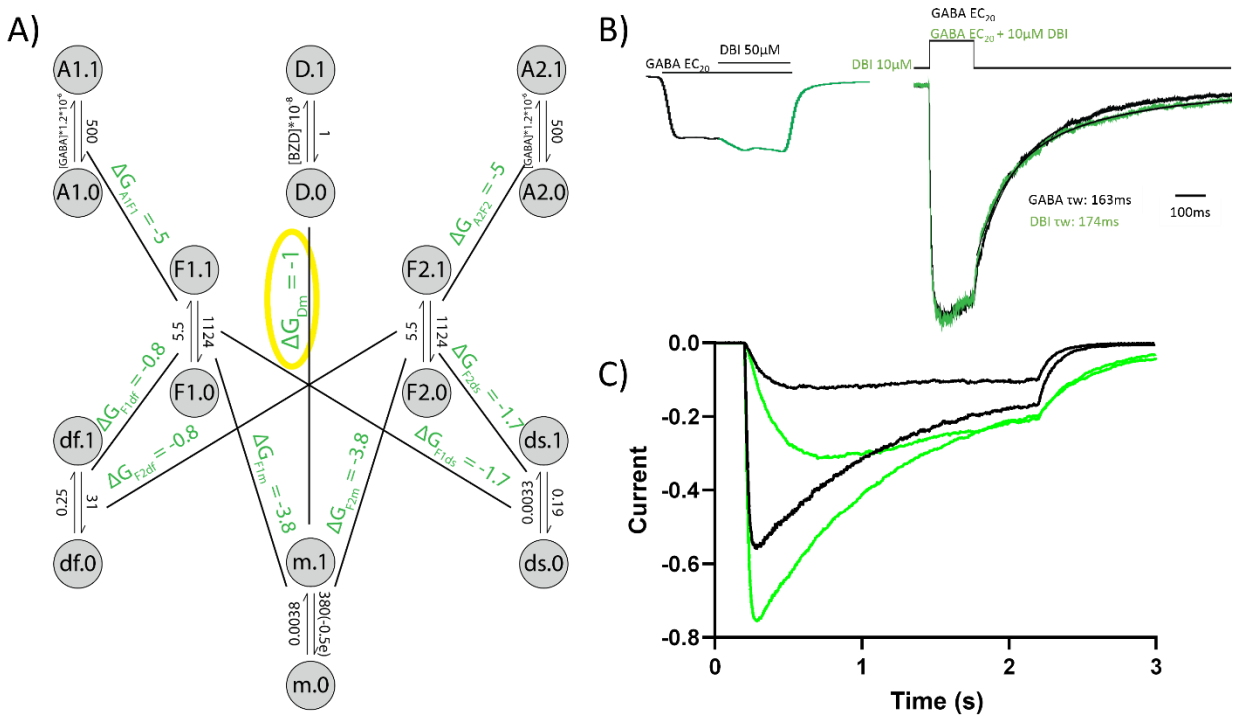

Supplemental Figure 4.4 – A stabilizing interaction between DBI and the main channel gate does not accurately simulate experimental data. A DBI element (D) is added to the elements-based model described in Figure 4.5, with a direct interaction with the main channel gate M where $\Delta G_{Dm} = -1$. B) Sample two-electrode voltage clamping currents (left) showing subsequent application of 50μM DBI (green) slightly increases amplitude elicited by EC20 GABA. Sample averaged outside-out patch clamping currents (right) showing applications that co-application of DBI (green) does not increase the rate of deactivation for EC80 GABA. Traces were normalized at amplitude immediately before deactivation, though peak current amplitude was unaffected by DBI (data not shown). C) Simulated currents from 2s pulses of 5μM (EC20) and 50μM (EC80) GABA in the presence (green) and absence (black) of 10μM DBI. Simulated traces show that DBI binding causes an increase in amplitude and slower rate of deactivation at both GABA concentrations, which does not match experimental data.

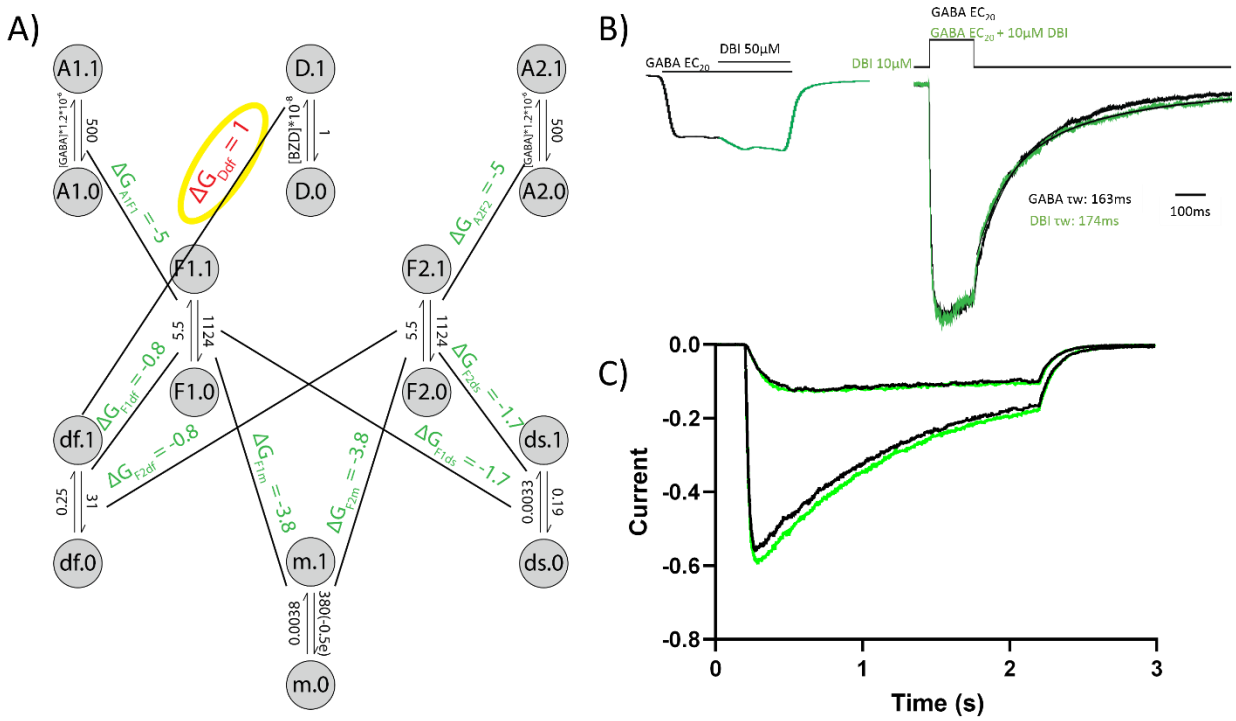

Supplemental Figure 4.5 – A destabilizing interaction between DBI and the fast desensitization gate does not accurately simulate experimental data. A DBI element (D) is added to the elements-based model described in Figure 4.5, with a direct interaction with the fast desensitization gate df where $\Delta G_{Ddf} = 1$. B) Sample two-electrode voltage clamping currents (left) showing subsequent application of 50μM DBI (green) slightly increases amplitude elicited by EC20 GABA. Sample averaged outside-out patch clamping currents (right) showing applications that co-application of DBI (green) does not increase the rate of deactivation for EC80 GABA. Traces were normalized at amplitude immediately before deactivation, though peak current amplitude was unaffected by DBI (data not shown). C) Simulated currents from 2s pulses of 5μM (EC20) and 50μM (EC80) GABA in the presence (green) and absence (black) of 10μM DBI. Simulated traces show that DBI binding does not affect the rate of deactivation, as seen experimentally, but the amplitude of EC80 is slightly increased by DBI while the EC20 current is not, which does not reflect the experimental data.

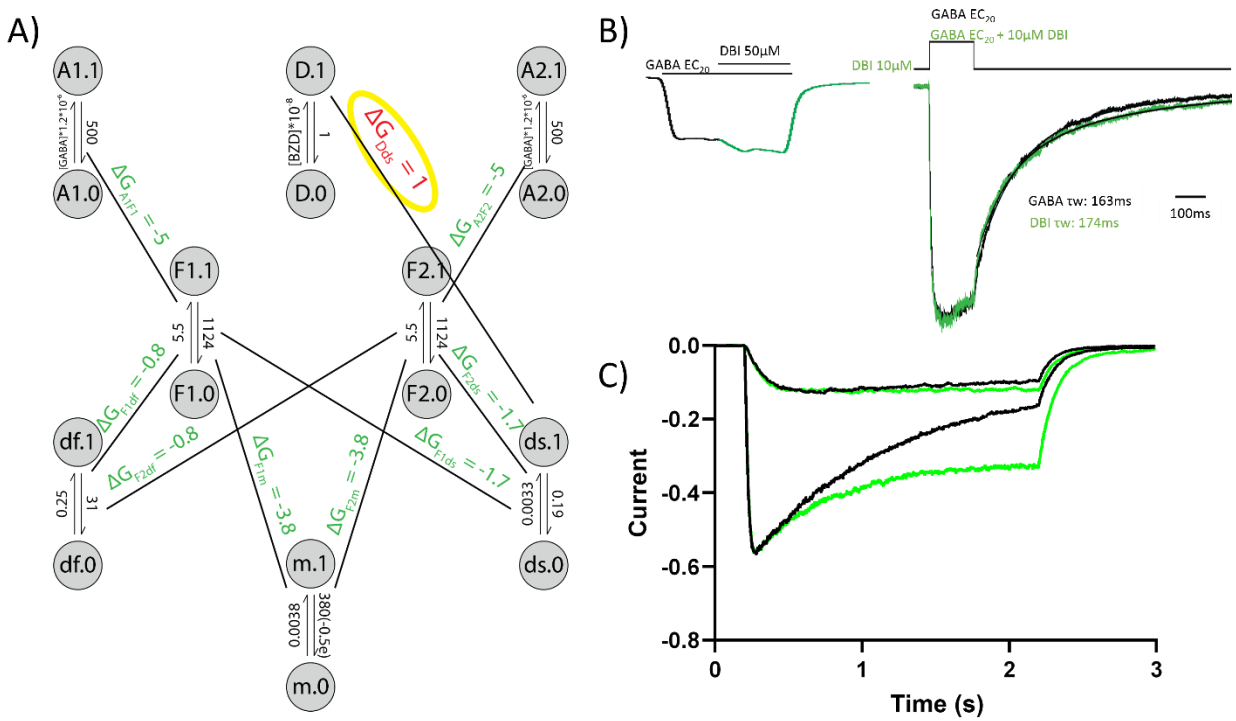

Supplemental Figure 4.6 – A destabilizing interaction between DBI and the slow desensitization gate does not accurately simulate experimental data. A DBI element (D) is added to the elements-based model described in Figure 4.5, with a direct interaction with the slow desensitization gate ds where $\Delta G_{Dds} = 1$. B) Sample two-electrode voltage clamping currents (left) showing subsequent application of 50μM DBI (green) slightly increases amplitude elicited by EC20 GABA. Sample averaged outside-out patch clamping currents (right) showing applications that co-application of DBI (green) does not increase the rate of deactivation for EC80 GABA. Traces were normalized at amplitude immediately before deactivation, though peak current amplitude was unaffected by DBI (data not shown). C) Simulated currents from 2s pulses of 5μM (EC20) and 50μM (EC80) GABA in the presence (green) and absence (black) of 10μM DBI. Simulated traces show that DBI binding does not affect the rate of deactivation, as seen experimentally, but the amplitude of EC20 GABA current is not affected by DBI, which does not reflect the experimental data.

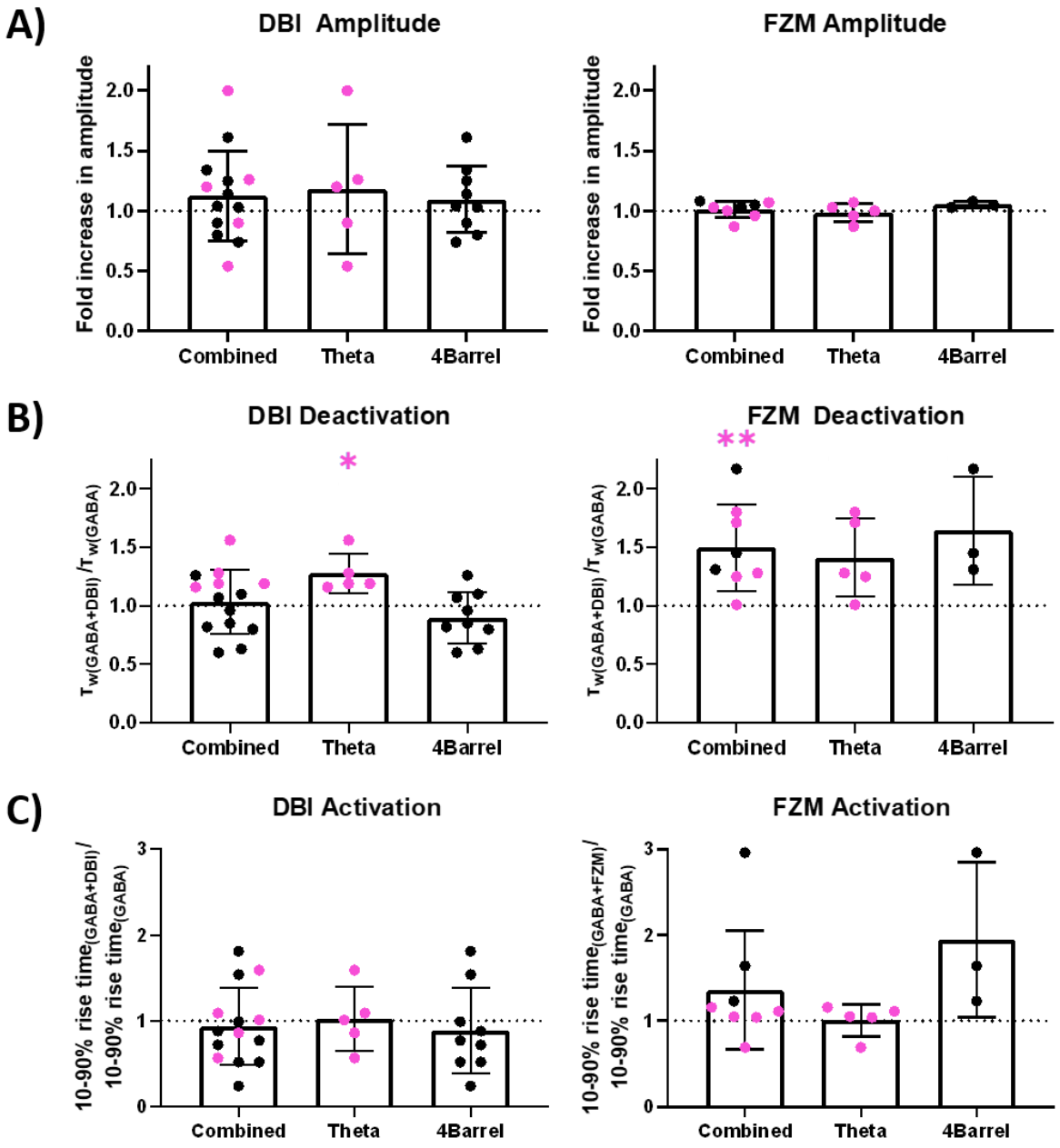

Supplemental Figure 4.7 – Effects of DBI and FZM on amplitude, rate of deactivation and rate of activation with separated results from theta-barrel and 4-channel application pipettes. Bar graphs for fold increase in amplitude, normalized τ_w, and normalized 10-90% rise time for DB and FZM. Each graph shows combined values, as well as data separated into data obtained from the theta application pipette and data from the 4-barrel application pipette. Data from the theta pipette are highlighted in pink. Error bars represent SD. One sample t-tests

comparing to a null hypothesis of 1 show that FZM significantly increases normalized τ_w for the combined data (p=0.007). DBI significantly increases normalized τ_w for the data acquired using the theta application pipette (p=0.02), but the cumulative data are not significantly different than 1 (p=0.65).

Chapter V:

$\alpha_5\beta_3$ GABARs are positively modulated by DBI

Introduction

Benzodiazepines have been a widely prescribed class of drugs since their discovery in the mid-20th century. These drugs exert their antiepileptic, anxiogenic, and somnogenic effects by binding to GABA-A receptors (GABARs). GABARs are pentameric ligand-gated ion channels (pLGICs) made up of five distinct subunits arranged around a central pore. There are a wide variety of GABAR subunit isoforms including six different α, three β and three γ. The most common GABARs are formed by α:β:α:β:γ subunits arranged clockwise around a central pore, though some GABARs are formed by only α and β subunits (Smart and Stephenson, 2019). Heterologously expressed αβ GABARs have been observed in both 3α:2β (Boileau, 2005; Wagoner and Czajkowski, 2010) and 2α:3β (Baumann et al., 2001; Chang et al., 1996; Gonzales et al., 2008; Tretter et al., 1997) stoichiometries. Some drugs, such as zolpidem, are selective for a specific αβ GABAR stoichiometry (3α:2β for zolpidem), suggesting they may be binding to a unique interface between two homologous subunits (Che Has et al., 2016).

Generally, αβγ receptors are found at the synapse where they mediate the majority of fast inhibition in the brain, whereas αβ receptors are generally located extrasynaptically (Brickley and Mody, 2012; Mortensen and Smart, 2006) where they may mediate tonic inhibition. αβ receptors have lower maximum open probabilities than αβγ receptors (Goldschen-Ohm et al., 2010; Wagner, 2004) and lower main conductance states (Mortensen and Smart, 2006).

The high affinity binding site for BZDs located in the extracellular domain of GABARs in an intersubunit pocket located between the α and γ subunits and is absent in αβ receptors. This

binding site has been well-characterized by mutagenesis, cysteine modification experiments, and high resolution cryoEM structures (Masiulis et al., 2019; Morlock and Czajkowski, 2011; Olsen and Sieghart, 2009; Zhu et al., 2018). Some BZDs like diazepam also have a second, lower affinity binding site located in transmembrane domain interface between α and β subunits (Masiulis et al., 2019).

The diazepam binding inhibitor (DBI) was identified as a putative endogenous benzodiazepine (BZD) based on its ability to displaced [^{3}H]-diazepam from binding GABARs (Guidotti et al., 1983). Experiments from the Huguenard lab also provided indirect evidence for an interaction between DBI and the BZD binding site. They showed that application of flumazenil (FLZ, Ro15-1788, a BZD-site antagonist) and the use of a BZD site knockout mutation shorten the durations of spontaneous inhibitory post synaptic currents (IPSCs) recorded from neurons in the thalamic reticular nucleus.

While DBI is posited as an endogenous benzodiazepine, there is little evidence that all of its effects are mediated by binding to the BZD site, or that it has the same modulatory effects as a BZD. In fact, in Chapter IV of this thesis I showed that while the positively modulating BZD, FZM, slowed the rate of GABA-elicited deactivation for $\alpha_5\beta_3\gamma_{2L}$ receptors, application of DBI did not. In this chapter, I used ultra-rapid solution exchange and outside-out patch experiments to examine the effects of DBI on GABA-elicited currents from $\alpha_5\beta_3$ receptors which lack the α/γ interface needed for high-affinity BZD binding. Surprisingly, I discovered that DBI increased high concentration GABA-elicited current amplitudes and slowed the rate of current deactivation for $\alpha_5\beta_3$ GABARs. Using an elements-based kinetic model, I showed that these effects on GABA-mediated current are reproduced by DBI directly interacting with the main gate.

Methods

HEK cell culture and DNA transfection

Human embryonic kidney (HEK 293T-17) cells were cultured in Eagle's minimum essential medium with Earle's salt (Mediatech, Manassas, VA). Media was supplemented with 10% fetal bovine serum (Atlanta Biologics, Flowery Branch, GA), penicillin-streptomyacin-glutamine (Sigma-Aldrich, St. Louis, MO), and plasmocin (InvivoGen, San Diego, CA). Cells were grown at 37°C with 5% CO_2, and plated on 12mm circular glass coverslips in 60mM dishes 48-72 hour before transfection.

Cells were transfected using lipofectamine 2000 (Invitrogen, Carlsbad, CA) at 85-90% confluency. 0.5-5µg of pUNIV GABAR DNA was used, with a 1:1:3-5 ratio of α5:β3:γ2L subunits or a 1:1 ratio of α5:β3 subunits, and 2-10ng of pUNIV GFP DNA. Cells were used for recording 24-60 hours post transfection.

DBI Purification

DBI was grown and purified as described in Chapter II of this thesis. In brief, BL21 DE3 chemically competent *E. coli* cells were transformed with histidine-tagged DBI cDNA in a pET28a vector. Single colonies were grown in 500mL LB-Kan media at 37°C until OD_{600}=0.6-0.8. Cells were spun at 10,000xg for 10min at 4°C. Pellet was resuspended in Buffer A (sodium phosphate, 50mM, pH 7.4; NaCl, 300mM) with 25mM imidazole (IDA) and protease inhibitors pepstatin, aprotinin and leupeptin. Cells were lysed using an Emulsiflex (ATA Scientific, Taren Point, NSW Australia) and homogenate was spun at 16,800xg for 20min at 4°C. DBI was bound to a Ni-NTA flowthrough column (Qiagen, Hilden, Germany), washed, and eluted using Buffer A and 250mM IDA. PD10 columns (Sigma-Aldrich, St. Louis, MO) were used to remove IDA, and eluted DBI in Buffer A. Purity and yield were evaluated via SDS-PAGE and Nanodrop (Thermo Fisher Scientific, Waltham, MA).

Patch-clamp solutions and drugs

Recording pipettes were pulled from borosilicate glass using a Flaming-Brown P-1000 mulitstage micropipette puller (Sutter Instruments, Novato, CA). Pipette tips were fire-polished with a Narishige MF-83 microforge (Narishige, Tokyo, Japan) until open tip resistance was

between 2-9 MΩ. Electrodes were filled with intracellular solution (140mM KCl, 10mM EGTA, 2mM MgATP, 10mM phosphocreatine, 10mM HEPES, pH 7.3-7.4).

HEPES normal Ringer (HNR) perfusion solution contained 145mM NaCl, 2.5mM KCl, 1mM $MgCl_2$, 1mM $CaCl_2$, and 10mM HEPES, pH 7.3-7.4, 300-310 mOsm. 1M stocks of GABA were prepared in water and frozen at -20°C. Fresh drug solutions were prepared daily in HNR and diluted to 10-50µM GABA in the presence and absence of 10µM DBI. Equivalent volumes of Buffer A were added to GABA solutions to ensure isosmolarity. Recordings were performed at room temperature.

Application Pipette Assembly and Function

4-barrel application pipettes were constructed using 4-Square Bore borosilicate glass (VitroCom, Mountain Lakes, NJ), approximately 1mm internal square width, 6mm outer width of all four squares. Glass was heated, pulled, and cut so that tip openings were approximately 200µm from the center of one opening to the next, and cut to be 2-3cm in length. Polyimide tubing threaded into 28-gauge PTFE was inserted into all four barrels, with poly-imide extended further into the barrels than PTFE tubing. The barrel/tubing interface was sealed using Norland Optical Adhesive 73 (Norland Products, Cranbury, NJ). Glue was cured using >20min exposure to UV light. After testing seals between each barrel, the 4-barrel application pipette was glued to a glass slide. Borders for glass slides were cut from polycarbonate and adhered to the slide using silicone grease.

The application pipette was installed on a piezoelectric biomorph (Physik Instrumente, Costa Mesa, CA). The biomorph is moved to position the application barrel in front of the cell by WinPos (ITK Dr. Kassen GmbH, Hahnau, Germany), with <1msec 10-90% solution exchange times, measured via liquid junction potential tests of open recording pipette tips after experiments.

Outside-out patch clamp recording

Recording pipettes were sealed onto the membrane of GFP-positive HEK cells to obtain a giga-seal with -5 to -10mmHg pressure. Once a high resistance seal was formed, increased negative pressure was used to break into the cell. The pipette was then immediately withdrawn from the cell, enabling the patch to reseal in an outside-out conformation with the extracellular side of the membrane facing out. Patches were held at -40mV. Currents were low-pass-filtered at 2 kHz with an eight-pole Bessel filter. Data was collected at 20kHz via an Axopatch 200B amplifier (Axon Instruments, Sunnyvale, CA) interfaced to a computer using a Digidata 1440A (Axon Instruments, Sunnyvale, CA). Amplifier function was controlled by Clampex (version 10.4.1.10; Molecular Devices, Sunnyvale, CA) and analyzed using Clampfit (version 10.4.1.10; Molecular Devices, Sunnyvale, CA). Patches were exposed to 150ms pulses of 10-50µM GABA with and without 10µM DBI, with 20sec of HNR wash between pulses.

Data Analysis

Averaged traces using 3-15 sweeps were generated in Clampfit and used to measure 10-90% rise time of activation and calculate the rate of deactivation via a weighted tau (τ_w). τ_w was calculated by fitting the current decline after GABA removal until a return to baseline with a bi-exponential equation ($I = A_1*e^{-t/\tau1} + A_2*e^{-t/\tau2}$), where I is current, t is time, A_1 and A_2 are the relative amplitudes for the fast and slow components respectively, and τ_1 and τ_2 are the time constants for the fast and slow components. See Figure 5.3 for sample curve fits. These values are used to calculate τ_w where $\tau_w = (A_1\tau_1+A_2\tau_2)/(A_1+A_2)$. Normalized τ_w values were calculated as $\tau_{w(GABA+DBI)}/\tau_{w(GABA)}$. Normalized 10-90% rise times were calculated as $RiseTime_{(GABA+DBI)}/RiseTime_{(GABA)}$. Significance was evaluated using a paired-test for GABA and GABA+DBI values within the same patch, and using a one-sample t-test of normalized data comparing to a hypothetical null value of 1. Data were analyzed and displayed using GraphPad Prism (version 9.1.2, GraphPad Software Inc, San Diego, CA).

Peak current responses from outside-out patches often decreased over the course of the experiment. In order to accurately assess drug-induced changes in amplitude, run-down was

taken into account. Peak amplitude for every sweep of GABA was plotted over time and fit with a one-phase exponential decay, where PeakCurrent = (PeakCurrent$_0$-Plateau)*e-^{Kt}. PeakCurrent$_0$ is the current at t=0, Plateau is PeakCurrent at t=∞, K = rate constant of decay (s^{-1}), and t is time. Current amplitudes of GABA and GABA+DBI traces were divided by the decay-predicted amplitude to generate current values corrected for run-down, described as fold increase in amplitude. These values were averaged for all initial GABA and all GABA+DBI sweeps in a single patch. Data were analyzed as paired data, and compared to a hypothetical null value of 1.

Kinetic Modeling

GABA-elicited currents were simulated in Kinetic Model Builder 2.0 (Goldschen-Ohm et al., 2014) in Monte Carlo mode. Currents were simulated from 2s pulses of 1mM, 30μM, 3μM, and 1μM GABA and adjusted to simulate to the experimental dose-response GABA by altering binary element rate constants and interactions between elements. 150ms pulses of 1m and 50μM GABA were also simulated in the presence and absence of 10μM DBI. This model describes the two agonist binding sites (A1 and A2), two intermediate elements (F1 and F2), fast and slow desensitization gates (Df and Ds, respectively), a DBI binding site (D), and the channel gate (m) as binary elements. These binary elements can transition between two metastable configurations, such as open or closed for the channel gate, or bound or unbound for a drug binding site. The transition between these states are governed by intrinsic rate constants for the forward and reverse reactions. Interactions between elements can contribute energy towards the transition to an alternate energy state. For this model, rate constants for each element were α_A = [GABA]*1.3*10^{-6} $M^{-1}s^{-1}$, β_A = 511 $M^{-1}s^{-1}$, α_F = 7.6 $M^{-1}s^{-1}$, β_F = 978 $M^{-1}s^{-1}$, α_{df} = 0.29 $M^{-1}s^{-1}$, β_{df} = 24 $M^{-1}s^{-1}$, α_{ds} = 0.0031 $M^{-1}s^{-1}$, β_{ds} = 0.07 $M^{-1}s^{-1}$, α_D = [BZD]*10^8 $M^{-1}s^{-1}$, β_D = 1 $M^{-1}s^{-1}$, is α_m = 0.0038 s^{-1}, β_m = 382 s^{-1}. Interactions between elements (kcal/mol at 298K) are ΔG_{AF} = -6, ΔG_{Fm} = -3.8, ΔG_{Fdf} = -0.9, ΔG_{Fds} = -1.4, and ΔG_{Dm} = -1.

Results

I expressed $\alpha_5\beta_3$ GABARs in HEK cells and used outside-out patch clamping and ultra-fast solution exchange to examine the effects of DBI on GABA-elicited currents. I examined the effects of DBI on GABA-mediated current amplitude, activation, and deactivation and compared them to DBI's effects on $\alpha_5\beta_3\gamma_{2L}$ GABARs. When recording from outside-out patches, it is common for the currents to rundown over time (Amico et al., 1998; Gyenes et al., 1994) and one observes smaller current responses to the same GABA concentration. In order to accurately assess the effects of DBI on GABA-elicited current amplitudes, I corrected the amplitudes to account for rundown as described in Methods. As shown in Figure 5.1C, DBI significantly increased peak current amplitude elicited by high concentration of GABA from $\alpha_5\beta_3$ but not $\alpha_5\beta_3\gamma_{2L}$ GABARs ($\alpha_5\beta_3$ p=0.0009 n=9, $\alpha_5\beta_3\gamma_{2L}$ p=0.25 n=14, Figure 5.1C). When comparing the mean fold increase in amplitude elicited by DBI between subunit combinations against a hypothetical null value of 1 (Figure 5.1D), amplitude of $\alpha_5\beta_3$ receptors was significantly increased (2.67±0.97, p=0.0009, n=9), but $\alpha_5\beta_3\gamma_{2L}$ amplitude was not increased (1.13±0.37, p=0.23, n=14). Peak current and adjusted amplitudes for every patch are included in Supplemental Figure S5.1 for $\alpha_5\beta_3$ and Supplemental Figure 4.1 for $\alpha_5\beta_3\gamma_{2L}$.

In order to evaluate the effects of DBI on activation, I measured 10-90% rise time for traces averaged from 3-15 sweeps of GABA and GABA+DBI (Figure 5.2). Comparing paired 10-90% rise times for GABA and GABA+DBI shows that DBI does not affect activation for either $\alpha_5\beta_3$ or $\alpha_5\beta_3\gamma_{2L}$ receptors ($\alpha_5\beta_3$ p=0.15, $\alpha_5\beta_3\gamma_{2L}$ p=0.09). Normalized 10-90% rise times were calculated by dividing rise times for GABA+DBI by rise times for GABA. Comparing these mean values to a hypothetical null value of 1 also confirms that DBI does not affect activation for either subunit combination ($\alpha_5\beta_3$ p=0.66, $\alpha_5\beta_3\gamma_{2L}$ p=0.61).

I also compare the effects of DBI on deactivation rates for $\alpha_5\beta_3$ and $\alpha_5\beta_3\gamma_{2L}$ receptors by measuring weighted tau (τ_w). Plotting paired τ_w for GABA and GABA+DBI illustrates that DBI slowed the rate of deactivation for $\alpha_5\beta_3$ (p=0.01) but not $\alpha_5\beta_3\gamma_{2L}$ receptors (p=0.57). Normalized

τ_w was calculated as $\tau_{w(GABA+DBI)}/\tau_{w(GABA)}$ and compared against a null hypothesis of 1. DBI significantly increased the normalized τ_w for $\alpha_5\beta_3$ (1.54±0.62, p=0.03, n=9), but not for $\alpha_5\beta_3\gamma_{2L}$ (1.03±0.27, p=0.65, n=14).

Table 5.1 lists mean values±standard deviation for DBI's effects on rundown-corrected amplitude, normalized rise time, normalized deactivation rate, and n for $\alpha_5\beta_3$ and $\alpha_5\beta_3\gamma_{2L}$. A summary table of the fold increase in amplitude, normalized deactivation, activation, starting amplitude and percent noise/amplitude can be found in Supplemental Table 5.1.

I used an elements-based kinetic model to identify a possible mechanism for DBI's effects. I created a model for $\alpha_5\beta_3$ traces by fitting dose-response traces previously obtained by Dr. Paul Burkat and Dr. Robert Pearce using $\alpha_5\beta_2$ receptors (Burkat et al., 2014) where EC50=3.3μM. In order to reflect the lower maximum open probability of $\alpha_5\beta$ receptors, I normalized the reference data to -0.4 instead of -1. I altered the intrinsic rate constants for each element and the changes in free energy associated with each interaction (Figure 5.4A) in order to model currents elicited by 2s exposures of 1mM, 30μM, 3μM, and 1μM GABA (Figure 5.4B) which closely matched the experimental traces recorded under the same conditions (Figure 5.4C). Using this model, I evaluated with which element DBI may interact in order to slow the rate of deactivation and increase the peak current amplitude by 2.5-fold even at saturating or near-saturating GABA concentrations. I simulated 150ms applications of 50μM and 1mM GABA in the presence and absence of 10μM DBI and found that a large amplitude increase, as measured experimentally, could only be created by a direct interaction between the DBI element and the main channel gate (Figure 5.5). Interactions between the DBI element and an F-element (Supplemental Figure 5.2), GABA binding site (Supplemental Figure 5.3), and desensitization gates (Supplemental Figure 5.4 for the fast gate, Supplemental Figure 5.5 for the slow gate) do not accurately simulate experimental data.

Discussion

Outside-out patch clamp experiments demonstrated that DBI does not affect the peak current amplitude, 10-90% rise time, or deactivation rate for $\alpha_5\beta_3\gamma_{2L}$ receptors. In this chapter, I discovered that DBI significantly slows the rate of deactivation ($\tau_{w(GABA+DBI)}/\ \tau_{w(GABA)}$=1.54±0.62) and increases the peak current amplitudes elicited by saturating concentration of GABA (2.67±0.97 fold) for $\alpha_5\beta_3$ GABARs. DBI's minimal effects on macroscopic currents from $\alpha_5\beta_3\gamma_{2L}$ GABARs but large effects on $\alpha_5\beta_3$ GABARs are surprising, given DBI's proposed role as an endogenous BZD. The high-affinity BZD site located at the α/γ interface is clearly not required to mediate DBI's effects on αβ GABARs. Moreover, the inclusion of a γ subunit significantly reduces the modulatory effects of DBI on αβγ GABARs.

Radioligand displacement experiments have shown that DBI can displace BZD binding to membrane homogenates prepared from rat and bovine brain (Guidotti et al., 1983; Shoyab et al., 1986). Additionally, Christian and Huguenard showed that use of a BZD antagonist or a BZD-insensitive mutant had the same effect on spontaneous IPSC duration as a DBI knockout (Christian et al., 2013). These experiments support the idea that DBI interacts with GABARs at the BZD site. However, it is possible that DBI has multiple binding sites on the GABAR, and that the removal of the high affinity BZD site allows increased DBI binding to another site which is responsible for DBI effects on $\alpha_5\beta_3$ GABARs current responses. Alternatively, $\alpha_5\beta_3$ have unique subunit interfaces, either α/α or β/β depending on the stoichiometry of the pentamer (see Figure 7.2). It is possible that DBI mediates its $\alpha_5\beta_3$ effects by binding to one or both of these unique interfaces which are absent in a $\alpha_5\beta_3\gamma_{2L}$ conformation, as has been seen with zolpidem (Che Has et al., 2016).

In addition, the radioligand binding assays and Christian slice recordings examine endogenously expressed GABARs and DBI, or DBI purified from animal brain. In my experiments, DBI was expressed in *E. coli* and purified, and heterologously expressed GABARs of a single subtype in HEK cells were used. Post-translational modifications of DBI or cleavage

into one of its biologically active peptide products such as ODN may alter how DBI interacts with a GABAR, but *E. coli* lack the enzymes required for post-translational modifications. Also, the GABAR subtypes expressed may differ between my experiments and previously published work. The radioligand binding experiments used crude synaptic membrane homogenates prepared from rat or bovine brain (which contain a variety of GABAR subtypes) and the Christian experiments used slices from the thalamic reticular nucleus where α3 is highly expressed. It is possible that GABARs with different alpha subunit isoforms bind DBI differently, which results in different functional effects. In addition to alternative GABAR subunit composition, GABARs in neurons interact with accessory subunits such as GARLH or Shisa7 (Thul et al., 2017; Uhlén et al., 2015). One of these auxiliary proteins may be necessary to mediate DBI's effects on αβγ receptors.

One of DBI's most striking effects on the $\alpha_5\beta_3$ GABARs was the large increase in peak current, even at a near-saturating concentration of GABA. 50μM GABA is approximately EC90 for this receptor combination (Burkat et al., 2014) and yet co-application of DBI more than doubles the amplitude. This may be possible due to the low maximum open probability of αβ receptors of approximately 0.4 (Wagner, 2004). Modeling the effects of DBI on $\alpha_5\beta_3$ receptors using an elements-based kinetic model shows that in order for DBI to slow the rate of deactivation while significantly increasing the peak GABA response, DBI must interact directly with the main channel gate and stabilize an open state.

Future experiments are needed to understand how DBI is affecting $\alpha_5\beta_3$ receptors. It would be intriguing to see if these effects are similar across all possible αβ subunit combinations, or if this positive modulation is specific to $\alpha_5\beta_3$ receptors. Additionally, use of a GABAR αβ concatamer construct would allow us to control receptor stoichiometry and explore whether DBI binds a unique α/α or β/β interface.

αβ GABARs are generally expressed extrasynaptically, where they mediate tonic inhibition (Brickley and Mody, 2012; Mortensen and Smart, 2006). Tonic inhibition occurs when extrasynaptic receptors bind low, ambient levels of GABA and increase cell conductance to decrease the cell's firing rate in response to excitatory stimulation (Farrant and Nusser, 2005). By measuring a persistent, GABA-mediated cell conductance and abolishing it via the use of picrotoxin, a GABAR channel blocker, or bicuculine, a GABA-antagonist, scientists have observed tonic inhibition in hippocampal interneurons (Semyanov et al., 2003), CA1 (Bai et al., 2001), and dentate gyrus (Nusser and Mody, 2002), among other regions. In this chapter, I show that DBI is able to slow the rate of deactivation and significantly increase the peak current of αβ receptors. These modulatory effects may represent a new pathway that the brain uses to regulate tonic inhibition.

Though the specific mechanism for DBI's modulation of GABARs comprised of different subunits has yet to be fully characterized, the data in this chapter clearly refute the idea that a BZD binding site is necessary for DBI's modulation of the receptor. This raises many new questions about where DBI may be interacting with $\alpha_5\beta_3$ receptors, and why the same effects are not seen with $\alpha_5\beta_3\gamma_{2L}$. At high concentrations of GABA, the macroscopic channel kinetics of $\alpha_5\beta_3$ receptors are significantly affected by DBI while $\alpha_5\beta_3\gamma_{2L}$ receptors are not, suggesting that DBI much more strongly modulates the GABAR in the absence of a γ subunit.

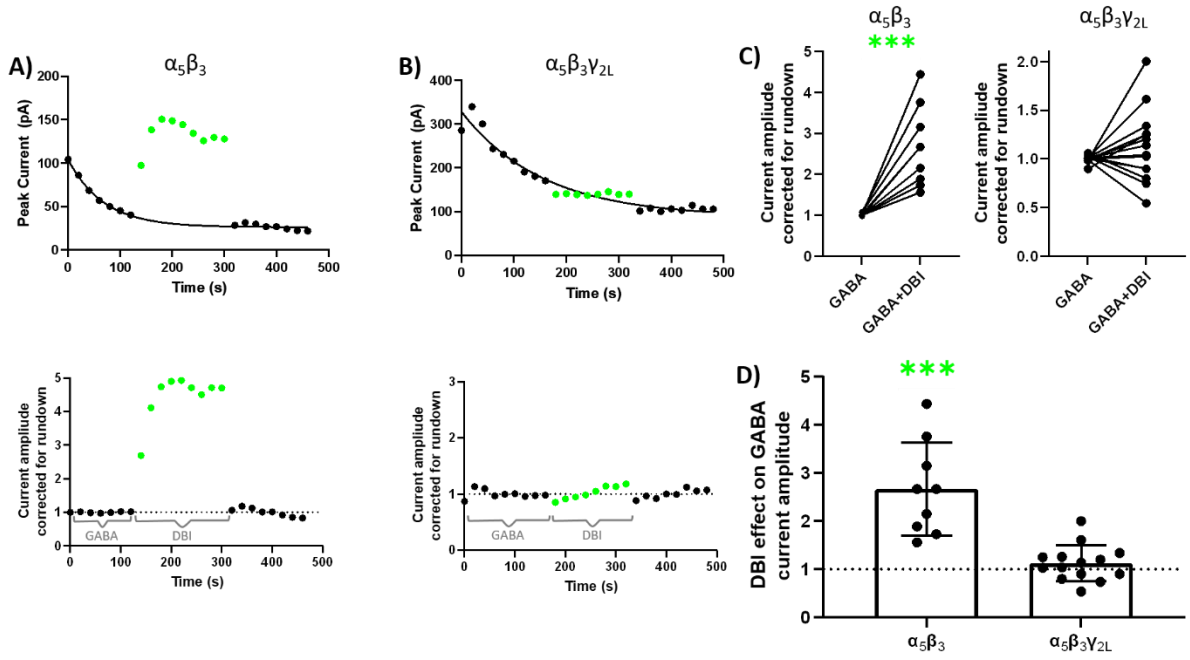

Figure 5.1 – DBI increases GABA-elicited amplitudes for $\alpha_5\beta_3$ receptors, but not $\alpha_5\beta_3\gamma_{2L}$. Top graphs showing peak current responses over time for GABA (black) and GABA+DBI (green) for $\alpha_5\beta_3$ (A) and $\alpha_5\beta_3\gamma_{2L}$ (B) receptors. GABA peak current responses are fit with a one-phase decay equation where PeakCurrent = (PeakCurrent$_0$-Plateau)*e-^{Kt}. PeakCurrent$_0$ is the current at t=0, Plateau is PeakCurrent at t=∞, K = rate constant of decay (s^{-1}), and t is time. Bottom graphs plot fold increase in amplitude (raw amplitude/one-phase decay predicted amplitude) over time. Brackets indicate data averaged to a single data point for C and D. C) Paired data averaging all initial GABA sweeps and all GABA+DBI sweeps current amplitude corrected for rundown. Paired t-tests show DBI significantly increases amplitude for $\alpha_5\beta_3$ receptors (p=0.0009), but not $\alpha_5\beta_3\gamma_{2L}$ (p=0.25). D) Mean DBI effect on GABA current amplitude for $\alpha_5\beta_3$ and $\alpha_5\beta_3\gamma_{2L}$ was compared to a null hypothesis of one using a one sample t-test. $\alpha_5\beta_3$ adjusted amplitude was significantly increased by DBI (p=0.0009), while $\alpha_5\beta_3\gamma_{2L}$ was not (p=0.23). Error bars represent SD.

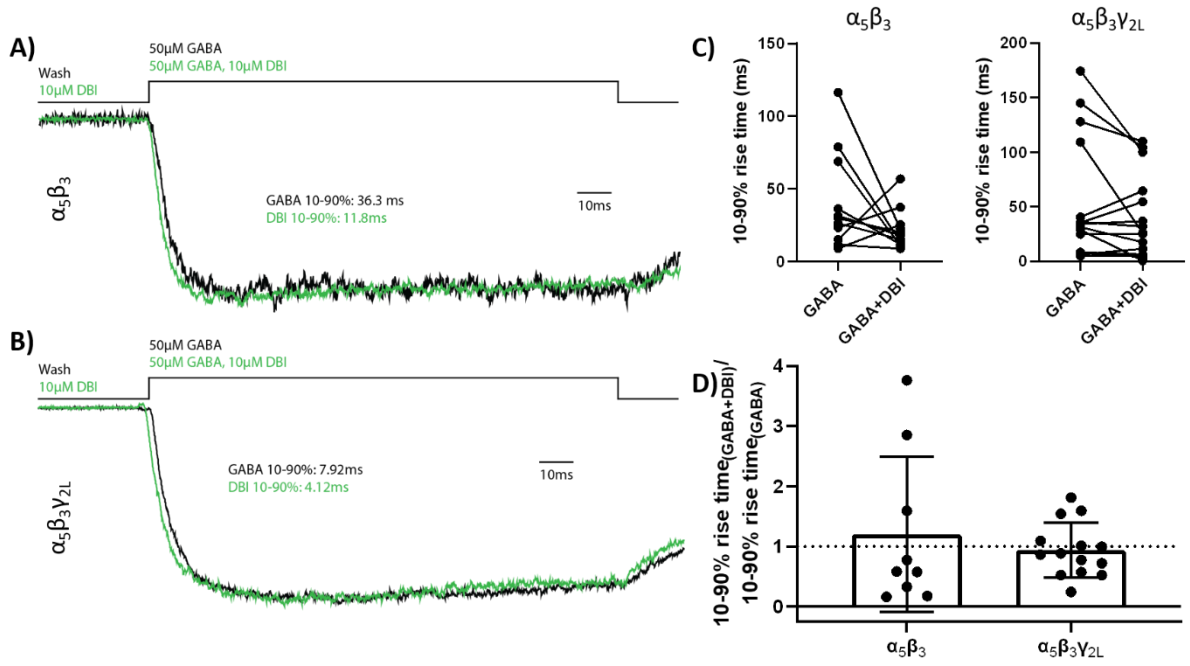

Figure 5.2 – DBI does not affect the 10-90% rise time of activation for $\alpha_5\beta_3$ or $\alpha_5\beta_3\gamma_{2L}$ receptors. Overlayed, averaged traces for GABA (black) and GABA + DBI (green), for $\alpha_5\beta_3$ (A) or $\alpha_5\beta_3\gamma_{2L}$ (B) receptors. Bars above indicate duration of 150ms GABA application. Traces are normalized to peak amplitude. C) Paired 10-90% rise times for GABA and GABA+DBI. DBI did not significantly affect 10-90% rise time for either subunit combination (paired t-test $\alpha_5\beta_3$ p=0.15, $\alpha_5\beta_3\gamma_{2L}$ p=0.09). D) Normalized 10-90% rise times show that DBI does not significantly affect activation for $\alpha_5\beta_3$ or $\alpha_5\beta_3\gamma_{2L}$ receptors when compared to a hypothetical null value of n=1 ($\alpha_5\beta_3$ p=0.66, $\alpha_5\beta_3\gamma_{2L}$ p=0.61). Error bars represent SD.

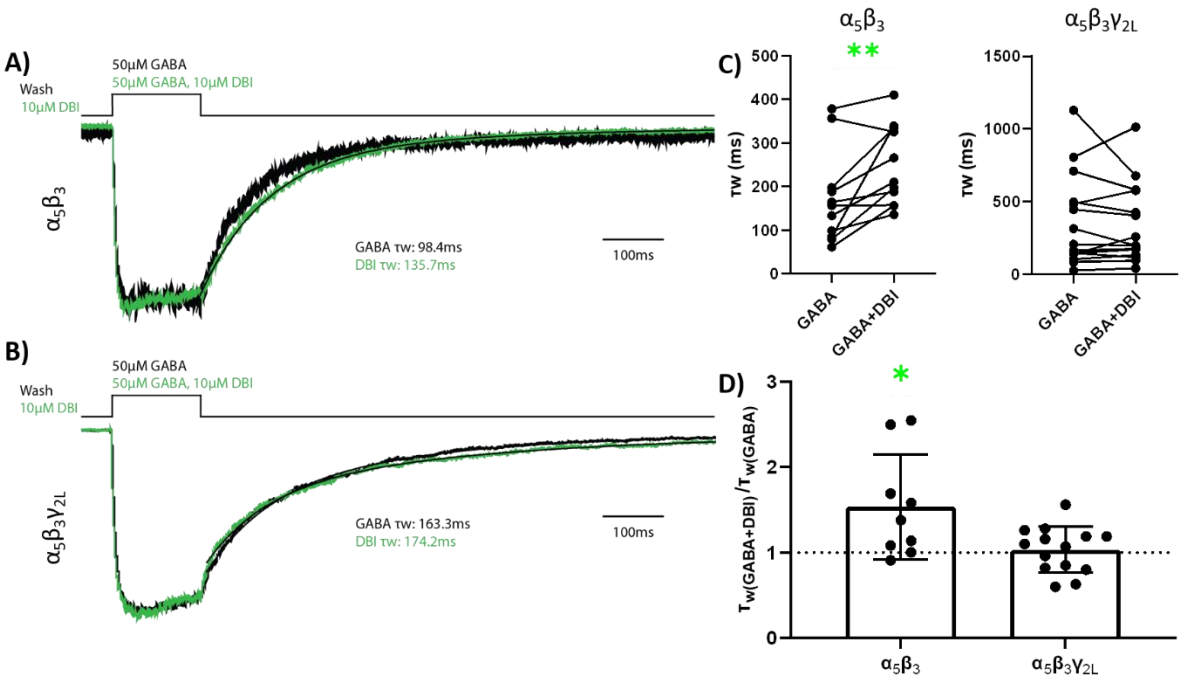

Figure 5.3 – DBI slows the rate of deactivation and increases τ_w for $\alpha_5\beta_3$ receptors, but not $\alpha_5\beta_3\gamma_{2L}$. Overlayed, averaged traces for GABA (black) and GABA + DBI (green), for $\alpha_5\beta_3$ (A) or $\alpha_5\beta_3\gamma_{2L}$ (B) receptors. Bars above indicate duration of 150ms GABA application. Traces are normalized to peak amplitude. C) Paired τ_w values for GABA and GABA+DBI calculated by fitting the curve immediately after GABA is removed with the equation $I = A_1*e^{-t/\tau1} + A_2*e^{-t/\tau2}$, where I is current, t is time, A_1 and A_2 are the relative amplitudes for the fast and slow components respectively, and τ_1 and τ_2 are the time constants for the fast and slow components. $\tau_w = (A_1\tau_1+A_2\tau_2)/(A_1+A_2)$. DBI significantly slowed the rate of deactivation for $\alpha_5\beta_3$ (paired t-test p=0.01) but not $\alpha_5\beta_3\gamma_{2L}$ (p=0.57). D) Normalized τ_w values for DBI applied to $\alpha_5\beta_3$ and $\alpha_5\beta_3\gamma_{2L}$ receptors. DBI significantly increases the normalized τ_w for $\alpha_5\beta_3$ receptors (one sample t-test p=0.03), but not $\alpha_5\beta_3\gamma_{2L}$ (p=0.65). Error bars represent SD.

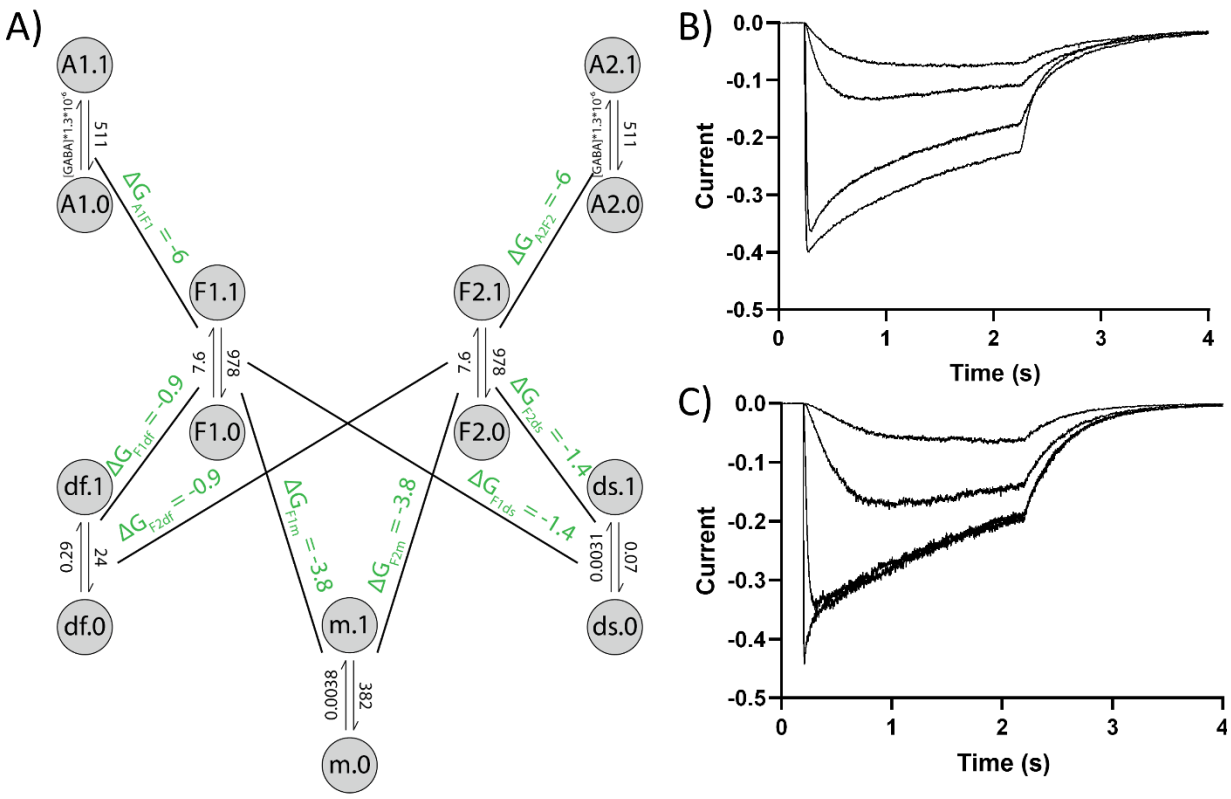

Figure 5.4 – Elements-based kinetic model of $\alpha_5\beta_3$ receptor macroscopic kinetics. An elements model adapted for $\alpha_5\beta$ receptors (A) was created to simulate GABA-elicited currents. ΔG values (kcal/mol at 298K) for interactions between elements are shown in green, and element rate constants ($M^{-1}s^{-1}$ for all but channel gate, m, s^{-1} for m) are shown between element states. A1 and A2 represent agonist binding sites, F1 and F2 are intermediate F elements, df is the fast desensitization gate, ds is the slow desensitization gate, and m is the main channel gate. Electrophysiology data provided by Dr. Burkat (B) is well modeled by simulated responses to 2s pulses of 1mM, 30μM, 3μM, and 1μM GABA (C). Reference data was normalized to -0.4 in to reflect the lower maximum open probability of αβ receptors.

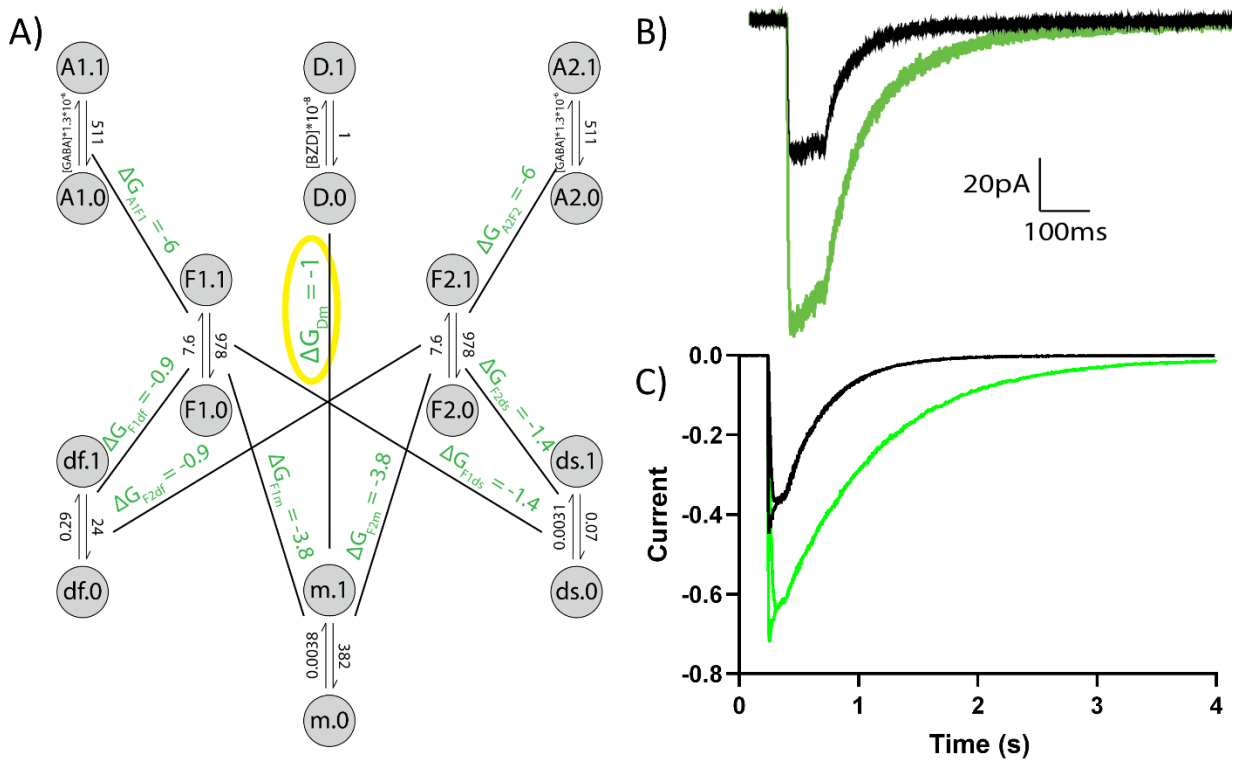

Figure 5.5 – DBI directly interacts with main gate to slow rate of deactivation and significantly increase peak currents even at high concentrations of GABA. A) A DBI element (D) is added to the elements-based model described in Figure 5.4, with a direct interaction with the main gate where $\Delta G_{Dm} = -1$. B) Sample outside-out patch clamp recording traces of 8 averaged 150ms pulses of 50μM GABA (black) and 50μM GABA + 10μM DBI (green). DBI co-application causes slower rates of deactivation and increased peak current amplitudes**.** C) Simulated currents from 150ms pulses of 1mM and 50μM GABA in the presence (green) and absence (black) of 10μM DBI. Simulated traces show slower rates of deactivation and roughly 2-times larger peak current amplitudes.

	Effect on GABA current amplitude		$\frac{\text{10-90\% Rise Time}_{(GABA+DBI)}}{\text{10-90\% Rise Time}_{(GABA)}}$		$\frac{\tau_{W(GABA+DBI)}}{\tau_{W(GABA)}}$		n
	Mean±SD	p-value	Mean±SD	p-value	Mean±SD	p-value	
$\alpha_5\beta_3$	2.67±0.97	0.0009	1.20±1.29	0.66	1.54±0.62	0.031	9
$\alpha_5\beta_3\gamma_{2L}$	1.13±0.37	0.23	0.94±0.45	0.61	1.03±0.27	0.65	14

Table 5.1 – Summary of DBI effects on amplitude, deactivation, and activation for $\alpha_5\beta_3$ and $\alpha_5\beta_3\gamma_{2L}$ receptors. Table showing mean±SD and p-values from one sample t-tests for rundown-corrected amplitude, 10-90% rise time$_{(GABA+DBI)}$/10-90% rise time$_{(GABA)}$, and $\tau_{w(GABA+DBI)}/\tau_{w(GABA)}$, as well as n of total patches for applying DBI to $\alpha_5\beta_3$ and $\alpha_5\beta_3\gamma_{2L}$ receptors.

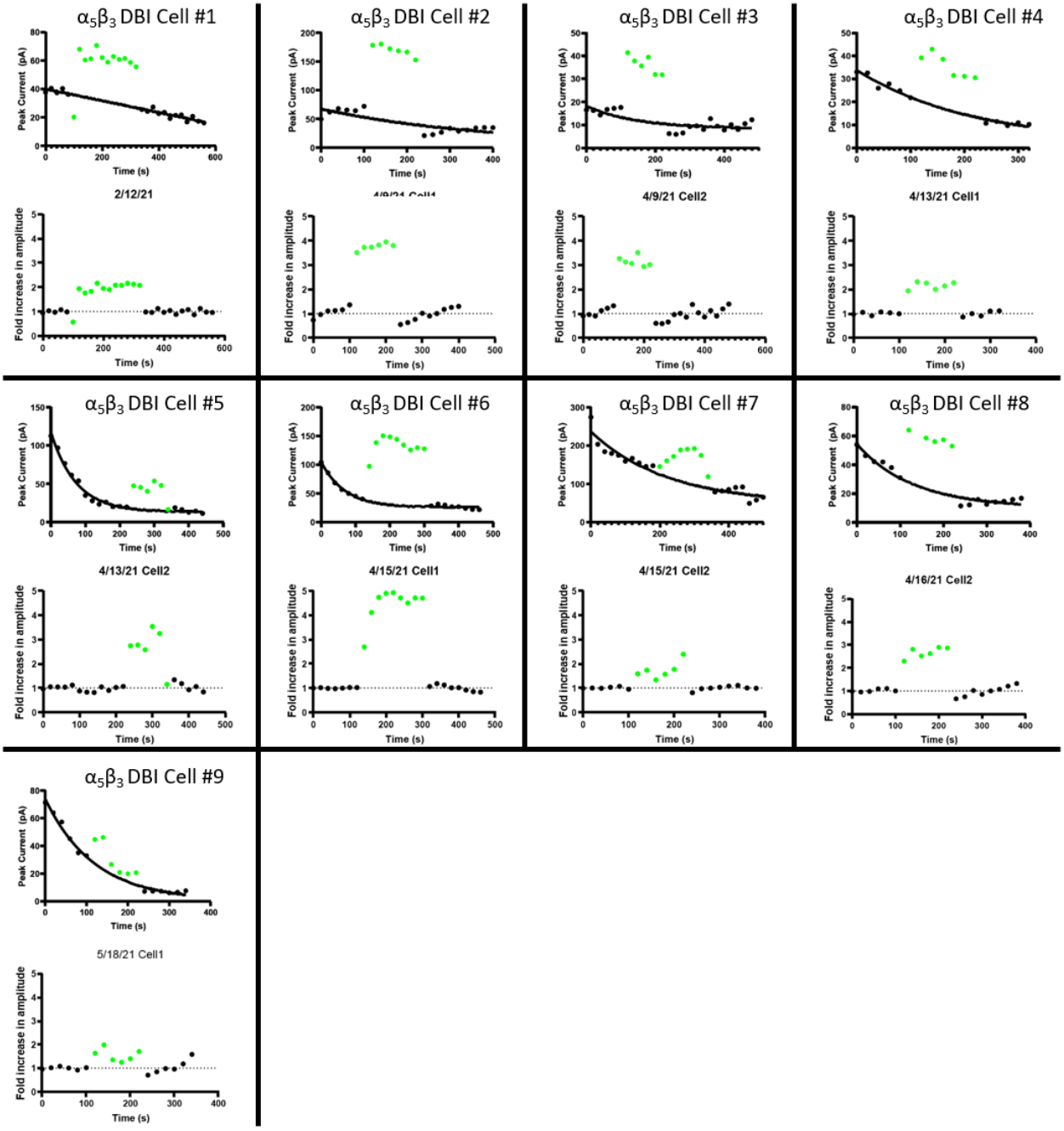

Supplemental Figure 5.1 – Plots of peak current and fold increase in amplitude for each patch of $\alpha_5\beta_3$ receptors in the presence of GABA and DBI. Top graphs showing peak current responses over time for GABA (black) and GABA+DBI (green). GABA peak current responses are fit with a one-phase decay equation where PeakCurrent = $(PeakCurrent_0\text{-}Plateau)*e^{-Kt}$. $PeakCurrent_0$ is the current at t=0, Plateau is PeakCurrent at t=∞, K = rate constant of decay (s^{-}

[1]), and t is time. Bottom graphs plot fold increase in amplitude (raw amplitude/one-phase decay predicted amplitude) over time.

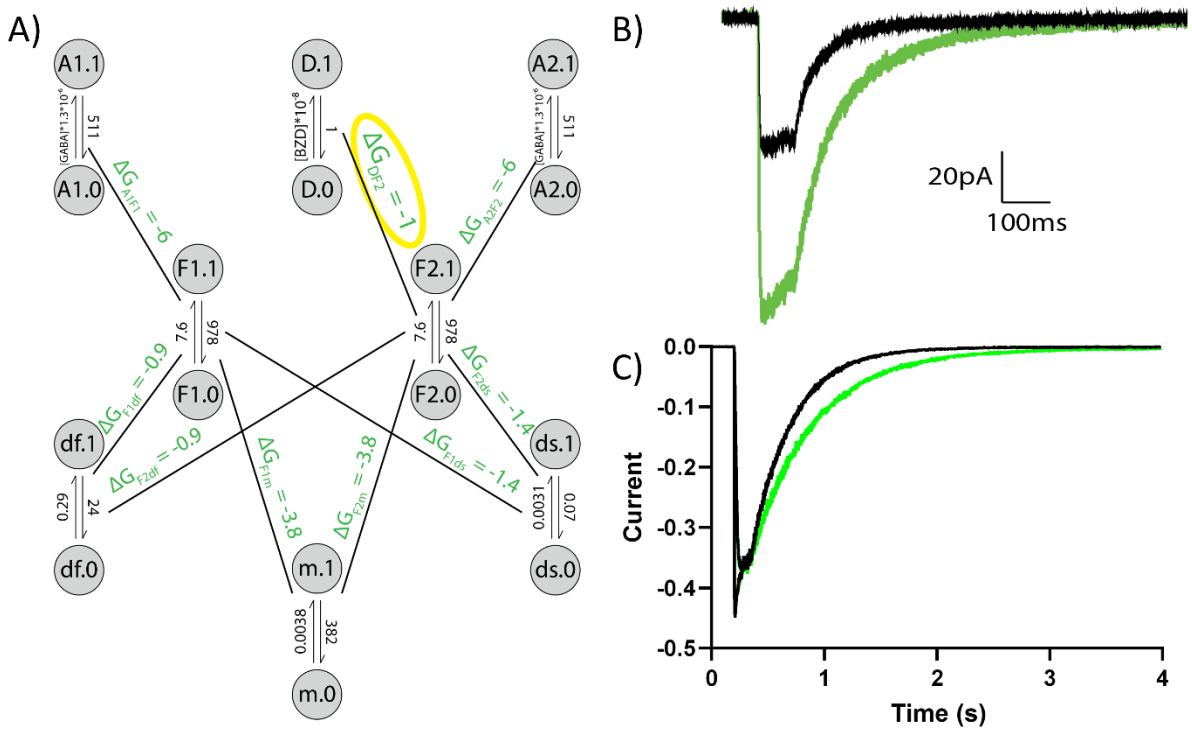

Supplemental Figure 5.2 – A stabilizing interaction between DBI and the F-element does not accurately simulate experimental data. A) A DBI element (D) is added to the elements-based model described in Figure 5.4, with a direct interaction with the F-element (F2) where $\Delta G_{DF2} = -1$. B) Sample outside-out patch clamp recording traces of 8 averaged 150ms pulses of 50μM GABA (black) and 50μM GABA + 10μM DBI (green). DBI co-application causes slower rates of deactivation and increased peak current amplitudes**.** C) Simulated currents from 150ms pulses of 1mM and 50μM GABA in the presence (green) and absence (black) of 10μM DBI. Simulated traces show that DBI binding slows the rate of deactivation as seen in the experimental data, but does not increase the peak current amplitude.

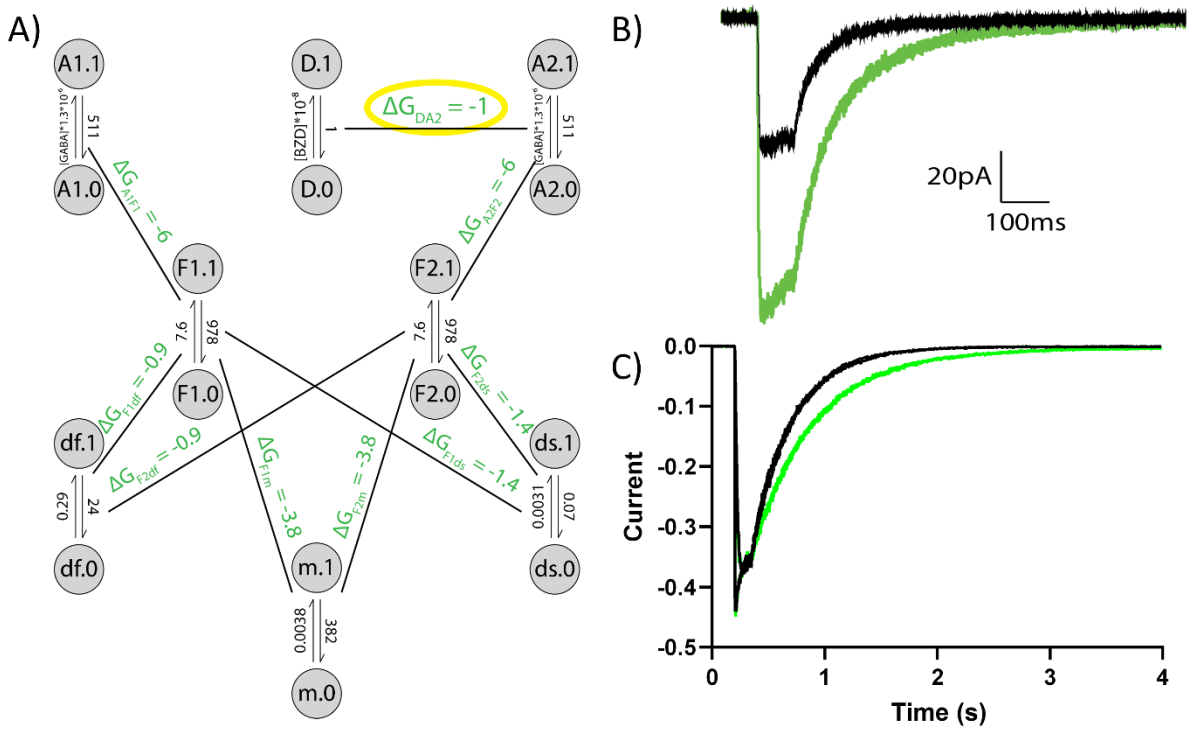

Supplemental Figure 5.3 – A stabilizing interaction between DBI and the GABA binding site does not accurately simulate experimental data. A) A DBI element (D) is added to the elements-based model described in Figure 5.4, with a direct interaction with the GABA binding site (A2) where $\Delta G_{DA2} = -1$. B) Sample outside-out patch clamp recording traces of 8 averaged 150ms pulses of 50μM GABA (black) and 50μM GABA + 10μM DBI (green). DBI co-application causes slower rates of deactivation and increased peak current amplitudes**.** C) Simulated currents from 150ms pulses of 1mM and 50μM GABA in the presence (green) and absence (black) of 10μM DBI. Simulated traces show that DBI binding slows the rate of deactivation as seen in the experimental data, but does not increase the peak current amplitude.

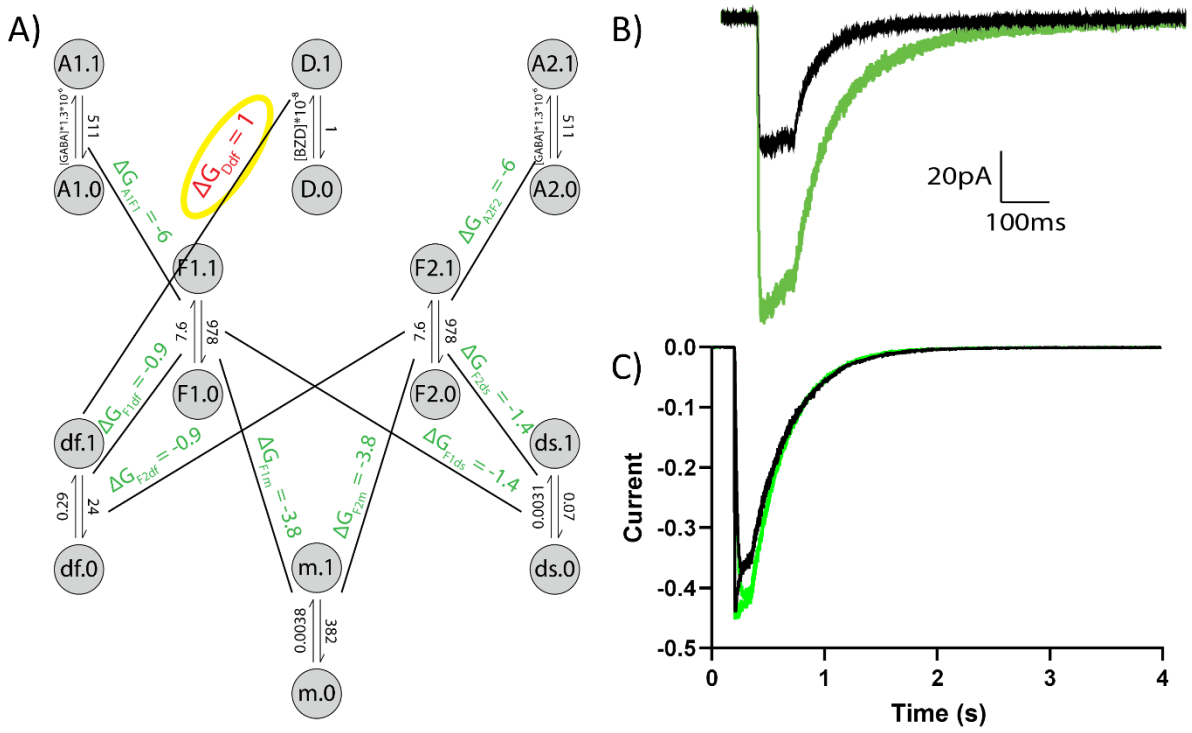

Supplemental Figure 5.4 – A destabilizing interaction between DBI and the fast desensitization gate does not accurately simulate experimental data. A) A DBI element (D) is added to the elements-based model described in Figure 5.4, with a direct interaction with the fast desensitization gate (df) where $\Delta G_{Ddf} = 1$. B) Sample outside-out patch clamp recording traces of 8 averaged 150ms pulses of 50μM GABA (black) and 50μM GABA + 10μM DBI (green). DBI co-application causes slower rates of deactivation and increased peak current amplitudes**.** C) Simulated currents from 150ms pulses of 1mM and 50μM GABA in the presence (green) and absence (black) of 10μM DBI. Simulated traces show that DBI binding slightly increases peak current amplitude for 50μM GABA, though not as strongly as seen in the experimental data. Deactivation rates are unchanged by the presence of DBI, which does not match the experimental data.

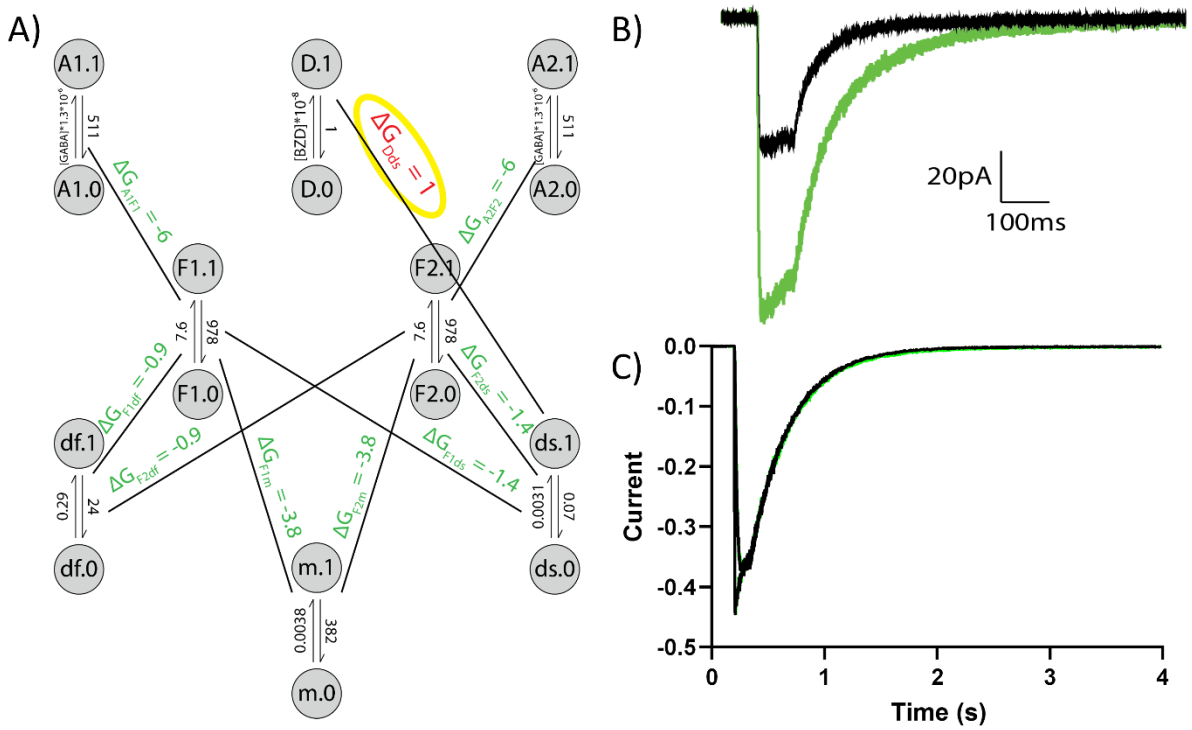

Supplemental Figure 5.5 – A destabilizing interaction between DBI and the slow desensitization gate does not accurately simulate experimental data. A) A DBI element (D) is added to the elements-based model described in Figure 5.4, with a direct interaction with the slow desensitization gate (ds) where $\Delta G_{Dds} = 1$. B) Sample outside-out patch clamp recording traces of 8 averaged 150ms pulses of 50μM GABA (black) and 50μM GABA + 10μM DBI (green). DBI co-application causes slower rates of deactivation and increased peak current amplitudes**.** C) Simulated currents from 150ms pulses of 1mM and 50μM GABA in the presence (green) and absence (black) of 10μM DBI. Simulated traces show that DBI binding does not affect peak current amplitude or the rate of deactivation for 150ms pulses, which does not reflect experimental data.

		Effect on GABA current amplitude	Normalized deactivation	Normalized activation	Starting Amp	Noise/ Amp %
$\alpha_5\beta_3$ DBI	Cell #1	1.89	2.55	3.76	27.1	9.23
	Cell #3	2.67	2.50	0.58	18.6	10.75
	Cell #9	1.56	1.69	2.85	46.7	2.14
	Cell #4	4.44	1.58	0.16	55.6	3.60
	Cell #7	3.76	1.38	0.33	57	3.51
	Cell #6	2.67	1.14	1.59	35.4	5.65
	Cell #2	2.15	1.08	0.17	21.9	9.13
	Cell #8	3.15	1.00	0.57	12.4	4.03
	Cell #5	1.73	0.91	0.77	37.3	6.70
α5β3γ2L DBI	Cell #13	2.00	1.56	1.01	13.07	7.65
	Cell #12	1.26	1.28	1.09	14.69	3.40
	Cell #5	1.25	1.26	0.72	32.1	6.23
	Cell #10	0.90	1.19	0.86	71.52	2.10
	Cell #11	1.20	1.19	0.57	65.69	5.33
	Cell #14	0.54	1.16	1.59	56.21	2.67
	Cell #7	0.90	1.07	0.52	204.8	0.24
	Cell #8	1.04	0.96	0.88	17.2	2.91
	Cell #1	1.03	0.91	1.81	191.55	1.04
	Cell #6	1.34	0.85	0.52	96	2.08
	Cell #3	1.61	0.82	0.77	159.3	0.31
	Cell #4	0.74	0.80	1.54	153.7	1.30
	Cell #2	0.80	0.63	0.24	68.2	0.73
	Cell #9	1.14	0.60	0.99	75	0.67

Supplemental Table 5.1 - Fold increase in amplitude, normalized deactivation, normalized activation, noise to amplitude ratio and starting amplitude for each patch of $\alpha_5\beta_3$ and $\alpha_5\beta_3\gamma_{2L}$ receptors. Table showing rundown-corrected amplitude, normalized deactivation and activation, noise to amplitude ratios and the starting amplitude for DBI applied to $\alpha_5\beta_3$ (top) and $\alpha_5\beta_3\gamma_{2L}$ receptors (bottom) for every patch. Columns are colored from white to darkest shade to

indicate lowest to highest value. Rows have been sorted by highest normalized deactivation value.

CHAPTER VI:

Evidence for the Release of DBI Derived Peptides in Brain Cell Cultures

Introduction

The diazepam binding inhibitor (DBI) is a protein which was identified by its ability to block the binding of benzodiazepines (BZDs) to the GABA-A receptor (GABAR) (Guidotti et al., 1983). Direct application of DBI and its peptide cleavage product, octadecaneuropeptide (ODN), can alter GABA-elicited currents, as shown in earlier chapters of this thesis as well as evidence from patch clamp recordings of outside-out patches from neurons located in the subgranular and subventricular zones (Alfonso et al., 2012; Dumitru et al., 2017). However, which cells release DBI and ODN, and the mechanism(s) by which they are released to act on the GABAR are not well established.

Numerous studies using cultured astrocytes have demonstrated the release of DBI and modulation of release by a variety of different factors: beta-amyloid protein increases the astrocytic release of DBI (Tokay et al., 2008), while application of GABA and somatostatin reduce the release of DBI (Masmoudi et al., 2005; Patte et al., 1995). Other experiments in cultured astrocytes revealed that release of DBI can be blocked by using inhibitors of PKA, PKC and phospholipase C, as well as an ABC transport blocker, which suggests that not only is DBI released from astrocytes, this release is mediated by an ABC transporter protein (Tokay et al., 2008). Additionally, slice recordings in the thalamic reticular nucleus show that the use of fluorocitrate, a gliotoxin, alters GABAR currents in wild-type mice but does not affect GABAR currents for DBI knockout mice, suggesting astrocytes are necessary in order for DBI to act on neuronal GABARs in this region (Christian and Huguenard, 2013).

While there is strong evidence showing astrocytes express and release DBI, there is little evidence regarding neuronal release of DBI. Immunohistochemistry experiments have shown that DBI protein is expressed in neurons (Alho et al., 1989; Alho et al., 1990; Ferrarese et al., 1987) and RNA-Seq detects DBI mRNA in both mouse and human neurons (Zhang et al., 2014; Zhang et al., 2016), but the ability of these neurons to release DBI or ODN has not been explored. My initial experiments using a multielectrode array (MEA) described below suggested that neurons derived from induced pluripotent stem cells (iPSCs) may be releasing an endogenous BZD, based on the ability of the BZD-site antagonist, flumazenil (FLZ), to alter neuronal communication. I then utilized four different mass spectrometry techniques (MALDI-TOF, Orbitrap, Triple-Quad coupled with nanospray, and FTICR) to evaluate whether the DBI-derived peptide ODN could be detected in media conditioned by iPSC-derived glutamatergic neurons, GABAergic neurons, or astrocytes. We were unable to detect ODN in the media from any of the cell types, even astrocytes. We cannot exclude the possibility that ODN may be present but at too low of a concentration to detect or that the relatively pure populations of neurons derived from iPSCs do not have the correct signaling cues needed to foster robust DBI expression and/or signaling.

Methods

IPSC-derived brain cell cultures

Human iPSC derived brain cells were obtained from Cellular Dynamics, Inc (Madison, WI). Glutamatergic neurons (iCell GlutaNeurons) and GABAergic neurons (iCell GABANeurons, FujiFilm Cellular Dynamics Inc, Madison, WI) were grown on plates coated with 0.01% poly-L ornithine (PLO) and Matrigel (Corning, Corning, NY), and cultured in BrainPhys neuronal culture medium without phenol red (STEMCELL, Vancouver, BC) with iCell Neural Supplement A (Cellular Dynamics Inc, Madison, WI) for GABAergic neurons, and Neural Supplement B (Cellular Dynamics Inc, Madison, WI), iCell Nervous System Supplement (Cellular Dynamics

Inc, Madison, WI), N-2 supplement (Thermo Fisher Scientific, Waltham, MA), laminin (Sigma-Aldrich, St. Louis, MO) and penicillin-streptomycin (Thermo Fisher Scientific, Waltham, MA) for glutamatergic neurons. Cells were plated at $2x10^5$ cells/cm^2 in 6-well plates and incubated at 37°C, 5% CO_2. Media was replaced every 48-72 hours. Four lots of glutamatergic neurons were thawed from individual vials and were designated Lots 1-4. iCell astrocytes were provided by Dr. Sheibani's lab (UW-Madison) and were initially plated and grown in DMEM with FBS for 14 days, but were switched to the same supplemented BrainPhys media as glutamatergic neurons for 72h before use.

Multielectrode array recording

Glutamaterigic neurons were plated on a MEA (Axion, Atlanta, GA) with 48 wells per plate and 16 electrodes per well. Plates were left in the same supplemented BrainPhys media for 48h prior to experimentation. Baseline recordings were obtained, after which 30x concentrations of FLZ were added in 10µL samples to 300µL wells. Final FLZ concentrations were 0.3, 1, 3, 5, 10, 30 and 50µM (in < 0.5% DMSO final) with six replicates per condition. A control plate was also used with cells in unchanged media for 60h, with 0.5% DMSO, added to each well. 10 min after drug additions, a second MEA recording was obtained. 20 min later, the media was exchanged for fresh media in the control plate and a third MEA reading was recorded.

Mass spectrometry

iPSC derived GABAergic, glutamatergic and astrocytic cells were cultured in 6 well plates for fourteen days after thawing, with media changes every 72h. 17 days after thawing, 1mL samples of media from a total volume of 2mL were taken from each well and processed for a variety of mass spectrometry techniques to detect ODN.

Working with UW Madison's Biotechnology Center, samples were fractionated using high-performance liquid chromatography. Fractionations of synthetic ODN (Alfa Aeser, Ward Hill, MA) or isotopically-labelled ODN (Thermo Fisher, Waltham, MA) suspended in BrainPhys to determine the elution pattern of ODN. Spectra were then obtained from the HPLC fractions, which should contain ODN, using three different mass spectrometry methodologies: matrix-assisted laser desorption/ionization (MALDI), an Orbitrap ion trap mass analyzer, or a triple-quad 5500 fitted with a nanospray ionization.

Media samples were also studied in collaboration with Dr. Ying Ge at the Human Proteomics Core Facility (UW Madison). Media samples and synthetic ODN in BrainPhys were prepped for FTICR using Pierce C18 tips (Thermo Scientific). Samples were adjusted to 0.5% trifluoracetic acid (TFA) using 2.5% TFA in water and filtered through Pierce C18 tips that were initially washed with 50% acetonitrile (ACN) in water and equilibrated with 0.1% TFA. Protein bound to the C18 resin was rinsed with 0.1% TFA/5% ACN and eluted with 0.1% formic acid in 95% ACN solution. A SpeedVac vacuum concentrator was used to remove solvent, and samples were reconstituted in 20µL of 0.1% formic acid in 50% ACN in water. Samples were then analyzed Using Fourier-transform ion cyclotron resonance (FTICR) and mass spectra were obtained. Six starting concentrations of synthetic ODN (1mM, 10µM, 100nM, 1nM, 10pM and 100fM) were used to determine the lowest concentration of ODN that was detectable using this method.

Results and Discussion

We utilized an MEA to examine if an endogenous, secreted compound targeting GABARs affected synchronous bursting in IPSC-derived glutamatergic cells. The MEA is a plate with sixteen 50µm electrodes arranged in a four-by-four grid with 350µm between electrodes at the bottom of each well in a 48-well plate (Figure 6.1A and B). These electrodes detect network-level electric events between neurons plated in each well. The electrical activity is represented

as both a heatmap (Figure 6.1C) and as individual lines on a raster plot corresponding to each action potential detected by the electrode (Figure 6.1D). Raster plots from each of the sixteen electrodes are displayed together showing electrical activity over time, which an overlayed histogram of activity showing potential synchronous activity across the well (Figure 6.1E).

Glutamatergic neurons in fresh media tend to burst synchronously across the well, with cells firing at the same time at multiple electrodes at regular intervals (Figure 6.1E). However, the neurons lose this synchronous bursting phenotype following 48h in the same media (Figure 6.2), where 16 of 36 wells were not bursting synchronously. Application of FLZ (Ro15-1788, BZD binding site antagonist, final concentration in well 0.3, 1, 3, 10, 30 and 50μM) restored bursting in 13 of the 16 non-bursting wells in a dose-dependent manner, leading to synchronous activity in 33 out of 36 wells.

A second, control plate of neurons had lost the bursting phenotype in all wells. Application of DMSO (0.5% final concentration, vehicle used for dissolving FLZ) did not affect signaling, but changing the media restored bursting for 47 of 48 wells (Figure 6.2B). Overall, the data suggest that glutamatergic neurons are releasing a compound into the media that builds up over time and inhibits rhythmic, synchronous bursting. The effects of this compound are blocked by FLZ. The ability of this BZD-site zero modulator to restore rhythmic signaling suggests that a released compound may bind at the BZD site. At the time of these experiments, biosafety restrictions at Cellular Dynamics prevented us from applying purified DBI to cells on the MEA. Instead, we used mass spectrometry to evaluate the presence of the DBI cleavage product, ODN, in media conditioned by these glutamatergic neurons.

To examine if this released compound could be DBI or one of its cleavage products, we collected media from iPSC-derived glutamatergic and GABAergic neurons, as well as astrocytes and used a variety of mass spectrometry techniques to determine if ODN was present in the media. In order to simplify the analysis of our mass spectra, we looked for the shorter ODN

peptide rather than full-length DBI. I worked with both the UW Madison Biotechnology Center and the Human Proteomics Core Facility (Table 6.1).

Initially, we used MALDI-TOF to look for ODN in media conditioned by glutamatergic neurons. MALDI-TOF is one of the fastest and least expensive methods for peptide mass fingerprinting (Sommerer et al., 2007). After culturing neurons in six-well plates for seventeen days and replacing media every 72h, we took 1mL samples from each well (total volume per well was 2mL). Synthetic ODN in water was used as a control. Synthetic ODN and media samples were fractionated using HPLC, and the relevant fractions were dried down and resuspended with 0.1% formic acid. Initial MALDI and MS/MS spectra indicated that ODN was present in two of the six wells (Figure 6.3), based on similarities in molecular mass and comparable relative abundances of ions during fragmentation.

In order to examine these samples with higher sensitivity, we used an Orbitrap which has higher resolution and greater mass accuracy than MALDI-TOF and allows a targeted method to detect ODN which increases the sensitivity. ODN was detected in the media samples similar to what was seen using MALDI. However, ODN was also detected in the water blank, raising concerns that residual synthetic ODN may have contaminated the experimental samples during fractionation. We then switched to using isotopically labelled ODN as a control since it can be readily distinguished from endogenous ODN by changes in its mass. Thus, we spiked each media sample with isotopically labelled ODN to act as an internal control. Repeating the Orbitrap experiment with the new standard, we detected very low levels of ODN in two of the six wells suggesting that ODN was being released in these wells (Figure 6.4). When we repeated the MALDI-TOF and Orbitrap experiments with media exposed for 72h to a second lot of glutamatergic neurons 14 days post-thaw, and isotopically labelled ODN, ODN was not detected in any of the samples. However, following the fractionation, these samples had lower than expected levels of even the labelled peptide standard.

In an effort to further increase our sensitivity, we switched to a Triple Quad 5500 LC-MS/MS system coupled with nanospray, which should increase detection of ODN. We analyzed glutamatergic neurons from lots 1-3 using this technique and did not detect ODN in lots 1 or 2 (Figure 6.5). For the third lot, we detected low levels of ODN in both the media samples and surprisingly also in the water blanks. After conversation with the manufacturer of the isotopically labelled ODN, we learned that their peptides are not fully labelled, and still contain low levels of unlabeled protein (1%). This makes it challenging to determine if low levels of detected ODN are endogenously released into media or if they originated from our partially-labelled control.

While we had some early positive indications that ODN was present in glutamatergic-conditioned media, we were ultimately unable to consistently detect this peptide using MALDI, Orbitrap, or Triple Quad. Our initial positive mass spectrometry results may have been caused by contamination from a variety of sources, including both our synthetic and isotopically-labeled ODN controls. After our initial experiments using synthetic ODN as a control, we detected ODN present even in a water blank, suggesting carryover likely originating from our synthetic control. Switching to isotopically labeled ODN spiked into each sample also led to contamination, due to low levels of unlabeled ODN present in the isotopic control samples.

Spectra for media incubated for 72 hours with GABAergic neurons 17 days post-thaw were also obtained using Orbitrap and Triple-Quad instruments. Six biological replicates of media were fractionated using the same technique as the glutamatergic media samples. Neither experiment detected endogenous ODN in any media samples or blanks.

After exhausting our efforts with the Biotechnology Center, we worked with the Human Proteomics Core Facility to use their FTICR instrument, which is generally thought to be the highest level of performance and resolving power. In order to determine the detection limits for ODN, we used a range of concentrations of synthetic ODN from 1mM to 1pM in media. Samples were dried down using a speed-vacuum. C18 resin was used to clean and resuspend samples

in 0.1% formic acid in 50% ACN in water. FTICR spectra for these samples (Figure 6.6A) revealed that the $[ODN\text{-}NH_3]^{2+}$ peak was in a low background area of the spectra and would be the best species to monitor for detecting ODN (Figure 6.6B). Examining this peak from spectra obtained from different concentrations of synthetic ODN revealed ODN suspended in BrainPhys media can be detected at 1nM but not 10pM (Figure 6.6C)

I calculated a rough estimate of how much ODN we might expect to be present in our media samples (Figure 6.7). Given the cell density plated in each well ($>1.5x10^6$ cells/cm^2) and an estimated 150 synapses per cultured neuron (Cullen et al., 2010), I estimate about $2.2x10^6$ synapses per well. Using two different estimates for synaptic volumes (Bracciali et al., 2008; Rangaraju et al., 2014) and an approximated synaptic ODN concentration of 10μM ODN (Masmoudi-Kouki et al., 2020), ODN concentration in the media may range between 10pM and 1nM ODN. These rough calculations are at the threshold range of detection.

We then used FTICR to analyze media samples taken from a fourth lot of glutamatergic neurons, but did not detect ODN in any of the samples. We were also unable to detect ODN in media from astrocytes. Drying down larger initial volumes of conditioned media may result in detectable levels of ODN given a greater theoretical number of moles of peptide in a larger volume.

It is also possible that we were unable to detect ODN in the media of glutamatergic neurons because of manufacturing changes in these IPSC-derived cells. Our initial experiments using the MEA relied on cells that lost the synchronous bursting phenotype over time but, due to pressure from larger corporate partners who found this loss of bursting to be inconvenient, current commercially available iPSC-derived glutamatergic neurons from Cellular Dynamics have been engineered to never lose the synchronous bursting phenotype. It is possible that in preventing the loss of bursting, Cellular Dynamics disrupted the cells' production or release of ODN. It would be helpful to compare RNASeq or DBI protein levels between the older

glutamatergic cells we used for the MEA experiments and the newer commercial cells we used for collecting mass spectra.

Our inability to detect ODN in media conditioned by astrocytes also suggests we may need to use larger initial volumes of media, given astrocytes have frequently been shown to release ODN using HPLC and radioimmunoassay (Farzampour et al., 2015). Multiple studies have demonstrated release of ODN or DBI from cultured astrocytes, and were able to modulate that release via the use of extracellular factors like GABA, somatostatin (Masmoudi et al., 2005; Patte et al., 1995) or beta-amyloid (Tokay et al., 2008). In the future, it would be interesting to see if it is possible to detect ODN in media conditioned by IPSC-derived astrocytes if a larger starting sample volume is used during initial concentration. Also, while my experiments were focused on using pure populations of neuronal cell types obtained from iPSC cells to help distinguish the type of cell that was releasing DBI, it is possible that these cells do not mimic the conditions seen *in vivo*. Current mass spectrometry methodology that I used was unable to detect ODN released from either of our iPSC-derived neuronal cell types, nor iPSC-derived astrocytes.

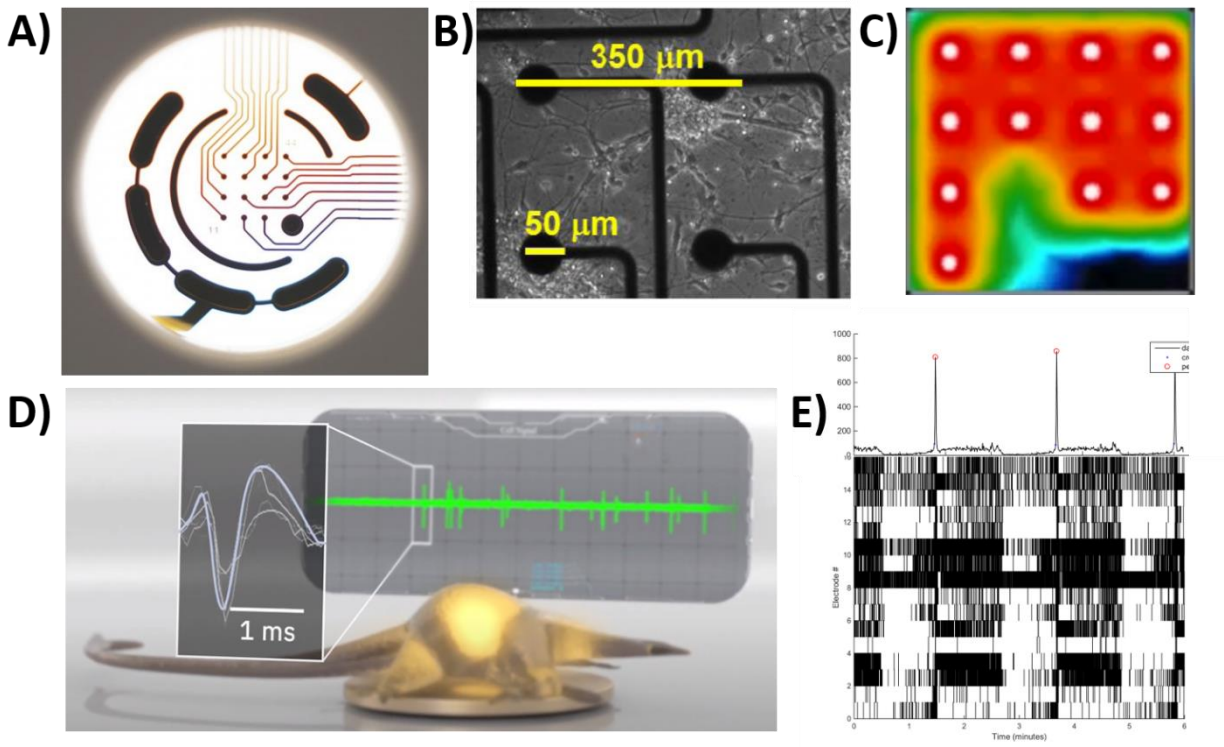

Figure 6.1 – Multielectrode array records electrical signals from plated neurons. A) Cartoon of multielectrode array (MEA) consisting of sixteen electrodes arranged in a four-by-four grid on the bottom of the well. B) Photo showing electrodes are 50µm wide and spaced 350µm apart. Neurons are plated on top of electrode grid. Electrical recordings can be presented either as a heatmap of activity at all sixteen electrodes in well (C), or as individual dashes on raster plot corresponding to a single action potential. D) Cartoon of neuron plated on electrode with inset showing an action potential in inset corresponding to lines on a raster plot. E) Sample raster plots from each of sixteen electrodes are depicted in rows. A histogram of activity for every electrode is shown above raster plots, demonstrating synchronous bursting across the well. Figure adapted from Axion Biosystems and Cellular Dynamics.

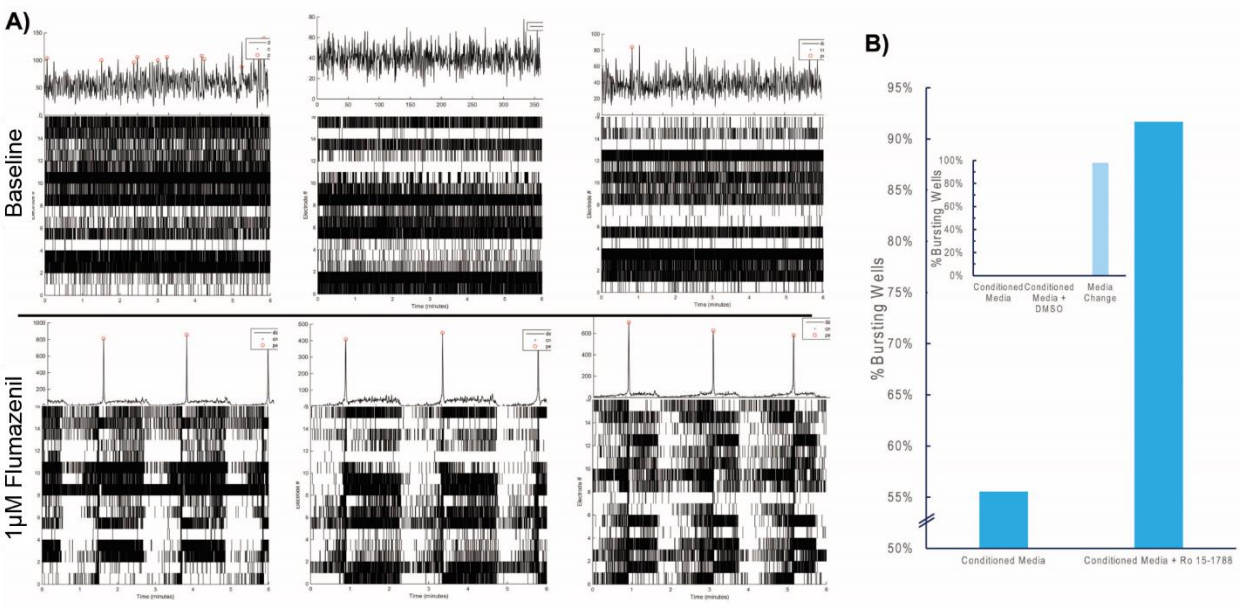

Figure 6.2 – Flumazenil restores bursting phenotype in iPSC-derived glutamatergic neurons. A) Example raster plots from MEA recordings of 3 wells of iPSC-derived glutamatergic neurons, with histograms at the top. GNCs lose bursting phenotype after >48 exposure to conditioned media (top). Application of BZD antagonist FLZ restores synchronous bursting (bottom). B) Bar graph showing percent of wells bursting synchronously. After 48h in conditioned media, only 55% of wells were bursting, but the addition of FLZ led to bursting in 92% of wells. Inset shows that a total loss of bursting after >48h exposure to conditioned media can be complete restored by changing media, but not by adding 0.5% DMSO, the solvent for FLZ. These experiments were done with the help of Dr. Kile Mangan and our collaborators at FujiFilm Cellular Dynamics, Inc.

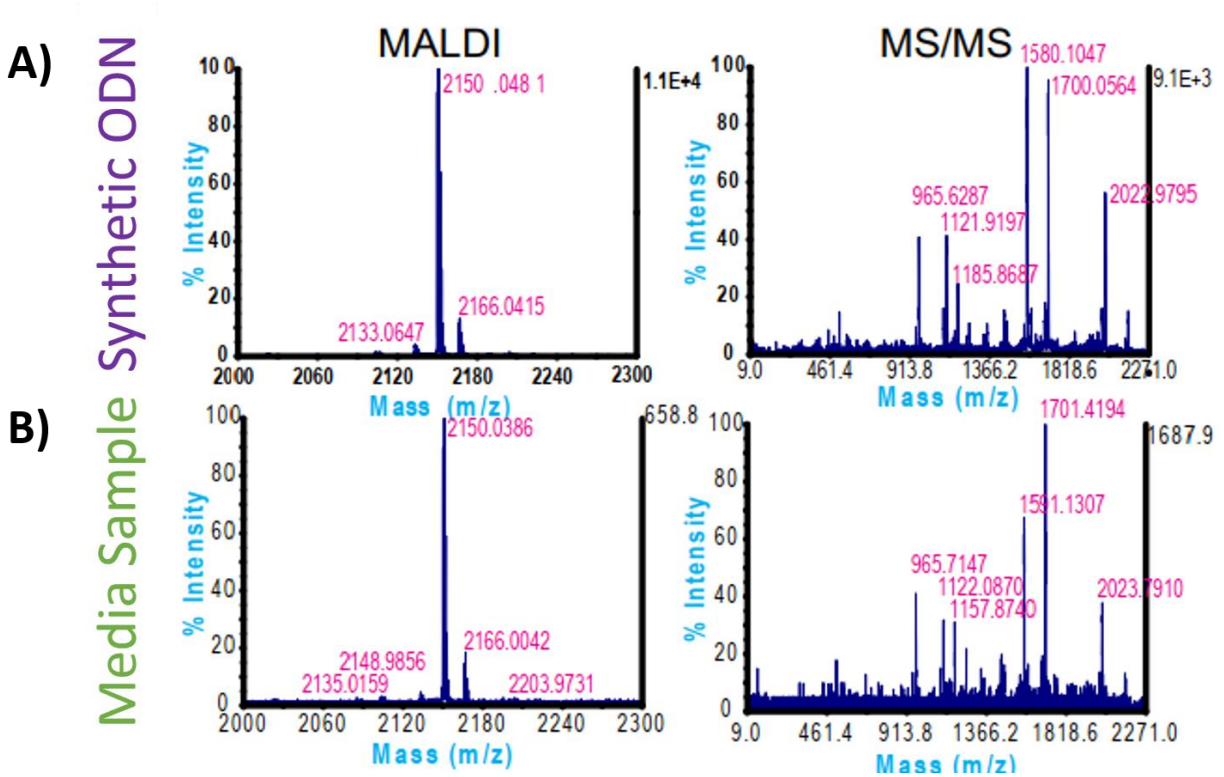

Figure 6.3 – MALDI detects ODN in media from glutamatergic neurons. Sample MALDI (left) and MS/MS (right) spectra from synthetic ODN (A) and glutamatergic neuron media (B) indicates presence of ODN in neuron-conditioned media. The synthetic and endogenous peptides have the same molar mass and produce the same ions with similar relative abundances during fragmentation. MALDI experiments were performed by Dr. Greg Barrett-Wilt at the University of Wisconsin-Madison Biotechnology Center.

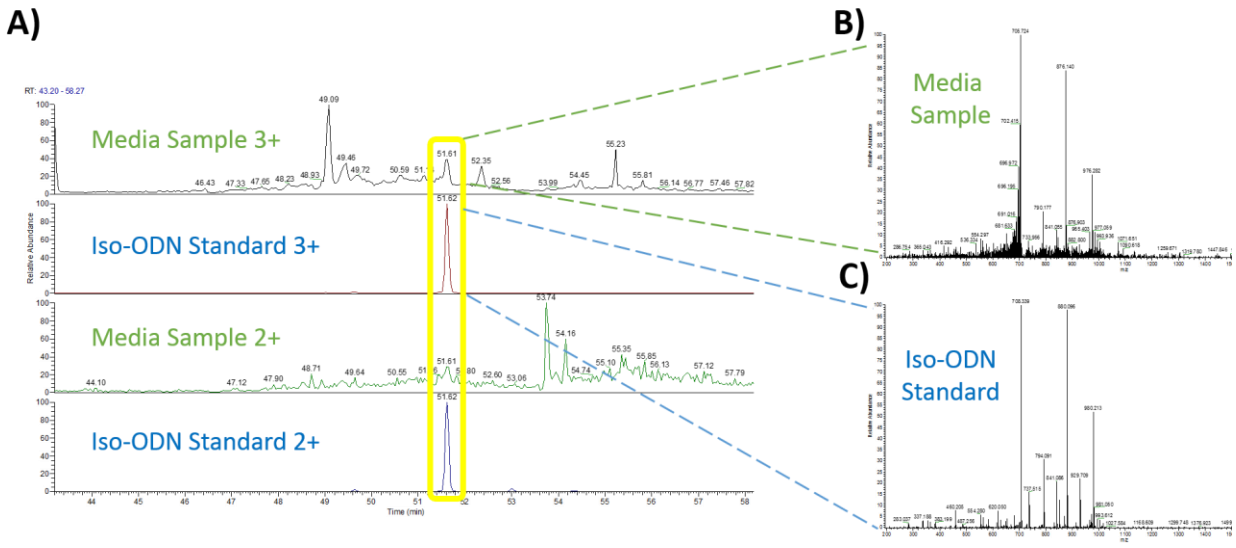

Figure 6.4 – Initial Orbitrap spectra show presence of ODN in media from glutamatergic neurons. Sample spectra of A) 3+ and 2+ species spectra showing peaks from endogenous peptide in media samples (first and third rows) and isotopically-labeled ODN. Peaks highlighted in yellow boxes are detected endogenously in media and from the isotopically-labeled control peptide. MS/MS spectra for 3+ peaks from media sample (B) and isotopically-labeled control peptide (C) are similar in fragmentation and abundance, suggesting the presence of ODN in media. Orbitrap experiments were performed by Dr. Greg Barrett-Wilt at the University of Wisconsin-Madison Biotechnology Center.

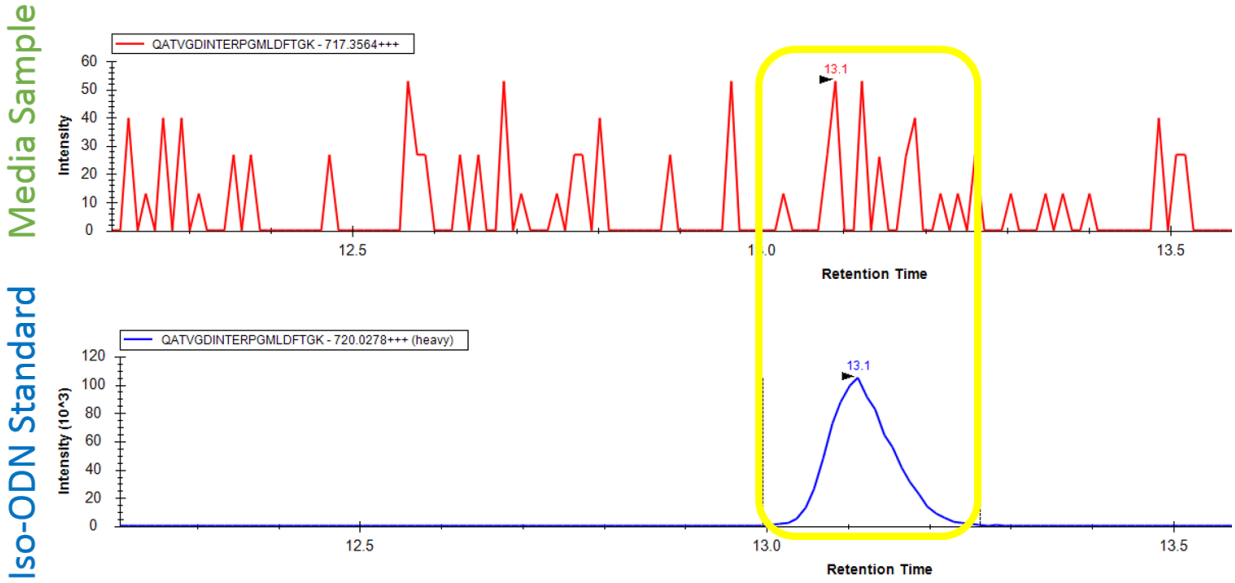

Figure 6.5 – Triple-Quad does not detect ODN in glutamatergic-conditioned media samples. Sample spectra showing no peaks discernable amidst noise in neuron-conditioned media when compared to isotopically-labeled ODN peptide standard. Yellow box highlights expected peak location. Triple-Quad experiments were performed by Dr. Greg Barrett-Wilt at the University of Wisconsin-Madison Biotechnology Center.

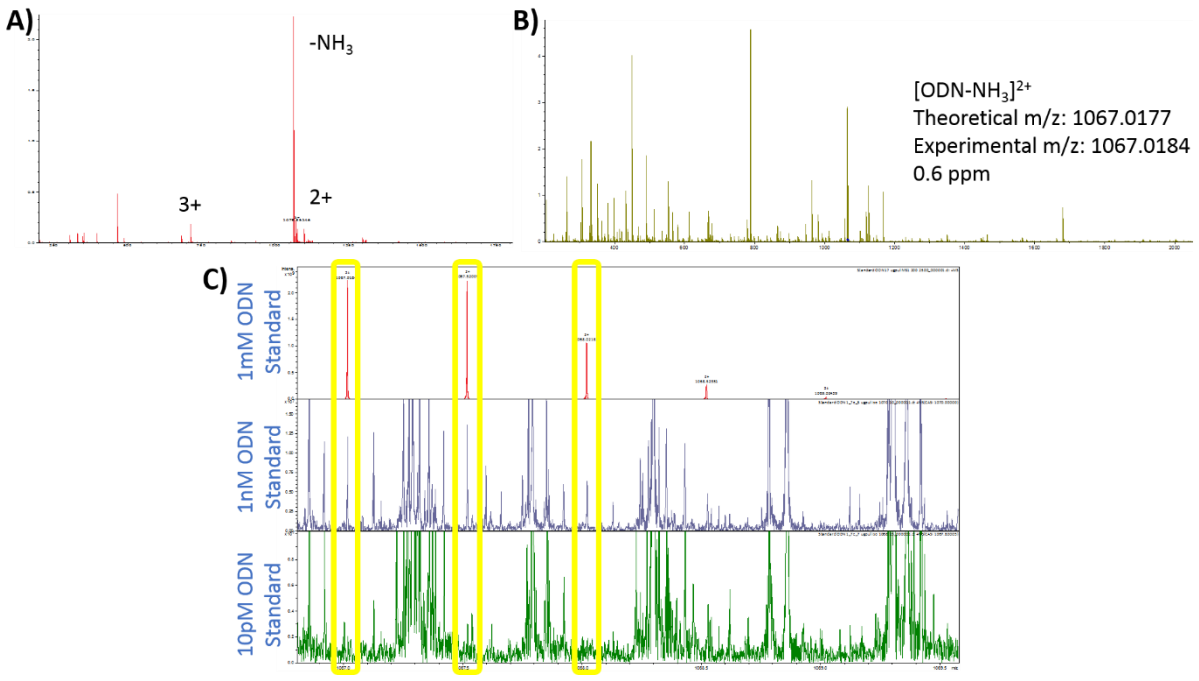

Figure 6.6 – FT-ICR can detect synthetic ODN in media at 1nM starting concentration, but not 10pM. A) Spectra of synthetic ODN suspended in BrainPhys at 1mM. B) Peaks for $[ODN\text{-}NH_3]^{2+}$ are in a low-noise region of the spectra and will be used to identify ODN. C) Comparing spectra of $[ODN\text{-}NH_3]^{2+}$ peaks (highlighted in yellow boxes) for 1mM, 1nM and 10pM starting concentrations of ODN in BrainPhys demonstrates that ODN can be detected at 1nM but not 10pM. FT-ICR experiments were performed with the help of Dr. Yanlong Zhu at the University of Wisconsin – Madison Human Proteomics Program Mass Spectrometry Facility.

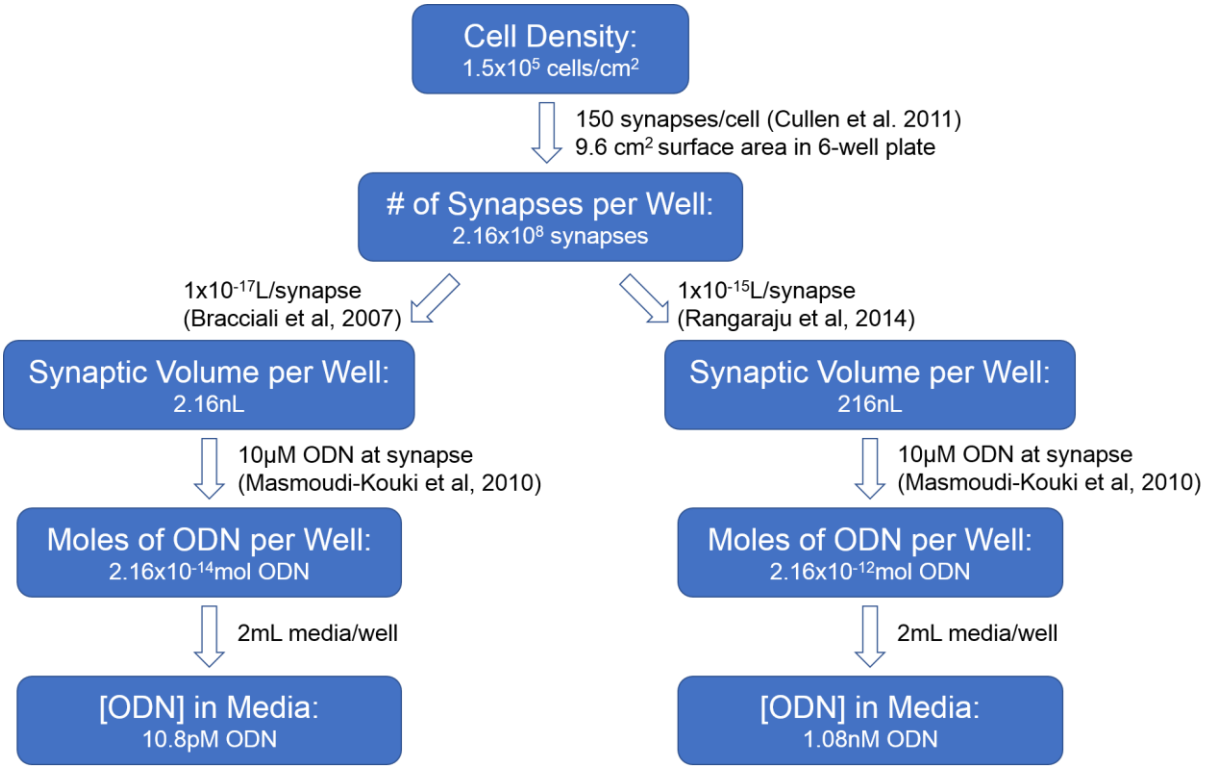

Figure 6.7 – Flow chart calculating theoretical ODN concentration of ODN in media. Flow chart shows how using the number of cells plated in each well, I estimated the concentration of ODN in media samples based on the assumptions of 150 synapses per cultured neuron, two different estimates of synaptic volume, and a potential concentration of 10μM ODN at each synapse. These assumptions allowed me to calculate the potential concentration of ODN in each well to be between 10pM and 1nM.

Instrument	Cell Type	Standard	Result
MALDI-TOF	Glutamatergic neurons - Lot 1	Synthetic ODN	ODN detected in samples
	Glutamatergic neurons - Lot 2	Isotopically-labelled ODN	No/very low ODN deteced in samples, standard levels are lower than expected
Orbitrap	Glutamatergic neurons - Lot 1	Synthetic ODN	ODN detected in samples and water blank
	Glutamatergic neurons - Lot 1	Isotopically-labelled ODN	Maybe very low ODN detected in samples, not blanks
	Glutamatergic neurons - Lot 2	Isotopically-labelled ODN	No/very low ODN detected in samples, standard levels are lower than expected
	GABAergic neurons	Isotopically-labelled ODN	No ODN detected in samples or blanks
Triple-Quad 5500 w/ Nanospray	Glutamatergic neurons - Lot 1	Isotopically-labelled ODN	No ODN detected in samples or blanks
	Glutamatergic neurons - Lot 2	Isotopically-labelled ODN	No ODN detected in samples
	Glutamatergic neurons - Lot 3	Isotopically-labelled ODN	Potentially very low levels, but learned isotopic standard is not fully labelled
	GABAergic neurons	Isotopically-labelled ODN	No ODN detected in samples or blanks
FTICR	Unconditioned media	Synthetic ODN	Control experiment to determine level of detection is between 10pM and 1nM
	Glutamatergic neurons - Lot 4	Synthetic ODN	No ODN detected in samples or blanks
	Astrocytes	Synthetic ODN	No ODN detected in samples or blanks

Table 6.1 – Table summarizing the cell types studied using different mass spectrometry instruments. Media samples taken from glutamatergic neurons are highlighted in green, with each lot from different vials shown in different shades. Media samples from GABAergic neurons are highlighted in yellow and astrocytes in pink. For each instrument, the cell types tested are listed, along with what type of ODN standard was used, and the results of the experiment.

CHAPTER VII:

Discussion and Future Directions

Since its discovery in 1983, DBI has been referred to as a putative endogenous benzodiazepine (Guidotti et al., 1983). In addition to its ability to displace [^{3}H]-diazepam from binding the BZD site on GABARs in brain membrane homogenates (Guidotti et al., 1983), loss of DBI has been connected to disruptions in hippocampal-dependent learning, memory, and social behavior (Ujjainwala et al., 2018; Ujjainwala et al., 2019). Interestingly, DBI has been suggested as a positive modulator of GABARs in the thalamic reticular nucleus (Christian et al., 2013), but a NAM in the subventricular and hippocampal subgranular zones (Alfonso et al., 2012; Dumitru et al., 2017). Experiments in the Monyer lab showed that exogenously applied DBI-derived peptide, ODN, negatively modulated GABAR currents from wild-type stem cells in the subgranular zone of hippocampal slices, and that ODN modulation of BZD-insensitive GABAR mutants was significantly decreased (Dumitru et al., 2017). However, evidence for DBI's direct modulation of GABARs is limited. In this thesis, I took a reductionist approach to uncover DBI's modulatory effects on heterologously expressed GABARs and found that the effects of DBI are dependent on the GABAR subunit composition. I found:

1. DBI purified from *E. coli* heterologously expressing DBI is pure, non-aggregated and correctly folded, as indicated by SDS-PAGE and NMR (Chapter II).
2. The effect of DBI on GABARs is α subunit isoform dependent. α3-containing GABARs are weakly negatively modulated, while DBI is a PAM for α5-containing GABARs (Chapter III).
3. DBI does not modulate $\alpha_5\beta_3\gamma_{2L}$ receptors via the same mechanism as the BZD FZM. Data from outside-out patch clamp experiments show that, when coapplied with a near-saturating concentration of GABA (EC_{80}), FZM slows the rate of current deactivation while DBI does not. (Chapter IV).

4. DBI acts as a PAM and strongly modulates $\alpha_5\beta_3$ GABARs. Outside-out patch clamp experiments revealed that DBI slows the rate of current deactivation and significantly increases the peak current amplitude of saturating concentration of GABA (Chapter V).
5. DBI's modulation of GABARs does not require binding to the BZD site. Receptors lacking the α/γ BZD binding site are strongly modulated by DBI.
6. Use of an elements kinetic model suggests that DBI exerts its effects on αβ GABARs by directly stabilizing the main gate, rather than stabilizing an intermediate element like a PAM BZD (Chapter V). Modeling suggests that DBI may exert its effects on the $\alpha_5\beta_3\gamma_{2L}$ GABARs by weakly stabilizing a GABA-bound state (Chapter IV).

DBI's effects are subunit-dependent

In Chapter III, I used two-electrode voltage clamping (TEVC) and low concentrations of GABA to show that α3-containing GABARs heterologously expressed in *Xenopus* oocytes are weakly negatively modulated by DBI, while GABARs containing α5 subunits are positively modulated. These results provide an answer to a question raised by previously published work in the Monyer and Huguenard labs – how can DBI seemingly act as a NAM in some regions of the brain and a PAM in others? GABAR subunit composition varies by brain region (Olsen and Sieghart, 2009) and I have shown that DBI can act as either a PAM or a NAM depending on the α subunit identity.

While my results show that the effects of DBI can vary based on subunit combination, they contrast with the effects seen by the Monyer and Huguenard groups. Recordings in the hippocampal subgranular zone show that DBI or its peptide cleavage product, ODN, may be acting as a NAM (Dumitru et al., 2017). Given α5 subunits are highly expressed in the hippocampus (Sequeira et al., 2019), these published experiments would predict that heterologously expressed α5-containing receptors should be negatively modulated by DBI. Similarly, patch clamp recordings from the thalamic reticular nucleus where α3 is highly

expressed (Hörtnagl et al., 2013) show that these receptors may be positively modulated by DBI (Christian et al., 2013), while my experiments with heterologously expressed $\alpha_3\beta_3\gamma_{2L}$ receptors show that DBI acts as NAM.

There are several possible explanations for the differences between my data detailed in this thesis and published *in vivo* electrophysiology results. While I used full-length DBI purified from *E. coli,* the Monyer and Huguenard experiments relied primarily on up- or down-regulating endogenous DBI expression. DBI has several biologically active cleavage products, multiple predicted sites for post-translational modifications, and can bind long-chain fatty acids. Changes in any of these features may alter DBI's effects on GABAR modulation. While my initial experiments showed that preincubation with the long-chain fatty acid palimitoyl-CoA did not alter DBI's effects (Supplemental Figure 3.1), future study is needed to evaluate the effects of various DBI peptide cleavage products, possible post-translational modifications of DBI that might be present in eukaryotic cells, and alternate DBI protein isoform expression on GABAR function.

Additionally, future experiments should determine concentration-dependance of DBI actions. Some drugs such as propofol and barbiturates like pentobarbital exhibit dose-dependent effects on GABAR modulation. For example, pentobarbital positively modulates GABARs at low concentrations, directly causes the channel to open at concentrations above 50-500μM, and blocks the GABAR channel at greater than 1mM (Jackson et al., 1982; Muroi et al., 2009; Rüsch et al., 2004).

GABARs may also differ when comparing receptors endogenously expressed in neurons to those heterologously expressed in *Xenopus* oocytes. While *Xenopus* oocytes have been shown to be able to phosphorylate, glycosylate, and acetylate some exogenous proteins, they lack the tissue-specific enzymes necessary for post-translational modifications of some proteins (Colman et al., 1984; Lane, 1983). It is possible that some endogenous post-translational modifications are lacking when GABARs are expressed in *Xenopus* oocytes, which may alter the modulatory effects of DBI. Additionally, GABARs in neurons are likely associated with

accessory subunits like GARLH or Shisa7 (Han et al., 2019; Yamasaki et al., 2017). The potential absence of these accessory subunits in *Xenopus* oocytes and HEK-293 cells may alter the effects of DBI on the GABAR. Future experiments should be conducted to evaluate whether co-expression of GARLH or Shisa7 alongside GABARs alters the modulatory actions of DBI.

Future experiments to evaluate the effects of DBI on additional GABAR subunit compositions are needed. $\alpha_1\beta_2\gamma_{2L}$ receptors are the most widely expressed receptor combination across the brain (Olsen and Sieghart, 2009). The effects of DBI on this subunit combination are particularly important to evaluate due to its abundance.

Reconciling DBI TEVC and outside-out patch clamp effects

One point of interest in my thesis is the effect of DBI on $\alpha_5\beta_3\gamma_{2L}$ GABARs. In Chapter III, I used TEVC and showed that co-application of DBI potentiates GABA EC20 currents, but in Chapter IV, I demonstrated that DBI does not affect the amplitude, rise-time, or deactivation rate of currents elicited by GABA EC80. While the solution exchange times for TEVC are too slow to measure changes in deactivation, the potentiating effects of DBI can be measured via the increase in GABA EC20 current amplitudes. When using ultra-rapid solution exchange and patch clamping, drug-induced changes in the current deactivation rate are detectable at high near-saturating GABA concentrations when increases in GABA amplitude are difficult or near impossible to measure (e.g. BZD PAM effects). I believe that the different DBI effects that I observe when examining $\alpha_5\beta_3\gamma_{2L}$ GABARs are due to differences in the GABA concentration used in TEVC versus patch clamp experiments.

To test this idea, I used an elements-based kinetic model (as shown in Figure 4.6) to see what kinetic parameters DBI could be altering to generate my experimental observation that DBI potentiated GABA currents at low GABA concentrations (EC20) but had no effect on GABA current amplitude, rise-time, or deactivation at high GABA concentrations (EC80). I showed that a weak stabilizing interaction between a DBI element and a GABA-binding element caused a modest increase in peak current amplitude without altering the rate of deactivation at low

concentrations of GABA. As GABA approaches a saturating concentration, this stabilizing interaction has less of an effect, and the simulated peak currents are unchanged by the presence of DBI (Figure 7.1A, B).

Future experiments should test whether the differences in DBI's effects are due to GABA concentration. Experiments could be conducted using higher concentrations of GABA and TEVC or using lower GABA concentrations and patch clamping. Due to the propensity of an outside-out patch to run down, accurately recording small GABA currents can be difficult with this technique; these experiments would be more effective using whole-cell patch clamp to generate larger currents from a greater number of GABARs in an entire cell.

In the elements model, BZD potentiation is mediated by a direct interaction with an intermediate "F" element which couples GABA binding to channel gating (Goldschen-Ohm et al., 2014). In Dr. Vicki Tsao's thesis, she proposed that this F element represents an actual physical component of the GABAR, namely the β4-β5 linker of the α subunit which links the inner and outer β sheets in the ECD (Tsao, 2018). Our lab has previously shown that disruption of this linker via glycine insertion can significantly reduce the PAM effects of FZM (Venkatachalan and Czajkowski, 2012), and ongoing work in our lab indicates that disruption of this linker does not alter inhibition by a NAM like DMCM. In Appendix I of this thesis, I propose that DMCM modulates GABAR function through a direct interaction with a GABA binding site rather than an F-element. Similarly, I propose that DBI is modulating $\alpha_5\beta_3\gamma_{2L}$ GABA-binding directly rather than interacting with an F-element. Given the similarities between the proposed interactions for DBI and DMCM, it would be interesting to perform the TEVC experiments using α subunits with a disrupted β4-β5 linker to see if DBI can still positively modulate these mutants.

It would also be worthwhile to evaluate the kinetic effects of DBI on $\alpha_3\beta_3\gamma_{2L}$ GABARs. Experiments should be conducted using outside-out or whole cell patch using high and low concentrations of GABA in the presence and absence of DBI. I hypothesize that DBI binding would weakly destabilize the GABA-bound state, leading to kinetic changes similar to those

seen in the presence of DMCM (Supplemental Figure 7.1). If so, I would expect to see a reduction in amplitude at non-saturating concentrations of GABA and no changes in the rate of deactivation.

Another difference between the TEVC and outside-out patch clamp experimental approach is that in the outside-out patch clamping experiments, the patch is continually perfused with DBI and then switched to a GABA+DBI solution, whereas for the TEVC data, there was no preincubation with DBI. Further experiments should be conducted to evaluate whether preincubation with DBI has any effect on DBI's effect on GABAR currents during TEVC recording.

Implications for DBI's different effects on GABARs with and without γ subunit

Though DBI has often been described as an endogenous BZD, my thesis shows that DBI does not act like a BZD when it interacts with the GABAR. Not only do the macroscopic kinetic effects of DBI differ significantly from the BZD FZM, but a γ subunit is not even necessary for DBI to modulate a GABAR. Currents from αβ GABARs, which do not contain a BZD α/γ interface binding site, are significantly potentiated by DBI, as demonstrated by a 1.5-fold slowing in the rate of deactivation and a greater than two-fold increase in the peak current amplitude even at GABA EC90. In Chapter V, I demonstrate that DBI could exert its effects on $\alpha_5\beta_3$ GABARs by directly stabilizing the main gate using an elements-based kinetic model to simulate traces which resemble those recorded from $\alpha_5\beta_2$ receptors and reflect the lower open probability of αβ GABARs (Figure 7.1C). In future experiments, the maximum open probabilities for $\alpha_5\beta_3$ and $\alpha_5\beta_3\gamma_{2L}$ receptors in the presence and absence of DBI should be measured directly to confirm that $\alpha_5\beta_3$ GABARs have a lower maximum open probability and to evaluate whether DBI can increase the open probability.

My experiments suggest that underlying mechanisms underlying DBI's effects on αβ versus αβγ GABARs are different. It would be interesting to see if $\alpha_5\beta_3\gamma_{2L}$ receptors lacking a functional BZD site via a αH101R or γF77I mutation lose the ability to be potentiated by DBI at

low concentrations of GABA. Future experiments should also try a locate where DBI binds on the $\alpha_5\beta_3$ GABARs. One possibility is that γ-containing GABARs have a high affinity binding site for DBI at the BZD site in addition to a lower affinity binding site also present on $\alpha_5\beta_3$ receptors (Figure 7.2A, B).

Alternatively, $\alpha_5\beta_3$ GABARs may possess a unique binding site for DBI (Figure 7.2C, D). These receptors have unique inter-subunit interfaces compared to $\alpha_5\beta_3\gamma_{2L}$ receptors, either α/α or β/β depending on their stoichiometry. Some drugs like zolpidem are selective for a specific interface between homologous subunits of αβ receptors (α/α in the case of zolpidem) (Che Has et al., 2016). Further experiments could use concatemers of α-β-α-β-α or α-β-α-β-β receptors to assess whether DBI preferentially binds or potentiates one stoichiometry over another. Obtaining cryoEM structures of $\alpha_5\beta_3$ and $\alpha_5\beta_3\gamma_{2L}$ receptors in the presence of DBI would also shed more light on the differences in DBI binding.

DBI in the brain

DBI's effects on $\alpha_5\beta_3$ GABARs also raise questions about the physiological role αβ receptors have in GABAergic signaling in the brain, and what purpose might be served by an endogenous modulator for this receptor combination. αβ receptors are generally located extrasynaptically (Brickley and Mody, 2012; Mortensen and Smart, 2006) and are thought to mediate tonic inhibition. GABA-mediated tonic inhibition has been measured in the dentate gyrus (Nusser and Mody, 2002), hippocampal interneurons (Semyanov et al., 2003), and hippocampal CA1 (Bai et al., 2001), as well as other regions, by measurement of a persistent GABA-mediated conductance which can be abolished with the use of a GABA-antagonist like bicuculine or a channel-blocker like picrotoxin. This tonic current leads to increased cell conductance which affects the cell's likelihood of responding to an excitatory signal, leading to a reduction in a neuron's firing rate (Farrant and Nusser, 2005). If DBI is able to substantially increase the peak current and open probability of αβ receptors, this may be a new avenue through which the brain can regulate tonic inhibition. In addition, my data demonstrating that

DBI's effects on $\alpha_5\beta_3\gamma_{2L}$ receptors are only seen at low GABA concentrations would suggest that its effects on this GABAR subtype would be observed at extrasynaptic sites where GABA concentrations are low versus at synaptic sites where GABA concentration is in the millimolar range (Mody et al., 1994).

In order to explore this idea, future experiments should examine effects of DBI when recording from neurons. It would be intriguing to compare the effects of exogenously applied DBI on spontaneous IPSC duration and size, as well as evaluating DBI's effects on the inward holding current in the presence and absence of bicuculine or picrotoxin.

My results demonstrate DBI can modulate GABAR currents, and its effect on αβ receptors is especially robust. Dysfunctions in GABAergic signaling are linked to various diseases. Some forms of epilepsy are linked to a reduction in extracellular GABA concentration (Bai et al., 2001; During et al., 1995), which may be relevant for DBI as a regulator of tonic inhibition. Additionally, the Christian group has seen that loss of DBI in the hippocampus leads to disruptions in learning, memory, and social behavior in mice (Ujjainwala et al., 2018; Ujjainwala et al., 2019). These hippocampal-dependent processes are often mediated via α5-containing GABARs (Collinson et al., 2006; Crestani et al., 2002; Joksimović et al., 2013; Timić et al., 2013).

DBI's effects on α5-containing GABARs may also be linked to Alzheimer's disease. Alzheimer's patients are found to have elevated levels of DBI and ODN in cerebral spinal fluid as well as altered DBI transcript variant expression in the parietal zone (Barbaccia et al., 1986; Miettinen et al., 1995; Mills et al., 2013). Beta-amyloid, which accumulates and forms plaques in the brains of Alzheimer's patients as the disease progresses, has been shown to increase expression and secretion of DBI cleavage products (Tokay et al., 2008). Additionally, disruptions in adult hippocampal neurogenesis have been associated with the progression of Alzheimer's disease (Moreno-Jiménez et al., 2019), and DBI has been shown to modulate GABARs regulating neurogenesis in this region (Dumitru et al., 2017). It would be interesting to compare

the expression and release of DBI in the hippocampus of healthy and Alzheimer's disease model animals. In Chapter VI, I described our inability to use mass spectrometry to detect ODN in the media of iPSC-derived human neurons and astrocytes, but ODN may be present in higher concentrations in a native environment rather than isolated neuronal or astrocytic cultures. It would also be possible to use DBI-specific antibodies rather than mass spectrometry to evaluate DBI expression both intra- and extracellularly.

Conclusions

In summary, the findings of this thesis demonstrate that DBI's modulation of the GABAR is subunit dependent. I show for the first time that DBI potentiates $\alpha_5\beta_3$ GABARs and thus its actions do not depend on a BZD binding site. The data in this thesis provide valuable insights into understanding DBI's role in GABA-mediated inhibition and suggest mechanisms by which DBI can regulate both phasic and tonic inhibition in the brain.

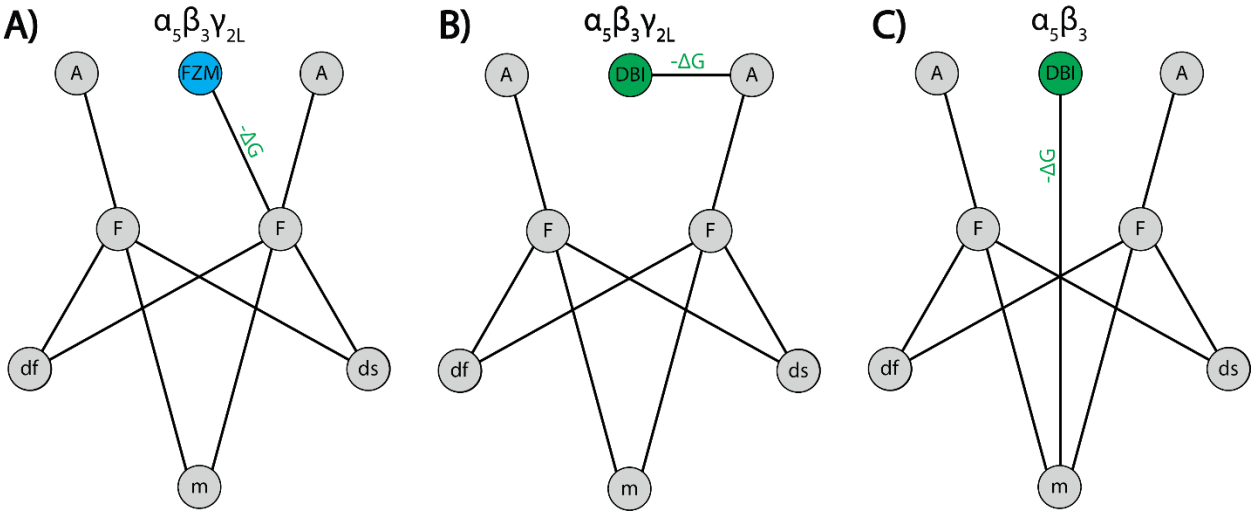

Figure 7.1 – Simplified elements models showing proposed interactions for FZM and DBI. Elements models showing interactions between elements: agonist binding sites (A), intermediate F-elements (F), fast and slow desensitization gates (df, ds respectively), and the main channel gate (m). When modeling $\alpha_5\beta_3\gamma_{2L}$ receptors, an FZM element has a stabilizing interaction with an F-element which increases the GABA-elicited current at low [GABA], has no effect on high [GABA] current amplitudes and slows the rate of current deactivation at all [GABA] (A). For the same receptor combination, the DBI element (B) interacts directly with an agonist binding site to increase GABA-elicited current at low [GABA] without changing the rate of current deactivation. When using a model for $\alpha_5\beta_3$ receptors, the DBI element interacts directly with the main channel gate to stabilize an open state. This increases the GABA-elicited amplitude even at high [GABA] and slows the rate of deactivation.

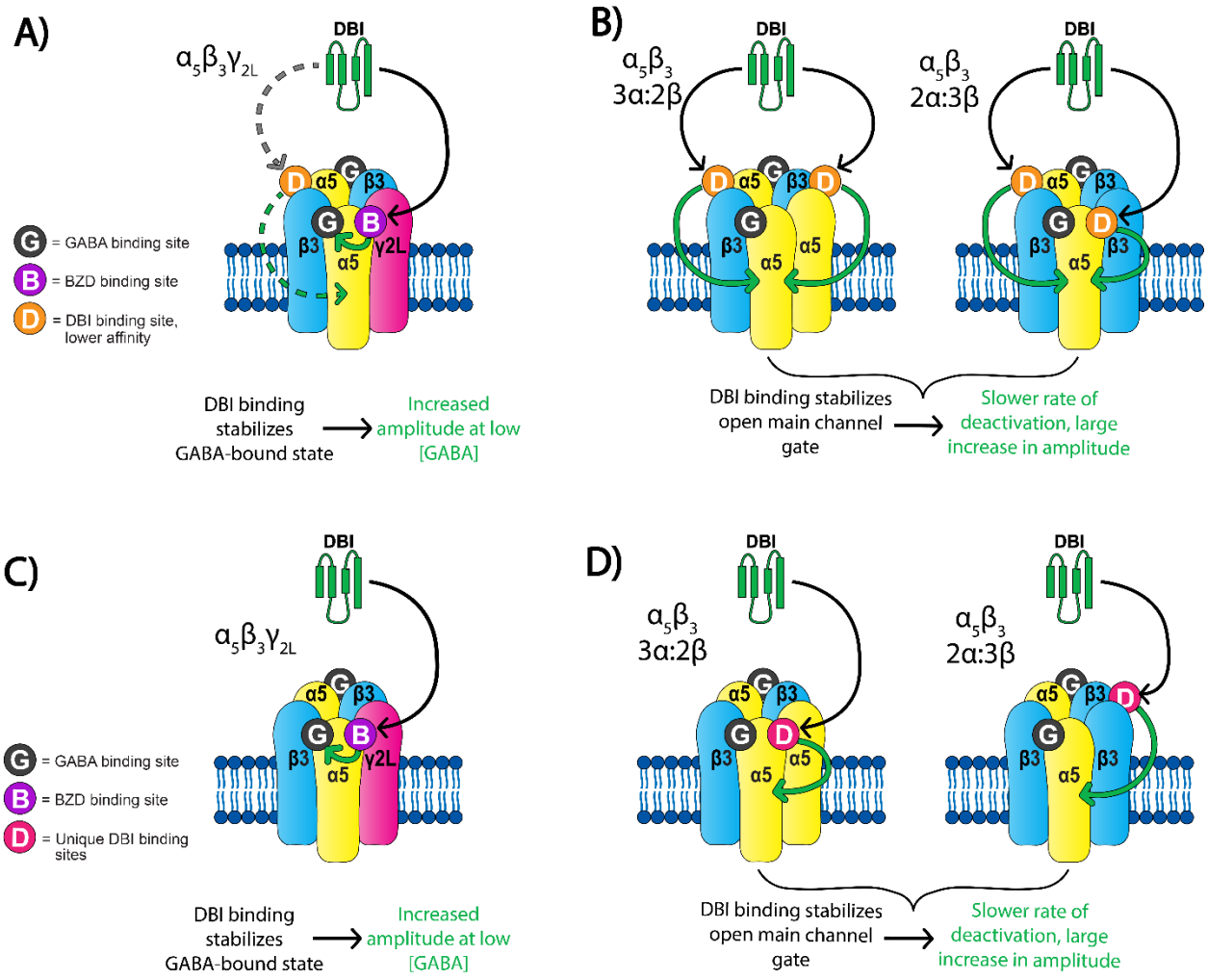

Figure 7.2 – Cartoons showing proposed mechanisms for effects of DBI on $\alpha_5\beta_3\gamma_{2L}$ and $\alpha_5\beta_3$ receptors. Receptor cartoons showing pentameric GABARs spanning a plasma membrane. α subunits shown in yellow, β in blue, and γ in pink. Binding sites shown as circles for GABA (G, grey), BZDs (B, purple), and DBI (D, pink or orange). Cartoons in the top row depict DBI's interaction with $\alpha_5\beta_3\gamma_{2L}$ (A) and $\alpha_5\beta_3$ (B) GABARs if DBI preferentially binds at the BZD site rather than a lower-affinity site at α^+/β^- interfaces (A, orange DBI circles). When DBI binds the BZD site present only in $\alpha_5\beta_3\gamma_{2L}$ receptors, it stabilizes the GABA-binding site and increases amplitude at low [GABA]. In $\alpha_5\beta_3$ receptors, only the lower affinity site is present. DBI binding at this site stabilizes the open main channel gate which slows the rate of deactivation and increases the peak GABA-elicited amplitude. Cartoons in the bottom row depict a possible

scheme where DBI binds the BZD site (C) and a unique site at the α/α (left) or β/β (right) interfaces in $\alpha_5\beta_3$ (D, pink DBI circles). Binding the BZD site stabilizes the GABA-bound state as described above. Binding either of the unique $\alpha_5\beta_3$ interfaces stabilizes the open main gate as described above.

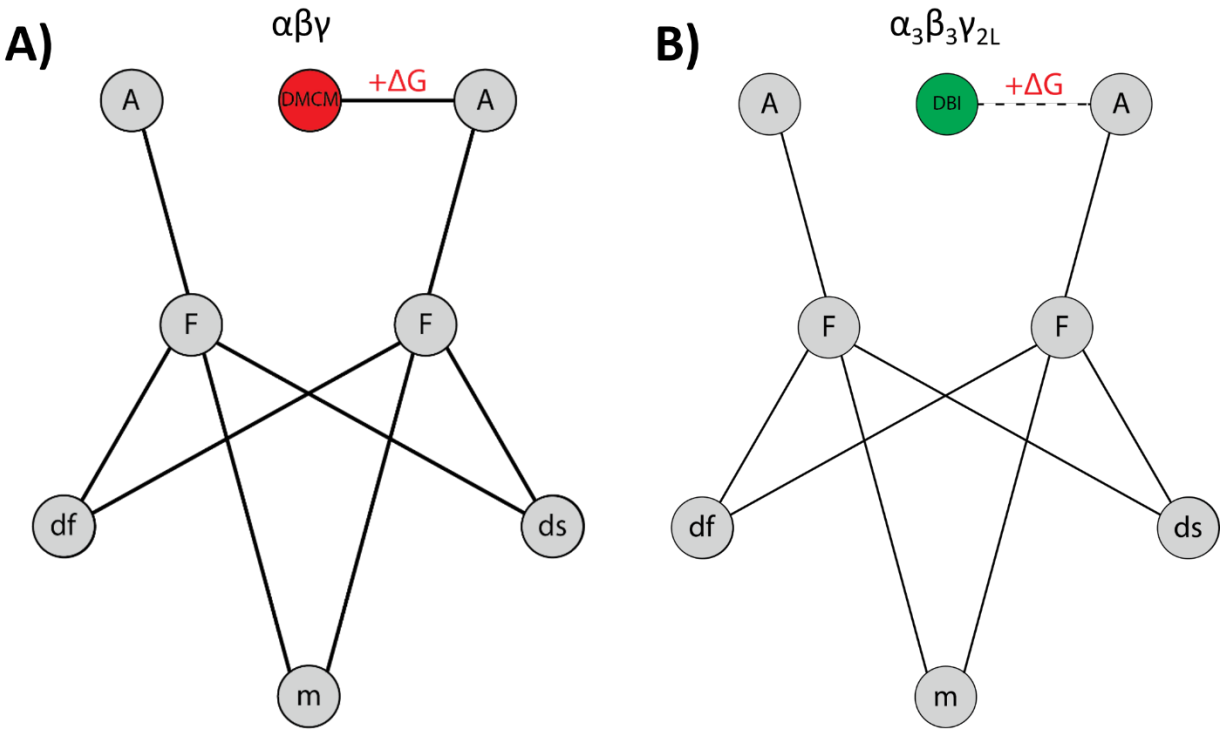

Supplemental Figure 7.1 – Simplified elements models showing proposed interactions for DMCM on αβγ and DBI on $\alpha_3\beta_3\gamma_{2L}$ receptors. Elements models showing interactions between elements: agonist binding sites (A), intermediate F-elements (F), fast and slow desensitization gates (df, ds respectively), and the main channel gate (m). A) A DMCM element (red circle) has a destabilizing interaction with the GABA binding site A, as discussed in Appendix I. This leads to a decrease in GABA-elicited amplitude, but no changes in deactivation. B) When modeling $\alpha_3\beta_3\gamma_{2L}$ GABARs, a hypothesized destabilizing interaction (dotted line) between the DBI binding element (green circle) has a destabilizing interaction with the GABA binding site A, which leads to a decrease in GABA-elicited amplitude, but no changes in deactivation. Further patch clamp experiments are necessary to determine if co-application of DBI alters the deactivation rate of $\alpha_3\beta_3\gamma_{2L}$ GABARs.

APPENDIX I:

Comparing kinetic effects of positive and negative modulators

Rationale:

Benzodiazepines (BZDs) have been a widely used class of GABA-A receptor (GABAR) modulators since their discovery in the mid-1950s. These drugs bind an inter-subunit pocket in the extracellular domain of GABARs, between α and γ subunits (Masiulis et al., 2019). Depending on their structure, BZDs can either act as positive allosteric modulators (PAMs) and increase the amount of GABA-elicited current, or act as negative allosteric modulators (NAMs) and decrease the amount of GABA-elicited current. Some BZDs can act as either PAMs or NAMs depending on the subunit composition of the GABAR (Knoflach et al., 1996). While much of my thesis focuses on the diazepam binding inhibitor, a persistent question during many of my experiments was what is the real difference between positive and negative modulation? How can ligand binding at the same site lead to such different effects?

In general, the effects of BZD PAMs like diazepam or flurazepam (FZM) have been more thoroughly studied than NAMs like methyl-6,7-dimethoxy-4-ethyl-beta-carboline-3-carboxylate (DMCM). Mutagenesis, cysteine modification experiments, and cryoEM structures all identified key residues in PAM binding (Masiulis et al., 2019; Morlock and Czajkowski, 2011; Olsen and Sieghart, 2009; Zhu et al., 2018). Additionally, multiple kinetic models have been proposed which seek to explain how positive modulation works – the resting-active-desensitized (RAD) model suggests PAMs increase GABA binding by stabilizing a high-affinity receptor state (Akk et al., 2020), while the elements model suggests that a BZD PAM modulates an intermediate element between ligand binding and channel gating, stabilizing the transition from agonist binding to opening the channel gate (Goldschen-Ohm et al., 2014). There is limited published data modeling the effects of a NAM. Is a NAM acting as a true opposite of a PAM and destabilizing the intermediate element, or are the effects of a NAM mediated by a different

interaction entirely? In this appendix, I show outside-out patch data for GABARs in the presence of either FZM or DMCM, and compare effects on peak current and deactivation. I also use the elements model to explore what interactions may be responsible for the effects of positive versus negative modulation.

Methods:

HEK cell culture and DNA transfection

Human embryonic kidney (HEK 293T-17) cells were cultured in Eagle's minimum essential medium with Earle's salt (Mediatech, Manassas, VA). Media was supplemented with 10% fetal bovine serum (Atlanta Biologics, Flowery Branch, GA), penicillin-streptomyacin-glutamine (Sigma-Aldrich, St. Louis, MO), and plasmocin (InvivoGen, San Diego, CA). Cells were grown at 37°C with 5% CO_2, and plated on 12mm circular glass coverslips in 60mM dishes 48-72 hours before transfection.

Cells were transfected at 85-90% confluency using lipofectamine 2000 (Invitrogen, Carlsbad, CA). 0.5-2µg of pUNIV GABAR (either $\alpha_1\beta_2\gamma_{2L}$ or $\alpha_5\beta_3\gamma_{2L}$) DNA was used, with a 1:1:3-5 ratio of α:β:γ subunits, and 2-10ng of pUNIV GFP DNA. Cells were used for recording 24-60 hours post transfection.

Patch-clamp solutions and drugs

Recording pipettes were pulled from borosilicate glass using a Flaming-Brown P-1000 mulitstage micropipette puller (Sutter Instruments, Novato, CA). Pipette tips were fire-polished with a Narishige MF-83 microforge (Narishige, Tokyo, Japan) until open tip resistance was between 2-9 MΩ. Electrodes were filled with intracellular solution (140mM KCl, 10mM EGTA, 2mM MgATP, 10mM phosphocreatine, 10mM HEPES, pH 7.3-7.4).

HEPES normal Ringer (HNR) perfusion solution contained 145mM NaCl, 2.5mM KCl, 1mM $MgCl_2$, 1mM $CaCl_2$, and 10mM HEPES, pH 7.3-7.4, 300-310 mOsm. 1M stocks of GABA and 10mM stocks of flurazepam (FZM) were prepared in water and frozen at -20°C. 10mM stocks of methyl-6,7-dimethoxy-4-ethyl-beta-carboline-3-carboxylate (DMCM) were prepared in

DMSO and frozen at -20°C. Fresh drug solutions were prepared daily in HNR and diluted to 10-50µM GABA in the presence and absence of 10µM FZM and 1-10µM DMCM. Recordings were performed at room temperature.

Application Pipette Assembly and Function

Theta-barreled glass (thin walled, filamented glass capillary, outer-diameter (OD) 1.5mm, inner diameter (ID) 1.2mm) was pulled until tip openings were approximately 100µm between the centers of both channels. Glass was cut to 2-3 cm in length and end was fire-polished. 10cm lengths of polyimide tubing (0.24mm OD, 0.2mm ID, Cole-Parmer, Vernon Hills, IL) were inserted into both sides of the theta barrel and pushed up to the tip. The free ends of polyimide tubing were threaded into 30cm lengths of 28 gauge polytetrafluoroethylene (PTFE) tubing. PTFE tubing was pushed flush to the end of the theta-barreled glass. 2-3cm lengths of fused silica tubing (170µm OD, 110µm ID, Trajan Scientific, Victoria, Australia) were inserted into theta barrels to sit 0.5cm behind the openings of polyimide tubing to serve as drains for dead space within glass barrels to increase liquid exchange time. Glass and tubing were sealed together at interface with PTFE/fluorinated ethylene propylene (FEP) dual shrink tubing (Cole-Parmer, Vernon Hills, IL), and tested for leaking at the end of glass or between channels of glass. Gripper fittings were attached to the ends of PTFE tubing.

Glass slides were prepared with Sylgard 184 (Dow Corning, Midland, MI) material as a border to create approximately 5mL wells. The assembled application pipette was glued to glass slide with the theta perpendicular to the bottom of the plate. Pipette was secured with quick drying epoxy and left to cure overnight.

The application pipette was installed on a piezoelectric biomorph (Physik Instrumente, Costa Mesa, CA) and connected to 6-way Rheodyne low pressure valves (IDEX Health and Science, Rohnert Park, CA). Valves were connected to tubes containing HNR and drug solution via 26 gauge PTFE tubing. The biomorph is moved to position the application barrel in front of the cell by WinPos (ITK Dr. Kassen GmbH, Hahnau, Germany), with <1msec 10-90% solution

exchange times, measured via liquid junction potential tests of open recording pipette tips after experiments. Valve switches took <30sec to fully exchange from low to high concentration and 1min to exchange from high to low concentrations (100% HNR to 10% HNR).

Outside-out patch clamp recording

Recording pipettes were sealed onto the membrane of GFP-positive HEK cells to obtain a giga-seal with -5 to -10mmHg pressure. Once the pipette was sealed, increased negative pressure was used to break into the cell. The pipette was immediately withdrawn from the cell, enabling the patch to reseal in an outside-out conformation with the extracellular side of the resealed membrane facing out. Patches were held at -40mV. Currents were low-pass-filtered at 2 kHz with an eight-pole Bessel filter. Data was collected at 20kHz via an Axopatch 200B amplifier (Axon Instruments, Sunnyvale, CA) interfaced to a computer using a Digidata 1440A (Axon Instruments, Sunnyvale, CA). Amplifier function was controlled by Clampex (version 10.4.1.10; Molecular Devices, Sunnyvale, CA) and analyzed using Clampfit (version 10.4.1.10; Molecular Devices, Sunnyvale, CA). Patches were exposed to 100ms pulses of 10-50µM GABA with and without 10µM FZM and 1µM DMCM, with 10sec of HNR wash between pulses.

Data Analysis

Averaged traces using 3-15 sweeps were generated in Clampfit and used to measure peak current responses and calculate the rate of deactivation via a weighted tau (τ_w). τ_w was calculated by fitting the curve after GABA removal until a return to baseline with a bi-exponential equation ($I = A_1*e^{-t/\tau1} + A_2*e^{-t/\tau2}$, where I is current, t is time, A_1 and A_2 are the relative amplitudes for the fast and slow components respectively, and τ_1 and τ_2 are the time constants for the fast and slow components. These values are used to calculate τ_w where $\tau_w = (A_1\tau_1+A_2\tau_2)/(A_1+A_2)$. Normalized τ_w values were calculated as $\tau_{w(GABA+Drug)}/\tau_{w(GABA)}$. Normalized peak responses were calculated as $I_{GABA+Drug}/I_{GABA\ Initial}$ and $I_{GABA\ Recovery}/I_{GABA\ Initial}$. Significance was evaluated using a one-sample t-test comparing against a null hypothesis of 1. Data was analyzed and displayed using GraphPad Prism (version 9.1.2, GraphPad Software Inc, San Diego, CA).

Kinetic Modeling

GABA-elicited currents were simulated in Kinetic Model Builder 2.0 (Goldschen-Ohm et al., 2014) in Monte Carlo mode. Currents were simulated from 150ms pulses of 10m and 50μM GABA in the presence and absence of 10μM benzodiazepine (BZD). This model describes the two agonist bindings sites (A1 and A2), two intermediate elements (F1 and F2), fast and slow desensitization gates (Df and Ds, respectively), a benzodiazepine binding site (D), and the channel gate (m) as binary elements. These binary elements can transition between two metastable configurations, like open or closed for the channel gate, or bound or unbound for a drug binding site. The transition between these states are governed by intrinsic rate constants for the forward and reverse reactions. Interactions between elements can contribute energy towards the transition of to an alternate energy state. For this model, rate constants for each element were α_A = [GABA]*1.2*10^{-6} $M^{-1}s^{-1}$, β_A = 500 $M^{-1}s^{-1}$, α_F = 5.5 $M^{-1}s^{-1}$, β_F = 1124 $M^{-1}s^{-1}$, α_{df} = 0.25 $M^{-1}s^{-1}$, β_{df} = 31 $M^{-1}s^{-1}$, α_{ds} = 0.0033 $M^{-1}s^{-1}$, β_{ds} = 0.19 $M^{-1}s^{-1}$, α_D = [BZD]*10^8 $M^{-1}s^{-1}$, β_D = 0.3 $M^{-1}s^{-1}$, is α_m = 380*(-0.5e) s^{-1}, β_m = 380 s^{-1}. Interactions between elements (kcal/mol at 298K) are ΔG_{AF} = -5, ΔG_{Fm} = -3.8, ΔG_{Fdf} = -0.8, ΔG_{Fds} = -1.7, and $\Delta G_{D\text{-}F}$ = -2 for FZM or 0 for DMCM, $\Delta G_{D\text{-}A}$ = 0 for FZM, 1 for DMCM. These values were used to generate a revised kinetic model for $\alpha_5\beta_3\gamma_{2L}$ receptors to match outside-out patch data, as described in Chapter IV.

Results and Conclusions:

Comparing effects of FZM and DMCM on GABAR outside-out patches

In order to compare the effects on macroscopic kinetics of a PAM and NAM, I applied both FZM and DMCM to outside-out patches of GABARs and compared the resulting peak amplitudes and rates of deactivation. I compared mean peak amplitudes for GABA and GABA+Drug and found that FZM did not significantly affect amplitude, but co-application of DMCM caused a significant reduction in peak current (Figure A1.1). GABA-elicited currents recover to close to the original amplitude after drug is washed off. Conversely, FZM significantly slowed the rate of deactivation, while DMCM had no significant effect (Figure A1.2)

Modeling PAM vs NAM

In an effort to explore possible mechanisms for the difference in FZM versus DMCM, we used a version of the elements model created in Kinetic Model Builder 2.0 (Goldschen-Ohm et al., 2014). Dr. Robert Pearce assisted in changing values for element rate constants and energies for interactions so that simulated responses to GABA matched the $\alpha_5\beta_3\gamma_{2L}$ GABA dose response curve described in Chapter IV, Figure 4.1. We can model to the effects of FZM as primarily slowing the rate of deactivation without largely affecting amplitude at high concentrations of GABA by including an interaction between the BZD binding site (D) and an F element (F2) to stabilize a pre-open state (Figure A1.3).

If a NAM like DMCM is thought of as a true opposite of a PAM, binding at the BZD site should destabilize the F element. However, when the energy values for this interaction are altered to reflect this destabilization, the resulting simulated traces showed a decrease in amplitude, but also much faster rates of deactivation, which did not match my electrophysiology data (Figure A1.4). In order to accurately model the data, we needed to introduce a separate interaction between the BZD site and a GABA binding site (A2). By modeling the binding of a NAM stabilizing an unbound-GABA state, we were able to simulate a reduction in amplitude without altering deactivation kinetics (Figure A1.5).

Conclusions

The electrophysiology data shows clear differences in the kinetic effects of the PAM FZM versus the NAM DMCM. Where FZM slows the rate of deactivation and has little effect on amplitude at high GABA concentrations, DMCM decreases peak currents without altering the rate of deactivation. Our modeling data suggests that these results may be due to different interactions, even though both drugs bind the same BZD site on the receptor. We can accurately model our PAM data by including an interaction where BZD binding stabilizes a pre-open state, while modeling the NAM data requires a new interaction where the binding of a NAM to the BZD site directly destabilizes GABA binding. These results suggest new insights

into the difference between positive and negative modulators, and offer a perspective on how two ligands can bind the same site but yield such different effects.

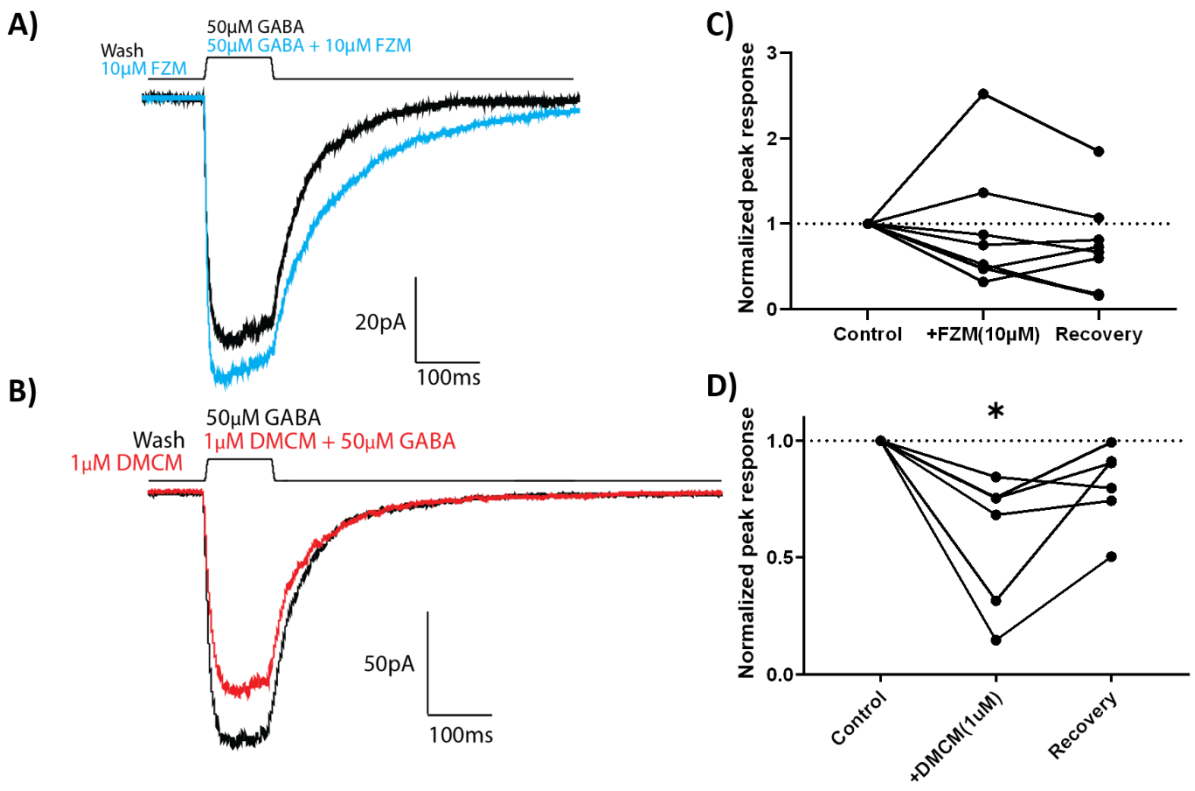

Figure A1.1 – GABA-elicited peak currents are not affected by FZM, but are inhibited by DMCM. Sample averaged traces showing 100ms applications of 50μM GABA (black) and 50μM GABA + 10μM FZM (blue, A) or 50μM GABA + 1μM DMCM (red, B). Scale bars included. Peak responses normalized to initial GABA amplitudes are shown for FZM in C and DMCM in D. One-sample t-tests comparing to a hypothetical value of 1 show that FZM does not significantly affect amplitude at 50μM GABA, but DMCM does ($p=0.02$). GABA-elicited peak responses recover after DMCM is washed off.

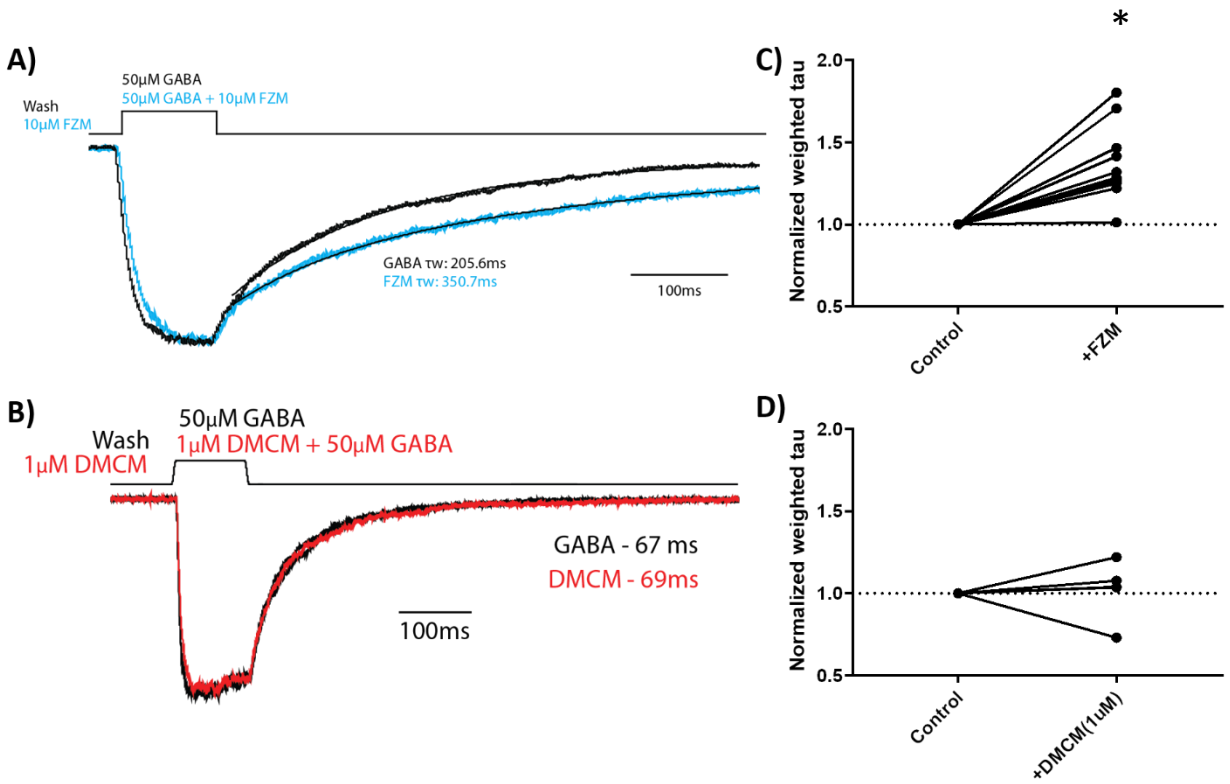

Figure A1.2 – FZM affects the rate of deactivation, but DMCM does not. Sample averaged traces showing 100ms applications of 50μM GABA (black) and 50μM GABA + 10μM FZM (blue, A) or 50μM GABA + 1μM DMCM (red, B). Scale bars included. Traces have been normalized to amplitude immediately before removal of GABA. τ_w are shown below for GABA and GABA+Drug. τ_w for rate of deactivation for GABA+Drug is normalized to τ_w for GABA. FZM (C) significantly slows the rate of deactivation (one-sample t-test of null=1, p= 0.0070), while DMCM does not have a significant effect on deactivation.

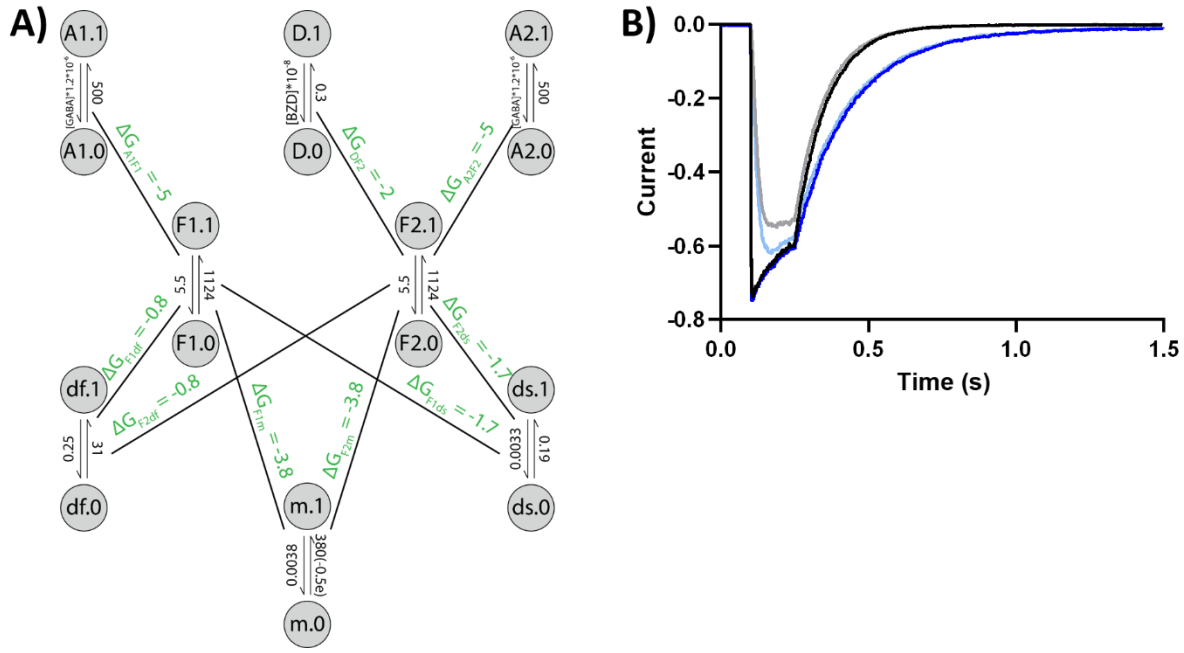

Figure A1.3 – Elements model for FZM. An elements model adapted for $\alpha_5\beta_3\gamma_{2L}$ receptors (A) accurately models the effects of FZM when an energetically favorable interaction is introduced between the BZD site (D) and an intermediate F-element (F2). ΔG values (kcal/mol at 298K) for interactions between elements are shown in green, and element rate constants ($M^{-1}s^{-1}$ for all but channel gate, m, s^{-1} for m) are shown between element states. A1 and A2 represent agonist binding sites, D is the BZD binding site, F1 and F2 are intermediate F elements, df is the fast desensitization gate, ds is the slow desensitization gate, and m is the main channel gate. B) Modeled traces for 150ms applications of 1mM GABA (black), 50μM GABA (grey), 1mM GABA+10μM FZM (blue), and 50μM GABA+10μM FZM (light blue). Modeled traces show FZM does not have substantial effect on amplitude at high GABA concentrations, but does slow the rate of deactivation.

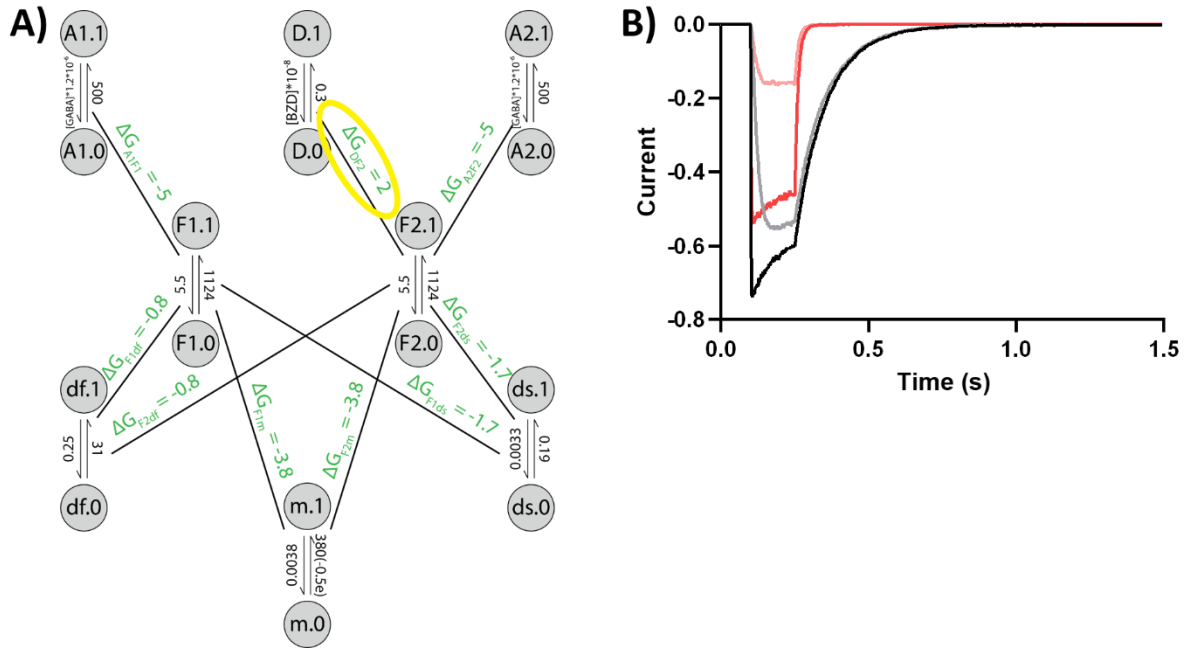

Figure A1.4 – A destabilizing interaction between DMCM and the F-element does not accurately simulate experimental data. Using the same elements model as described in Figure A1.3, the ΔG_{DF2} was switched from -2 to 2 kcal/mol (A, circled in yellow) to represent a BZD which would destabilize the F2 element, rather than stabilizing it as a PAM. B) This change does not generate simulated traces that match experimental data, as the modeled data shows an increase in the rate of deactivation unlike what experimental results. Simulated traces for 150ms applications of 1mM GABA (black), 50μM GABA (grey), 1mM GABA+10μM DMCM (red), and 50μM GABA+10μM DMCM (light red).

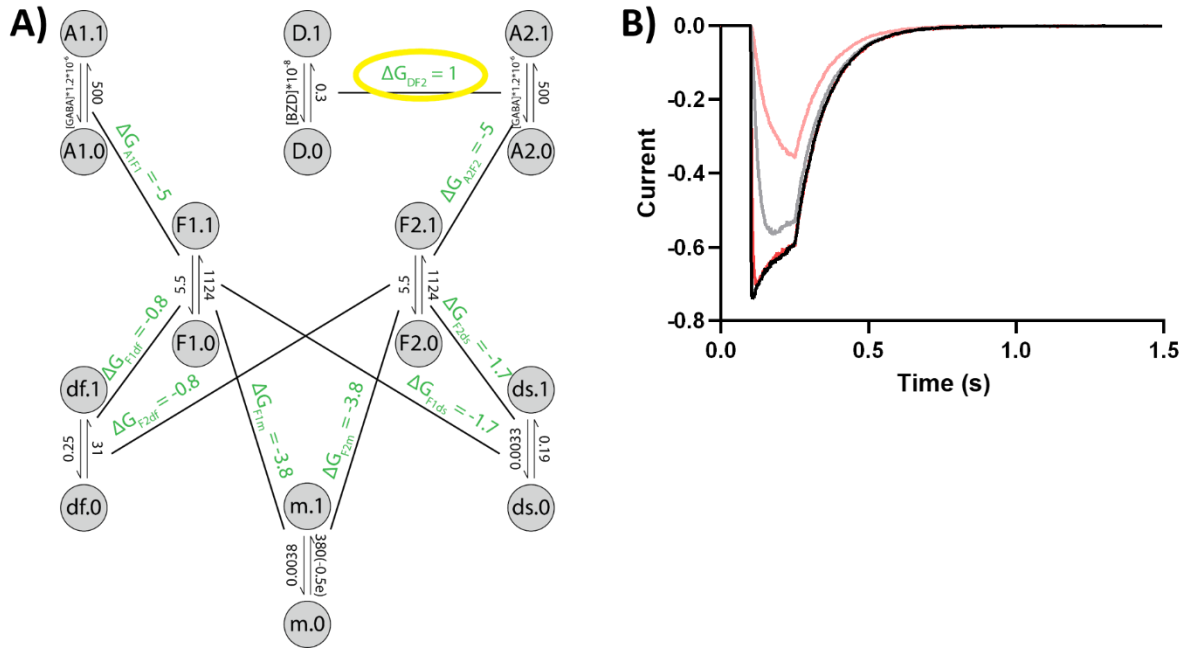

Figure A1.5 – DMCM stabilizes non-GABA-bound state. A) Using the same elements model as described in Figure A1.3, the interaction between the BZD binding site and F2 element was removed, and a new interaction was introduced between the BZD binding site and a GABA binding site, with ΔG_{DF2} = 1 kcal/mol (circled in yellow). B) This new interaction simulates traces which are a good match for our experimental data, where peak currents are decreased in the presence of DMCM, but the rate of deactivation is unaffected. Simulated traces for 150ms applications of 1mM GABA (black), 50μM GABA (grey), 1mM GABA+10μM DMCM (red), and 50μM GABA+10μM DMCM (light red).

APPENDIX II:

Testing function of GLIC liposomes injected in *Xenopus* oocytes

Rationale:

In addition to my thesis research, I assisted Dr. Varun Tiwari in testing the function of multiple mutations in the extracellular domain of *Gleobacter violaceus* (GLIC), a bacterial pentameric ligand-gated ion channel made up of five homologous subunits. He introduced cysteine residues at the top of the extracellular domain β-strands and used site-directed spin labeling electron paramagnetic resonance (SDSL EPR) spectroscopy to study ligand-induced structural changes in GLIC.

I injected samples of his purified GLIC protein reconstituted in lipids into *Xenopus* oocytes to confirm the cysteine mutant channels were functional and proton-gated. I confirmed that all twelve of his GLIC mutants were functional. Additionally, I injected cRNA to test the function of double-mutants designed to measure how the GLIC extracellular domain moves in the presence of a non-activating mutant. I found that T248A/Q101C GLIC mutants were gated by protons, even though T248A was thought to be a non-activating mutant. I confirmed that Y251A/N19C GLIC mutants do not open in the presence of protons. Once I assessed the function of these mutants, Dr. Tiwari used them in his EPR studies to determine that proton activation causes an inward motion at the top of the extracellular domain, and that this motion is associated with a pre-activated state rather than directly accompanying channel gating. I am a co-author of a paper published in bioRxiv describing these results, which is conditionally accepted in eLife pending revisions.

Methods:

Liposome injection

As described previously (Tiwari et al., 2020), GLIC mutant protein was purified and reconstituted into 1-palmitoyl-2-oleoyl-sn-glycero-3-phosphoethanolamine (PE, Avanti Polar Lipids) and 1-palmitoyl-2-oleoyl-sn-glycero-3- phospho- (1'-rac-glycerol) (PG, Avanti Polar Lipids) at a PE: PG = 2.7:1 molar ratio. Pelleted samples were thawed on ice and resuspended in buffer B1 (20 mM Tris, 150 mM NaCl, pH 7.6) at approximately 1mg/mL, assuming 70% reconstitution efficiency.

Oocytes were harvested from an in-house *X. laevis* colony and treated as described previously (Boileau et al., 1998) or directly obtained from Ecocyte Biosciences. Due to the viscous nature of liposome solutions, glass injection pipette diameter was widened to approximately 5-10 5-10 µm for injecting the purified lipid reconstituted GLIC protein into oocytes. Each oocytes was injected with 27 nL containing approximately 1µg/µL protein. Protein-injected oocytes were incubated for 16-24 h at 16°C before recording in ND96 (5 mM HEPES pH 7.4, 96 mM NaCl, 2 mM KCl, 1 mM $MgCl_2$, 1.8 mM $CaCl_2$) supplemented with 100 µg/ml of gentamycin and 100 µg/mL of bovine serum albumin.

cRNA purification and injection

cDNA for WT GLIC was subcloned into pUNIV vector for oocyte expression (Venkatachalan et al., 2007). QuikChange site-directed mutagenesis was used to create GLIC mutants in a pUNIV backbone. Capped cRNAs encoding WT and mutant GLIC were transcribed *in vitro* from the pUNIV cDNA constructs using the mMessage mMachine T7 kit (Ambion).

Single oocytes were injected with 27 nL of cRNA (100 ng/µL). Injected oocytes were incubated at 16°C in ND96 supplemented with 100 µg/ml of gentamycin and 100 µg/mL of bovine serum albumin for 2–4 days before use for electrophysiological recordings.

Two-electrode voltage clamping

Oocytes were perfused continuously with ND96 at pH 7.4 at a flow rate of 5 mL/min in a 200 µL bath while being held under two-electrode voltage clamp at −40 mV. Borosilicate glass electrodes (Warner Instruments) used for recordings were filled with 3 M KCl and had resistances of 0.4 to 1.0 MΩ. Electrophysiological data were collected using Oocyte Clamp OC-725A (Warner Instruments) interfaced to a computer with a Digidata 1440A (Axon CNS) and were recorded using the AxoScope program, version 10.2 (Molecular Devices). Proton-induced currents were measured by perfusing ND96 buffered at pH 7.0-3.0. pH 4.6-3.0 buffers used 5mM Na Citrate to replace HEPES as the buffering agent. Proton-induced currents were measured at pH 3.0 until peak current amplitudes varied by <10%, then measured at pH 7.0 as a control, followed by a final application of pH 3.0. pH-induced currents from uninjected oocytes were used as controls. Dose-response traces were generated using pH 6.4, 4.6, 3.5 and 3.0. Statistical significance of the effect of pH 3.0 was assessed using a one-way analysis of variation (ANOVA) and a Dunnett's multiple comparisons test versus the uninjected oocyte current responses (GraphPad Prism 8.2.1).

Results and Conclusions:

Mutant GLIC protein reconstituted in lipids was injected into *Xenopus* oocytes (Jarecki et al., 2013; Morales et al., 1995) and tested for proton-gating function. I injected proteoliposomes containing wild-type (wt) GLIC and GLIC mutants T17C, N19C, S46C, K48C, G60C, D91C, I92C, S93C, T99C, Q101C, I140C and V141C. Dose-response curves were recorded using pH solutions of 6.4, 4.6, 3.5 and 3.0 for each mutant, as well as wild-type GLIC and uninjected oocytes (Figure A2.1A). I compared the current elicited by pH 3.0 for n=5 for each mutant to the pH 3.0 response of uninjected oocytes (Figure A2.1B) and used a one-way ANOVA and Dunnett's multiple comparisons test to determine that each of these mutants was significantly different than uninjected oocytes, indicating that the channels were still functional.

I also tested cRNA and liposomes for two GLIC double mutants, Q101C/T248A and N19C/Y251A. Both the T248A and Y251A mutants render the channel insensitive to the proton agonist by stabilizing an agonist-bound, closed-channel state (Bertozzi et al., 2016; Gonzalez-Gutierrez et al., 2013). I found that combining the Q101C and T248A mutations caused GLIC to still be activated by protons when recording from oocytes injected with cRNA as well as liposomes. N19C/Y251A mutants functioned as expected and were not activated by protons (Figure A2.2). Dr. Tiwari then used the N19C/Y251A GLIC double mutant rather than the Q101C/T248A for his experiments examining motions caused by agonist binding decoupled from channel gating.

Once I had confirmed the function of Dr. Tiwari's twelve single GLIC mutants and identified the appropriate double mutant to study non-activating channels, he was able to perform the necessary EPR experiments. His results suggested that channel activation leads to an inward tilt of GLIC extracellular domains, and that these motions were associated with a pre-activation closed state rather than directly accompanying an open channel. These results provide more insight into the gating transitions of pentameric ligand-gated ion channels.

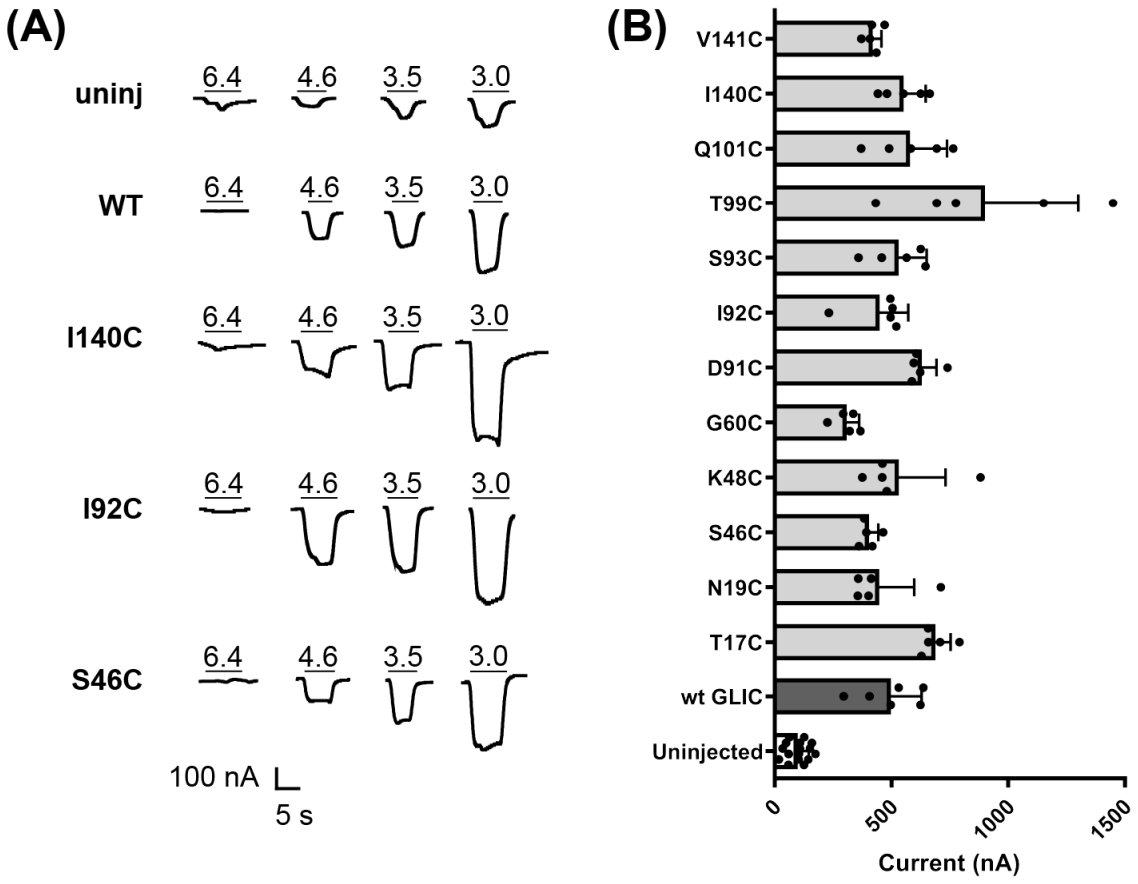

Figure A2.1 – Purified GLIC mutants reconstituted in liposomes are functional. A) Sample dose-response traces for uninjected oocytes as well as wild-type (wt), I140C, I92C and S46C elicited by pH 6.4, 4.6, 3.5 and 3.0. B) Summary of pH 3.0 responses for uninjected, wt, T17C, N19C, S46C, K48C, G60C, D91C, I92C, S93C, T99C, Q101C, I140C and V141C mutants. Bars represent ± SD for ≥5 ooctyes. One-way ANOVA and Dunnett's post-test shows currents elicited by mutants and wt are significantly larger than uninjected ($p<0.05$).

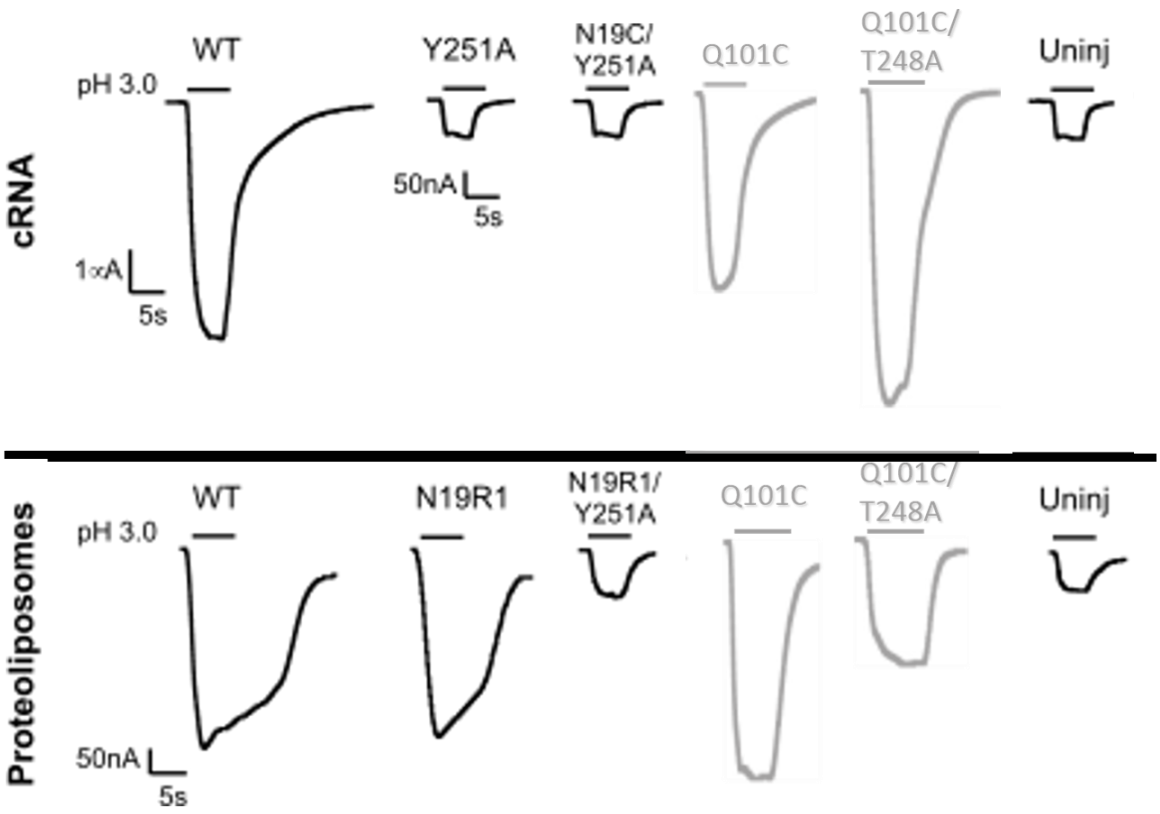

Figure A2.2 – N19C/Y251A mutants are not proton-activated, but Q101C/T248A mutants are. Sample pH 3.0 elicited currents from wt, Y251A, N19C/Y251A, Q101C, Q101C/T248A, and uninjected cRNA (top) and proteoliposomes (bottom). N19C/Y251A channels are non-conducting the presence of pH 3.0, but Q101C/T248A channels still have larger pH 3.0 current responses than uninjected oocytes, indicating that these channels are still proton-activated.

REFERENCES

Aimone, J.B., Li, Y., Lee, S.W., Clemenson, G.D., Deng, W., and Gage, F.H. (2014). Regulation and Function of Adult Neurogenesis: From Genes to Cognition. Physiological Reviews *94*, 991-1026. 10.1152/physrev.00004.2014.

Akk, G., Germann, A.L., Sugasawa, Y., Pierce, S.R., Evers, A.S., and Steinbach, J.H. (2020). Enhancement of Muscimol Binding and Gating by Allosteric Modulators of the GABA_A Receptor: Relating Occupancy to State Functions. Mol Pharmacol *98*, 303-313. 10.1124/molpharm.120.000066.

Alfonso, J., Le Magueresse, C., Zuccotti, A., Khodosevich, K., and Monyer, H. (2012). Diazepam Binding Inhibitor Promotes Progenitor Proliferation in the Postnatal SVZ by Reducing GABA Signaling. Cell Stem Cell *10*, 76-87. 10.1016/j.stem.2011.11.011.

Alho, H., Bovolin, P., Jenkins, D., Guidotti, A., and Costa, E. (1989). Cellular and Subcellular-Localization of an Octadecaneuropeptide Derived from Diazepam Binding Inhibitor - Immunohistochemical Studies in the Rat-Brain. J Chem Neuroanat *2*, 301-318.

Alho, H., Bovolin, P., and Slobodyansky, E. (1990). Diazepam Binding Inhibitor (DBI) processing: Immunohistochemical studies in the rat brain. Neurochem Res *15*, 209-216. 10.1007/bf00972211.

Alho, H., Kolmer, M., Harjuntausta, T., and Helen, P. (1995). Increased expression of diazepam binding inhibitor in human brain tumors. Cell Growth and Differentiation *6*, 309-314.

Ali, A.B., and Thomson, A.M. (2008). Synaptic 5 Subunit-Containing GABAA Receptors Mediate IPSPs Elicited by Dendrite-Preferring Cells in Rat Neocortex. Cerebral Cortex *18*, 1260-1271. 10.1093/cercor/bhm160.

Althoff, T., Hibbs, R.E., Banerjee, S., and Gouaux, E. (2014). X-ray structures of GluCl in apo states reveal a gating mechanism of Cys-loop receptors. Nature *512*, 333-337. 10.1038/nature13669.

Amico, C., Cupello, A., Fossati, C., and Robello, M. (1998). Involvement of phosphatase activities in the run-down of GABAA receptor function in rat cerebellar granule cells in culture. Neuroscience *84*, 529-535. 10.1016/s0306-4522(97)00555-1.

Augoff, K., Kolondra, A., Chorzalska, A., Lach, A., Grabowski, K., and Sikorski, A.F. (2010). Expression, purification and functional characterization of recombinant human acyl-CoA-binding protein (ACBP) from erythroid cells. Acta Biochim Pol *57*, 533-540.

Bai, D., Zhu, G., Pennefather, P., Jackson, M.F., Macdonald, J.F., and Orser, B.A. (2001). Distinct Functional and Pharmacological Properties of Tonic and Quantal Inhibitory Postsynaptic Currents Mediated by γ-Aminobutyric AcidA Receptors in Hippocampal Neurons. Mol Pharmacol *59*, 814-824. 10.1124/mol.59.4.814.

Ball, J.A., Ghatei, M.A., Sekiya, K., Krausz, T., and Bloom, S.R. (1989). Diazepam binding inhibitor-like immunoreactivity(51–70): distribution in human brain, spinal cord and peripheral tissues. Brain Res *479*, 300-305. https://doi.org/10.1016/0006-8993(89)91632-6.

Barbaccia, M.L., Costa, E., Ferrero, P., Guidotti, A., Roy, A., Sunderland, T., Pickar, D., Paul, S.M., and Goodwin, F.K. (1986). Diazepam-Binding Inhibitor: A Brain Neuropeptide Present in Human Spinal Fluid: Studies in Depression, Schizophrenia, and Alzheimer's Disease. Archives of General Psychiatry *43*, 1143-1147. 10.1001/archpsyc.1986.01800120029007.

Barnard, E.A., Skolnick, P., Olsen, R.W., Mohler, H., Sieghart, W., Biggio, G., Braestrup, C., Bateson, A.N., and Langer, S.Z. (1998). International Union of Pharmacology. XV. Subtypes of γ-Aminobutyric Acid_A Receptors: Classification on the Basis of Subunit Structure and Receptor Function. Pharmacol Rev *50*, 291-314.

Basak, S., Gicheru, Y., Rao, S., Sansom, M.S.P., and Chakrapani, S. (2018a). Cryo-EM reveals two distinct serotonin-bound conformations of full-length 5-HT(3A) receptor. Nature *563*, 270-274. 10.1038/s41586-018-0660-7.

Basak, S., Gicheru, Y., Samanta, A., Molugu, S.K., Huang, W., Fuente, M.l.d., Hughes, T., Taylor, D.J., Nieman, M.T., Moiseenkova-Bell, V., and Chakrapani, S. (2018b). Cryo-EM structure of 5-HT3A receptor in its resting conformation. Nature Communications *9*, 514. 10.1038/s41467-018-02997-4.

Baumann, S.W., Baur, R., and Sigel, E. (2001). Subunit Arrangement of γ-Aminobutyric Acid Type A Receptors. J Biol Chem *276*, 36275-36280. 10.1074/jbc.m105240200.

Belelli, D., and Lambert, J.J. (2005). Neurosteroids: endogenous regulators of the GABA(A) receptor. Nat Rev Neurosci *6*, 565-575. 10.1038/nrn1703.

Ben-Ari, Y. (2002). Excitatory actions of gaba during development: the nature of the nurture. Nat Rev Neurosci *3*, 728-739. 10.1038/nrn920.

Bertozzi, C., Zimmermann, I., Engeler, S., Hilf, R.J., and Dutzler, R. (2016). Signal Transduction at the Domain Interface of Prokaryotic Pentameric Ligand-Gated Ion Channels. Plos Biol *14*, e1002393. 10.1371/journal.pbio.1002393.

Bianchi, M.T. (2010). Context dependent benzodiazepine modulation of GABA(A) receptor opening frequency. Current neuropharmacology *8*, 10-17. 10.2174/157015910790909467.

Bohlhalter, S., Weinmann, O., Mohler, H., and Fritschy, J.M. (1996). Laminar compartmentalization of GABAA-receptor subtypes in the spinal cord: an immunohistochemical study. The Journal of neuroscience : the official journal of the Society for Neuroscience *16*, 283-297. 10.1523/JNEUROSCI.16-01-00283.1996.

Boileau, A.J. (2005). Tandem Subunits Effectively Constrain GABAA Receptor Stoichiometry and Recapitulate Receptor Kinetics But Are Insensitive to GABAA Receptor-Associated Protein. J Neurosci *25*, 11219-11230. 10.1523/jneurosci.3751-05.2005.

Boileau, A.J., Baur, R., Sharkey, L.M., Sigel, E., and Czajkowski, C. (2002). The relative amount of cRNA coding for gamma2 subunits affects stimulation by benzodiazepines in GABA(A) receptors expressed in Xenopus oocytes. Neuropharmacology *43*, 695-700. 10.1016/s0028-3908(02)00036-9.

Boileau, A.J., Kucken, A.M., Evers, A.R., and Czajkowski, C. (1998). Molecular dissection of benzodiazepine binding and allosteric coupling using chimeric gamma-aminobutyric acidA receptor subunits. Mol Pharmacol *53*, 295-303. 10.1124/mol.53.2.295.

Borchardt, J., Blecker, L., Tung, A., Satyshur, K., and Czajkowski, C. (2021). The diazepam binding inhibitor's modulation of the GABA-A receptor is subunit-dependent. bioRxiv.

Bornhorst, J.A., and Falke, J.J. (2000). Purification of proteins using polyhistidine affinity tags. Methods Enzymol *326*, 245-254. 10.1016/s0076-6879(00)26058-8.

Bouyakdan, K., Taib, B., Budry, L., Zhao, S.G., Rodaros, D., Neess, D., Mandrup, S., Faergeman, N.J., and Alquier, T. (2015). A novel role for central ACBP/DBI as a regulator of long-chain fatty acid metabolism in astrocytes. J Neurochem *133*, 253-265. 10.1111/jnc.13035.

Bracamontes, J.R., Li, P., Akk, G., and Steinbach, J.H. (2012). A neurosteroid potentiation site can be moved among GABAA receptor subunits. J Physiol *590*, 5739-5747. 10.1113/jphysiol.2012.237255.

Bracciali, A., Brunelli, M., Cataldo, E., and Degano, P. (2008). Synapses as stochastic concurrent systems. Theoretical Computer Science *408*, 66-82. https://doi.org/10.1016/j.tcs.2008.07.008.

Brickley, S.G., and Mody, I. (2012). Extrasynaptic GABA(A) receptors: their function in the CNS and implications for disease. Neuron *73*, 23-34. 10.1016/j.neuron.2011.12.012.

Burkat, P.M., Lor, C., Perouansky, M., and Pearce, R.A. (2014). Enhancement of α5-Containing γ-Aminobutyric Acid Type A Receptors by the Nonimmobilizer 1,2-Dichlorohexafluorocyclobutane (F6) Is Abolished by the β3(N265M) Mutation. Anesthesia & Analgesia *119*, 1277-1284. 10.1213/ane.0000000000000423.

Calvo-Flores Guzmán, B., Vinnakota, C., Govindpani, K., Waldvogel, H.J., Faull, R.L.M., and Kwakowsky, A. (2018). The GABAergic system as a therapeutic target for Alzheimer's disease. J Neurochem *146*, 649-669. 10.1111/jnc.14345.

Carver, C.M., and Reddy, D.S. (2013). Neurosteroid interactions with synaptic and extrasynaptic GABA(A) receptors: regulation of subunit plasticity, phasic and tonic inhibition, and neuronal network excitability. Psychopharmacology (Berl) *230*, 151-188. 10.1007/s00213-013-3276-5.

Chang, Y., Wang, R., Barot, S., and Weiss, D.S. (1996). Stoichiometry of a Recombinant GABAAReceptor. The Journal of Neuroscience *16*, 5415-5424. 10.1523/jneurosci.16-17-05415.1996.

Che Has, A.T., Absalom, N., Van Nieuwenhuijzen, P.S., Clarkson, A.N., Ahring, P.K., and Chebib, M. (2016). Zolpidem is a potent stoichiometry-selective modulator of α1β3 GABAA receptors: evidence of a novel benzodiazepine site in the α1-α1 interface. Scientific Reports *6*, 28674. 10.1038/srep28674.

Chiara, D.C., Dostalova, Z., Jayakar, S.S., Zhou, X., Miller, K.W., and Cohen, J.B. (2012). Mapping General Anesthetic Binding Site(s) in Human α1β3 γ-Aminobutyric Acid Type A Receptors with [3H]TDBzl-Etomidate, a Photoreactive Etomidate Analogue. Biochemistry-Us *51*, 836-847. 10.1021/bi201772m.

Chiara, D.C., Jayakar, S.S., Zhou, X., Zhang, X., Savechenkov, P.Y., Bruzik, K.S., Miller, K.W., and Cohen, J.B. (2013). Specificity of intersubunit general anesthetic-binding sites in the transmembrane domain of the human α1β3γ2 γ-aminobutyric acid type A (GABAA) receptor. J Biol Chem *288*, 19343-19357. 10.1074/jbc.M113.479725.

Cho, C.-H. (2017). Commentary: GARLH Family Proteins Stabilize GABA(A) Receptors at Synapses. Front Mol Neurosci *10*, 169-169. 10.3389/fnmol.2017.00169.

Christian, C.A., Herbert, A.G., Holt, R.L., Peng, K., Sherwood, K.D., Pangratz-Fuehrer, S., Rudolph, U., and Huguenard, J.R. (2013). Endogenous Positive Allosteric Modulation of GABA(A) Receptors by Diazepam binding inhibitor. Neuron *78*, 1063-1074. 10.1016/j.neuron.2013.04.026.

Christian, C.A., and Huguenard, J.R. (2013). Astrocytes potentiate GABAergic transmission in the thalamic reticular nucleus via endozepine signaling. P Natl Acad Sci USA *110*, 20278-20283. 10.1073/pnas.1318031110.

Collinson, N., Atack, J.R., Laughton, P., Dawson, G.R., and Stephens, D.N. (2006). An inverse agonist selective for alpha5 subunit-containing GABAA receptors improves encoding and recall but not consolidation in the Morris water maze. Psychopharmacology (Berl) *188*, 619-628. 10.1007/s00213-006-0361-z.

Colman, A., Bhamra, S., and Valle, G. (1984). Post-translational modification of exogenous proteins in Xenopus laevis oocytes. Biochem Soc Trans *12*, 932-937. 10.1042/bst0120932.

Conti, E., Tremolizzo, L., Bomba, M., Uccellini, O., Rossi, M.S., Raggi, M.E., Neri, F., Ferrarese, C., and Nacinovich, R. (2013). Reduced fasting plasma levels of diazepam-binding inhibitor in adolescents with anorexia nervosa. Int J Eat Disorder *46*, 626-629. https://doi.org/10.1002/eat.22129.

Costa, E., and Guidotti, A. (1991). Diazepam Binding Inhibitor (Dbi) - a Peptide with Multiple Biological Actions. Life Sci *49*, 325-344. Doi 10.1016/0024-3205(91)90440-M.

Courtney, C.D., and Christian, C.A. (2018). Subregion-Specific Impacts of Genetic Loss of Diazepam Binding Inhibitor on Synaptic Inhibition in the Murine Hippocampus. Neuroscience *388*, 128-138. 10.1016/j.neuroscience.2018.07.012.

Crestani, F., Keist, R., Fritschy, J.-M., Benke, D., Vogt, K., Prut, L., Blüthmann, H., Möhler, H., and Rudolph, U. (2002). Trace fear conditioning involves hippocampal α₅ GABA_A receptors. Proceedings of the National Academy of Sciences *99*, 8980-8985. 10.1073/pnas.142288699.

Crestani, F., Löw, K., Keist, R., Mandelli, M.-J., Möhler, H., and Rudolph, U. (2001). Molecular Targets for the Myorelaxant Action of Diazepam. Mol Pharmacol *59*, 442-445. 10.1124/mol.59.3.442.

Crestani, F., and Rudolph, U. (2015). Behavioral Functions of GABAA Receptor Subtypes - The Zurich Experience. In (Elsevier), pp. 37-51. 10.1016/bs.apha.2014.10.001.

Cullen, D.K., Gilroy, M.E., Irons, H.R., and Laplaca, M.C. (2010). Synapse-to-neuron ratio is inversely related to neuronal density in mature neuronal cultures. Brain Res *1359*, 44-55. 10.1016/j.brainres.2010.08.058.

D'Agostino, R.B., Belanger, A., and D'Agostino, R.B. (1990). A Suggestion for Using Powerful and Informative Tests of Normality. The American Statistician *44*, 316. 10.2307/2684359.

daCosta, Corrie J.B., and Baenziger, John E. (2013). Gating of Pentameric Ligand-Gated Ion Channels: Structural Insights and Ambiguities. Structure *21*, 1271-1283. https://doi.org/10.1016/j.str.2013.06.019.

de Jonge, J.C., Vinkers, C.H., Hulshoff Pol, H.E., and Marsman, A. (2017). GABAergic Mechanisms in Schizophrenia: Linking Postmortem and In Vivo Studies. Frontiers in Psychiatry *8*. 10.3389/fpsyt.2017.00118.

Delaglio, F., Grzesiek, S., Vuister, G., Zhu, G., Pfeifer, J., and Bax, A. (1995). NMRPipe: A multidimensional spectral processing system based on UNIX pipes. J Biomol Nmr *6*. 10.1007/bf00197809.

Devor, A., Fritschy, J.M., and Yarom, Y. (2001). Spatial distribution and subunit composition of GABA(A) receptors in the inferior olivary nucleus. J Neurophysiol *85*, 1686-1696. 10.1152/jn.2001.85.4.1686.

Dumitru, I., Neitz, A., Alfonso, J., and Monyer, H. (2017). Diazepam Binding Inhibitor Promotes Stem Cell Expansion Controlling Environment-Dependent Neurogenesis. Neuron *94*, 125-137.e125. 10.1016/j.neuron.2017.03.003.

Duran, J.M., Anjard, C., Stefan, C., Loomis, W.F., and Malhotra, V. (2010). Unconventional secretion of Acb1 is mediated by autophagosomes. J Cell Biol *188*, 527-536. 10.1083/jcb.200911154.

During, M.J., Ryder, K.M., and Spencer, D.D. (1995). Hippocampal GABA transporter function in temporal-lobe epilepsy. Nature *376*, 174-177. 10.1038/376174a0.

Duvaud, S., Gabella, C., Lisacek, F., Stockinger, H., Ioannidis, V., and Durinx, C. (2021). Expasy, the Swiss Bioinformatics Resource Portal, as designed by its users. Nucleic Acids Research *49*, W216-W227. 10.1093/nar/gkab225.

Dyson, H.J., and Wright, P.E. (2004). Unfolded Proteins and Protein Folding Studied by NMR. Chemical Reviews *104*, 3607-3622. 10.1021/cr030403s.

Engin, E., Benham, R.S., and Rudolph, U. (2018). An Emerging Circuit Pharmacology of GABA A Receptors. Trends in Pharmacological Sciences *39*, 710-732. 10.1016/j.tips.2018.04.003.

Ernst, M., Brauchart, D., Boresch, S., and Sieghart, W. (2003). Comparative modeling of GABA(A) receptors: limits, insights, future developments. Neuroscience *119*, 933-943. 10.1016/s0306-4522(03)00288-4.

Færgeman, N.J., Wadum, M., Feddersen, S., Burton, M., Kragelund, B.B., and Knudsen, J. (2007). Acyl-CoA binding proteins; structural and functional conservation over 2000 MYA. Molecular and Cellular Biochemistry *299*, 55-65. 10.1007/s11010-005-9040-3.

Farges, R., Joseph-Liauzun, E., Shire, D., Caput, D., Le Fur, G., and Ferrara, P. (1994). Site-directed mutagenesis of the peripheral benzodiazepine receptor: identification of amino acids implicated in the binding site of Ro5-4864. Mol Pharmacol *46*, 1160-1167.

Farrant, M., and Nusser, Z. (2005). Variations on an inhibitory theme: Phasic and tonic activation of GABA(A) receptors. Nat Rev Neurosci *6*, 215-229. 10.1038/nrn1625.

Farzampour, Z., Reimer, R.J., and Huguenard, J. (2015). Endozepines. Adv Pharmacol *72*, 147-164. 10.1016/bs.apha.2014.10.005.

Ferrarese, C., Alho, H., Guidotti, A., and Costa, E. (1987). Colocalization and Corelease of Gaba and Putative Allosteric Modulators of Gaba Receptor. Neuropharmacology *26*, 1011-1018. Doi 10.1016/0028-3908(87)90080-3.

Ferrarese, C., Appollonio, I., Frigo, M., Meregalli, S., Piolti, R., Tamma, F., and Frattola, L. (1990). Cerebrospinal fluid levels of diazepam- binding inhibitor in neurodegenerative disorders with dementia. Neurology *40*, 632-635. 10.1212/wnl.40.4.632.

Ferrarese, C., Appollonio, I., Frigo, M., Piolti, R., Tamma, F., and Frattola, L. (1989). Distribution of a putative endogenous modulator of the GABAergic system in human brain. Neurology *39*, 443-445. 10.1212/wnl.39.3.443.

Ferrero, P., Guidotti, A., Conti-Tronconi, B., and Costa, E. (1984). A brain octadecaneuropeptide generated by tryptic digestion of DBI (diazepam binding inhibitor) functions as a proconflict ligand of benzodiazepine recognition sites. Neuropharmacology *23*, 1359-1362. 10.1016/0028-3908(84)90061-3.

Ferrero, P., Santi, M.R., Conti-Tronconi, B., Costa, E., and Guidotti, A. (1986). Study of an octadecaneuropeptide derived from diazepam binding inhibitor (DBI): biological activity and presence in rat brain. Proc Natl Acad Sci U S A *83*, 827-831. 10.1073/pnas.83.3.827.

Fischer, B.D., Atack, J.R., Platt, D.M., Reynolds, D.S., Dawson, G.R., and Rowlett, J.K. (2011). Contribution of GABAA receptors containing α3 subunits to the therapeutic-related and side effects of benzodiazepine-type drugs in monkeys. Psychopharmacology *215*, 311-319. 10.1007/s00213-010-2142-y.

Fritschy, J.M., Benke, D., Mertens, S., Oertel, W.H., Bachi, T., and Möhler, H. (1992). Five subtypes of type A gamma-aminobutyric acid receptors identified in neurons by double and triple immunofluorescence staining with subunit-specific antibodies. P Natl Acad Sci USA *89*, 6726-6730. 10.1073/pnas.89.15.6726.

Gandolfo, P., Patte, C., Leprince, J., Thoumas, J.-L., Vaudry, H., and Tonon, M.-C. (1997). The stimulatory effect of the octadecaneuropeptide (ODN) on cytosolic Ca2+ in rat astrocytes is not mediated through classical benzodiazepine receptors. Eur J Pharmacol *322*, 275-281. https://doi.org/10.1016/S0014-2999(97)00012-5.

García-Nafría, J., and Tate, C.G. (2020). Cryo-Electron Microscopy: Moving Beyond X-Ray Crystal Structures for Drug Receptors and Drug Development. Annual Review of Pharmacology and Toxicology *60*, 51-71. 10.1146/annurev-pharmtox-010919-023545.

Garcia, P.S., Kolesky, S.E., and Jenkins, A. (2010). General anesthetic actions on GABA(A) receptors. Curr Neuropharmacol *8*, 2-9. 10.2174/157015910790909502.

GE-Healthcare (2007). Affinity Chromatography: Principles and Methods. https://www.sigmaaldrich.com/content/dam/sigma-aldrich/docs/promo_NOT_INDEXED/General_Information/1/ge-affinity-chromatography.pdf

Germann, A.L., Pierce, S.R., Burbridge, A.B., Steinbach, J.H., and Akk, G. (2019). Steady-State Activation and Modulation of the Concatemeric α1β2γ2L GABA(A) Receptor. Mol Pharmacol *96*, 320-329. 10.1124/mol.119.116913.

Gielen, M.C., Lumb, M.J., and Smart, T.G. (2012). Benzodiazepines Modulate GABAA Receptors by Regulating the Preactivation Step after GABA Binding. J Neurosci *32*, 5707-5715. 10.1523/jneurosci.5663-11.2012.

Goldschen-Ohm, M.P., Haroldson, A., Jones, M.V., and Pearce, R.A. (2014). A nonequilibrium binary elements-based kinetic model for benzodiazepine regulation of GABAA receptors. J Gen Physiol *144*, 27-39. 10.1085/jgp.201411183.

Goldschen-Ohm, M.P., Wagner, D.A., Petrou, S., and Jones, M.V. (2010). An epilepsy-related region in the GABA(A) receptor mediates long-distance effects on GABA and benzodiazepine binding sites. Mol Pharmacol *77*, 35-45. 10.1124/mol.109.058289.

Gonzales, E.B., Bell-Horner, C.L., Dibas, M.I., Huang, R.-Q., and Dillon, G.H. (2008). Stoichiometric analysis of the TM2 6′ phenylalanine mutation on desensitization in α1β2 and α1β2γ2 GABAA receptors. Neurosci Lett *431*, 184-189. 10.1016/j.neulet.2007.11.039.

Gonzalez-Gutierrez, G., Cuello, L.G., Nair, S.K., and Grosman, C. (2013). Gating of the proton-gated ion channel from Gloeobacter violaceus at pH 4 as revealed by X-ray crystallography. Proceedings of the National Academy of Sciences *110*, 18716-18721. 10.1073/pnas.1313156110.

Govindpani, K., Calvo-Flores Guzmán, B., Vinnakota, C., Waldvogel, H.J., Faull, R.L., and Kwakowsky, A. (2017). Towards a Better Understanding of GABAergic Remodeling in Alzheimer's Disease. International Journal of Molecular Sciences *18*, 1813.

Graham, F.L., and Van Der Eb, A.J. (1973). Transformation of rat cells by DNA of human adenovirus 5. Virology *54*, 536-539. 10.1016/0042-6822(73)90163-3.

GraphPad (2021). Paired or ratio t test? https://www.graphpad.com/guides/prism/latest/statistics/stat_paired_or_ratio_t_test.htm.

Groen, M.R., Paulsen, O., Pérez-Garci, E., Nevian, T., Wortel, J., Dekker, M.P., Mansvelder, H.D., Ooyen, A.v., and Meredith, R.M. (2014). Development of dendritic tonic GABAergic inhibition regulates excitability and plasticity in CA1 pyramidal neurons. Journal of Neurophysiology *112*, 287-299. 10.1152/jn.00066.2014.

Guidotti, A., Forchetti, C.M., Corda, M.G., Konkel, D., Bennett, C.D., and Costa, E. (1983). Isolation, characterization, and purification to homogeneity of an endogenous polypeptide with

agonistic action on benzodiazepine receptors. Proc Natl Acad Sci U S A *80*, 3531-3535. 10.1073/pnas.80.11.3531.

Gyenes, M., Wang, Q., Gibbs, T.T., and Farb, D.H. (1994). Phosphorylation factors control neurotransmitter and neuromodulator actions at the gamma-aminobutyric acid type A receptor. Mol Pharmacol *46*, 542-549.

Han, W., Li, J., Pelkey, K.A., Pandey, S., Chen, X., Wang, Y.-X., Wu, K., Ge, L., Li, T., Castellano, D., et al. (2019). Shisa7 is a GABA_A receptor auxiliary subunit controlling benzodiazepine actions. Science *366*, 246-250. 10.1126/science.aax5719.

Hanson, S.M., and Czajkowski, C. (2008). Structural mechanisms underlying benzodiazepine modulation of the GABA(A) receptor. J Neurosci *28*, 3490-3499. 10.1523/jneurosci.5727-07.2008.

Hörtnagl, H., Tasan, R.O., Wieselthaler, A., Kirchmair, E., Sieghart, W., and Sperk, G. (2013). Patterns of mRNA and protein expression for 12 GABAA receptor subunits in the mouse brain. Neuroscience *236*, 345-372. 10.1016/j.neuroscience.2013.01.008.

Huang, X., Chen, H., and Shaffer, P.L. (2017a). Crystal Structures of Human GlyRα3 Bound to Ivermectin. Structure *25*, 945-950.e942. 10.1016/j.str.2017.04.007.

Huang, X., Shaffer, P.L., Ayube, S., Bregman, H., Chen, H., Lehto, S.G., Luther, J.A., Matson, D.J., McDonough, S.I., Michelsen, K., et al. (2017b). Crystal structures of human glycine receptor α3 bound to a novel class of analgesic potentiators. Nature Structural & Molecular Biology *24*, 108-113. 10.1038/nsmb.3329.

Jackson, M.B., Lecar, H., Mathers, D.A., and Barker, J.L. (1982). Single channel currents activated by gamma-aminobutyric acid, muscimol, and (-)-pentobarbital in cultured mouse spinal neurons. J Neurosci *2*, 889-894. 10.1523/jneurosci.02-07-00889.1982.

Jarecki, B.W., Makino, S., Beebe, E.T., Fox, B.G., and Chanda, B. (2013). Function of Shaker potassium channels produced by cell-free translation upon injection into Xenopus oocytes. Sci Rep *3*, 1040. 10.1038/srep01040.

Joksimović, S., Divljaković, J., Van Linn, M.L., Varagic, Z., Brajković, G., Milinković, M.M., Yin, W., Timić, T., Sieghart, W., Cook, J.M., and Savić, M.M. (2013). Benzodiazepine-induced spatial learning deficits in rats are regulated by the degree of modulation of α1 GABAA receptors. European Neuropsychopharmacology *23*, 390-399. https://doi.org/10.1016/j.euroneuro.2012.05.003.

Jones, M.V., and Westbrook, G.L. (1995). Desensitized states prolong GABAA channel responses to brief agonist pulses. Neuron *15*, 181-191. 10.1016/0896-6273(95)90075-6.

Kaddour, H., Hamdi, Y., Vaudry, D., Basille, M., Desrues, L., Leprince, J., Castel, H., Vaudry, H., Tonon, M.-C., Amri, M., and Masmoudi-Kouki, O. (2013). The octadecaneuropeptide ODN prevents 6-hydroxydopamine-induced apoptosis of cerebellar granule neurons through a PKC-MAPK-dependent pathway. J Neurochem *125*, 620-633. https://doi.org/10.1111/jnc.12140.

Karim, N., Wellendorph, P., Absalom, N., Johnston, G.A., Hanrahan, J.R., and Chebib, M. (2013). Potency of GABA at human recombinant GABA(A) receptors expressed in Xenopus oocytes: a mini review. Amino Acids *44*, 1139-1149. 10.1007/s00726-012-1456-y.

Kelly, M.D., Smith, A., Banks, G., Wingrove, P., Whiting, P.W., Atack, J., Seabrook, G.R., and Maubach, K.A. (2002). Role of the histidine residue at position 105 in the human alpha 5 containing GABA(A) receptor on the affinity and efficacy of benzodiazepine site ligands. Br J Pharmacol *135*, 248-256. 10.1038/sj.bjp.0704459.

King, G.L., Knox, J.J., and Dingledine, R. (1985). Reduction of inhibition by a benzodiazepine antagonist, Ro15-1788, in the rat hippocampal slice. Neuroscience *15*, 371-378. 10.1016/0306-4522(85)90219-2.

Knoflach, F., Benke, D., Wang, Y., Scheurer, L., Lüddens, H., Hamilton, B.J., Carter, D.B., Mohler, H., and Benson, J.A. (1996). Pharmacological modulation of the diazepam-insensitive recombinant gamma-aminobutyric acidA receptors alpha 4 beta 2 gamma 2 and alpha 6 beta 2 gamma 2. Mol Pharmacol *50*, 1253-1261.

Knudsen, J. (1991). Acyl-Coa-Binding and Transport, an Alternate Function for Diazepam Binding Inhibitor (Dbi), Which is Identical with Acyl-Coa-Binding Protein. Neuropharmacology *30*, 1405-1410.

Koester, C., Rudolph, U., Haenggi, T., Papilloud, A., Fritschy, J.-M., and Crestani, F. (2013). Dissecting the role of diazepam-sensitive γ-aminobutyric acid type A receptors in defensive behavioral reactivity to mild threat. Pharmacology Biochemistry and Behavior *103*, 541-549. 10.1016/j.pbb.2012.10.004.

Kozakov, D., Beglov, D., Bohnuud, T., Mottarella, S.E., Xia, B., Hall, D.R., and Vajda, S. (2013). How good is automated protein docking? *81*, 2159-2166. 10.1002/prot.24403.

Kozakov, D., Hall, D.R., Xia, B., Porter, K.A., Padhorny, D., Yueh, C., Beglov, D., and Vajda, S. (2017). The ClusPro web server for protein–protein docking. Nature Protocols *12*, 255-278. 10.1038/nprot.2016.169.

Kumar, P., Wang, Y., Zhang, Z., Zhao, Z., Cymes, G.D., Tajkhorshid, E., and Grosman, C. (2020). Cryo-EM structures of a lipid-sensitive pentameric ligand-gated ion channel embedded in a phosphatidylcholine-only bilayer. Proceedings of the National Academy of Sciences *117*, 1788-1798. 10.1073/pnas.1906823117.

Lane, C.D. (1983). The fate of genes, messengers, and proteins introduced into Xenopus oocytes. Curr Top Dev Biol *18*, 89-116. 10.1016/s0070-2153(08)60580-3.

Laverty, D., Desai, R., Uchański, T., Masiulis, S., Stec, W.J., Malinauskas, T., Zivanov, J., Pardon, E., Steyaert, J., Miller, K.W., and Aricescu, A.R. (2019). Cryo-EM structure of the human α1β3γ2 GABA(A) receptor in a lipid bilayer. Nature *565*, 516-520. 10.1038/s41586-018-0833-4.

Laverty, D., Thomas, P., Field, M., Andersen, O.J., Gold, M.G., Biggin, P.C., Gielen, M., and Smart, T.G. (2017). Crystal structures of a GABAA-receptor chimera reveal new endogenous neurosteroid-binding sites. Nature Structural & Molecular Biology *24*, 977-985. 10.1038/nsmb.3477.

Lee, V., and Maguire, J. (2014). The impact of tonic GABAA receptor-mediated inhibition on neuronal excitability varies across brain region and cell type. Frontiers in Neural Circuits *8*. 10.3389/fncir.2014.00003.

Leroy, C., Poisbeau, P., Keller, A., and Nehlig, A. (2004). Pharmacological plasticity of GABAA receptors at dentate gyrus synapses in a rat model of temporal lobe epilepsy. The Journal of Physiology *557*, 473-487.

Li, P., Eaton, M.M., Steinbach, J.H., and Akk, G. (2013). The benzodiazepine diazepam potentiates responses of α1β2γ2L γ-aminobutyric acid type A receptors activated by either γ-aminobutyric acid or allosteric agonists. The Journal of the American Society of Anesthesiologists *118*, 1417-1425.

Liu, X., Li, Y., Zhou, L., Chen, H., Su, Z., and Hao, W. (2005). Conditioned place preference associates with the mRNA expression of diazepam binding inhibitor in brain regions of the addicted rat during withdrawal. *137*, 47-54. 10.1016/j.molbrainres.2005.02.021.

Llinás, R., Urbano, F.J., Leznik, E., Ramírez, R.R., and Van Marle, H.J.F. (2005). Rhythmic and dysrhythmic thalamocortical dynamics: GABA systems and the edge effect. Trends in Neurosciences *28*, 325-333. 10.1016/j.tins.2005.04.006.

Loomis, W.F., Behrens, M.M., Williams, M.E., and Anjard, C. (2010). Pregnenolone Sulfate and Cortisol Induce Secretion of Acyl-CoA-binding Protein and Its Conversion into Endozepines from Astrocytes*. J Biol Chem *285*, 21359-21365. https://doi.org/10.1074/jbc.M110.105858.

Lorenz-Guertin, J.M., Bambino, M.J., and Jacob, T.C. (2018). γ2 GABAAR Trafficking and the Consequences of Human Genetic Variation. Front Cell Neurosci *12*. 10.3389/fncel.2018.00265.

Löw, K., Crestani, F., Keist, R., Benke, D., Brünig, I., Benson, J.A., Fritschy, J.M., Rülicke, T., Bluethmann, H., Möhler, H., and Rudolph, U. (2000). Molecular and neuronal substrate for the selective attenuation of anxiety. Science *290*, 131-134. 10.1126/science.290.5489.131.

Mann, E.O., and Paulsen, O. (2007). Role of GABAergic inhibition in hippocampal network oscillations. Trends in Neurosciences *30*, 343-349. 10.1016/j.tins.2007.05.003.

Marino, F., Cosentino, M., Ferrari, M., Cattaneo, S., Frigo, G., Fietta, A.M., Lecchini, S., and Frigo, G.M. (2004). Intracellular calcium changes induced by the endozepine triakontatetraneuropeptide in human polymorphonuclear leukocytes: Role of protein kinase C and effect of calcium channel blockers. Cell Communication and Signaling *2*, 6. 10.1186/1478-811X-2-6.

Marion, D. (2013). An Introduction to Biological NMR Spectroscopy. Molecular & Cellular Proteomics *12*, 3006-3025. 10.1074/mcp.o113.030239.

Masiulis, S., Desai, R., Uchański, T., Serna Martin, I., Laverty, D., Karia, D., Malinauskas, T., Zivanov, J., Pardon, E., Kotecha, A., et al. (2019). GABAA receptor signalling mechanisms revealed by structural pharmacology. Nature *565*, 454-459. 10.1038/s41586-018-0832-5.

Masmoudi-Kouki, O., Namsi, A., Hamdi, Y., Bahdoudi, S., Ghouili, I., Chuquet, J., Leprince, J., Lefranc, B., Ghrairi, T., Tonon, M.-C., et al. (2020). Cytoprotective and Neurotrophic Effects of

Octadecaneuropeptide (ODN) in in vitro and in vivo Models of Neurodegenerative Diseases. Frontiers in Endocrinology *11*. 10.3389/fendo.2020.566026.

Masmoudi, O., Gandolfo, P., Tokay, T., Leprince, J., Ravni, A., Vaudry, H., and Tonon, M.C. (2005). Somatostatin down-regulates the expression and release of endozepines from cultured rat astrocytes via distinct receptor subtypes. J Neurochem *94*, 561-571. 10.1111/j.1471-4159.2005.03076.x.

Miettinen, H., Kononen, J., Haapasalo, H., Helén, P., Sallinen, P., Harjuntausta, T., Helin, H., and Alho, H. (1995). Expression of Peripheral-Type Benzodiazepine Receptor and Diazepam Binding Inhibitor in Human Astrocytomas: Relationship to Cell Proliferation. Cancer Research *55*, 2691-2695.

Miller, P.S., and Aricescu, A.R. (2014). Crystal structure of a human GABAA receptor. Nature *512*, 270-275. 10.1038/nature13293.

Miller, P.S., Scott, S., Masiulis, S., De Colibus, L., Pardon, E., Steyaert, J., and Aricescu, A.R. (2017). Structural basis for GABAA receptor potentiation by neurosteroids. Nature Structural & Molecular Biology *24*, 986-992. 10.1038/nsmb.3484.

Mills, J.D., Nalpathamkalam, T., Jacobs, H.I.L., Janitz, C., Merico, D., Hu, P.Z., and Janitz, M. (2013). RNA-Seq analysis of the parietal cortex in Alzheimer's disease reveals alternatively spliced isoforms related to lipid metabolism. Neurosci Lett *536*, 90-95. 10.1016/j.neulet.2012.12.042.

Mody, I., De Koninck, Y., Otis, T.S., and Soltesz, I. (1994). Bridging the cleft at GABA synapses in the brain. Trends Neurosci *17*, 517-525. 10.1016/0166-2236(94)90155-4.

Mody, I., and Pearce, R.A. (2004). Diversity of inhibitory neurotransmission through GABAA receptors. Trends in Neurosciences *27*, 569-575. 10.1016/j.tins.2004.07.002.

Mohler, H. (2011). The rise of a new GABA pharmacology. Neuropharmacology *60*, 1042-1049. 10.1016/j.neuropharm.2010.10.020.

Monod, J., Wyman, J., and Changeux, J.P. (1965). ON THE NATURE OF ALLOSTERIC TRANSITIONS: A PLAUSIBLE MODEL. J Mol Biol *12*, 88-118. 10.1016/s0022-2836(65)80285-6.

Morales-Perez, C.L., Noviello, C.M., and Hibbs, R.E. (2016). X-ray structure of the human α4β2 nicotinic receptor. Nature *538*, 411-415. 10.1038/nature19785.

Morales, A., Aleu, J., Ivorra, I., Ferragut, J.A., Gonzalez-Ros, J.M., and Miledi, R. (1995). Incorporation of reconstituted acetylcholine receptors from Torpedo into the Xenopus oocyte membrane. Proceedings of the National Academy of Sciences *92*, 8468-8472. 10.1073/pnas.92.18.8468.

Moreno-Jiménez, E.P., Flor-García, M., Terreros-Roncal, J., Rábano, A., Cafini, F., Pallas-Bazarra, N., Ávila, J., and Llorens-Martín, M. (2019). Adult hippocampal neurogenesis is abundant in neurologically healthy subjects and drops sharply in patients with Alzheimer’s disease. Nature Medicine *25*, 554-560. 10.1038/s41591-019-0375-9.

Morlock, E.V., and Czajkowski, C. (2011). Different Residues in the GABA(A) Receptor Benzodiazepine Binding Pocket Mediate Benzodiazepine Efficacy and Binding. Mol Pharmacol *80*, 14-22. 10.1124/mol.110.069542.

Morris, H.V., Dawson, G.R., Reynolds, D.S., Atack, J.R., and Stephens, D.N. (2006). Both alpha2 and alpha3 GABAA receptor subtypes mediate the anxiolytic properties of benzodiazepine site ligands in the conditioned emotional response paradigm. Eur J Neurosci *23*, 2495-2504. 10.1111/j.1460-9568.2006.04775.x.

Mortensen, M., Kristiansen, U., Ebert, B., Frølund, B., Krogsgaard-Larsen, P., and Smart, T.G. (2004). Activation of single heteromeric GABA(A) receptor ion channels by full and partial agonists. J Physiol *557*, 389-413. 10.1113/jphysiol.2003.054734.

Mortensen, M., Patel, B., and Smart, T.G. (2012). GABA Potency at GABAA Receptors Found in Synaptic and Extrasynaptic Zones. Front Cell Neurosci *6*. 10.3389/fncel.2012.00001.

Mortensen, M., and Smart, T.G. (2006). Extrasynaptic αβ subunit GABAAreceptors on rat hippocampal pyramidal neurons. J Physiol *577*, 841-856. 10.1113/jphysiol.2006.117952.

Mozrzymas, J.W., Żarmowska, E.D., Pytel, M., and Mercik, K. (2003). Modulation of GABAAReceptors by Hydrogen Ions Reveals Synaptic GABA Transient and a Crucial Role of the Desensitization Process. The Journal of Neuroscience *23*, 7981-7992. 10.1523/jneurosci.23-22-07981.2003.

Muroi, Y., Theusch, C.M., Czajkowski, C., and Jackson, M.B. (2009). Distinct structural changes in the GABAA receptor elicited by pentobarbital and GABA. Biophys J *96*, 499-509. 10.1016/j.bpj.2008.09.037.

Neelands, T.R., and Macdonald, R.L. (1999). Incorporation of the π Subunit into Functional γ-Aminobutyric AcidA Receptors. Mol Pharmacol *56*, 598-610. 10.1124/mol.56.3.598.

Neess, D., Bloksgaard, M., Bek, S., Marcher, A.-B., Elle, I.C., Helledie, T., Due, M., Pagmantidis, V., Finsen, B., Wilbertz, J., et al. (2011). Disruption of the Acyl-CoA-binding Protein Gene Delays Hepatic Adaptation to Metabolic Changes at Weaning. J Biol Chem *286*, 3460-3472. 10.1074/jbc.m110.161109.

Nimmich, M.L., Heidelberg, L.S., and Fisher, J.L. (2009). RNA editing of the GABA(A) receptor alpha3 subunit alters the functional properties of recombinant receptors. Neurosci Res *63*, 288-293. 10.1016/j.neures.2009.01.003.

Nitz, I., Döring, F., Schrezenmeir, J., and Burwinkel, B. (2005). Identification of new acyl-CoA binding protein transcripts in human and mouse. The International Journal of Biochemistry & Cell Biology *37*, 2395-2405. https://doi.org/10.1016/j.biocel.2005.06.008.

Nitz, I., Kruse, M.L., Klapper, M., and Doring, F. (2011). Specific regulation of low-abundance transcript variants encoding human Acyl-CoA binding protein (ACBP) isoforms. J Cell Mol Med *15*, 909-927. 10.1111/j.1582-4934.2010.01055.x.

Nusser, Z., and Mody, I. (2002). Selective modulation of tonic and phasic inhibitions in dentate gyrus granule cells. J Neurophysiol *87*, 2624-2628. 10.1152/jn.2002.87.5.2624.

Nusser, Z., Roberts, J.D.B., Baude, A., Richards, J.G., Sieghart, W., and Somogyi, P. (1995). Immunocytochemical Localization of the α1 and β2/3 Subunits of the GABAAReceptor in Relation to Specific GABAergic Synapses in the Dentate Gyrus. European Journal of Neuroscience *7*, 630-646. 10.1111/j.1460-9568.1995.tb00667.x.

Nusser, Z., Sieghart, W., and Somogyi, P. (1998). Segregation of different GABAA receptors to synaptic and extrasynaptic membranes of cerebellar granule cells. J Neurosci *18*, 1693-1703. 10.1523/jneurosci.18-05-01693.1998.

Olsen, R.W. (2006). Picrotoxin-like channel blockers of GABAA receptors. Proc Natl Acad Sci U S A *103*, 6081-6082. 10.1073/pnas.0601121103.

Olsen, R.W. (2018). GABA(A) receptor: Positive and negative allosteric modulators. Neuropharmacology *136*, 10-22. 10.1016/j.neuropharm.2018.01.036.

Olsen, R.W., and Sieghart, W. (2008). International Union of Pharmacology. LXX. Subtypes of γ-Aminobutyric AcidA Receptors: Classification on the Basis of Subunit Composition, Pharmacology, and Function. Update. Pharmacol Rev *60*, 243-260. 10.1124/pr.108.00505.

Olsen, R.W., and Sieghart, W. (2009). GABAA receptors: Subtypes provide diversity of function and pharmacology. Neuropharmacology *56*, 141-148. 10.1016/j.neuropharm.2008.07.045.

Organization, W.E.C.o.t.S.o.E.D.W.H. (1977). The selection of essential drugs : report of a WHO expert committee [meeting held in Geneva from 17 to 21 October 1977].

Palma, E., Ruffolo, G., Cifelli, P., Roseti, C., Vliet, E.A.V., and Aronica, E. (2017). Modulation of GABAA Receptors in the Treatment of Epilepsy. Curr Pharm Des *23*, 5563-5568. 10.2174/1381612823666170809100230.

Pangratz-Fuehrer, S., Sieghart, W., Rudolph, U., Parada, I., and Huguenard, J.R. (2016). Early postnatal switch in GABAA receptor α-subunits in the reticular thalamic nucleus. Journal of Neurophysiology *115*, 1183-1195. 10.1152/jn.00905.2015.

Papadopoulos, V., Berkovich, A., Krueger, K.E., Costa, E., and Guidotti, A. (1991). Diazepam Binding Inhibitor and Its Processing Products Stimulate Mitochondrial Steroid Biosynthesis via an Interaction with Mitochondrial Benzodiazepine Receptors*. Endocrinology *129*, 1481-1488. 10.1210/endo-129-3-1481.

Patte, C., Gandolfo, P., Leprince, J., Thoumas, J.L., Fontaine, M., Vaudry, H., and Tonon, M.C. (1999). GABA inhibits endozepine release from cultured rat astrocytes. Glia *25*, 404-411.

Patte, C., Vaudry, H., Desrues, L., Gandolfo, P., Strijdveen, I., Lamacz, M., and Tonon, M.C. (1995). The endozepine ODN stimulates polyphosphoinositide metabolism in rat astrocytes. Febs Lett *362*, 106-110. https://doi.org/10.1016/0014-5793(95)00209-R.

Perrais, D., and Ropert, N. (1999). Effect of zolpidem on miniature IPSCs and occupancy of postsynaptic GABAA receptors in central synapses. The Journal of Neuroscience *19*, 578-588.

Phulera, S., Zhu, H., Yu, J., Claxton, D.P., Yoder, N., Yoshioka, C., and Gouaux, E. (2018). Cryo-EM structure of the benzodiazepine-sensitive α1β1γ2S tri-heteromeric GABA(A) receptor in complex with GABA. Elife *7*, e39383. 10.7554/eLife.39383.

Pichitpunpong, C., Thongkorn, S., Kanlayaprasit, S., Yuwattana, W., Plaingam, W., Sangsuthum, S., Aizat, W.M., Baharum, S.N., Tencomnao, T., Hu, V.W., and Sarachana, T. (2019). Phenotypic subgrouping and multi-omics analyses reveal reduced diazepam-binding inhibitor (DBI) protein levels in autism spectrum disorder with severe language impairment. PLOS ONE *14*, e0214198. 10.1371/journal.pone.0214198.

Rangaraju, V., Calloway, N., and Timothy (2014). Activity-Driven Local ATP Synthesis Is Required for Synaptic Function. Cell *156*, 825-835. 10.1016/j.cell.2013.12.042.

Reddy, D.S. (2010). Neurosteroids: endogenous role in the human brain and therapeutic potentials. Prog Brain Res *186*, 113-137. 10.1016/B978-0-444-53630-3.00008-7.

Regan, J.W., Yamamura, H.I., Yamada, S., and Roeske, W.R. (1981). High affinity renal [3H]flunitrazepam binding: Characterization, localization, and alteration in hypertension. Life Sci *28*, 991-998. https://doi.org/10.1016/0024-3205(81)90744-X.

Rodgers, F.C., Zarnowska, E.D., Laha, K.T., Engin, E., Zeller, A., Keist, R., Rudolph, U., and Pearce, R.A. (2015). Etomidate Impairs Long-Term Potentiation In Vitro by Targeting 5-Subunit Containing GABAA Receptors on Nonpyramidal Cells. J Neurosci *35*, 9707-9716. 10.1523/jneurosci.0315-15.2015.

Rosano, G.N.L., and Ceccarelli, E.A. (2014). Recombinant protein expression in Escherichia coli: advances and challenges. Frontiers in Microbiology *5*. 10.3389/fmicb.2014.00172.

Rowlett, J.K., Platt, D.M., Lelas, S., Atack, J.R., and Dawson, G.R. (2005). Different GABAA receptor subtypes mediate the anxiolytic, abuse-related, and motor effects of benzodiazepine-like drugs in primates. Proc Natl Acad Sci U S A *102*, 915-920. 10.1073/pnas.0405621102.

Rudolph, U., Crestani, F., Benke, D., Brünig, I., Benson, J.A., Fritschy, J.M., Martin, J.R., Bluethmann, H., and Möhler, H. (1999). Benzodiazepine actions mediated by specific gamma-aminobutyric acid(A) receptor subtypes. Nature *401*, 796-800. 10.1038/44579.

Rudolph, U., and Knoflach, F. (2011). Beyond classical benzodiazepines: novel therapeutic potential of GABAA receptor subtypes. Nature Reviews Drug Discovery *10*, 685-697. 10.1038/nrd3502.

Rupprecht, R., Papadopoulos, V., Rammes, G., Baghai, T.C., Fan, J., Akula, N., Groyer, G., Adams, D., and Schumacher, M. (2010). Translocator protein (18 kDa) (TSPO) as a therapeutic target for neurological and psychiatric disorders. Nature Reviews Drug Discovery *9*, 971-988. 10.1038/nrd3295.

Rüsch, D., Zhong, H., and Forman, S.A. (2004). Gating Allosterism at a Single Class of Etomidate Sites on α1β2γ2L GABAA Receptors Accounts for Both Direct Activation and Agonist Modulation. J Biol Chem *279*, 20982-20992. 10.1074/jbc.m400472200.

Scott, S., and Aricescu, A.R. (2019). A structural perspective on GABA(A) receptor pharmacology. Curr Opin Struct Biol *54*, 189-197. 10.1016/j.sbi.2019.03.023.

Semyanov, A., Walker, M.C., and Kullmann, D.M. (2003). GABA uptake regulates cortical excitability via cell type–specific tonic inhibition. Nature Neuroscience *6*, 484-490. 10.1038/nn1043.

Sequeira, A., Shen, K., Gottlieb, A., and Limon, A. (2019). Human brain transcriptome analysis finds region- and subject-specific expression signatures of GABAAR subunits. Communications Biology *2*. 10.1038/s42003-019-0413-7.

Shilling, P.J., Mirzadeh, K., Cumming, A.J., Widesheim, M., Köck, Z., and Daley, D.O. (2020). Improved designs for pET expression plasmids increase protein production yield in Escherichia coli. Communications Biology *3*. 10.1038/s42003-020-0939-8.

Shoyab, M., Gentry, L.E., Marquardt, H., and Todaro, G.J. (1986). Isolation and characterization of a putative endogenous benzodiazepineoid (endozepine) from bovine and human brain. J Biol Chem *261*, 11968-11973. 10.1016/s0021-9258(18)67188-1.

Siejka, A., Jankiewicz-Wika, J., Stępień, H., Fryczak, J., Świętosławski, J., and Komorowski, J. (2015). Reduced plasma level of diazepam-binding inhibitor (DBI) in patients with morbid obesity. Endocrine *49*, 859-862. 10.1007/s12020-014-0522-5.

Sigel, E., and Ernst, M. (2018). The Benzodiazepine Binding Sites of GABAA Receptors. Trends in Pharmacological Sciences *39*, 659-671. 10.1016/j.tips.2018.03.006.

Slobodyansky, E., Guidotti, A., Wambebe, C., Berkovich, A., and Costa, E. (1989). Isolation and characterization of a rat brain triakontatetraneuropeptide, a posttranslational product of diazepam binding inhibitor: specific action at the Ro 5-4864 recognition site. J Neurochem *53*, 1276-1284. 10.1111/j.1471-4159.1989.tb07425.x.

Smart, T.G., and Stephenson, F.A. (2019). A half century of γ-aminobutyric acid. Brain and Neuroscience Advances *3*, 239821281985824. 10.1177/2398212819858249.

Smith, G.B., and Olsen, R.W. (1995). Functional domains of GABAA receptors. Trends Pharmacol Sci *16*, 162-168. 10.1016/s0165-6147(00)89009-4.

Sommerer, N., Centeno, D., and Rossignol, M. (2007). Peptide mass fingerprinting: identification of proteins by MALDI-TOF. Methods Mol Biol *355*, 219-234. 10.1385/1-59745-227-0:219.

Somogyi, P., Fritschy, J.M., Benke, D., Roberts, J.D., and Sieghart, W. (1996). The gamma 2 subunit of the GABAA receptor is concentrated in synaptic junctions containing the alpha 1 and beta 2/3 subunits in hippocampus, cerebellum and globus pallidus. Neuropharmacology *35*, 1425-1444. 10.1016/s0028-3908(96)00086-x.

Squires, R.F., and Braestrup, C. (1977). Benzodiazepine receptors in rat brain. Nature *266*, 732-734. 10.1038/266732a0.

Stell, B.M., Brickley, S.G., Tang, C.Y., Farrant, M., and Mody, I. (2003). Neuroactive steroids reduce neuronal excitability by selectively enhancing tonic inhibition mediated by subunit-containing GABAA receptors. Proceedings of the National Academy of Sciences *100*, 14439-14444. 10.1073/pnas.2435457100.

Taskinen, J.P., Van Aalten, D.M., Knudsen, J., and Wierenga, R.K. (2006). High resolution crystal structures of unliganded and liganded human liver ACBP reveal a new mode of binding for the acyl-CoA ligand. *66*, 229-238. 10.1002/prot.21124.

Taskinen, J.P., van Aalten, D.M., Knudsen, J., and Wierenga, R.K. (2007). High resolution crystal structures of unliganded and liganded human liver ACBP reveal a new mode of binding for the acyl-CoA ligand. PROTEINS: Structure, Function, and Bioinformatics *66*, 229-238.

Thul, P.J., Åkesson, L., Wiking, M., Mahdessian, D., Geladaki, A., Ait Blal, H., Alm, T., Asplund, A., Björk, L., Breckels, L.M., et al. (2017). A subcellular map of the human proteome. Science *356*. 10.1126/science.aal3321.

Timić, T., Joksimović, S., Milić, M., Divljaković, J., Batinić, B., and Savić, M.M. (2013). Midazolam impairs acquisition and retrieval, but not consolidation of reference memory in the Morris water maze. Behavioural Brain Research *241*, 198-205. https://doi.org/10.1016/j.bbr.2012.12.014.

Tiwari, V., Borchardt, J., Schuh, A., Klug, C., and Czajkowski, C. (2020). Ligand-induced motions in pentameric ligand-gated ion channels revealed by EPR spectroscopy. bioRxiv.

Tokay, T., Hachem, R., Masmoudi-Kouki, O., Gandolfo, P., Desrues, L., Leprince, J., Castel, H., Diallo, M., Amri, M., and Vaudry, H. (2008). Beta-amyloid peptide stimulates endozepine release in cultured rat astrocytes through activation of N-formyl peptide receptors. Glia *56*, 1380-1389.

Tonon, M.C., Vaudry, H., Chuquet, J., Guillebaud, F., Fan, J., Masmoudi-Kouki, O., Vaudry, D., Lanfray, D., Morin, F., Prevot, V., et al. (2020). Endozepines and their receptors: Structure, functions and pathophysiological significance. Pharmacol Ther *208*, 107386. 10.1016/j.pharmthera.2019.06.008.

Tretter, V., Ehya, N., Fuchs, K., and Sieghart, W. (1997). Stoichiometry and Assembly of a Recombinant GABAAReceptor Subtype. The Journal of Neuroscience *17*, 2728-2737. 10.1523/jneurosci.17-08-02728.1997.

Tsao, T.-W. (2018). Uncovering structural mechanisms underlying GABA-A receptor activation and drug modulation. Doctor of Philosophy (University of Wisconsin-Madison).

Uhlén, M., Fagerberg, L., Hallström, B.M., Lindskog, C., Oksvold, P., Mardinoglu, A., Sivertsson, Å., Kampf, C., Sjöstedt, E., Asplund, A., et al. (2015). Proteomics. Tissue-based map of the human proteome. Science *347*, 1260419. 10.1126/science.1260419.

Ujjainwala, A.L., Courtney, C.D., Rhoads, S.G., Rhodes, J.S., and Christian, C.A. (2018). Genetic loss of diazepam binding inhibitor in mice impairs social interest. Genes, Brain and Behavior *17*, e12442. 10.1111/gbb.12442.

Ujjainwala, A.L., Courtney, C.D., Wojnowski, N.M., Rhodes, J.S., and Christian, C.A. (2019). Differential impacts on multiple forms of spatial and contextual memory in diazepam binding inhibitor knockout mice. Journal of Neuroscience Research. 10.1002/jnr.24393.

Vajda, S., Yueh, C., Beglov, D., Bohnuud, T., Mottarella, S.E., Xia, B., Hall, D.R., and Kozakov, D. (2017). New additions to the ClusPro server motivated by CAPRI. Proteins: Structure, Function, and Bioinformatics *85*, 435-444. 10.1002/prot.25219.

Van der Aa, N., and Kooy, R.F. (2020). GABAergic abnormalities in the fragile X syndrome. Eur J Paediatr Neurol *24*, 100-104. 10.1016/j.ejpn.2019.12.022.

Venkatachalan, S.P., Bushman, J.D., Mercado, J.L., Sancar, F., Christopherson, K.R., and Boileau, A.J. (2007). Optimized expression vector for ion channel studies in Xenopus oocytes and mammalian cells using alfalfa mosaic virus. Pflugers Arch *454*, 155-163. 10.1007/s00424-006-0183-1.

Venkatachalan, S.P., and Czajkowski, C. (2012). Structural link between γ-aminobutyric acid type A (GABAA) receptor agonist binding site and inner β-sheet governs channel activation and allosteric drug modulation. The Journal of biological chemistry *287*, 6714-6724. 10.1074/jbc.M111.316836.

Vien, T.N., Modgil, A., Abramian, A.M., Jurd, R., Walker, J., Brandon, N.J., Terunuma, M., Rudolph, U., Maguire, J., Davies, P.A., and Moss, S.J. (2015). Compromising the phosphodependent regulation of the GABA(A)R beta 3 subunit reproduces the core phenotypes of autism spectrum disorders. P Natl Acad Sci USA *112*, 14805-14810. 10.1073/pnas.1514657112.

Vranken, W.F., Boucher, W., Stevens, T.J., Fogh, R.H., Pajon, A., Llinas, M., Ulrich, E.L., Markley, J.L., Ionides, J., and Laue, E.D. (2005). The CCPN data model for NMR spectroscopy: Development of a software pipeline. Proteins: Structure, Function, and Bioinformatics *59*, 687-696. https://doi.org/10.1002/prot.20449.

Wagner, D.A. (2004). An Arginine Involved in GABA Binding and Unbinding But Not Gating of the GABAA Receptor. J Neurosci *24*, 2733-2741. 10.1523/jneurosci.4316-03.2004.

Wagoner, K.R., and Czajkowski, C. (2010). Stoichiometry of Expressed α4β2δ γ-Aminobutyric Acid Type A Receptors Depends on the Ratio of Subunit cDNA Transfected. J Biol Chem *285*, 14187-14194. 10.1074/jbc.m110.104257.

Walsh, R.M., Roh, S.-H., Gharpure, A., Morales-Perez, C.L., Teng, J., and Hibbs, R.E. (2018). Structural principles of distinct assemblies of the human α4β2 nicotinic receptor. Nature *557*, 261-265. 10.1038/s41586-018-0081-7.

Wang, D., Liu, D., Yuchi, J., He, F., Jiang, Y., Cai, S., Li, J., and Xu, D. (2020). MusiteDeep: a deep-learning based webserver for protein post-translational modification site prediction and visualization. Nucleic Acids Research *48*, W140-W146. 10.1093/nar/gkaa275.

Wisden, W., Yu, X., and Franks, N.P. (2019). GABA Receptors and the Pharmacology of Sleep. Handb Exp Pharmacol *253*, 279-304. 10.1007/164_2017_56.

Yamasaki, T., Hoyos-Ramirez, E., Martenson, J.S., Morimoto-Tomita, M., and Tomita, S. (2017). GARLH Family Proteins Stabilize GABA(A) Receptors at Synapses. Neuron *93*, 1138-1152.e1136. 10.1016/j.neuron.2017.02.023.

Yip, G.M., Chen, Z.W., Edge, C.J., Smith, E.H., Dickinson, R., Hohenester, E., Townsend, R.R., Fuchs, K., Sieghart, W., Evers, A.S., and Franks, N.P. (2013). A propofol binding site on mammalian GABAA receptors identified by photolabeling. Nat Chem Biol *9*, 715-720. 10.1038/nchembio.1340.

Zhang, Y., Chen, K., Sloan, S.A., Bennett, M.L., Scholze, A.R., O'Keeffe, S., Phatnani, H.P., Guarnieri, P., Caneda, C., Ruderisch, N., et al. (2014). An RNA-Sequencing Transcriptome and

Splicing Database of Glia, Neurons, and Vascular Cells of the Cerebral Cortex. J Neurosci *34*, 11929-11947. 10.1523/jneurosci.1860-14.2014.

Zhang, Y., Sloan, S.A., Clarke, L.E., Caneda, C., Plaza, C.A., Blumenthal, P.D., Vogel, H., Steinberg, G.K., Edwards, M.S.B., Li, G., et al. (2016). Purification and Characterization of Progenitor and Mature Human Astrocytes Reveals Transcriptional and Functional Differences with Mouse. Neuron *89*, 37-53. 10.1016/j.neuron.2015.11.013.

Zhu, S., Noviello, C.M., Teng, J., Walsh, R.M., Jr., Kim, J.J., and Hibbs, R.E. (2018). Structure of a human synaptic GABA(A) receptor. Nature *559*, 67-72. 10.1038/s41586-018-0255-3.